BINDING SERVICES
Tel +44 (0)29 2087 4949
Fax +44 (0)29 20371921
e-mail bindery@cardiff.ac.uk

FRACTURE AND FATIGUE OF CARDIFRC®

A thesis submitted for the degree of
Doctor of Philosophy

by

Demetris Nicolaides

School of Engineering
Cardiff University
United Kingdom

September 2004

ProQuest LLC
789 East Eisenhower Parkway
P.O. Box 1346
Ann Arbor, MI 48106-1346

"Build me straight, O worthy Master!

Staunch and strong, a goodly vessel,

That shall laugh at all disaster,

And with wave and whirlwind wrestle!"

from *The Building of the Ship*,

Henry Wadsworth Longfellow

To my beloved family

ACKNOWLEDGEMENT

First of all, I would like to express my sincere thanks and gratitude to my supervisor, Professor Bhushan Karihaloo, for his continuous advice, encouragement, support and guidance throughout, without which, this work would not have been completed.

I would like to thank the civil engineering laboratory staff, in particular Des Sanford, Brian Hooper, Carl Wadsworth, Andrew Sweeney, whose assistance was invaluable. I am also grateful to Dr Qizhi Xiao due to his valuable comments in the theoretical parts of the study. Special tribute is also due to my colleagues and friends Antonios Kanellopoulos and Farhat Farhat for their valuable support and continuous encouragement.

Finally, I would like to pay a special tribute to my family, without the love, understanding, encouragement and support of whom I could not have sustained such a lengthy dedicated period of work:

...Τά των τεκόντων τα όμμαθ' ήδιστον βλέπειν...
(...it is pleasant to look into your parents eyes...)
Οιδίπους Τύραννος, Στ. 999

SYNOPSIS

The flexural fracture and fatigue response of high performance fibre reinforced cementitious composites, designated CARDIFRC®, was investigated in this study. CARDIFRC® is characterised by high tensile/flexural strength and high energy absorption capacity (i.e. ductility). The special characteristics of CARDIFRC® make it particularly suitable for repair, remedial and upgrading activities (i.e. retrofitting) of existing concrete structures.

One of the major factors affecting the flexural fracture and fatigue behaviour of CARDIFRC® specimens was found to be the distribution of fibres within the mix, and it is on this factor that the greater part of this thesis is focused. An even and proper distribution of fibres can lead to excellent flexural fracture behaviour and an extremely high fatigue life of CARDIFRC® specimens. On the other hand, poor fibre distribution results in undesirable performance and failure, well below the designed capacity of the material.

In particular, the thesis addresses the following key points. The first point concerns the static flexural behaviour of CARDIFRC® specimens and the prediction of their load-displacement behaviour. A nonlinear cracked hinge model has been used for the simulation, and the analytical results were found to be in very good agreement with the test results. In addition, a combined damage/fracture mechanics approach to the description of the flexural behaviour is presented, in which a continuum damage model is used up to the peak load followed by a fracture mechanics approach when the damage has localised along the eventual fracture plane.

The second key point concerns the flexural fatigue behaviour of CARDIFRC®, subjected to several stress amplitude ranges. Careful preparation of CARDIFRC® specimens guarantees an excellent and absolutely consistent fatigue response. The endurance limit of the material is very high, not very often observed in the relevant literature. This is an indication that CARDIFRC® has an excellent flaw tolerance. Despite the excellent fatigue performance, some small internal damage was noticed, after a very large number of cycles, but this damage is distributed, without the development of any visible crack on the surface.

The last key point concerns the distribution of a large volume of short steel fibres in the mix. A thorough investigation of the fibre distribution was accomplished by image analysis of selected planes of failure, in order to explain the corresponding specimen fatigue behaviour. Moreover, a near linear correlation between the image analysis data and a novel non-destructive technique based on computerised tomography (CT) imaging was observed.

TABLE OF CONTENTS

Acknowledgements *i*

Synopsis *ii*

List of Figures *ix-xii*

List of Tables *xiii*

Chapter 1: Introduction **1**

1.1 Introduction 1

1.2 Scope and objectives of the thesis 4

1.3 Outline of the thesis 4

Chapter 2: Fracture mechanics of concrete 7

2.1 Introduction 7

2.1.1 Why apply fracture mechanics to concrete? 7

2.2 Linear elastic fracture mechanics (LEFM) 9

2.2.1 Griffith's theory of brittle fracture 9

2.2.2 Irwin's theory of brittle fracture 12

2.2.3 Irwin theory and local energy considerations 16

2.2.4 Barenblatt's cohesive crack model 17

2.2.5 Why LEFM is not applicable to HPFRCCs 19

2.2.6 Fracture process zone (FPZ) 20

2.3 Nonlinear fracture mechanics (NLFM) 22

2.3.1 Fictitious crack model (FCM) 23

2.3.2 Crack band model (CBM) 25

2.3.3 Fracture parameters needed for NLFM 27

Chapter 3: HPFRCCs and CARDIFRC® **28**

3.1 Introduction 28

3.2 HPFRCCs 28

3.2.1 The effect of high temperature curing conditions 29

3.2.2 The effect of silica fume 30

3.2.3 The effect of dispersing agent (superplasticiser) 32

3.2.4 The effect of steel fibres 33

3.2.4.1 Volume fraction of fibres 34

3.2.4.2 Aspect ratio of fibre (*l/d*) 35

3.2.4.3 Bridging action of the fibres 35

3.2.5 Constitutive model 38

3.2.5.1 Linear elastic behaviour 39

3.2.5.2 Strain-hardening behaviour 40

3.2.5.3 Tensile strength (f_t') 42

3.2.5.4 Tension softening behaviour 43

3.2.6 Types of HPFRCC 45

3.2.6.1 Macro-Defect-Free cement (MDF) 45

3.2.6.2 Slurry Infiltrated Fibre Concrete (SIFCON) 46

3.2.6.3 Engineered Cementitious Composites (ECC) 46

3.2.6.4 Reactive Powder Concrete (RPC) 47

3.2.6.5 DSP cementitious materials 47

3.3 CARDIFRC® 48

3.3.1 Constitutive description of CARDIFRC® 50

3.4 Conclusions 52

Chapter 4: Dynamic response of concrete **53**

4.1 Introduction 53

4.2 Fatigue response 55

4.2.1 Introduction 55

4.2.2 Fatigue loading testing configurations 56

4.2.3 Experimental works 59

4.2.4 Discussion 66

4.2.5 Fatigue modelling 70

4.2.5.1 Introduction 70

4.2.5.2 Models for fatigue strength and fatigue life prediction 71

4.2.5.3 Cyclic behaviour 72

4.2.5.4 Macromechanics based models 74

4.2.5.5 Micromechanics based models 80

4.2.5.6 Models originally developed for ceramic composites 87

4.3 High strain or stress rate 88

4.3.1 Introduction 88

4.3.2 High strain rate testing configurations 88

4.3.3 High strain rate testing problems 94

4.3.4 Experimental works 95

4.3.5 Discussion and conclusions 100

4.4 Impact loading 103

4.4.1 Introduction 103

4.4.2 Impact testing configurations 103

4.4.3 Impact testing problems 107

4.4.4 Improvement of performance of concrete against impact loading 109

4.4.5 Experimental works 110

Chapter 5: Determination of the size-independent specific fracture energy of CARDIFRC® from three-point bend tests **114**

5.1 Introduction 114

5.2 Experimental results 119

5.3 Discussion 122

Chapter 6: Static and fatigue response of CARDIFRC® - Experimental results **125**

6.1 Introduction 125

6.2 Mix preparation 125

6.2.1 Mix I 125

6.2.2 Mix II 126

6.3 Control tests 128

6.3.1 Compressive strength tests 128

6.3.2 Tensile splitting tests 130

6.3.3 Modulus of elasticity (E) 132

6.3.4 Modulus of rupture (MOR) 133

6.3.5 Three-point bend tests (100x100x500 mm) 135

6.4 Fatigue tests (100x100x500 mm) 138

6.4.1 Test variables 140

6.4.2 Experimental results 141

6.4.3 Analysis of experimental results 143

6.5 Three-point bend tests 144

6.5.1 Cut specimens (250x100x33 mm) 144

6.5.2 Specimens of dimensions 360x90x35 mm 146

6.6 Fatigue tests (360x90x35 mm) 148

6.7 Examination of the compliance of fatigue specimens 153

Chapter 7: Fibre distribution **158**

7.1 Introduction 158

7.2 CT imaging 158

7.3 Image analysis 160

7.3.1 Optical microscope results 162

7.3.2 Analysis of optical microscope results 163

7.4 Comparison of CT imaging and image analysis results 169

7.4.1 Discussion 177

7.5 Fatigue specimens 185

7.6 Conclusions 193

Chapter 8: Modelling of the static flexural response of CARDIFRC® beams **194**

8.1 Fictitious crack propagation in fibre-reinforced concrete BEAMS 194

8.1.1 Introduction 194

8.1.2 Cracked hinge model 195

8.1.3 Application to a three-point bend beam 200

8.1.4 Modelling of the static response of CARDIFRC® beams tested in 3-point bending 202

8.1.5 Results and discussion 204

8.1.6 Conclusions 207

8.2 Combined damage/fracture mechanics approach to the description of concrete flexural behaviour 208

8.2.1 Introduction 208

8.2.2 Continuum damage mechanics approach 208

8.2.3 Fracture mechanics approach for post-peak response 213

8.2.4 Fracture mechanics approach for load-COD response of CARDIFRC® 217

8.2.4.1 Condition of smooth closure of crack faces 218

8.2.4.2 Crack opening compatibility equation 222

8.2.5 Conclusions 224

Chapter 9: Conclusions and recommendations for future work 225

9.1 Conclusions 225

9.2 Recommendations for future work 228

List of references 230

Appendix A: Fatigue test results 247

Appendix B1: Derivation of the moment μ and the crack length a_h for phases I, II, and III 271

Appendix B 2: The algorithm for the cracked hinge model 290

Appendix C: A comparison of hinge model prediction with test results 298

List of Figures

Figure		Page
2.1	The principle of superposition (a) the plate is under external tension (b) uncracked plate under σ (c) plate without external σ but with equal and opposite stress applied to the crack to create a stress-free crack.	10
2.2	Modes of crack propagation.	13
2.3	An infinite elastic body with a sharp crack of length $2a$ under Mode I.	14
2.4	Shapes of traction-free crack tip zones and distribution of normal stress, σ_{yy} in front of the crack tip for $K_I > 0$, $K_I < 0$ and $K_I = 0$.	14
2.5	Barenblatt cohesive crack model in Mode I. Note $c << a$.	18
2.6	Typical load-deformation response of a quasi-brittle material in tension/flexure (a) and the fracture process zone ahead of the real traction-free crack (b).	20
2.7	Schematic representation of the fracture process zone (a) microcracking at aggregate, (b) debonding and microcracking, (c) coalescence of debond crack with macrocrack, and microcracking, (d) crack bridging, debonding, crack branching and microcracking.	21
2.8	Distinguishing features of fracture in (a) a linear material, (b) a ductile material, (c) a quasi-brittle material. L refers to linear elastic region, N to nonlinear zone, and F to fracture process zone.	23
2.9	(a) A real traction-free crack of length a_0 terminating in a fictitious crack of length l_p whose faces close smoothly near its tip (K_I=0). The material ahead of the fictitious crack tip is assumed to be linear (b), but the material within the fracture process zone is softening; the area under softening curve equals fracture energy G_F(c).	24
2.10	Crack band model for fracture of concrete (a) a microcrack band fracture and (b) stress-strain curve for the microcrack band.	26
3.1	Microsilica Particles.	30
3.2	(a) Flocculated particles in ordinary cement paste. (b) Densely packed cement grains and microsilica in DSP paste.	32
3.3	(a) Flocculated particles in cement paste. (b) Superplasticised cement particles.	33
3.4	(a) A single fibre pull-out without snubbing $(\phi = 0)$ and (b) with snubbing $(\phi \neq 0, \phi = \varphi)$.	36
3.5	A linearised bridging law describing the relation between the bridging force and the crack opening displacement.	36
3.6	Idealised interfacial matrix-fibre shear stress (τ) vs. half crack mouth opening for single fibre (dashed line) and multiple fibre (solid line) pull-out.	37
3.7	Complete pre- and post-peak tensile response of two short fibre-reinforced cementitious composites.	38
3.8	(a) Representative unit volume of the matrix containing one microcrack of length $2a$ (note that the volume V of this unit = W*H*1 and the surface area of the crack S =2a*1); (b) an enlarged view of the crack opening.	42
3.9	(a) Crack configuration prior to coalescence of crack (b) after coalescence of cracks during tension softening of fibre-reinforced quasi-brittle materials.	45
3.10	Complete pre- and post peak tensile curve for CARDIFRC®.	51
4.1	Types of stress cycle: (a) alternating (b) repeating (c) fluctuating.	56
4.2	Loading device of WST and specimen geometry.	57
4.3	Experimental setup for direct tension testing of notched specimens.	58
4.4	Stress-deformation relation under cyclic loading.	69
4.5	Load-deformation histogram for specimen with 0.5% steel fibre content.	72
4.6	Strain accumulation histogram for SFRC at stress-strength ratio 0.90.	73
4.7	Damage accumulation histogram (measured by energy ratio) for SFRC at stress-strength 0.90.	74
4.8	Model of fatigue crack growth.	76
4.9	Material behaviour in loading part and unloading part.	76

Figure		Page
4.10	Mechanical model for thermodynamically consistent constitutive equation.	77
4.11	Strain evolution for a stable process.	78
4.12	Strain evolution for an unstable process.	78
4.13	Setup for the crack cyclic behaviour model.	79
4.14	Fatigue damage on material constituents.	80
4.15	Typical SHPB setup.	89
4.16	Direct Impact Hopkinson Bar (DIHB) test.	90
4.17	Experimental technique based on Hopkinson Bar principle combined with the spalling phenomenon.	91
4.18	Configuration of the plate impact experiment.	92
4.19	Configuration of the Hopkinson Bar Bundle (HBB) experiment.	93
4.20	Test setup for impact tests.	104
4.21	a) Test setup for the determination of crack velocity, b) Dimensions of specimen.	106
4.22	General features of the modified Charpy test.	107
5.1	The fracture process zone and discreet bridging stresses. The FPZ is divided into the inner softening zone and the outer micro-fracture zone. w_c is related to the width of the inner softening zone w_{sf}.	115
5.2	If g_f decreases monotonically along the ligament, G_f has to be dependent on the a/W ratio, as observed in many experiments.	117
5.3	The distribution of fracture energy (G_f and g_f) along the un-notched ligament, W-a (b) of a notched test specimen of depth W and notch depth a (a).	118
5.4	Specimen shapes and dimensions.	119
5.5	3-point bend testing configuration.	120
5.6	3-point bend test graphs for CARDIFRC mixes I and II, notches 5 and 50 mm.	121
6.1	FARNELL compression testing machine.	129
6.2	The jig used for the tensile splitting test.	131
6.3	Schematical presentation of the modulus of rupture (MOR) test.	134
6.4	Schematical presentation of the 3 – point bending test.	137
6.5	Load – displacement response of CARDIFRC® - Mix I beams tested in 3 – point bending.	137
6.6	Load – displacement response of CARDIFRC® - Mix I beams tested in 3 – point bending at higher strain rates.	138
6.7	Logging system of the fatigue response of CARDIFRC® specimens.	140
6.8	Fatigue life of CARDIFRC® - Mix I beams (100x100x500 mm).	142
6.9	Schematical presentation of the cut specimens and the fibres density in top, middle and bottom specimens.	145
6.10	Load – displacement response of CARDIFRC® - Mix I beams (360x90x35 mm) tested in 3 – point bending.	147
6.11	Distribution of probability ultimate load P_u be lower than μ-2σ.	148
6.12	Load – displacement response of CARDIFRC® - Mix I beams (360x90x35 mm) tested in 3 – point bending, after subjected fatigue loading (1000000 cycles) between 10%-80% P_u.	152
6.13	Load – displacement response of CARDIFRC® - Mix I beams (360x90x35 mm) tested in 3 – point bending, after subjected fatigue loading (1000000 cycles) between 10%-85% P_u.	152
6.14	Load – displacement response of CARDIFRC® - Mix I beams (360x90x35 mm) tested in 3 – point bending, after subjected fatigue loading (1000000 cycles) between 10%-90% P_u.	153
6.15	Typical load-displacement curve of CARDIFRC® - Mix I specimen (360x90x35 mm) tested in fatigue (load amplitude 10%-90% P_u, specimen failed after 21564 cycles).	156
6.16	Compliances of the loading branch of fatigue cycles (360x90x35 mm CARDIFRC® beams, load amplitude 10%-90% P_u).	156

Figure		Page
6.17	Compliances of the loading and unloading branches of fatigue cycles (360x90x35 mm CARDIFRC® beams, load amplitude 10%-85% P_u).	157
7.1	Figures showing the cast face (i.e. the surface finished with the trowel during casting) in relation to the orientation of the scans. (a) beam, (b) 20 mm thick strip, (c) 16 mm thick strip and (d) cylinder.	159
7.2	10 mm x 10 mm grids used for image analysis. (a) 100 mm x 100 mm beam, (b) 100 mm diameter cylinder, (c) 20 mm thin strip and (d) 16 mm thin strip (grid in row 2 is only 6 mm x 10 mm).	162
7.3	Buffon needle problem in two-dimensions.	164
7.4	Pictures of CARDIFRC® specimen sections used for image analysis.	172
7.5	Contour plots showing the X-ray absorption densities for the beam cross-section (100 mm x 100 mm) for (a) slice 2 and (b) slice 18.	173
7.6	Contour plots showing the X-ray absorption densities for the cylinder (100 mm diameter) for (a) slice 3 and (b) slice 10.	173
7.7	Contour plots showing the X-ray absorption densities for the 16 mm strip cross-section (100 mm width) for (a) slice 2 and (b) slice 22.	174
7.8	Contour plots showing the X-ray absorption densities for the 20 mm strip cross-section (100 mm width) for (a) slice 3 and (b) slice 20.	174
7.9	Contour plots showing the fibre distribution for the 100x100 mm beam cross-section for (a) slice 2 and (b) slice 18.	175
7.10	Contour plots showing the fibre distribution for the cylinder (100 mm diameter) cross-section for (a) slice 3 and (b) slice 10.	175
7.11	Contour plots showing the fibre distribution for the 16 mm strip cross-section (100 mm width) for (a) slice 2 and (b) slice 22.	176
7.12	Contour plots showing the fibre distribution for the 20 mm strip cross-section (100 mm width) for (a) slice 3 and (b) slice 20.	176
7.13	Uniform distribution of fibres.	178
7.14	Clustered distribution of fibres.	178
7.15	Specimen area detected twice during image analysis.	180
7.16	Contour plots showing the X-ray absorption densities (a) and (c), and the fibre count (b) and (d) for the cylinder slices 10 and 3, respectively.	181
7.17	Contour plots showing the X-ray absorption densities (a) and (c), and the fibre count (b) and (d) for the beam slices 2 and 18, respectively.	182
7.18	X-ray absorption density vs. number of fibres per cm^2 in (a) cylinder slice 10 and (b) cylinder slice 3.	183
7.19	X-ray absorption density vs. number of fibres per cm^2 in (a) beam slice 2 and (b) beam slice 18.	184
7.20	Contour plot showing the fibre distribution for the 100x100 mm beam plane of failure, after fatigue testing between 10-70% P_u (failure after 4 cycles).	187
7.21	Plane of failure of the 100x100 mm beam after fatigue testing between 10-70% P_u (failure after 4 cycles).	187
7.22	Contour plot showing the fibre distribution for the 100x100 mm beam plane of failure, after fatigue testing between 10-70% P_u (failure after 3 cycles).	188
7.23	Plane of failure of the 100x100 mm beam after fatigue testing between 10-70% P_u (failure after 3 cycles).	188
7.24	Contour plot showing the fibre distribution for the 100x100 mm beam plane of failure, after fatigue testing between 10-70% P_u (failure after 437 cycles).	189
7.25	Contour plot showing the fibre distribution for the 100x100 mm beam plane of failure, after fatigue testing between 10-70% P_u (failure after 5910 cycles).	190
7.26	Contour plot showing the fibre distribution for the 100x100mm beam plane of failure, after fatigue testing between 10-70% P_u (failure after 110999 cycles).	190
7.27	Contour plot showing the fibre distribution for the 100x100 mm beam plane of failure, after fatigue testing between 10-70% P_u (failure after 527988 cycles).	191
7.28	Contour plot showing the fibre distribution for the 100x100 mm beam plane of failure, after fatigue testing between 10-70% P_u (no failure after 1000000 cycles).	191
7.29	Relation between average number of fibres and number of cycles to failure.	192

Figure		Page
8.1	Three-point notched bend beam with a non-linear hinge modelling the propagation of a crack at mid-section, with the illustration of an incremental horizontal layer of the hinge shown below the beam. To the right: geometry of the hinge deformation.	195
8.2	Geometry, loading and deformation of cracked hinge.	196
8.3	Definition of a bi-linear stress-crack opening relationship and the four different phases of crack propagation. Phase 0 = State of stress prior to cracking; Phases I-III = States of stress during crack propagation.	196
8.4	Definition of parameters of bilinear stress-crack opening relationship for CARDIFRC®.	203
8.5	The load-deformation curves generated by the hinge model for the two bilinear approximations (HM1 and HM2) of the softening branch of CARDIFRC®, for Mix I specimens (100x100x500 mm) tested in three-point bending.	204
8.6	The experimental load-deformation curves for CARDIFRC® - Mix I specimens (100x100x500 mm) and the load-deformation curve generated by the hinge model (HM1).	205
8.7	The experimental load-deformation curves for CARDIFRC® - Mix I specimens (100x100x500 mm) and the load-deformation curve generated by the hinge model (HM2).	205
8.8	Plane of failure of CARDIFRC® - Mix I specimen No.3 (100x100x500 mm) tested in three-point bending.	207
8.9	Schematical explanation of the damage evolution, quantified by the scalar damage parameter ω.	210
8.10	Distributed damage in the form of bridged microcracks in the material, corresponding to $\sigma_{th}<\sigma\leq\sigma_{max}$ and $\omega>0$ (pre-peak nonlinear part of the stress-strain diagram).	211
8.11	The experimental load-deformation curves for CARDIFRC® - Mix I specimens (100x100x500 mm) and the pre-peak curve generated according to damage mechanics theory (DM).	212
8.12	Evolution of the scalar damage parameter ω with flexural stress, in the pre-peak part.	213
8.13	Schematical explanation of crack geometry and loading.	215
8.14	Schematical explanation of cohesive crack geometry and cohesive stress distribution.	216
8.15	Free body diagram of the dominant flexural crack in CARDIFRC® beams.	218
8.16	Smooth closure crack faces.	219
8.17	Towards the discretisation of the bridging stresses.	220

List of Tables

Table		Page
3.1	Mix proportions for optimised CARDIFRC® Mix I and Mix II (per m^3).	50
3.2	Typical material properties of CARDIFRC® Mix I and Mix II.	50
5.1	Experimental results.	121
5.2	Experimental results.	122
5.3	Experimental results.	123
6.1	Compressive strength results for CARDIFRC® Mix I – *sp/w* = 0.18.	129
6.2	Compressive strength results for CARDIFRC® Mix I – *sp/w* = 0.21.	129
6.3	Compressive strength results for CARDIFRC® Mix II – *sp/w* = 0.40.	130
6.4	Tensile splitting strength results for CARDIFRC® Mix I – *sp/w* = 0.18.	131
6.5	Tensile splitting strength results for CARDIFRC® Mix I – *sp/w* = 0.21.	131
6.6	Tensile splitting strength results for CARDIFRC® Mix II – *sp/w* = 0.40.	132
6.7	MOR results for CARDIFRC® Mix I – *sp/w* = 0.18.	134
6.8	Tensile/flexural strength results for CARDIFRC® Mix I – *sp/w* = 0.18.	136
6.9	Number of cycles sustained by CARDIFRC® - Mix I beams (100x100x500 mm).	142
6.10	Experimental peak loads of cut specimens of CARDIFRC® - Mix I.	146
6.11	Tensile/flexural strength results for CARDIFRC® - Mix I (360x90x35 mm).	147
6.12	Flexural fatigue tests experimental results (CARDIFRC® -Mix I, 360x90x35 mm).	149
6.13	Experimental peak loads and tensile/flexural strengths of CARDIFRC® - Mix I beams (360x90x35 mm), tested in 3 – point bending, after they have been subjected fatigue loading.	151
7.1	Average number of fibres resulting from image analysis of specimen sections.	163
7.2	Average number of fibres resulting from image analysis of specimens tested under fatigue loading.	185
7.3	Statistical analysis of the results of the image analysis of specimens tested under fatigue loading.	185
8.1	Parameters of bilinear stress-crack opening relationship for CARDIFRC®.	203

CHAPTER 1: INTRODUCTION

1.1 INTRODUCTION

Plain and reinforced concrete structures are full of flaws, even before they are mechanically loaded. These flaws, and especially the small cracks (microcracks), grow stably under external loading, coalesce with existing or newly-formed microcracks until large fractures are formed which cause the collapse of the structure. When a load is applied there will be high stress concentrations around these cracks, higher than those at other points within the structure. During service, these cracks propagate and can be a serious problem in such structures.

To date, these structures are designed without regard to either the propagation of large cracking zones through them or an energy failure criterion. Fracture mechanics provides an energy based failure theory that could be used in designing cement-based structures, since it studies the response and failure of structures as a consequence of crack initiation and propagation (Karihaloo, 1995). The application of fracture mechanics to concrete structures has provided new ways of understanding and modelling phenomena which could only be treated empirically before.

As long as cracking in concrete is unavoidable, we have to try to minimise their detrimental effect. This objective can be achieved by resisting propagation of existing cracks. The research on the development of Fibre Reinforced Concretes (FRCs) and particularly of High Performance Fibre Reinforced Cementitious Composites (HPFRCCs) is focused on this. HPFRCCs represent a class of cement composites whose stress-strain response in tension undergoes strain hardening behaviour accompanied by multiple cracking, leading to a high failure strain capacity. HPFRCCs result from advances in manufacturing processing that permit the inclusion of a large amount of fibres in the cement based matrix without affecting the workability of the mix. These advances are based on the use of silica fume and surfactants which reduce water demand and densify the matrix, thereby improving the fibre-matrix interfacial bond (Morin et al., 2001; Bache, 1981). The inclusion of fibres contributes substantially to the reduction of the brittleness of the matrix and also to the reduction of the tendency of the matrix cracks to propagate. Therefore, the

even distribution of fibres in the material is of vital importance for the fracture behaviour of the structure.

Rheological studies were carried out at Cardiff to optimise HPFRCC. The aim was to achieve good workable mixes with a very low water/binder ratio and a high volume fraction of steel fibre, in order that the resulting concrete, in its hardened state, was very ductile with a relatively high tensile strength. This was achieved by using large amounts (up to 8 % by volume) of short steel fibres (6-13 mm long, 0.16 mm diameter) in a cementitious matrix densified by the use of silica fume. The matrix contains only very fine quartz sands (maximum size up to 2 mm), instead of ordinary river sand and coarse aggregates. By optimising the grading of fine sands, the water demand is considerably reduced without affecting the workability of the mix. Two different mixes (designated CARDIFRC®, Mix I and Mix II) of high-performance FRC differing mainly by the maximum size of quartz sand used in the mix have been developed using novel mixing procedures. These procedures are described in patent application GB 0109686.6.

In order to verify that the mixing and compaction procedures used to make HPFRCCs do indeed result in the steel fibres being uniformly distributed in the hardened HPFRCCs, both destructive and non-destructive techniques can be applied. The destructive method consists of the traditional image analysis, whereas the non-destructive method is a novel technique of computerised tomography (CT) imaging. This idea was first introduced for plain concrete by Karihaloo and Jefferson (2001) and can also be extended to study the influence of mixing and compaction procedures on the distribution of fibres in fibre reinforced concretes. It is important to achieve the best possible correlation between the image analysis data on fibre distribution in the cross-section with the X-ray absorption density data. Such a correlation would open a route for fast and non-destructive evaluation of the fibre distribution in a factory environment.

In addition to static loads, many concrete structures are often subjected to short-duration dynamic loads. Under these loads, the crack development and propagation is a complex and still unclear phenomenon. Therefore, resisting the propagation of existing cracks is an even more difficult task. All fracture is dynamic in nature,

meaning it is a rate dependent process in which a discontinuity is created by cracks and voids in a previously intact material. Response of concrete to dynamic loading is of interest in a variety of civilian and military applications, such as long-span bridges, offshore structures, protective shelters, nuclear reactor containment and reinforced concrete pavements. These loads originate from sources such as vehicular traffic, impact from missiles or flying objects, projectiles, vehicle collisions, impulses due to explosions, wind gusts, machine vibrations and earthquakes.

The dynamic loading can be classified into three major types:

- Fatigue Loading
- Loading at High Strain or Stress Rate
- Impact Loading

In recent years there has been more interest in the fatigue behaviour of concrete subjected to fatigue loading, since fatigue is known to be responsible for the majority of failures of structural components. Fatigue failure occurs when a concrete structure fails catastrophically at less than the design load after being exposed to a large number of stress cycles. Concrete fatigue is a process of progressive, permanent development of small imperfections existing in the material by repetitive loads. These imperfections may be present in concrete due to concrete shrinkage, or may be caused by application of external loads.

The flexural fracture and fatigue behaviour of HPFRCCs is best described by the concepts of fracture mechanics appropriate to cementitious materials. For this description two material parameters, besides the strength and stiffness values, are needed, namely the true specific fracture energy G_F and the tension softening diagram.

The true specific fracture energy of any type of concrete G_F is the most useful material parameter in the analysis of cracked concrete structures (Karihaloo, 1995). The test method for the determination of G_F and even its precise definition has been a subject of intense debate among researchers because it has been found to vary with

the size and shape of the test specimen and with the test method used. Guinea et al. (1992) identified several sources of energy dissipation that may influence the measurement of G_F, for example the influence of curtailing the P-δ tail in a bend test (Elices et al., 1992). They concluded that when all factors are taken into account, an almost size-independent specific fracture energy G_F can be obtained. Recently it has been demonstrated that the size-independent fracture energy can be determined based on the concept of boundary effect model proposed by Duan et al. (2001), and its additional verifications by Abdalla and Karihaloo (2003), and Karihaloo et al. (2003).

1.2 SCOPE AND OBJECTIVES OF THE THESIS

The main objective of this thesis is to investigate the fracture behaviour of CARDIFRC® under static flexural loading and to predict the complete pre- and post-peak behaviour in flexure, based on the constitutive relations of the material measured in uniaxial tension. Moreover, it is aimed to shed some light on the fatigue response of CARDIFRC® under cyclic flexure and on the major parameters affecting this response. These objectives are achieved by the following experimental and theoretical investigations:

- Static and fatigue flexural testing of appropriate CARDIFRC® specimens.
- Investigation of the uniformity of the distribution of fibres in the mix.
- Prediction of the static flexural behaviour of the beams from known uniaxial tension response.

1.3 OUTLINE OF THE THESIS

The contents of the thesis are organised in chapters as follows.

In Chapter 2, an introduction to fracture mechanics of cement-based materials is provided. An introduction into the Linear Elastic Fracture Mechanics (LEFM) for brittle materials is first given. It is then shown that LEFM is not applicable to concrete. Therefore, the concepts of non-linear fracture theories for concrete are

explained. Chapter 2 provides a brief description of those aspects of fracture mechanics which will be useful for subsequent chapters.

Chapter 3 is devoted to the behaviour of HPFRCCs that have been presented to the industry so far. The chapter focuses on the benefits of this class of material and the effect of silica fume, superplasticiser and fibres on the mechanical behaviour. A constitutive model for the stress-strain behaviour of short fibre-reinforced cementitious composite in tension is described. Finally, the main types of HPFRCCs are identified, giving emphasis on CARDIFRC® which is the material under investigation.

The aim of Chapter 4 is to highlight the different types of dynamic loading and discuss the parameters affecting the dynamic response of concrete, giving emphasis on the work done on fatigue. Furthermore, it is aimed to review the various methods of testing and the problems encountered, describe some important experimental and theoretical works on dynamic loading and finally, bring to light the main damage mechanisms proposed by several researchers for dynamic loading response. Finally, a literature survey is performed on the modelling of the fatigue response of FRCs and a discussion provided on the several modelling options.

The concept of boundary effect model for the determination of the size independent specific fracture energy proposed by Duan et al. (2001) is introduced in Chapter 5. The size independent specific fracture energy for the two mixes of CARDIFRC® is estimated based on an observation made by Abdalla and Karihaloo (2003) and Karihaloo et al. (2003). They showed that the size-independent fracture energy can also be obtained from testing specimens of a single size, one half of them containing a very shallow starter crack and the other half a deep starter crack. Three-point bend (TPB) tests have been conducted on the two different mixes (I and II) of CARDIFRC® and G_F determined on the basis of the concept of local fracture energy.

Chapter 6 describes the experimental work on CARDIFRC® specimens. Information on the specimen preparation, testing procedures, instrumentation and details, all the experimental results and the problems encountered during testing is given in this chapter. The reasons for the transition from one specific specimen geometry to another are explained and the measured results are discussed and analysed.

Chapter 7 is devoted to the investigation of the fibre distribution in the mix, as it was suspected to be the critical parameter affecting the flexural fracture and fatigue response of CARDIFRC®. This was performed by sectioning and image analysis of cylinders, prisms and thin strips. These specimens had previously been investigated by the non-destructive technique of computerised tomography by Benson (2003). It is shown that a reasonable correlation exists between the image analysis data on fibre distribution in the cross-section with the X-ray absorption density data. In addition, planes of failure of specimens tested earlier in fatigue were also examined under the optical microscope, aiming to reveal the correlation between the fibre distribution and the fatigue life of the specimen.

The nonlinear cracked hinge model proposed by Olesen (2001) and described in Chapter 8 has been used for the simulation of the static response of CARDIFRC® beams, under three point bending. The model is based on the fracture mechanics concepts of the fictitious crack model, with a bilinear stress-crack opening relationship. The post-peak response (i.e. stress-crack mouth opening) of the constitutive behaviour of CARDIFRC® in uniaxial tension presented analytically in Chapter 3, is approximated by two alternative bilinear relationships. The response predicted by the nonlinear cracked hinge model is compared with the experimental curves. In addition, a combined damage/fracture mechanics approach to the description of concrete flexural behaviour is presented in Chapter 8.

Chapter 9 concludes the thesis with a summary of major conclusions and recommendations for future work.

CHAPTER 2: FRACTURE MECHANICS OF CONCRETE

This chapter will provide a broad review of the fundamental concepts of the fracture mechanics approach and its application to concrete and concrete structures.

2.1 INTRODUCTION

Based on their tensile stress-deformation response, most engineering materials can be categorised into three main classes:

- Brittle: stress suddenly drops to zero when a brittle material fractures.
- Ductile: stress remains constant when a ductile material yields.
- Quasi-brittle: is characterised by a gradually decreasing stress after the peak stress.

Concrete structures contain inherent flaws, such as water filled pores, air voids, lenses of bleed water under coarse aggregates and shrinkage cracks, even prior to the application of load. This is due to the fact that concrete is not a homogeneous material. These flaws, and especially the small cracks (microcracks), grow stably under external loading, coalesce with existing or newly- formed microcracks until large fractures are formed which lead to the collapse of the structure. When a load is applied there will be high stress concentrations around these cracks, higher than those at other points within the structure. During service, these cracks propagate and can be a serious problem in such structures. To date, these structures are designed without regard to either the propagation of large cracking zones through them or an energy failure criterion. Fracture mechanics provides an energy based failure theory that could be used in designing cement-based structures, since it studies the response and failure of structures as a consequence of crack initiation and propagation (Karihaloo, 1995).

2.1.1 Why apply fracture mechanics to concrete?

Three major obstacles are preventing the inclusion of fracture mechanics in the design codes of plain and reinforced concrete structures:

- Historical reasons; lack of a fracture theory suitable for concrete.
- Concrete regarded as being devoid of any tension carrying capability.
- Lack of training.

However, there are many provisions in the current codes of practice that lack a sound physical basis. Hawkins (1985) identified twenty-nine provisions in the ACI Code alone which could be put on a firm physical footing using the theory of fracture mechanics. Among these provisions are the various ductility limitations, and limits on minimum flexural and shear reinforcement. There are also other phenomena which cannot be adequately explained by the conventional strength failure criteria that form the basis of the current codes of practice, such as strain softening in the post- cracking behaviour, the non- simultaneous failure due to propagating cracks, as in the punching shear failure of slabs, the influence of the size of a structure upon its shear capacity, etc (Karihaloo, 1995). There are five strong reasons which support the argument for including the theory of fracture mechanics into the codes of practice, according to the ACI Committee report (ACI 446.1R-91), which are:

- Energy requirement for crack growth.
- Energy absorbing capacity and ductility.
- Size effect.
- Objectivity of load - response calculations.
- Lack of yield plateau.

An analytical description of the points listed above is given by Karihaloo (1995). As a conclusion, the above five mentioned reasons provide significant support for the inclusion of the theory of fracture mechanics in the design of concrete structures.

The five points summarised below draw the picture why fracture mechanics is made for concrete:

- Provide rational explanations for the many empirical provisions in the current design codes.
- Help achieve uniform safety margins over a wide range of structural sizes.

- Improve assessment procedures.
- Help in assessing the efficacy of repair measures.
- Stimulate the introduction of innovative materials and designs to improve structural durability and integrity.

2.2 LINEAR ELASTIC FRACTURE MECHANICS (LEFM)

2.2.1 Griffith's theory of brittle fracture

Griffith (1920) explained the large discrepancy between the theoretically predicted and the real tensile strengths of hard brittle materials. He demonstrated that the tensile fracture strength of an elastic brittle material, such as glass, is greatly affected by the presence of defects (e.g. small cracks) and other impurities in the material. These defects introduce high stress concentrations near their tips and therefore, the tensile strength of material is exceeded earlier than when the stress is uniformly distributed in the material. These cracks could be present prior to the application of any load or may form during the load application. The Griffith theory is based on the assumption that fracture initiates at these cracks as a result of very high tensile stress concentrations, which are induced around the crack tips when the load is applied (Anthony and Newman, 1965).

Griffith has demonstrated that in practice the true tensile strength of brittle materials is so much lower than their theoretically expected strength because of the presence of cracks in these brittle materials (Karihaloo, 1995). The Griffith theory is also called "the energy-balance concept of fracture", because his analysis was based on energy considerations. He considered a large plate of unit thickness containing a crack of length $2a$ subjected to a uniform tensile stress σ (Figure 2.1a).

From Inglis's (1913) solution for a slit-like cut of length $2a$, the vertical displacement of the upper face of the cut is given by:

$$v(x) = \frac{2\sigma}{E}\sqrt{a^2 - x^2}, \qquad 0 \le |x| \le a \tag{2.1}$$

where E is Young's modulus.

With reference to Figure 2.1, it is seen that the elastic plate with the slit-like cut of length $2a$ can be considered as the superposition of an elastic plate without a crack under an external load σ and the same plate without external load σ but with equal and opposite stresses (i.e. $-\sigma$) applied gradually to the faces of the crack. In this process, the stress σ on each of the two faces is displaced by the amount $v(x)$ of Equation (2.1), so that the amount of the work done is:

$$W = 2\left(-\frac{\sigma}{2}\int_{-a}^{a} v(x)dx\right) = -\frac{\pi a^2 \sigma^2}{E} \tag{2.2}$$

The factor 2 in Equation (2.2) indicates the two faces of the crack, whereas the factor $\frac{1}{2}$ appears because the stress gradually increases from 0 to σ.

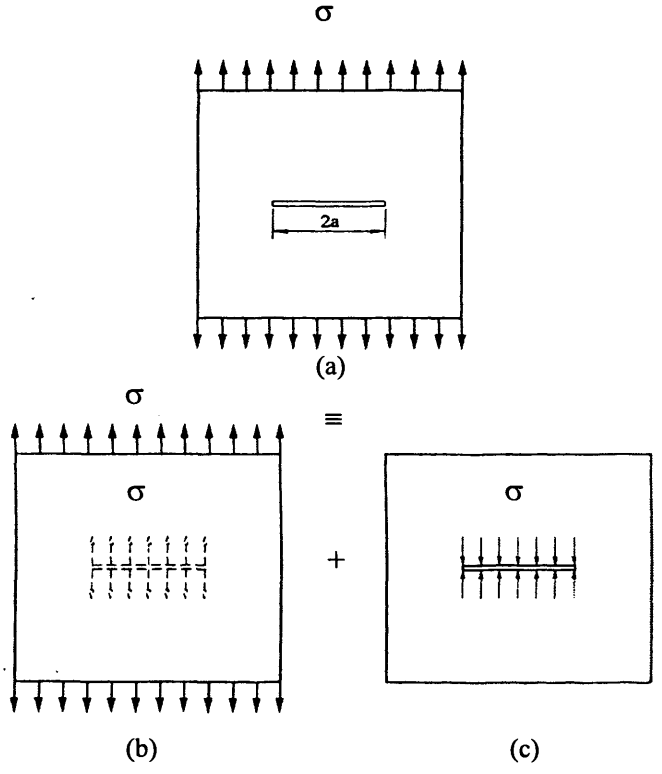

Figure 2.1: The principle of superposition (a) the plate is under external tension (b) uncracked plate under σ *(c)* plate without external σ but with equal and opposite stress applied to the crack to create a stress-free crack (After Karihaloo, 1995).

The work done W (Equation (2.2)) is equal to the elastic strain energy released during the crack formation if the loaded panel boundaries are fixed and cannot displace (Karihaloo, 1995). On the other hand, if the panel boundaries are free to move, the

elastic strain energy U of the panel increases during the crack formation and W is equal to the change of the potential energy Π of the system.

If the crack is growing stably, then for an increment of crack growth,

$$dW = -d\Gamma \tag{2.3}$$

Γ is the surface energy consumed in the creation of the crack and is given by:

$$\Gamma = 4a\gamma \tag{2.4}$$

where γ is the surface energy density, that is the energy required to create a unit crack surface.

For a stable crack growth, the energy equilibrium condition may be obtained by minimizing the energy change in Equation (2.3) with respect to the change in crack length *da*:

$$\frac{\partial}{\partial a}(W + \Gamma) = 0 \tag{2.5}$$

The energy release rate G is defined as:

$$G = \frac{\partial W}{\partial a} \tag{2.6}$$

and the fracture resistance of the material (crack resistance force) is given by:

$$R = \frac{\partial \Gamma}{\partial a} \tag{2.7}$$

Substituting Equations (2.2) and (2.4) into Equation (2.5) gives:

$$\sigma^2 = \frac{2E\gamma}{\pi a} \tag{2.8}$$

Equation (2.8) is referred to as the Griffith fracture criterion.

For a given material (i.e. given E and γ) it follows that:

$$\sigma\sqrt{\pi a} = \sqrt{2E\gamma} = \text{const.} \tag{2.9}$$

According to the Griffith fracture criterion or the global energy criterion a brittle material will fracture when the stress σ reaches a critical value σ_c that satisfies Equation (2.9). It shows that the strength of a brittle material is dependent upon physical parameters such as the Young modulus, the specific surface energy and the length of cracks. It also indicates that the fracture of a brittle material can be explained by the difference between the energy released during crack extension and that needed to create new cracks (if gain in surface energy is equal to loss of strain energy, the crack is able to propagate enough to fracture a material). The Griffith theory is only applicable to elastic homogeneous brittle materials, such as glass.

2.2.2 Irwin's theory of brittle fracture

According to Griffith's theory, in a brittle body, the entire fracture process takes place at the crack tips where the stress field is singular; the rest of the body remains elastic. Besides this fact, Irwin (1957) also noted that in the neighbourhood of the sharp crack tips, the stress components are the same regardless of the shape of the elastic body and the manner of loading. He suggested that Griffith's theory could be applied to materials that exhibit plastic deformation (ductile materials), if the energy used in the plastic deformation is included in Equation (2.9). Hence Equation (2.9) becomes,

$$\sigma = \sqrt{\frac{2E(\gamma + \gamma_p)}{\pi a}} \tag{2.10}$$

where, γ_p is the energy used in the plastic deformation associated with crack extension.

Irwin (1957) also identified three types of independent stress states that can cause a crack to move relative to the applied load:

- The Opening Mode. This is the common type of fracture modes and the crack surfaces move in the y-direction (Figure 2.2a). The forces are perpendicular to the crack and is denoted by Mode *I*.
- The Sliding Mode. In this mode of fracture the crack surfaces move horizontally in the x-direction (Figure 2.2b). The forces are acting parallel to the crack

creating a shear crack. This mode of cracking is also referred to as in-plane shear and is denoted by Mode *II*.

- The Tearing Mode. In this mode of fracture (also called as out-of plane shear) the crack surfaces move across each other in the z-direction (Figure 2.2c). The forces are parallel to the crack and cause the material to separate and slide along itself out of its original plane and is denoted by Mode *III*.

The most severe of the loading states is Mode *I*, as the propagation of a crack in real material under pure Mode *II* or *III* conditions requires a great amount of energy, due to high friction between crack faces.

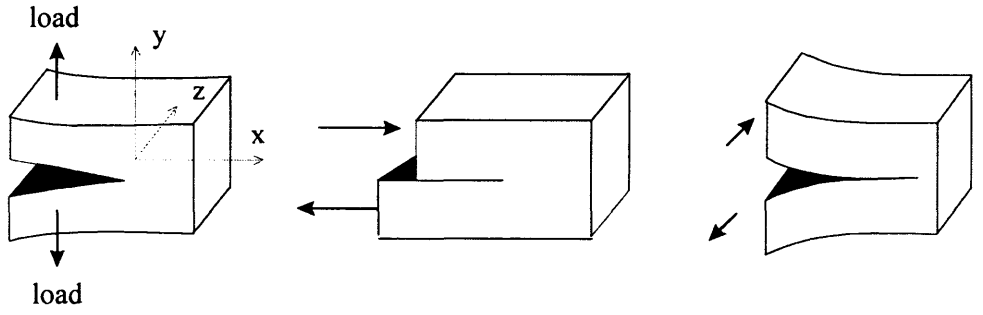

(a) Opening Mode I (b) Sliding Mode II (c) Tearing Mode III

Figure 2.2: Modes of crack propagation.

Figure 2.3 shows a two-dimensional (plane) body of infinite extent, subjected to a uniform stress remote from the crack, which induces an opening mode (Mode *I*) of stress at the crack tips. The stress and displacement components of a point in the vicinity of the crack tip can be written as:

$$\sigma_{ij} = \frac{K_I}{\sqrt{2\pi r}} f_{ij}(\theta) + ... \qquad i,j \in \{x,y\} \tag{2.11}$$

$$u_i = \frac{K_I(1+\nu)}{E}\sqrt{\frac{2r}{\pi}}\, g_i(\theta) + ... \qquad i \in \{x,y\} \tag{2.12}$$

where r and θ are the polar co-ordinates of the point with respect to the crack tip. E and ν are the Young modulus and Poisson ratio of the material, respectively.

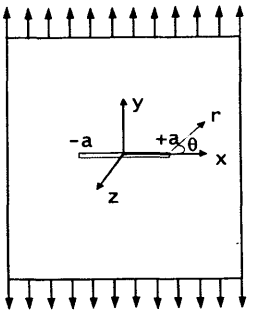

Figure 2.3: An infinite elastic body with a sharp crack of length *2a* under Mode *I*.

The parameter K_I (*I* denotes Mode *I*) called the *stress intensity factor* depends on the geometry of the body and the manner in which the loading is applied. For the geometry shown in Figure 2.3, K_I is given by:

$$K_I = \sigma\sqrt{\pi a} \tag{2.13}$$

In general, K_I is finite and positive. There can be situations when K_I vanishes, but it can never be negative. The shapes of the crack tip zones and the stress distributions ahead of the tips are shown in Figure 2.4 for $K_I > 0$, $K_I < 0$ and $K_I = 0$. When $K_I = 0$ (Figure 2.4c), the crack faces close smoothly and the stress ahead of the crack tip is finite. It should be noted that the constant terms or terms that depend on r and thus vanish as $r \rightarrow 0$, have been omitted from Equations (2.11) and (2.12).

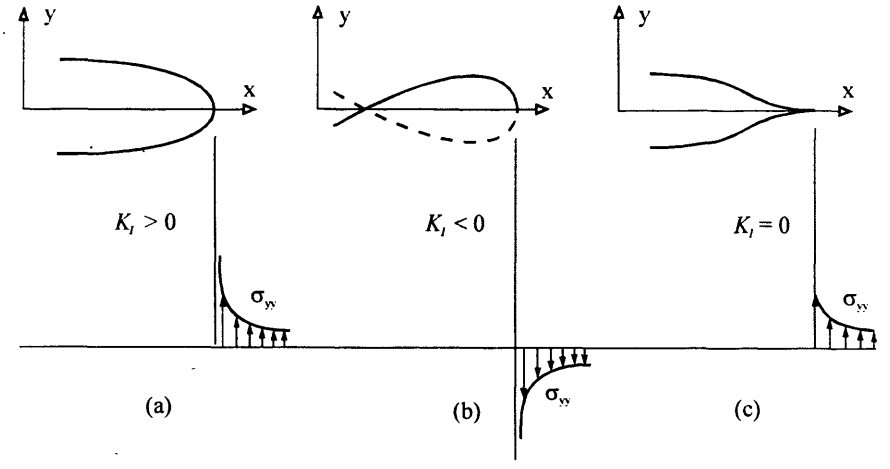

Figure 2.4: Shapes of traction-free crack tip zones and distribution of normal stress, σ_{yy} in front of the crack tip for $K_I > 0$, $K_I < 0$ and $K_I = 0$ (After Karihaloo, 1995).

Irwin stated that, a sharp crack in the brittle material will propagate when the stress intensity factor K_I reaches a critical value, denoted as K_{Ic}. This critical value is a material constant and is called the *fracture toughness* of the material. The distinction between K_{Ic} and K_I is important, and is similar to the distinction between strength and stress. In other words, K_{Ic} is related to the stress intensity factor K_I for the opening mode crack in the same way that a material's tensile strength is related to the stress in a tensile specimen (Brown and Srawley, 1966). For the geometry and Mode *I* of Figure 2.3, Irwin criterion gives:

$$\sigma_c \sqrt{\pi a} = K_{Ic} \tag{2.14}$$

According to this relation, when the external stress reaches the value σ_c the crack will propagate.

Comparing Equations (2.14) with (2.9) indicates that the Irwin local stress criterion at the crack tip where the fracture takes place is exactly identical to the Griffith global energy criterion. The constant in the right hand side of Equation (2.9) can be identified with K_{Ic}, i.e.

$$\sqrt{2E\gamma} = K_{Ic} \tag{2.15}$$

or

$$K_{Ic}^2 = EG_c, \tag{2.16}$$

where G_c is the critical Griffith surface energy density or the critical energy release rate, with $G_c = 2\gamma$.

Today, Irwin's fracture theory is more widely used than Griffith's because it is much easier to determine directly the fracture toughness K_{Ic} than it is to determine the fracture energy density γ, for materials with limited ductility (plasticity) (Karihaloo, 1995).

The fracture toughness of a material can be determined from a pre-cracked specimen. The most commonly used specimen shape for the determination of K_{Ic} is a notched beam loaded in three-point bending. The specimen is loaded gradually until the sharp notch begins to propagate. The corresponding maximum load is used for the

calculation of the bending moment at midspan (M_{max}) and the critical stress intensity factor K_{Ic} is then calculated using the formula (Karihaloo, 1995):

$$K_{Ic} = \frac{6YM_{max}\sqrt{\alpha}}{BW^2} \tag{2.17}$$

where Y is a function of $\alpha=a/W$ (i.e. the ratio of the depth of notch to the height of the specimen), B and W are the width and height of the beam, respectively.

2.2.3 Irwin theory and local energy considerations

Let us consider a crack of length $2a$ in an infinite body of unit thickness under mixed Mode I loading (Figure 2.3) and calculate the potential energy when the crack grows by an infinitesimal amount Δa at each end. Using the superposition approach, the stress σ_{yy} due to the remote Mode I loading at the location of the crack is cancelled by applying equal stresses of opposite sign and calculate the work done by these stresses when the crack faces open relative to each other. As mentioned earlier, this work done equals the change in the potential energy of the body, $\Delta\Pi$,

$$\Delta\Pi = -2\int_0^{\Delta a} \sigma_{yy} u_y dx \tag{2.18}$$

The negative sign in front of the integral indicates that the displacement and corresponding stresses have opposite signs, and the multiplier 2 allows the symmetric growth of the two crack tips. The stress and displacement components (i.e. σ_{yy} and u_y) are chosen from Equations (2.11) and (2.12), respectively, corresponding to $\theta=0$ (i.e. in the direction of crack advance). After integrating Equation (2.18), the following is obtained:

$$\Delta\Pi = -\frac{2K_I^2}{E}\Delta a \tag{2.19}$$

On the other hand, the energy required to extend the crack by an amount Δa is $\Delta\Gamma=4\gamma\Delta a$. Noting that $-\Delta\Pi=\Delta\Gamma$, the relation between γ and stress intensity factor in the loading Mode I can be written as:

$$\frac{2K_I^2}{E} = 4\gamma \tag{2.20}$$

At the critical instant of crack propagation, this relation would take the form $K_{Ic}^2 = 2E\gamma = EG_c$, which is identical to Equation (2.16). Therefore, the important relationship between Griffith and Irwin criteria of fracture from energy considerations alone is re-established. From Equation (2.19) the rate of change in the potential energy for growing a crack tip in a brittle material under Mode *I* loading can be derived:

$$-\frac{d\Pi}{da} \equiv G = \frac{K_I^2}{E} \tag{2.21}$$

where G is the energy release rate (Karihaloo, 1995).

2.2.4 Barenblatt's cohesive crack model

The main features of LEFM described above are (Karihaloo, 1995):

(i) The description of brittle fracture involves only one additional material parameter, besides the usual two elastic constants E and v. This parameter may be related to the energy of the body (G_c) or to the stress field near the tip of a sharp crack present in the body (K_{Ic}).
(ii) The stresses and strains in the vicinity of a sharp crack tip are very large (at the tip itself they tend to infinity).
(iii) During the fracture process the entire body remains elastic, and energy is only dissipated at a point (crack tip).

The last two features of LEFM contravene the basic principles of the linear theory of elasticity relating to small strains and Hooke's law. Griffith (1920) had observed the inconsistency between the linear elastic fracture model and the real physical situation prevailing at the crack tip. He therefore, proposed that the crack faces should be allowed to close smoothly (Figure 2.4c) under the influence of large cohesive forces.

Barenblatt (1959) gave the first fracture mechanics analysis based on the concept of a crack-tip cohesive zone in which he assumed that there were large cohesive forces $q(x)$ acting over a small zone of length c ($c << a$; Figure 2.5) near the crack tip and

that the crack faces close smoothly. The distribution of these cohesive forces is generally unknown and due to the presence of other defects it is difficult to ascertain. Because of this problem, Irwin's linear elastic fracture model, which was found to be equivalent to Barenblatt's cohesive crack model, is preferred for brittle materials, since no need for introduction of cohesive forces exists. Moreover, Irwin (1957) had also realised that the fracture process could not be concentrated at a point but should take place over a finite, though small, zone, the so-called *Fracture Process Zone (FPZ)*. He provided a crude estimate of its size (r_p) by limiting the transverse normal stress in the fracture criterion Equation (2.14) to the tensile strength f_t of the brittle material.

$$r_p = \frac{1}{\pi}\frac{K_{Ic}^2}{f_t^2} = \frac{1}{\pi}\frac{EG_c}{f_t^2} \tag{2.22}$$

Dugdale (1960) and Bilby et al. (1963) used a similar cohesive zone model to describe the behaviour of the elastic-plastic materials. However, they considered the cohesive stress to be constant and invariant with respect to the crack opening. In fact, a plastic zone will form at each crack tip and extend as far as is necessary to satisfy the yield condition ($\sigma_{yy} \leq \sigma_y$). Therefore, the closing stress over the plastic zone will be constant and equal to the yield stress of the material (σ_y).

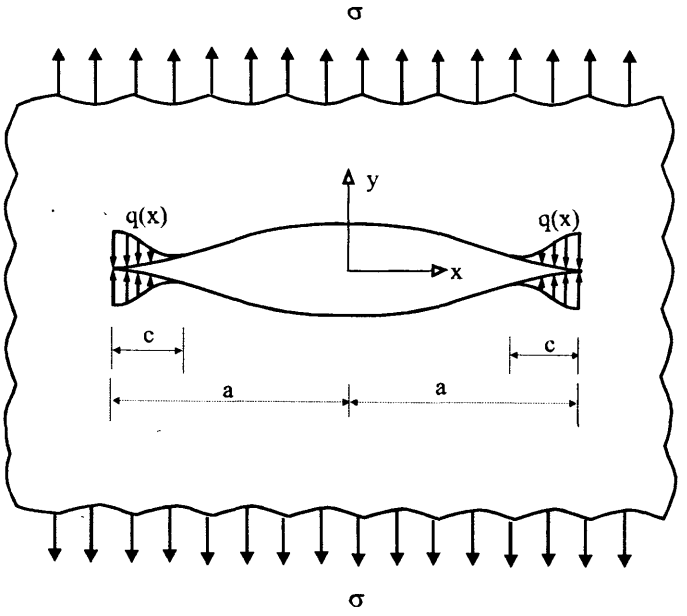

Figure 2.5: Barenblatt cohesive crack model in Mode *I*. Note $c << a$ (After Karihaloo, 1995).

2.2.5 Why LEFM is not applicable to HPFRCCs

Attempts were made to apply LEFM to concrete, which was thought to be a brittle material, but these proved unsuccessful, since cement-based materials exhibit a totally different response. In Figure 2.6a is shown the typical load-deformation curve for a quasi-brittle material in tension/flexure. For a quasi-brittle material like concrete, a substantial non-linearity exists before the maximum stress is reached (AB). This is the strain hardening response of the material. There is also a region of tension softening (i.e. an increase in deformation with decreasing tension carrying capacity) after the attainment of the maximum load (BC). These are primarily a result of randomly formed microcracks. The tail region of tension softening (CD) is caused by the aggregate interlock and other frictional effects. The pre-peak non-linearity has only a minor influence on the fracture behaviour of concrete. The major influence in fact comes from the tension softening response because it reduces the flux of energy which can be released into the crack tip and thus leads to an increase in the fracture surface area. Hence, the application of LEFM to concrete structures is limited, due to the existence of the tension softening response. In other words, the fracture behaviour of concrete is influenced by the formation of an extensive fracture process zone ahead of the pre-existing notch/crack, as illustrated in Figure 2.6b.

2.2.6 Fracture process zone (FPZ)

The Fracture Process Zone (FPZ) is defined as the inelastic zone around the crack tip and corresponds to the region of tension softening of the load-deformation curve (Figure 2.6).

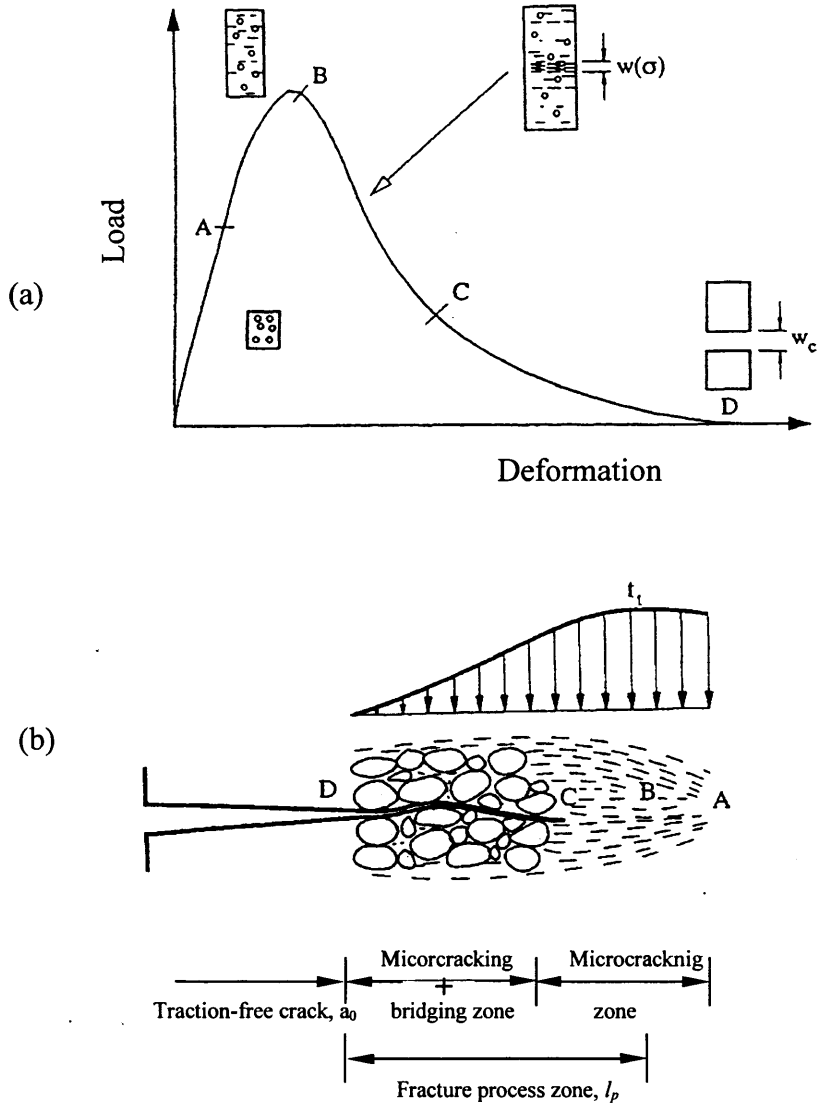

Figure 2.6: Typical load-deformation response of a quasi-brittle material in tension/flexure (a) and the fracture process zone ahead of the real traction-free crack (b) (After Karihaloo, 1995).

Many mechanisms that are responsible for fracture process in concrete are related to the development of the fracture process zone. Some of these mechanisms are indicated in Figure 2.7 such as, microcracking at aggregate due to the presence of a macrocrack, debonding and microcracking, coalescence of debond crack with a

macrocrack and the crack bridging, debonding, branching and microcracking. These are inelastic toughening mechanisms that appear around a crack when it propagates.

The size of the fracture process zone depends on the microstructure of the material and the stress field existing ahead of an introduced macrocrack (Karihaloo, 1995).

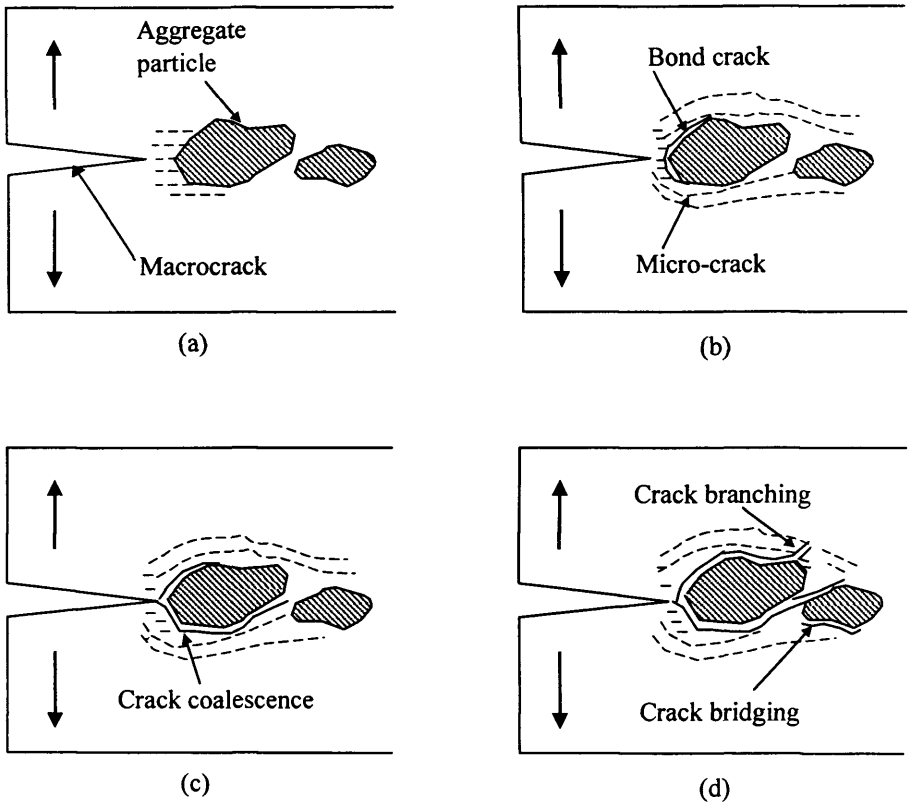

Figure 2.7: Schematic representation of the fracture process zone (a) microcracking at aggregate, (b) debonding and microcracking, (c) coalescence of debond crack with macrocrack, and microcracking, (d) crack bridging, debonding, crack branching and microcracking (After Karihaloo, 1995).

Fracture behaviour of concrete is greatly influenced by the FPZ. Since the FPZ consumes a substantial amount of the energy supplied by the applied load, a crack can propagate steadily prior to the peak load. Therefore, the presence of the FPZ results in stable crack growth before the peak load.

The FPZ is also responsible for the quasi-brittle fracture response of concrete after the peak load. Since some parts of crack surfaces may still be in contact after cracking, catastrophic failure of concrete structures immediately after the peak load is

prevented. As a result, stress gradually decreases after the peak load, and a softening type of concrete stress-strain relationship is obtained.

Experimental results have indicated that the strength of concrete usually decreases with increasing size of structures and then remains constant. This size effect on concrete strength may be primarily explained by the FPZ. When a concrete structure is loaded, the strain energy produced by the applied load is converted to the energy consumed to create a new fracture surface and the energy absorbed in the FPZ. For large-size structures that have long ligament lengths on the cracked sections, the latter is negligible compared to the former, whereas for small-size structures the latter can be of the same magnitude as the former. Therefore, the larger the structure's size, the lower the nominal strength. However, the concrete strength approaches a constant when sizes of concrete structures become very large (Shah et al., 1995).

The presence of the FPZ hinders the application of LEFM to cement-based materials.

2.3 NONLINEAR FRACTURE MECHANICS (NLFM)

LEFM is not applicable to concrete due to the existence of the inelastic toughening mechanisms (i.e. Fracture Process Zone) that appear around a crack when it propagates. A fracture theory capable to describe the material softening process that takes place in the fracture process zone must be a non-linear fracture theory.

The non-linear fracture theory applicable to ductile materials, such as metals is different from that applicable to quasi-brittle materials like concrete or rock. This is because in ductile materials the fracture process zone, though small, is surrounded by a large nonlinear plastic zone, whereas in quasi-brittle materials the fracture process zone occupies nearly the entire zone of nonlinear deformation. In comparison, the nonlinear zone is nearly absent in brittle materials. This is illustrated in Figure 2.8 below.

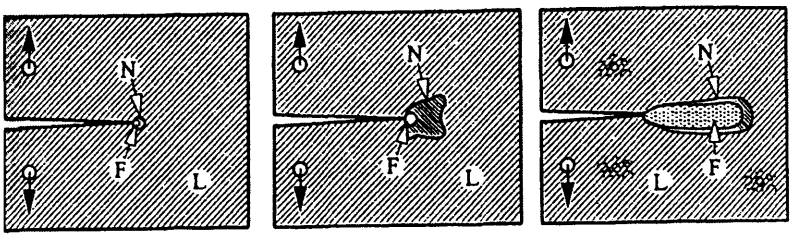

(a) Linear elastic (b) Nonlinear plastic (c) Nonlinear quasi-brittle

Figure 2.8: Distinguishing features of fracture in (a) a linear material, (b) a ductile material, (c) a quasi-brittle material. *L* refers to linear elastic region, *N* to nonlinear zone, and *F* to fracture process zone (After ACI Report 446.1 R.91).

The first non-linear theory of fracture mechanics for quasi-brittle materials like concrete was proposed by Hillerborg et al. (1976). Bazant (1984) proposed the second non-linear theory of fracture. The two non-linear theories are briefly described below.

2.3.1 Fictitious crack model (FCM)

The so-called Fictitious Crack Model (FCM) proposed by Hillerborg et al. (1976) is the first nonlinear theory of fracture mechanics of concrete. It includes the tension softening fracture process zone through a fictitious crack ahead of the pre-existing crack whose faces are acted upon by certain closing stresses such that there is no stress concentration at the tip of this extended crack (Figure 2.9). In this model the crack is composed of two parts; a real traction-free crack of length a_0 (the true or physical crack through which no stresses can be transmitted) and a fictitious crack or fracture process zone (FPZ) ahead of the true crack.

The fictitious crack model (FCM) is similar in some points to the Dugdale and Barenblatt models mentioned above. Like these models, it assumes that the FPZ is of negligible thickness and the crack tip faces close smoothly (K_I=0). However, there are also some major differences. The closing stresses in the FCM are not constant, as they are in the Dugdale model. They increase from zero at the tip of the pre-existing stress-free crack to the tensile strength of the material, f_t, at the tip of the fictitious crack. In fact the distribution of the closing stress, $\sigma(w)$, along the fracture process zone (FPZ) depends on the opening of the fictitious crack faces, w. Unlike the Barenblatt model,

the size of the fracture process zone (l_p in Figure 2.9) in the FCM may not be small in comparison with the length of the pre-existing macrocrack.

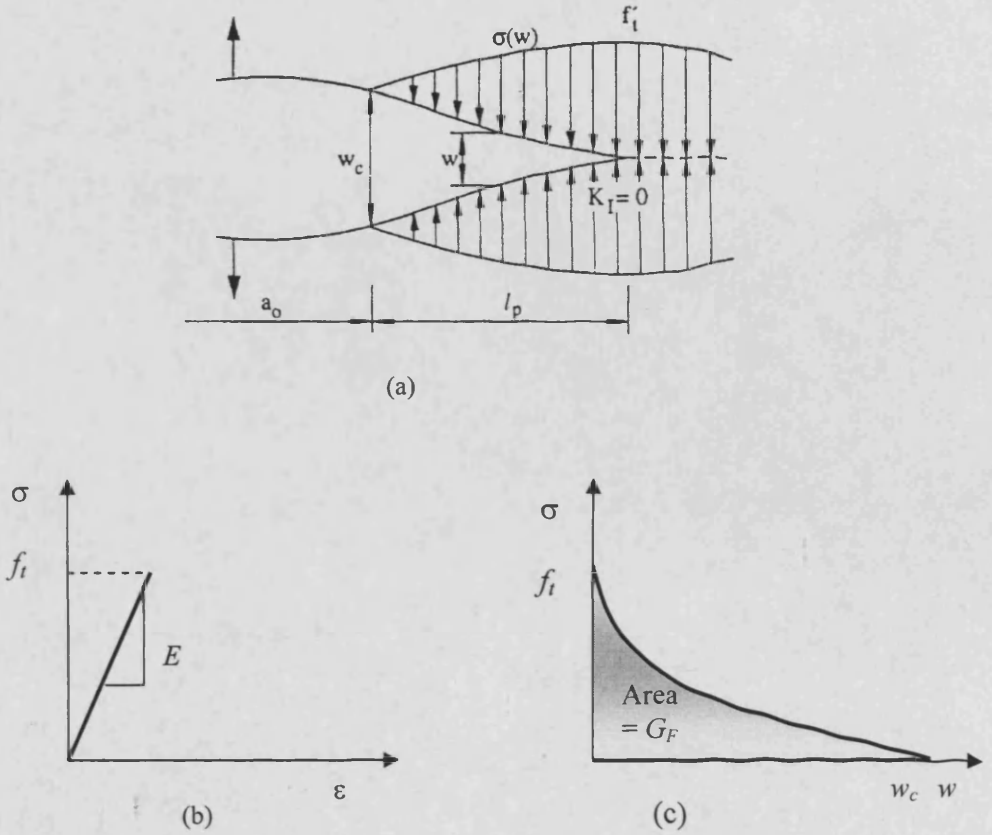

Figure 2.9: (a) A real traction-free crack of length a_0 terminating in a fictitious crack of length l_p whose faces close smoothly near its tip (K_I=0). The material ahead of the fictitious crack tip is assumed to be linear (b), but the material within the fracture process zone is softening; the area under softening curve equals fracture energy G_F(c) (After Karihaloo, 1995).

In contrast to LEFM which needs a single parameter to describe a brittle material (e.g. K_{Ic} in Irwin's theory), in the FCM it is necessary to have two material parameters. These are:

- The shape of the stress-displacement relation $\sigma(w)$ in the softening zone.
- The area under the tension softening curve which is the specific fracture energy G_F of concrete

$$G_F = \int_0^{w_c} \sigma(w)dw \tag{2.23}$$

where, w_c is the critical crack opening displacement when the closing stress is equal to zero.

Since the direct determination of the tension softening relationship $\sigma(w)$ from uniaxial tension tests is a very difficult task, the $\sigma(w)$ relationship is often inferred indirectly from load-deformation diagrams recorded on notched three-point bend specimens (TPB).

There is also another important parameter which can be obtained from the above information, namely the characteristic length of the material.

$$l_{ch} = \frac{EG_F}{f_t^2} \tag{2.24}$$

The characteristic length, l_{ch}, is related to the heterogeneity of the material microstructure, giving an indication of its brittleness. It has a value proportional to the length of the fracture process zone. The longer the characteristic length, l_{ch}, of the material is, the more ductile will be the material (i.e. less brittle). This is attributed to the fact that a bigger value of the characteristic length is an indication of more inelastic toughening mechanisms getting involved around a crack when it propagates, resulting in greater energy absorption. Therefore, the characteristic length is a very powerful tool for designing cement based materials with high ductility. The characteristic length has a value for mortar and concrete in the range of 100 to 200 mm and 150 to 500 mm, respectively (Karihaloo, 1995). The corresponding value for CARDIFRC® exceeds 1000 mm.

The fictitious crack model is widely used in the finite element analysis of concrete structures. Petersson (1980) and Hillerborg (1983) have proposed a simple approximate method for the determination of G_F from tests on three-point bend beams which has been adopted as a standard test procedure by RILEM (1985).

2.3.2 Crack band model (CBM)

In the fictitious crack model described above, the fracture process zone is assumed to be a line crack with negligible width. Bazant and Oh (1983) modelled the FPZ by a band of uniformly and continuously distributed (smeared) microcracks with a fixed width of h_b (Figure 2.10a). This is the so-called Crack Band Model (CBM). Stable

crack propagation is then simulated by progressively microcracking within this band, which is described by a stress-strain relationship (Figure 2.10b).

The crack opening displacement w is equal to the product of the strain and the width of the crack band, h_b.

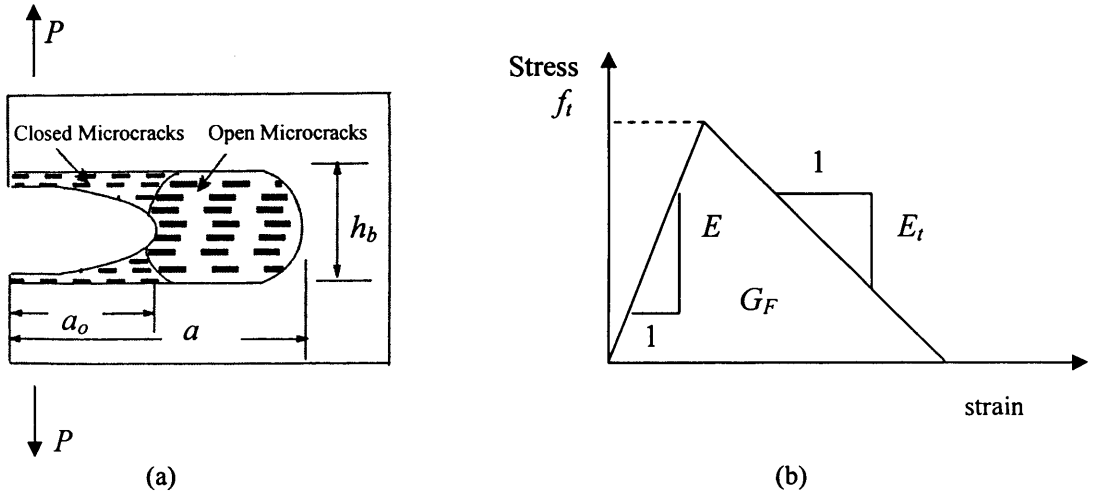

Figure 2.10: Crack band model for fracture of concrete (a) a microcrack band fracture and (b) stress-strain curve for the microcrack band (After Shah et al., 1995).

Based on the assumption that the energy produced by the applied load is completely balanced by the cohesive pressure $\sigma(w)$ in the fictitious crack approach, the energy consumed due to the crack advance per unit area of the crack band, G_F, is the product of the area under the stress-strain curve (Figure 2.10b), and the width of the crack band, h_b. This leads to:

$$G_F = h_b\left(1+\frac{E}{E_t}\right).\frac{f_t^2}{2E} \tag{2.25}$$

where E is the modulus of elasticity,

E_t is the strain-softening modulus, and

f_t is the tensile strength of the material.

The values of E and E_t are defined as positive. It may be seen that in addition to E, three material fracture parameters, h_b, f_t and E_t are required in the crack band model. An approximate function $h_b = n_a d_a$ has been proposed to calculate the h_b value, where

d_a is the maximum aggregate size in concrete and n_a is a constant, which is equal to 3 for concrete.

It should be noted that the main difference between the two mentioned non-linear models (FCM and CBM) is the thickness of the fracture process zone. As the band width h_b in the CBM tends to zero, the two models will merge.

The CBM is generally used when the cracks are diffuse and numerous. That is why it is also called as the smeared crack model. The FCM, on the other hand, is used when the cracks are few and isolated. That is why it is also called as the discrete crack model.

2.3.3 Fracture parameters needed for NLFM

We have seen that linear elastic fracture mechanics needs a single parameter to describe a brittle material (e.g K_{Ic} in Irwins's theory). However in non-linear fracture mechanics, it is necessary to have at least two material parameters to describe the fracture process of concrete structure. The two material parameters are: (i) the stress-displacement relationship $\sigma(w)$ in the tension softening zone, and (ii) the area under the softening curve (true fracture energy G_F), as defined in Equation (2.23).

Instead of $\sigma(w)$ and G_F, any combination of two independent parameters may be chosen. For example, it could be w_c and G_F, or even $\sigma(w)$ and the characteristic length, l_{ch},(Equation (2.24)). Methods for the determination of $\sigma(w)$ and G_F of CARDIFRC® are described in Chapter 5.

CHAPTER 3: HPFRCCs AND CARDIFRC®

3.1 INTRODUCTION

High Performance Fibre Reinforced Cementitious Composites (HPFRCCs) represent a class of cement composites whose stress-strain response in tension undergoes strain hardening behaviour accompanied by multiple cracking, leading to a high failure strain capacity. HPFRCCs result from advances in manufacturing processing that permit the inclusion of a large amount of fibres in the cement based matrix without affecting the workability of the mix. These advances are based on the use of silica fume and surfacants which reduce water demand and densify the matrix, thereby improving the fibre-matrix interfacial bond (Morin et al., 2001; Bache, 1981).

A new class of HPFRCC materials has been recently developed at Cardiff University designated CARDIFRC®. It is characterised by high tensile/flexural strength and high-energy absorption capacity (Karihaloo et al., 2002). This chapter will focus on the behaviour of this class of material, as well as other HPFRCCs that have been presented to the industry so far.

3.2 HPFRCCs

Fibre reinforced cementitious composites can be classified into three groups. FRC employing low fibre volume fractions (< 1%) utilize the fibre for reducing shrinkage cracking (Balaguru and Shah, 1992). FRC with moderate fibre volume fractions (between 1% and 2%) exhibit improved mechanical properties including modulus of rupture (MOR), fracture toughness, and impact resistance. In the last decade, a third class of FRCs, generally labelled as high performance FRC, or simply HPFRCC, has been introduced. HPFRCC exhibits apparent strain-hardening behaviour by employing high fibre contents.

FRCs can be categorised into two classes according to their tensile response: conventional FRC and high performance FRC (HPFRCC). Conventional FRC exhibits an increase in ductility over that of plain concrete, whereas HPFRCCs exhibit

a substantial strain-hardening response, leading to a large improvement in both strength and toughness compared with those of plain concrete (Shah et al., 1999).

HPFRCCs include materials such as SIFCON (Slurry Infiltrated Fibre Concrete), MDF (Macro Defect Free), ECC (Engineered Cementitious Composites), Fibre Reinforced DSP (Densified Small Particle Systems), CRC (Compact Reinforced Composite), RPC (Reactive Powder Concrete) and CARDIFRC®. These materials have been shown to develop outstanding combinations of strength and ductility as well as long-term durability (Reinhardt, 1991; Karihaloo et al., 2001).

HPFRCCs can be designed systematically, based on the knowledge of how crack-like defects in the composite grow and on the influence of fibre bridging on the mode of composite failure. Fracture mechanics plays a significant role in the development of composite design strategy (Li, 1993).

3.2.1 The effect of high temperature curing conditions

Curing conditions and curing temperature influence the properties of hardened concrete. Neville (1995) reported that, a rise in the curing temperature speeds up the chemical reactions of hydration and thus affects beneficially the early strength of concrete. Typically, the remarkable strength properties observed in HPFRCCs are obtained by curing at 90° C. For example, the compressive strength of CARDIFRC® reaches up to 200 MPa when the specimens are cured at high temperature up to 90°C for only 7 days. At this temperature the microstructure of such materials changes leading to:

- A homogeneous and cohesive interface between CSH paste and the sand.
- A dense CSH matrix.
- A fibril CSH nanostructure.

Zanni et al. (1996) investigated the effect of heat treatment on the hydration of RPC. The investigations showed that silica fume consumption was highly dependent on heat treatment temperature and duration. Moreover, crushed quartz reactivity was also proved to be dependent on heat treatment and duration.

Heat treatment accelerates the hydration process, activates the pozzolanic reaction of silica fume and reduces the curing time of concrete. Karihaloo and de Vriese (1999) showed that, the curing time of RPC specimens could be reduced from 28 to 16 days, when the specimens are cured under the following regime:

7 days	at	ambient temperature
3 days	at	90°C
7 days	at	ambient temperature

The curing time can be reduced further to seven days. Sullivan (1999) confirmed this by exposing RPC specimens to high temperature curing for the entire seven days at 90° C immediately after the moulds are stripped. Similarly, the strengths attained for CARDIFRC® specimens cured at 90° C for seven days have been found to be the equivalent of standard 28-day water curing at 20° C (Alaee, 2002).

3.2.2 The effect of silica fume

Silica fume is an extremely fine powder whose particles are about 100 times smaller than cement. The particles of such material pack tightly against the surface of the aggregate and fit in-between the cement particles, thus greatly improving packing. Neville (1995) reported that because the extremely fine particles of silica fume reduce the size and volume of voids near the surface of the aggregate, the so-called interface zone has improved properties with respect to microcracking and permeability. The bond between the aggregate and the cement paste is improved, allowing the aggregate to participate better in stress transfer.

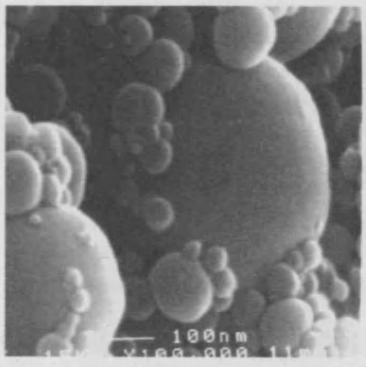

Figure 3.1: Microsilica Particles.

The main functions of silica fume in HPFRCCs as reported by Richard and Cheyrezy (1995) are:

- Filling the voids between the next larger size particles (cement).

- Enhancement of rheological characteristics by the lubrication effect resulting from the perfect spherical shape of the basic particles.
- Production of secondary hydrates by pozzolanic reaction with the lime resulting from primary hydration.

One of the main advantages of using silica fume particles (particle size 0.1-0.2 μm) with cement (particle size 5-10 μm) is to fill the spaces between the cement particles and thus to achieve a very dense packing system. Bache (1981) attributed these to the following: a) the silica particles are smaller than even the finest cement we can produce by grinding and are therefore more conducive to dense packing into the spaces between the cement particles, b) the silica particles, being formed by condensation from gas phase, are spherical in shape (unlike crushed cement particles, which are angular) and this makes the silica particles even more suitable for dense packing than very fine cement, and finally c) the particles are chemically less reactive than cement, which eliminates the problem of too rapid hardening encountered with very fine cement; in addition, the silica is likely to ensure the formation of a coherent structural skeleton between the cement particles, resulting in a fine dense microstructure.

The use of microsilica in HPFRCCs can improve the bond by increasing the contact area between the fibre and the surrounding matrix. This introduction of fine microsilica particles will increase the density of the matrix, filling any pore spaces around the fibre. The increase in the surface contact area increases the pull-out force (Bache, 1981).

Another important property of microsilica is its pozzolanic behaviour. The material is extremely reactive, and hence can react with the surplus of calcium hydroxide, which in ordinary cement paste will crystallize out as a separate and relatively weak phase. The reaction of microsilica with the remaining calcium hydroxide, from the primary cement water reaction, results in the production of an extra C-S-H. The chemical representation of this process is shown below:

Primary reaction: Cement + Water

$$2C_3S + 6H \rightarrow C_3S_2H_3 + 3Ca(OH)_2$$

$$(C\text{-}S\text{-}H) + [CH] \qquad (3.1)$$

Secondary Reaction: Silica + Calcium Hydroxide + Water

$$S + CH + H \rightarrow C\text{-}S\text{-}H \qquad (3.2)$$

The extra production of C-S-H results in a microstructure, which is very dense in the freshly mixed state and gets even denser during the succeeding hydration process. The effect of microsilica in the cement paste is shown in Figure 3.2.

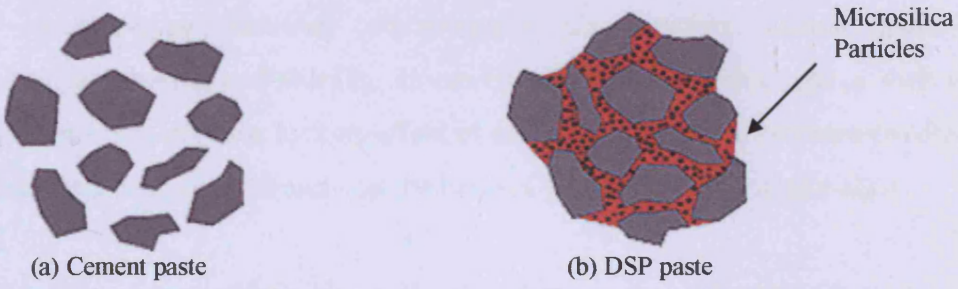

Figure 3.2: (a) Flocculated particles in ordinary cement paste. (b) Densely packed cement grains and microsilica in DSP paste.

3.2.3 The effect of dispersing agent (superplasticiser)

As mentioned earlier, the silica fume (SF) is a finally ground material and as such, generally increases the water requirement for a given degree of workability at low water/cement ratio. Thus, a high range water-reducing admixture is often introduced to promote the workability. Neville (1995) reported that, superplasticisers are long and heavy molecules, which wrap themselves around the cement particles and give them a highly negative electrical charge so that they repel each other. This results in deflocculation and dispersion of the cement particles (Figure 3.3) and therefore, in high workability.

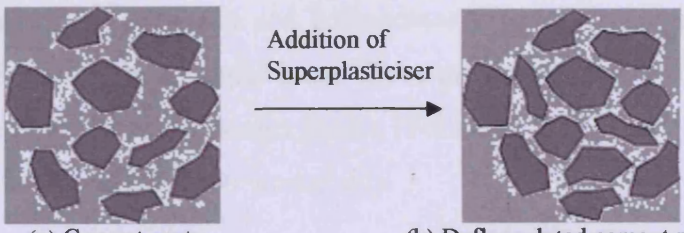

(a) Cement paste (b) Deflocculated cement paste

Figure 3.3: (a) Flocculated particles in cement paste. (b) Superplasticised cement particles.

Superplasticisers are added to the CARDIFRC® matrix in order to obtain a very workable mix at low water/cement ratio, thus achieving dense packing which results in high strength and durable concrete. One of the main difficulties of achieving such a system, as described by Bache (1987) is the presence of surface forces. These forces interlock neighbouring particles, consequently counteracting mutual particle movement during mixing and shaping. However, effective dispersing agents such as superplasticizers eliminate the locking effect of surface forces and it becomes possible to pack fine particle systems densely on the basis of purely geometrical principle.

The combination of superplasticisers with silica fume in the concrete mix results in high strength and/or high durability. Dugat et al. (1996) reported that by using superplasticisers with silica fume it is possible to reduce the water/cement ratio to less than 0.15. This helps reduce the total pore volume of the cement paste and the average diameter of the pores, hence improving durability. Moreover, experience with RPC, DSP and CARDIFRC® showed remarkable strength properties when superplasticisers and silica fume are incorporated in the original mix.

The amount of superplasticiser used in CARDIFRC® mixes is somewhat higher than that of the original RPC and DSP mixes. This causes the mixes to be very workable.

3.2.4 The effect of steel fibres

The incorporation of fibres in the CARDIFRC® matrix increases the tensile load-carrying capacity and turns an otherwise brittle material into a very ductile one. As mentioned earlier, brass-coated steel fibres (diameter 0.16 mm, 6 mm or 13 mm long) are used to prevent corrosion. The use of long and short fibres was found necessary to improve the material properties whilst minimising loss of workability. The short

fibres prevent microcrack growth and coalescence (Tjiptobroto and Hansen, 1993) and provide a high tensile strength. Long fibres provide increased ductility, greater pullout strength and will bridge longer cracks (Sullivan, 1999). Their disadvantage is that they have an adverse effect on workability.

3.2.4.1 Volume fraction of fibres

The volume fraction of fibres in concrete affects both the fresh and hardened state. Hoy and Bartos (1999) reported that when higher volumes of steel fibre are added to concrete, there is a more significant loss of workability and greater chance that fibres will interlock. For these reasons, there is an optimum fibre content for any given fibre-matrix combination. Higher fibre contents will produce mixes which lack homogeneity and have poor workability, while lower fibre contents will result in less efficient reinforcement. By a careful selection of mix proportions, the optimum fibre content can be increased with a resulting performance improvement.

Basically, as the volume fraction of fibre increases and as the fibres are more uniformly dispersed, the growth of microcracks is hindered, and the localisation of deformation is delayed with a consequent substantial increase in the tensile strength and strain capacities of the composite (Balaguru and Shah, 1992). Mobasher et al. (1990) carried out an experimental programme on the effect of fibre content on the fracture properties of concrete. They concluded that as the volume fraction of fibres increases the growth of microcracks was hindered through an arrest mechanism and the matrix fracture toughness was increased. The higher the volume fraction of fibres, the higher the peak load, and the higher the matrix contribution and the higher the acoustic emission (AE) rate. The higher AE event count means that there is a greater number of microcracks.

Karihaloo and de Vriese (1999) studied the effect of volume fraction of fibres on RPC mix. They found that increasing the volume fraction of steel fibres V_f led to major improvements in the properties of RPC, namely, specific fracture energy and indirect tensile strength. Furthermore, Shannag and Hansen (2000) showed that incorporating large volume fractions of short steel fibres (more than 2% by volume) in DSP composites results in a dramatic increase in matrix tensile strength (up to 100%).

3.2.4.2 Aspect ratio of fibre (*l/d*)

The physical shape of steel fibres is described by their aspect ratio (length/diameter). As a general rule, higher aspect ratio fibres perform better than lower aspect ones. Gopalaratnam and Shah (1986) found a monotonic increase in compressive strength and ductility when the aspect ratio increased from 47 to 100. Sullivan (1999) also found that long fibres increased both the tensile strength and ductility of concrete. Karihaloo and de Vriese (1999) reported that an increase in fibre length – and consequently of aspect ratio- seems to be more effective than an increment only in volume fraction of fibres. The incorporation of long fibres (13 mm) in CARDIFRC® mixes was a primary cause of enhancing the ductility.

3.2.4.3 Bridging action of the fibres

Extensive research has shown that the most fundamental property of a fibre reinforced cementitious material is the fibre bridging across a matrix crack (Li, 1992b; Li et al., 1991).

Incorporation of fibres in HPFRCCs is a vital factor for increasing the tensile strength of the composite and for improving its ductility (turns a brittle material into a very ductile one). When the composite is first loaded, the load-displacement response is approximately linear and the fibres act as a crack arrester, thus increasing the required energy for crack propagation. The response starts to become non-linear just before the matrix first crack. The region after the initiation of first crack is called the multiple cracking region in which the stress-strain curve deviates from linearity. The first crack strength depends primarily on the matrix properties and is only minimally dependent on the fibre parameters. As the load is further increased, some microcracks will emerge. These microcracks will be bridged by fibres. Very high shear stresses are developed between the fibres and the matrix where the fibres emerge from the crack face. The shear stress values attained depend on the difference on the elastic modulus between the fibres and the matrix and on the fibre volume fraction. This shear stress helps transfer some of the load to the fibres. According to Balaguru and Shah (1992) when the matrix cracks, the fibre transmits the load across the crack.

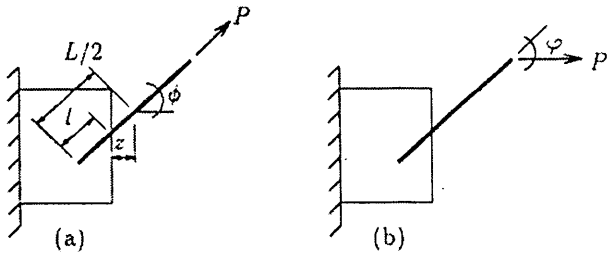

Figure 3.4: (a) A single fibre pull-out without snubbing ($\phi = 0$) and (b) with snubbing ($\phi \neq 0, \phi = \varphi$) (After Karihaloo and Wang, 2000).

Since fibres are randomly dispersed throughout the matrix, their orientations relative to the direction of the applied load are an important factor. In a matrix containing randomly distributed fibres, few fibres align in the direction of applied load; instead almost all fibres are oriented at different angles to the load direction (Figure 3.4). When a fibre is pulled out from the cementitious matrix, the snubbing friction at the fibre exit point can increase the pull-out resistance, and contributes to the overall composite action. Experimental observations showed that inclined fibres can sustain a greater load as they bend. This is known as dowel action. Naaman and Shah (1976) reported that after matrix cracking, the load and energy required to pull a steel fibre out from the matrix can be higher for fibres inclined to the load direction.

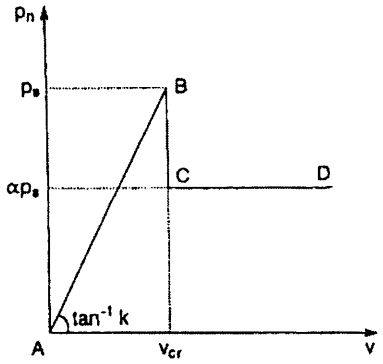

Figure 3.5: A linearised bridging law describing the relation between the bridging force and the crack opening displacement (After Karihaloo and Wang, 1996).

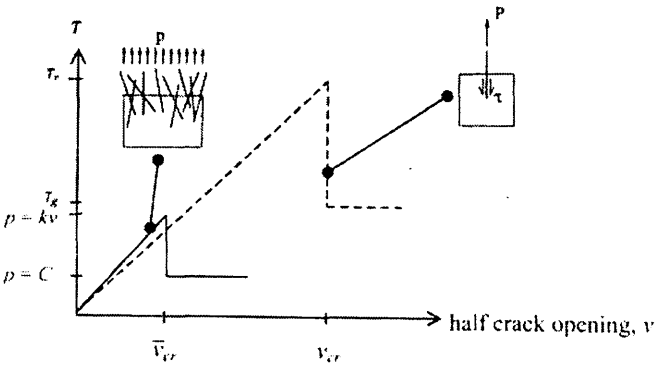

Figure 3.6: Idealised interfacial matrix-fibre shear stress (τ) vs. half crack mouth opening for single fibre (dashed line) and multiple fibre (solid line) pull-out (After Lange-Kornbak, 1997).

It is assumed that when the crack opening displacement reaches a critical value v_{cr} , some of the fibres bridging the crack will debond from the matrix, resulting in a sudden drop in the bridging force (BC), whereafter these fibres will exert a reduced closure force by frictional pull-out (CD) (Figure 3.5). This is based on single pull-out tests. From this single fibre relationship, the average closure force on crack faces bridged by many fibres is obtained through an approximation to the fibre distribution function (Figure 3.6). The slope of the elastic part of this averaged pullout diagram gives directly the parameter *k* in Equation (3.4) below.

When the crack opening exceeds the critical value $\bar{v}_{cr}$, the bridging stress $p(v)=kv$ drops to the constant frictional pull-out value, the parameter C in Equation (3.5) below.

The bridging stress for multiple fibre bridging is expressed in terms of single fibre properties $\tau_{v,}$ the adhesive bond strength of the fibre and the matrix, and τ_g the frictional pull-out strength of fibre. This is achieved by introducing the ratio:

$$\zeta = \frac{\bar{v}_{cr}}{v_{cr}} \tag{3.3}$$

where $\bar{v}_{cr}$ follows from the multiple crack model, since it assumes that slip is initiated immediately after reaching the ultimate tensile load, whereby the corresponding maximum half opening of the crack equals $\bar{v}_{cr}$ (Lange-Kornback and Karihaloo, 1997).

The bridging forces are:

$$p(v) \approx 2V_f \frac{\tau_v}{\tau_g} E_f \frac{h}{L} v \equiv kv \qquad v < \bar{v}_{cr} \tag{3.4}$$

$$p(v) \approx \frac{1}{2} V_f \tau_g \frac{L}{d} h \frac{\bar{v}_{cr}}{v_{cr}} \equiv C \qquad v \geq \bar{v}_{cr} \tag{3.5}$$

where V_f is the volume fraction of fibre, L the length of the fibre, d the diameter of the fibre, k is the bridging stiffness and h is the snubbing factor, defined by Karihaloo and Wang (2000)

$$h = \frac{2}{(4+f^2)}(e^{f\pi/2}+1) \tag{3.6}$$

where f is the snubbing friction coefficient.

3.2.5 Constitutive model

The constitutive model describes the stress-strain behaviour of short fibre-reinforced cementitious composite in tension/flexure. The similarities and differences in the constitutive behaviour of two types of FRC (conventional FRC and high-performance FRC), as described by Karihaloo and Wang (2000), follow.

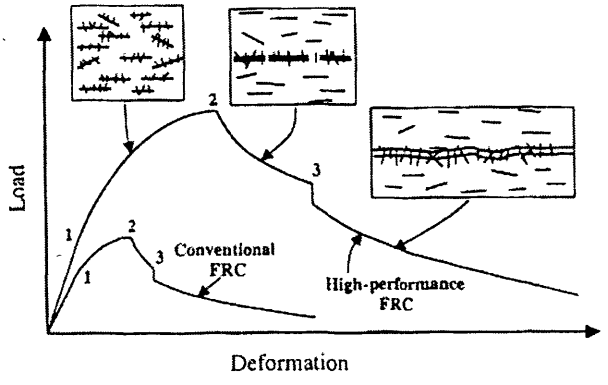

Figure 3.7: Complete pre- and post-peak tensile response of two short fibre-reinforced cementitious composites (After Karihaloo and Wang, 2000).

Figure 3.7 illustrates the load-deformation response of conventional and high performance FRC to tensile/flexural loading. As can be seen, the total tensile strain and load carrying capacity of HPFRCC are higher than for the conventional FRC, and the amount of stored energy represented by the area under the curve in HPFRCC is much higher than that of conventional FRC. The deformation is generally expressed in terms of strain up to the peak load (point 2) and through crack opening displacement thereafter.

Both materials exhibit the following responses:

- Linear elastic behaviour up to 1.
- Strain hardening behaviour between 1 and 2.
- Tension softening due to localisation of damage in the form of unconnected macrocracks 2 and 3.
- Continued tension softening due to localisation of damage in the form of a through crack until complete rupture.

The complete constitutive relation will be briefly outlined in the following.

3.2.5.1 Linear elastic behaviour

As can be seen in Figure 3.7 both materials exhibit linear elastic behaviour up to point 1 at which the transition from linear elastic to strain hardening behaviour takes place. This is only governed by the tensile strength of the matrix but is mostly unaffected by the fibres parameters (i.e. fibre aspect ratio, volume fraction and bond strength). Due to the fact the HPFRCC contains no coarse aggregate it is extremely brittle, therefore the stress at transition point 1, is uniquely related to the matrix fracture toughness:

$$K_{IC,m} = f(w/c, g, V_a) \tag{3.7}$$

where $K_{IC,m}$ is the fracture toughness of the matrix (where I denotes Mode I cracking), w/c is the water to cement ratio, g is the maximum size of aggregate and V_a is the volume fraction of fine aggregate. For the calculation of Young's modulus of

fibre reinforced concrete Karihaloo and Lange-Kornbak (2001) used the following equation for a two-phase system based on the work of Nielsen (1992)

$$E = E_m \frac{n + \Theta + V\Theta(n-1)}{n + \Theta - V(n-1)} \tag{3.8}$$

where V is the volume fraction of discrete phase, Θ is the geometry function accounting for the configuration (aspect ratio) of the discrete phase and n is the ratio of the modulus of elasticity of the discrete phase to that of continuous phase E_m (i.e. of matrix). The Young modulus for HPFRCC mix can be obtained by applying Equation (3.8) twice (Benson, 2003). First to a two-phase system in which the continuous phase is the cement-silica binder paste and the discrete phase is the fine aggregate, and then to a system in which the cement-silica-fine aggregate mortar is the continuous phase and the fibres the discrete phase. The values of n, V, E_m and Θ are different in the two steps.

3.2.5.2 Strain-hardening behaviour

As can be seen in Figure 3.7, the strain hardening region is located between points 1 and 2. This is known to be a result of the bridging action of fibres on microcracks which prevents their growth and coalescence. This region, which is inelastic strain region due to micro-cracking (also called multiple cracking region), is a unique property of HPFRCCs (Tjiptobroto and Hansen, 1993). Multiple cracking is a property of the bulk material, since no strain localisation occurs. The density of microcracks increases with increasing tensile/flexural loading until it reaches a saturation level (point 2). The extent of strain hardening is determined by the microstructure of the cementitious matrix, the volume fraction of fibres and the bond strength of the fibres.

The occurrence of multiple cracking was explained in an analytical approach developed by Tjiptobroto and Hansen (1993) assuming that the first crack is also the failure crack (observed from failure tests). If the energy needed to form new microcracks is smaller than the energy needed to open the first microcrack (i.e. the onset of failure) then multiple cracking takes place. The model predicts that the existence of a multiple cracking process depends on the fibre properties (fibre length

and fibre diameter), interface and matrix properties (debonding energy, interface frictional stress, matrix strength, and water-cement ratio). Moreover, their analyses predict that the major energy term determining the behaviour of multiple cracking is the fibre debonding energy.

Bridging of the multiple cracks by short fibres is a significant mechanism for increasing the strength and toughness of the composite and for preventing a sudden loss of the overall stiffness when the microcracks coalesce into large bands (Wang and Karihaloo, 2000). The role of fibres in the composite matrix was explained by Balaguru and Shah (1992) and Karihaloo et al. (1996).

When the matrix is loaded, part of the load is transferred to the fibres along its surface. As mentioned earlier due to the difference in stiffness of fibre and matrix, shear stresses develop along the surface of the fibre. This shear stress helps transfer some of the load to the fibre. When the matrix cracks, the fibre transmits the load across the crack. Fibres added to concrete arrest cracks and distribute imposed deformation into many microcracks.

These microcracks are arbitrarily orientated. Because of this reason modelling of the constitutive behaviour of a material with microcracks is a difficult and complicated problem. One simplified way to model a microcracked solid from a fracture mechanics point of view is to assume that the cracks are arranged in a regular pattern, among which the simplest form is the doubly periodically arranged array (Karihaloo et al., 1996). Karihaloo et al. (1996) solved the problem of doubly periodic arrays of cracks when the cracks are free of traction and when they are subjected to a closure pressure. They showed that the stiffness decreases in the strain hardening region between 1 and 2 according to the following formula:

$$\frac{E_y}{E} = \left[1 - \eta \frac{\omega}{\pi \Omega^2} \ln\left(\cos\frac{\pi}{2}\Omega\right)\right]^{-1} \tag{3.9}$$

where (Ey/E) is the normalised instantaneous modulus in the direction of loading, $\omega = a^2/(WH)$ is the crack density and $\Omega = 2a/W$. W and H are the horizontal and vertical crack spacings, respectively (Figure 3.8).

The coefficient

$$\eta = \frac{1}{1+\alpha+\beta} \tag{3.10}$$

and

$$\alpha = 4\sin^2\frac{\pi a}{W}e^{-2\frac{H}{W}\pi}\left[\frac{1}{1-e^{-2\frac{H}{W}\pi}} + \frac{2\frac{H}{W}\pi}{\left(1-e^{-2\frac{H}{W}\pi}\right)^2}\right] \tag{3.11}$$

$$\beta = -\frac{kW^2}{\pi a E}\ln\left(\cos\frac{\pi a}{W}\right) \tag{3.12}$$

Note that k is the bridging stiffness (Equation (3.4)) and for unbridged cracks $\beta = 0$.

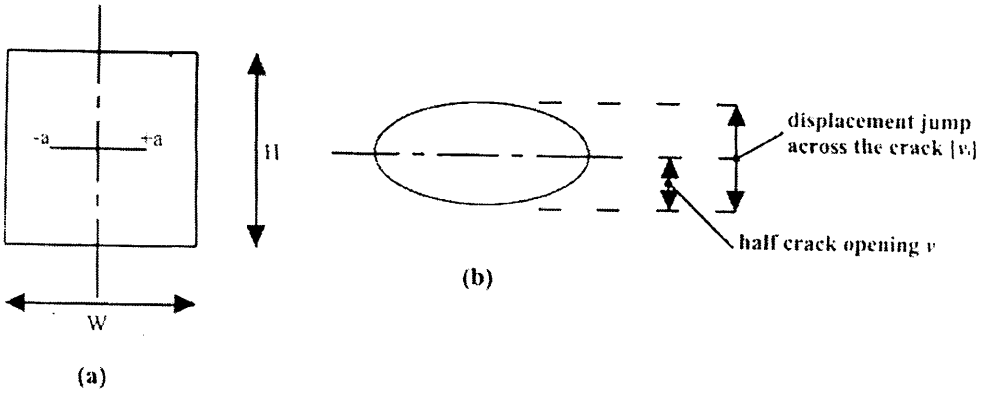

Figure 3.8: (a) Representative unit volume of the matrix containing one microcrack of length $2a$ (note that the volume V of this unit = $W*H*1$ and the surface area of the crack S =$2a*1$); (b) an enlarged view of the crack opening (After Benson, 2003).

3.2.5.3 Tensile strength (f_t')

The uniaxial tensile strength of the composite f_t' is the effective stress at the onset of localisation of deformation along the eventual failure plane. At this stage, the cracks in the localisation zone are still unconnected, so that the force is transmitted across the localisation zone partly by fibres (P_f) and partly by the unbroken matrix ligaments (P_b) (Karihaloo and Lange-Kornbak, 2001)

$$f_t' = \frac{P_b + P_f}{W^2} \tag{3.13}$$

where W is the centre-to-centre distance between the unconnected crack segments (Figure 3.8). The contribution of the unbroken matrix ligaments (P_b / W^2) and the contribution P_f / W^2 to f_t' can be evaluated. Lange-Kornbak and Karihaloo (1997) have shown that the rigorous estimate of f_t' given by this method is very close to that given by the rule of mixtures.

$$f_t' = \beta_1 \frac{\eta K_{Ic,m}}{\sqrt{\pi a_0}}(1 - V_f) + \beta_2 \tau_v V_f \frac{L}{d} \tag{3.14}$$

where $\beta_1 \approx 1, \beta_2 \approx 0.5$, τ_v is the average bond stress at the fibre-matrix interface at the attainment of f_t'. L and d are the length and diameter of fibres, respectively, $K_{Ic,m}$ is the fracture toughness of the matrix (cement-microsilica binder), a_0 is the half-length of each crack segment in the array at peak load and $\eta(>1)$ is a factor that depends on the volume fraction of the fine aggregate V_a.

3.2.5.4 Tension softening behaviour

This is due to localisation of damage in the form of unconnected crack fragments between points 2 and 3 (Figure 3.7). When the strain hardening capacity has been exhausted (i.e. the tensile/flexural strength of the composite has been reached), some of the fibres begin to debond from the matrix, resulting in the localisation of deformation along the eventual failure plane. The localisation manifests itself in the opening of cracks along this plane, but without their actual coalescence. The strain level away from this localised zone usually decreases first and then remains almost unchanged. The increased deformation is due to the progressive debonding of the fibre under decreased applied loading which results in the opening of fragmented cracks and their growth (region between 2 and 3).

The fraction of fibres that remains elastically bonded to the matrix progressively decreases from 2 to 3 until at 3 (Figure 3.7) all the fibres debond, resulting in an

instantaneous drop in the residual load carrying capacity and in the coalescence of crack fragments to form a through crack. Thereafter, the residual tensile carrying capacity is determined entirely by the frictional contact between the fibres and the matrix until the fibres are completely pulled out of the matrix, and failure occurs.
The tension softening response of short-fibre-reinforced cementitious composites (SFRCC) which exhibit extensive matrix cracking was modelled by Karihaloo et al. (1996) and Li et al. (1991). Karihaloo et al. (1996) model is suitable to describe the initial softening behaviour (prior to coalescence of the cracks). It is akin to that used by Horii et al. (1989) and Ortiz (1988) for the tension-softening of un-reinforced quasi-brittle materials. However, it differs from that used by Li et al. (1991) who assumed that the localized damage has resulted in a through crack. Thus, this model is more appropriate for describing the extensive tail region of this response when the crack fragments have coalesced and their faces are held together by frictional forces only (Karihaloo et al., 1996). The multiple crack model of Karihaloo et al. (1996) and the through crack model of Li et al. (1991) were combined to yield the complete tension softening behaviour of fibre reinforced composites (Lange-Kornbak and Karihaloo, 1997).

Karihaloo et al. (1996) modelled the tension softening response of SFRCC using a collinear array (row) of cracks subjected to bilinear bridging forces. They proposed that the initial tension softening curve (i.e. point 2 to 3 in Figure 3.7) was the result of the growth of discontinuous crack fragments in the localisation zone into the unbroken material (Figure 3.9a). The fibres in this zone are progressively pulled out beginning from the centre of each crack where the opening is largest, so that the crack can grow towards its neighbours. Eventually, when the neighbouring cracks have linked up, a through crack forms which is under the action of the residual frictional fibre bridging force (Figure 3.9b). Finally, at point 3 in Figure 3.7 only a few fibres remain elastically bonded to the matrix, hence a sudden drop in the stress is anticipated when the crack fragments link up to form a through crack (Lang-Kornbak and Karihaloo, 1997).

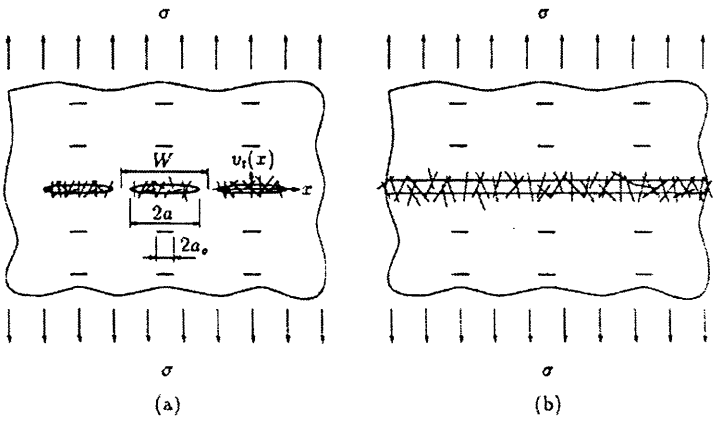

Figure 3.9: (a) Crack configuration prior to coalescence of crack (b) after coalescence of cracks during tension softening of fibre-reinforced quasi-brittle materials (After Karihaloo and Wang, 2000).

3.2.6 Types of HPFRCC

3.2.6.1 Macro-Defect-Free cement (MDF)

The MDF cementitious materials (also called new inorganic materials, NIMs or chemically bonded ceramics, CBCs) are composites combining portland or high-alumina cement with a water–soluble polymer of high molecular mass (e.g. polyvinyl alcohol, PVA, hydroxypropyl methyl cellulose, HPMC). The latter acts as a rheological aid, reduces the inter-particle friction coefficient and reacts with the hydration products. It prevents flocculation of cement particles, increases the viscosity of the mix at low water to solids ratio, thus permitting the use of intensive-high shear mixing processes without inducing cavitation (Shah and Young, 1990).

The MDF pastes have very high tensile strength (150 MPa or more) particularly when mixed with alumina cement. They are prepared under high shear, by mixing inorganic cement with a water-soluble polymer in the presence of limited amounts of water. The final product has very high bending strength, greater than 200 MPa, together with a high modulus of elasticity and relatively high fracture energy. However, the material may display some drawbacks like a high sensitivity to water (Lewis and Kriven, 1993). Moreover, the use of fibres in MDF cements is restricted (only long fibres may be used).

3.2.6.2 Slurry Infiltrated Fibre Concrete (SIFCON)

It is a high performance fibre reinforced concrete with very high fibre content, up to 20 percent by volume depending on the type of fibres used and manufacturing method (Lankard and Newell, 1984).

The matrix of this material has no coarse aggregate but a high cement content; however, it may contain fine sand and additives such as fly ash, microsilica, and latex emulsion (Naaman, 1991). Furthermore, steel fibres are primary candidates for this type of materials. Balaguru and Kendzulak (1986) have shown that in SIFCON the fibres are pre-placed in a mould to its full capacity and the corresponding fibre network is then infiltrated by cement-based slurry. The presence of fibres in SIFCON leads to an enhancement of ductility, as well as a reduction in crack width. The use of a SIFCON matrix in over-reinforced concrete beams can lead to ductility factors three to five times larger than control beams made from a plain concrete matrix (Naaman et al., 1990). They also observed that the use of such materials helps reduce crack widths in the tensile zone at least by one order of magnitude, and contributes to the spread of the zone of plasticity in the compression zone prior to failure.

3.2.6.3 Engineered Cementitious Composites (ECC)

Engineered Cementitious Composites are high performance fibre-reinforced cement based composite materials designed with micromechanical principles. Micromechanical parameters associated with fibre, matrix and interface are combined to satisfy a pair of criteria, the first crack stress criterion and steady state cracking criterion to achieve the strain hardening behaviour (Li, 1993). ECC has a tensile strain capacity of up to 6% and exhibits pseudo-strain hardening behaviour accompanied by multiple cracking. It also has high ultimate tensile strength (5-10 MPa), modulus of rupture (8-25 MPa), fracture toughness (25-30 kJ/m^2) and compressive strength (up to 80 MPa) and strain (0.6%). Due to its superior properties, the material can be used as a durable repair material.

3.2.6.4 Reactive Powder Concrete (RPC)

Reactive Powder Concrete RPC has been developed by the Scientific Division of Bouygues, SA, an international construction company with headquarters at St Quentin en Yvelines in France. The material is characterised by high silica fume content and very low water to cement ratio. It exhibits very high mechanical and durability properties (Richard and Cheyrezy, 1994). Compared to conventional concrete, the ductility estimated in terms of fracture energy is increased by one to two orders of magnitude, while the compressive strength values are in the range of 200 to 800 MPa. As reported by Richard and Cheyrezy (1995) the development of RPC was based on the following principles:

- Elimination of coarse aggregate significantly improves the homogeneity of the mix.
- Optimisation of the granular mixture. Microsilica improves the compacted density of the mix thereby reducing voids and defects.
- Incorporation of steel fibres results in a ductile material.
- Reduction of the water to cement ratio and inclusion of superplasticiser ensures a workable mix.

3.2.6.5 DSP cementitious materials

Densified cement ultra fine particle based materials DSP was developed by the Danish cement producer, Aalborg Portland-Cement. Production of this material is made possible by superplasticizers and silica fume to systems that can be densely packed in a low stress field and with very low water content (Bache, 1981). DSP belongs to a new class of materials formed from:

- Densely packed particles of a size ranging from 0.5 to 100 μm.
- Homogeneously arranged ultra fine particles ranging in size from about 50 Å to 0.5 μm and arranged in the spaces between the larger particles.

Dense packing of the particles (sand, cement and ultra-fine silica) together with fibres is essential for achieving the desired mechanical properties. It is also the prime feature

of HPFRCCs materials. Materials such as DSP combine very densely packed cement particles (5-10 μm) and ultra fine silica fume (0.1-0.2 μm) filled the spaces between the cement particles and normally densely arranged fibres (Bache, 1981; Bache, 1987).

Furthermore, the DSP matrix is a very strong and brittle material with a compressive strength of 150 MPa – 270 MPa. Due to its brittleness, it is difficult to utilize this material effectively without the incorporation of fine, strong and stiff fibres. The fibres improve the tensile properties of DSP based matrix, such as Densit®.

3.3 CARDIFRC®

Researchers at CARDIFF University (Karihaloo and de Vriese, 1999; Sullivan, 1999; Karihaloo et al., 2000) have attempted to reproduce RPC and Densit® with materials widely used by the UK concrete industry. The mechanical properties were found to be inferior to those reported in the literature (Richard and Cheyrezy, 1995; Bache, 1981), and the workability of some mixes was poor. These attempts however provided valuable clues on how to improve the mixing and processing techniques in order to produce HPFRCCs similar to RPC and Densit® but whose mechanical performance even exceeds that of the original mixes. Another type of mix, a HPFRCC with 6 mm coarse aggregate, was also investigated (Benson, 1999). The workability of this mix was satisfactory but the mechanical properties were inferior to those achieved with mixes containing no coarse aggregate (i.e. Densit® and RPC) (Benson, 2003).

Further rheological studies were continued at Cardiff to optimise HPFRCC. The aim was to achieve good workable mixes with a very low water/binder ratio and a high volume fraction of steel fibre, in order that the resulting concrete, in its hardened state, was very ductile with a relatively high tensile strength. This was achieved by using large amounts (up to 8 % by volume) of short steel fibres (6-13 mm long, 0.16 mm diameter) in a cementitious matrix densified by the use of silica fume. The matrix contains only very fine quartz sands (up to 2 mm), instead of ordinary river sand and coarse aggregates. By optimising the grading of fine sands, the water demand is considerably reduced without affecting the workability of the mix.

As a result of many trial mixes and testing, the mixes shown in Table 3.1 are the optimised ones. Two different mixes (designated CARDIFRC®, Mix I and Mix II) of high-performance concrete differing mainly by the maximum size of quartz sand used in the mix have been developed using novel mixing procedures. These procedures are described in patent application GB 0109686.6.

CARDIFRC® differs in several respects from RPC and DSP mixes. First of all, are the two different types of fibres used in combination with the high volume fraction adopted. This rather innovative technique was found to be quite beneficial to the load deflection response of the matrix in terms of both strength and ductility. Investigations showed that the use of two grades of fine quartz sand (Table 3.1) substantially improved the performance of Mix I. Similarly, in Mix II in order to maximize the dry density of the mix three grades of fine quartz were used. This optimisation of grading of quartz sands used led to considerable reduction in the water demand without any loss in workability

As claimed by Karihaloo et al. (2001) the produced material (CARDIFRC®) in its hardened state is characterised by very high compressive strength (in excess of 200 MPa), tensile/flexural strength (up to 30 MPa), high energy-absorption capacity (up to 20,000 J/m^2). Table 3.2 shows the material properties of CARDIFRC®.

Table 3.1: Mix proportions for optimised CARDIFRC® Mix I and Mix II (per m^3) (After Karihaloo et al., 2001).

Constituents (kg)	Mix I	Mix II
Cement	855	744
Microsilica	214	178
Quartz sand:		
9-300μm	470	166
250-600μm	470	-
212-1000μm	-	335
1-2mm	-	672
Water	188	149
Superplasticiser	28	55
Fibres: - 6mm	390	351
- 13mm	78	117
Water/cement	0.22	0.20
Water/binder	0.18	0.16

Table 3.2: Typical material properties of CARDIFRC® Mix I and Mix II.

Material Properties	Mix I	Mix II
Indirect tensile strength (MPa)	28.6	21.4
Size-Independent Specific Fracture Energy (N/m)	22909	17875
Compressive Strength (MPa)	194.0	207.0

3.3.1 Constitutive description of CARDIFRC®

As mentioned by many researchers (Karihaloo et al., 1996; Wang and Karihaloo, 2000; Karihaloo and Wang, 2000) the strain hardening of HPFRCC is due to the nucleation of microcracks under increased tensile/flexural stress. In the literature,

assumptions have been made on their evolution but no experimental evidence is available to validate them. An experimental programme was implemented on CARDIFRC® specimens to quantify the increase in the crack density ω (Equation (3.9)) as a function of applied tensile stress σ and fibre parameters (Benson, 2003). Their results show that the fracture process zone is not due to one dominant crack but is due to many cracks. In support of this, parallel cracks, crack branching, cracks linking-up and multiple cracking were all observed and recorded. Moreover, as the active crack opens, evidence of fibre bridging was confirmed. It was also noted that not all cracks continued to propagate; some cracks became dormant since the failure plane will occur along the path of least resistance.

Numerical expressions have been fitted to the test data to describe the behaviour of CARDIFRC in uniaxial tension. Figure 3.10 shows the three regions predicted by the equations. Laboratory test work shows clear evidence that the linear elastic region is larger than theoretically predicted (Karihaloo and Wang, 2000), a smaller strain hardening region with a distinct plateau at the peak load followed by a gradual decrease in the stress after the peak load.

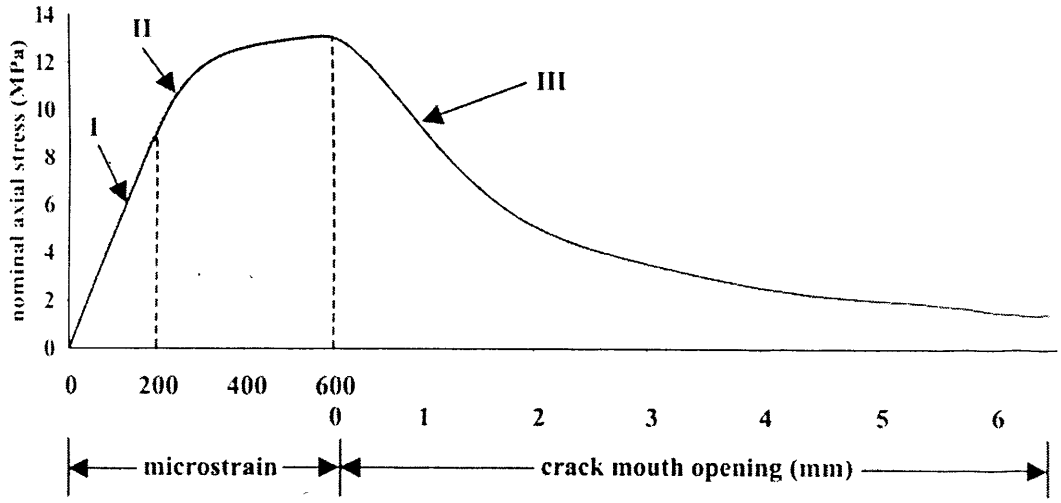

Figure 3.10: Complete pre- and post peak tensile curve for CARDIFRC®.

Stage I- Linear-elastic region

Applicable form 0 to 200 microstrain

$$\sigma_1 = 0.046\varepsilon \qquad (3.15)$$

Stage II- Strain hardening region

Applicable form 200 to 600 microstrain

$$\sigma = -4.34*10^{-10}\varepsilon^4 + 8.32*10^{-7}\varepsilon^3 - 6.03*10^{-4}\varepsilon^2 - 0.199\,\varepsilon - 12.62 \quad (3.16)$$

Stage III- Tension softening region

Applicable From 0 to 6.5 mm

$$\sigma = 3.07*10^{-3}w^7 - 0.08\,w^6 + 0.82\,w^5 - 4.42\,w^4 + 12.80\,w^3 - 18.10\,w^2 + 5.73\,w + 12.89 \quad (3.17)$$

In Equations (3.15)-(3.17) stress (σ) is in MPa, strain (ε) in microstrain and the COD (w) in mm.

3.4 CONCLUSIONS

From the foregoing literature review, it is clear that HPFRCC materials have superior characteristics in terms of material properties. Their mechanical and fracture properties have been enhanced very substantially compared to other types of concrete. In fact, the brittleness of concrete is reduced by incorporating fibres. The incorporation of small amount of fibres is mostly apparent in the post-cracking response. However, improvements in other properties such as first cracking strength, tensile strain capacity, and peak load are insignificant. With the advent of special processing methods (novel mixing procedures) and the use of high volume fraction of steel fibre, concretes of high compressive, tensile strength as well as high energy absorption have been reported. The produced material (CARDIFRC®) is characterized by strain hardening (multiple-cracking) and followed by tension softening due to localization of cracks.

CARDIFRC® is a new kind of high performance fibre reinforced cementitious composite (HPFRCC). It is an exciting durable material with great potential. It has many potential applications. This material can be used for retrofitting (Alaee, 2002; Karihaloo et al., 2002), for durable and reliable joining of pre-cast concrete elements, for the construction of structures for the containment and retention of hazardous materials and for the protection of valuable civilian and military assets, offshore and marine structures, overlays on ordinary concrete subjected to chemical attack, water and sewerage pipes, etc.

CHAPTER 4: DYNAMIC RESPONSE OF CONCRETE

4.1 INTRODUCTION

In addition to static loads, many concrete structures are often subjected to short-duration dynamic loads. All fracture is dynamic in nature, meaning it is a rate dependent process in which a discontinuity by cracks and voids is created in previously intact material. However, the term of "dynamic" is an arbitrary notion and must be defined with respect to time and length scales of the event. A common discriminator is the duration of load compared to the time required for a stress wave to traverse a characteristic length, say crack length. Response of concrete to dynamic loading is of interest in a variety of civilian and military applications, such as long-span bridges, offshore structures, protective shelters, nuclear reactor containment and reinforced concrete pavements. These loads originate from sources such as impact from missiles or flying objects, projectiles, vehicle collisions, impulses due to explosions, wind gusts, machine vibrations and earthquakes.

The dynamic loading can be classified into three major types:

- Fatigue Loading
- Loading at High Strain or Stress Rate
- Impact Loading

Several testing configurations and specimen geometries have been used for the experimental investigation of the damage mechanisms under each type of dynamic loading. The impact tests are mainly performed by several configurations of drop-weight impact machines, with instrumented Charpy test being the most popular amongst them. The most commonly used test of specimens at very high strain rates is the split Hopkinson pressure bar (SHPB) or Kolsky's apparatus. Moreover, several modifications have been developed, based on the Hopkinson bar principles. However, various experimental problems encountered in the testing of concrete with techniques using bars, have been discussed and improvements in the data processing have been proposed.

The fatigue behaviour has been tested with flexural fatigue tests, Charpy impact testers, wedge-splitting tests, dye penetration tests and some new innovative techniques. Nevertheless, there are no strict rules about the kind of test that can be used for each type of dynamic loading. Each type of the aforementioned test can be modified appropriately and can be used in almost all of the three different types of dynamic loading. The main specimen geometries used are notched-cavity splitting tension cylinders (Brazilian test), cube specimens, notched and unnotched prisms, and cylinders.

Several parameters were observed to affect the dynamic response of concrete, which are analysed and their influence role is explained. The most important of these parameters are the following: steel fibres, concrete confinement, curing conditions, humidity, temperature, number of load cycles, strain or stress rate.

In recent years there has been more interest in the fatigue behaviour of concrete subjected to fatigue loading, since fatigue is known to be responsible for the majority of failures of structural components. The fatigue strength of concrete is defined as a fraction of the static strength that it can support repeatedly for a given number of cycles. Fatigue failure occurs when a concrete structure fails catastrophically at less than design load after being exposed to a large number of stress cycles. Concrete fatigue is a process of progressive, permanent development of small imperfections existing in the material by repetitive loads. These imperfections may be present in concrete due to concrete shrinkage, or may be caused by application of external loads.

The fatigue mechanisms may be attributed to progressive bond deterioration between coarse aggregates and the cement paste or by development of cracks existing in the cement paste. These two mechanisms may act together or separately, which illustrates the complexity of the fatigue phenomenon. The addition of fibres to concrete has a double effect on the fatigue performance of concrete. By bridging cracks, they can sustain the crack growing process, providing an additional fatigue life to concrete. On the contrary, the fibres added to concrete may be the cause of further defects and reduce the fatigue life of concrete. Therefore a lot of attention is paid to the interfaces of fibres and matrix in fibre reinforced concretes (FRCs). As it will be elucidated in Chapters 6 and 7, the distribution of fibres in the internal possible planes of failure is a

critical factor, affecting severely the fatigue and fracture performance of FRC specimens. Finally, the addition of fibres makes the fatigue phenomenon more complicated and the development of an appropriate model extremely difficult. More work is required to explain the fatigue crack growth in cementitious matrix materials under the influence of external cyclic load and fibre and aggregate bridging. Studies have been made on the cyclic fatigue under normal tension-tension, tension-compression and bending loading regimes.

The aim of this chapter is to highlight the different types of dynamic loading and discuss the parameters affecting the dynamic response of concrete, giving emphasis to the work done on fatigue. Furthermore, it is aimed to review the various methods of testing and the problems encountered, describe some important experimental and theoretical works on dynamic loading and finally, bring to light the main damage mechanisms proposed by several researchers for dynamic loading response. Finally, a literature survey is performed on the modelling of the fatigue response of FRCs and a discussion provided on the several modelling options.

4.2 FATIGUE RESPONSE

4.2.1 Introduction

In recent years there has been more interest in the fatigue behaviour of concrete subjected to repeated loading, since fatigue is known to be responsible for the majority of failures of structural components. Fatigue failure occurs when a concrete structure fails catastrophically at less than design load after being exposed to a large number of stress cycles. The fatigue strength of concrete is defined as a fraction of the static strength that it can support repeatedly for a given number of cycles (ACI Committee 215, 1986).

Fatigue strength is influenced by concrete composition, environmental conditions and mechanical properties (Neville, 1995). For some other parameters, e.g. the strain rate or preloading, no consistent conclusion could be drawn by comparing the findings of different authors. The effect of the number of load cycles to failure has not been given much attention yet, although it is believed to be a significant fatigue parameter.

Fatigue is a process of progressive and permanent internal damage in a material subjected to repeated loading. This is attributed to the propagation of internal microcracks, which results in a significant increase of irrecoverable strain. Therefore, in fatigue research, in addition to fatigue strength, deformation properties of the concrete must be investigated. Much research has been done on the fatigue behaviour of concrete subjected to compression, but the problem of crack propagation in concrete specimens subjected to tension and bending cyclic loading is still open to further investigation. In recent years, there has been more interest in the fatigue behaviour of HPFRCCs and high strength concrete, because of their increased applications.

4.2.2 Fatigue loading testing configurations

A component or structure in service may be subjected to fluctuating or alternating cycles of stress but rarely can it be found that one constant type of loading cycle applies during the whole of the life of a component. Laboratory fatigue tests tend to be based on some uniform type of stress cycle be it alternating, repeating or fluctuating (Figure 4.1) (John, 1992).

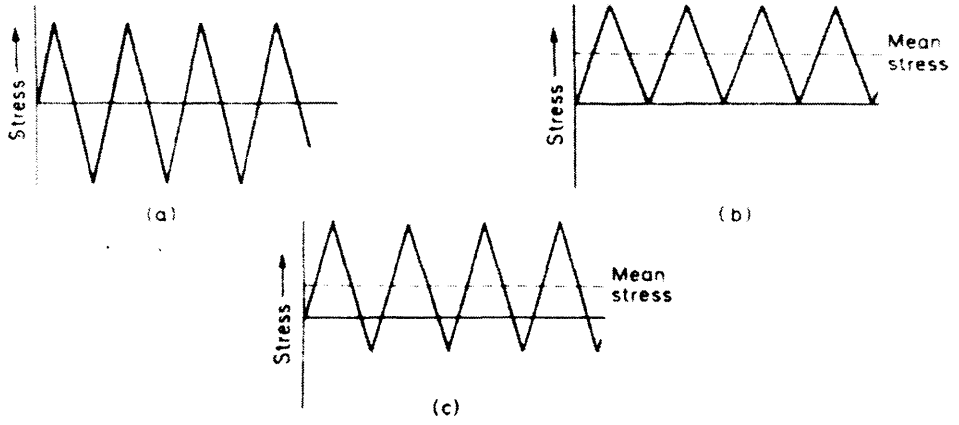

Figure 4.1: Types of stress cycle: (a) alternating (b) repeating (c) fluctuating (After John, 1992).

The most important testing approaches used nowadays are described below:

- The wedge-splitting test is an often-used technique for the fatigue crack growth (Figure 4.2). The fatigue machine used in this test can be a closed-loop servo-

hydraulic dynamic testing system. In order to increase the accuracy of the tests, a load cell is calibrated for this testing system and used for wedge-splitting testing. The crack mouth opening displacement (*CMOD*) can be measured by a clip gauge supported by two attached knife edges on the specimen.

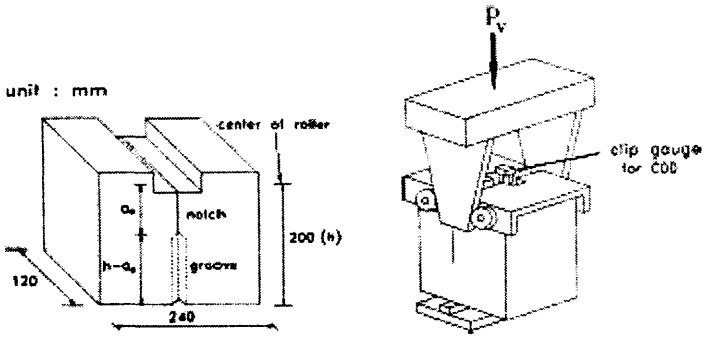

Figure 4.2: Loading device of WST and specimen geometry (After Kim and Kim, 1999).

- Dye penetration technique is a simple method for measuring the crack length by inserting dye into the crack surface. Generally, a coloured resin is used as a dye, of which the viscosity should be suitable for penetrating into a crack of desired width, and not for permeating the undamaged surface. This technique is usually used only for verifying the validity of other techniques, such as the *CMOD* compliance calibration technique, because of its single usage for the same specimen.
- Direct tension tests on notched specimens are performed on cylinders (Figure 4.3). The crack opening is acquired by three Linear Variable Differential Transducers (LVDTs), placed diametrically. In addition, three resistance full-bridge displacement transducers (clip-gauges) are fixed between the three LVDTs. The output from the three clip-gauges is averaged by coupling them in parallel. Two loading plates obtain a rigid coupling of the specimens to the loading system. The specimens are glued to the plates, previously bolted to the loading system, by an epoxy resin (Figure 4.3). During the tests the acoustic emission (A.E.) events can be monitored by means of two pre-amplifying transducers, attached to opposite sides of the specimen. The A.E. activity is acquired in terms of a cumulative count of acoustic events, which is considered as a measure of the development of the cracking process during the test.

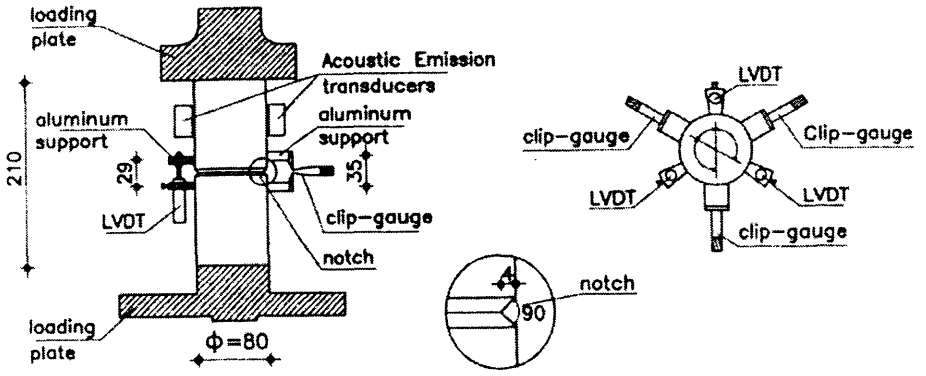

Figure 4.3: Experimental setup for direct tension testing of notched specimens (After Cangiano et al., 1997).

- Cyclic direct tension tests are also performed with unnotched specimens. Since there are no geometry induced stress concentrations in such specimens, the development of the fracture process zone should depend on the characteristics of the tested material only. In order to prevent the specimens from failing at its end faces special setups were designed (Cangiano et al., 1997).
- Another fatigue testing configuration is the flexural fatigue test, using notched bend specimens. The tests are conducted in a closed loop digitally controlled machine and the *CMOD* is measured by means of an LVDT located below the notch. Microscopical observations are often made by means of the replica technique in conjunction with scanning electron microscopy (SEM). The replica method permits the damage of concrete to be record either on lateral surfaces of specimens or on sections of specimens. The first is a non-destructive technique. Indeed, the evolution of the damage can be observed as a function of the load level in the case of the static tests or as a function of a number of cycles when the specimen is tested in fatigue. The second method is a destructive technique, which makes possible the visualisation of the state of the damage inside the specimen for only one stage of loading. Instead of the replica method, X-rays can be used for more effective microscopical observations.
- Finally, flexural fatigue tests using unnotched bend specimens are commonly performed, along the lines described for notched specimens. The tests are conducted in a closed loop digitally controlled machine and the bottom midspan deflection is measured by means of an LVDT located under the beam. In addition, the corresponding load values are recorded.

4.2.3 Experimental works

An experimental investigation of the behaviour of fibre reinforced concrete under cyclic flexural loading was made by Jun and Stang (1998). One type of polypropylene and two types of steel fibres in two volume concentrations were studied and the load-deflection responses were obtained for constant amplitude fatigue loading, as well as for static loading. The damage level was recorded under static and fatigue loading using acoustic emission techniques. Evaluation of the effect of fibres on the fatigue life of concrete subjected to bending depended very much on whether the change in static performance was taken into account or not. If the change in static performance was not taken into account, it could be concluded that all the tested steel fibre types improved the fatigue strength, and also that the fatigue strength improved with increasing fibre volume concentration. However, when taking into account the static improvement, the picture changed considerably. The fatigue performance of specimens with high fibre volume concentrations (2%) measured relative to the static strength was found to decrease compared to the lower fibre volume concentration (1%). Therefore, it was suggested that an optimum fibre volume concentration around 1% (vol.) should be used (less than 2 vol. percent). Furthermore, the results showed that the accumulated damage level at failure in the static test of unreinforced concrete was of the same order of magnitude as in the fatigue testing of the same material. However, using fibre reinforced concrete, the accumulated damage level in fatigue testing was 1-2 order of magnitude higher than the level reached in static testing of the same material. The same pattern of deflection and damage evolution was observed in plain and fibre reinforced concrete, where deflection and acoustic emission counts development consisted of 3 stages: a rapid increase in the first 5% of total lifetime, a uniform increase until 90% of total life and finally a rapid increase until failure.

The fatigue behaviour of fibre reinforced concrete in compression was investigated by Cachim et al. (2002), using two types of hooked-end steel fibres and their performance was compared. The authors measured the displacements and the acting load during the tests, so that several material parameters could be identified and assessed. The tested specimens were cylinders, 150 mm in diameter and 300 mm in height. The fatigue tests were carried out with load control between two limits (with a sinusoidal force variation with time). The minimum stress level, S_{min}, was 10% of the

monotonic strength and the maximum stress level, S_{max}, ranged from 60% to 90% of the monotonic strength. Before the cyclic process was started, the load was monotonically applied under displacement control until it reached the maximum stress level. The test stopped after failure or after a million cycles. It was observed that fatigue life of specimens with long fibres (60 mm length) was smaller than that of plain concrete, while the fatigue life of specimens with shorter fibres (30 mm length) was slightly longer than that of plain concrete. The main reason is related to the fact that the fatigue phenomenon is related to initial imperfections, such as microcracks or voids, existing in concrete. Thus, the presence of fibres, especially long ones, may be an additional cause of imperfections. An effect of the size of the fibres relative to the size of the tested specimens could also possibly occur, since for the 60 mm fibres the ratio between the cylinder diameter and the fibre length was 2.5, which was a relatively low value. Therefore, it was concluded that the key to the success of improving the fatigue life with the addition of fibres seemed to be related with the distribution of the fibres in concrete. In fact, if the fibres are not well dispersed in concrete, the addition of fibres may have a detrimental effect on the fatigue life of concrete. Wei et al. (1996) and Chang and Chai (1995) made similar works, investigating the effects of the fibre content, the fibre aspect ratio and length diameter ratio on fatigue performance of concrete, concluding that the role of the aforementioned parameters is very prominent. Moreover, Wei et al. (1996) showed that the fatigue behaviour is improved by the addition of silica fume to the concrete mix.

Singh and Kaushik (2000 and 2003) conducted experimental and theoretical studies to investigate the fatigue life distributions of steel fibre reinforced concrete (SFRC) containing different volume fractions of steel fibre, for various levels of the applied fatigue stress. The specimens were 100x100x500 mm beams and tested in flexure over a span of 450 mm. The fatigue stress ratio $R(f_{min} / f_{max})$ was kept constant at 0.10 throughout the investigation. By making use of the experimental results, the authors suggested that the probabilistic distribution of fatigue life of SFRC, at a particular stress level, can be approximately modelled by the two-parameter Weibull distribution, with statistical correlation coefficient values exceeding 0.90. The parameters of the Weibull distribution (shape parameter, α and characteristic extreme life u), were obtained by three different methods described. Using the two-parameter

Weibull distribution, the $P_f - S - N$ relationships have been generated for SFRC, thus incorporating failure probability P_f into the stress level (S) – fatigue life (N) relationships. These relationships can be used by the design engineers to obtain flexural fatigue strength of SFRC for the desired level of the failure probability.

Kim and Kim (1996) studied the fatigue behaviour of high strength concrete (HSC) in compression, by testing cylindrical specimens with various strength levels. The reference of the fatigue strength was the ultimate static strength acquired just before the fatigue testing. Generally, fatigue tests have been carried out for a given constant minimum stress or for a constant ratio between the minimum and maximum stress levels. In this study, a constant minimum stress level of 25% of the static uniaxial compressive strength was maintained and the maximum stress levels were varied from 75 to 95 % of the static strength. In fatigue tests, the first cycle of loading was loaded at standard rate, and the other cycles were loaded sinusoidally with a frequency of 1 Hz. It is accepted that fatigue strength is influenced by moisture condition; therefore the cylinders were wrapped in wet coverings to preserve the moisture content. It was observed that the total strain at the fatigue failure point approximately coincided with the strain of descending part in monotonic stress-strain curve. As a result, the fatigue life decreased with increasing concrete strength, that is to say, the internal damage is greatly localised for HSC at fatigue failure. While fatigue strain of HSC was smaller than that of LSC, the rate of fatigue strain increment of HSC was greater than that of NSC. Therefore, HSC was more brittle than NSC under fatigue loading. A mathematical relationship between maximum stress level (S_{max}) and the number of cycles to failure (N_f) was proposed, on the assumption that S_{max}-N_f curve consists of a sloping part and a horizontal part on a semi-log scale.

The same authors (1999) also investigated the fatigue crack growth of high strength concrete in wedge-splitting test. The selected test variables were the concrete compressive strength and the stress ratio. In order to apply the target stress ratio, the maximum and the minimum fatigue loadings were 75-85% and 5-10% of ultimate static load, respectively. Fatigue testing was preceded by *CMOD* compliance calibration, and then the fatigue crack growth was computed by crack length vs. the *CMOD* compliance relations acquired by the *CMOD* compliance calibration technique. To verify the applicability of the *CMOD* compliance calibration technique

to wedge-splitting testing, the crack lengths measured by this method were compared with those predicted by LEFM and dye penetration testing. Under the same maximum load level, fatigue life decreased with increasing concrete strength. This trend was also found in tests of cylinders subjected to compressive fatigue loading (Kim and Kim, 1996). It was observed that the fatigue crack growth rate increased with the strength of concrete. This trend was attributed to the rapid fatigue failure of higher-strength concrete. In addition, comparisons between the *CMOD* compliance calibration technique and the other methods supported the validity of this technique in the wedge-splitting test.

Cangiano et al. (1997) examined the fatigue crack growth in concrete with cyclic direct tension tests of cylindrical specimens made of NSC as well as HSC with and without steel (SFR) and carbon fibres (CFR). The tests were performed on both notched and unnotched cylinders. The material response obtained in the direct tension tests was compared to the structural response measured in bending tests. The envelope load-displacement curves obtained in cyclic tests on HSC-SFR and HSC-CFR specimens matched the static curves for both materials quite well. This showed that the envelope curve for the fibre reinforced concrete could be approximated with the static monotonic curve, as already found for normal strength concrete without fibres by other researchers. However, there are several doubts about this result, which are going to be discussed later. For the adopted volume fraction of fibres (0.38%) the carbon fibres did not significantly modify the load-displacement curve compared to the plain concrete, in contrast to the steel fibres. For higher cyclic load levels, the fibres played a minor role and no significant differences between plain and fibre reinforced concrete should be expected. However, for higher fibre contents the influence on the post-peak response was expected to be stronger. The maximum number of inner loops (N_{max}) measured from notched cylinders subjected to cyclic loading was influenced by the addition of both types of fibres (steel or carbon). The effect of steel fibres was more pronounced in HSC than in NSC. Carbon fibres had less influence on N_{max} than steel fibres. After a certain percentage of the maximum load was reached in the post-peak region of unnotched specimens, a cyclic loading was imposed. The higher the percentage of fibre the higher the maximum number of cycles. This was attributed to the different levels of microcracking and fracture process zone formation. The assumption that fatigue in concrete mainly occurred in

the process zone and not in the undamaged materials was supported by this observation. Finally, the maximum number of load cycles measured on the unnotched specimens was significantly larger than those for the notched, normal strength concrete specimens. A possible reason for this discrepancy might be the notches causing stress concentrations and supporting the development of the FPZ. However, it has to be taken into account that the scatter of experimental results from cyclic tests is usually large and the experimental results were obtained from concretes having different mechanical properties.

An experimental investigation of the fracture and damage of concrete due to fatigue was made by Kessler and Muller (1997), by performing a series of deformation-controlled three-point bend tests on notched beams. An improved experimental setup allowed the investigation of both the ascending and the descending branches of the load-crack opening relation and the load-deflection curve, respectively, even for high cycle fatigue loading (up to 10^6 cycles). The main test parameters in the experiments on fatigue were the number the cycles to failure, the crack opening rate and the curing conditions. Test results showed that in high cycle fatigue tests, an increase of the number of load cycles led to a decrease of the maximum load, the net flexural strength and the deflection at the maximum load, and to an increase of the critical crack mouth opening displacement and the critical deflection, respectively. In addition, it was shown that with an increase in the number of load cycles the envelope curves differ from the static curve. However, no clear tendency of the influence of the number of load cycles on the fracture energy G_F could be observed. It was assumed that the fracture energy was independent of the cyclic load history. It is believed that further experimental and theoretical studies are necessary to validate or reject this assumption. Finally, it was found that the curing conditions had no significant effect on the observed general trends with increasing number of load cycles. However, the individual test values for the unsealed specimens were somewhat higher in most cases. Such higher values for the net flexural strength, fracture energy and critical *CMOD* have also been observed in other investigations. The lower crack opening rate had no significant effect on the above-mentioned parameters.

Toumi et al. (1997) made a microscopical observation of mode *I* crack propagation in concrete subjected to fatigue. The fatigue tests were performed on notched concrete

beams, subjected to three point bending tests. Microscopic observations and crack length measurements were made by means of the replica technique associated with scanning electron microscopy (SEM). A comparison was also presented between the observed crack lengths determined by the replica method and the ones estimated by compliance calibration technique. It was shown that the compliance method underestimated the actual crack. Conversely, other researchers showed that the compliance method overestimated the crack length obtained by the dye penetration. Since it is questionable whether the crack length has the same value on the surface and inside a specimen, the researchers use indirect methods, such as a compliance calibration to evaluate a mean crack length. In order to clarify this point, this programme also included a lot of specimens, which were subjected to fatigue tests for a different number of cycles and next sawed to compare the crack length inside and outside. Under fatigue tests, the measured crack length on the lateral surface could represent the length of the damage inside the specimen. In addition, no discontinuous microcracks were observed inside the specimen, in contrast to static tests. Finally, it was concluded that the features of crack growth were more complex than under static tests, because more diffuse and branching phenomena were detected in both the matrix and the aggregates. These phenomena will be discussed in the next section.
Another investigation studied the crack propagation in plain concrete under three-point bending cyclic loading, by a displacement control actuator. From the measured strains along a crack as well as in front of a crack tip, it was found that at unloading compressive stresses were acting along the crack surface near the crack tip and that these compressive stresses caused tensile stresses in the concrete ahead of the crack tip. Both the compressive and tensile stresses increased with loading cycles. When the tensile stresses became large enough to cause cracking, the crack propagated. The increased tensile strain was considered to be the major source of the crack propagation during unloading (Ueda et al., 1997).

A study of the variations in the mechanical properties of concrete subjected to low cyclic loads was made by Ballatore and Bocca (1997). The work analysed the changes occurring in the mechanical properties of concrete subjected to uniaxial compressing loading cycles having low intensity and short duration. The concrete was seen to undergo strain hardening and an increase in stiffness due to effects of dynamic loading, as revealed by an increase in the material's failure load and modulus of

elasticity. In addition, it was observed that in poor quality concrete, a shift from ductile to brittle failure was experienced. In addition to the variations in failure load, the testing program also made it possible to analyse the variations in total fracture energy and the variations in the stress-strain curves occurring in concrete specimens of different quality. The procedure adopted was as follows: some of the specimens were subjected to a preliminary cyclic compressive loading of intensity equal to 10% and 20% of the failure load; after that such specimens were tested till failure through a uniaxial static compressive test by applying the load in the same direction as in previous tests. Two different types of concrete were used to assess the variations in these phenomena in relation to concrete quality. The dynamic loading reduced the pore space in the concrete, so that in the subsequent static compressive tests deformability was hindered by improved material compaction. In the poor quality concrete, on account of the improvement of mechanical properties of the material, the total fracture energy can be expected to increase, like the compressive strength, but in actual fact it was seen to decrease. This was an apparent contradiction and explanation for this lies in the fact that concrete has shifted to a different failure mode, with ductile failure having been replaced by brittle failure. Consequently, the uniaxial failure test was not able to measure the actual variations in the material's interior energy. It can be said conclusively that the energy stored up in the specimen during the cyclic loading partly produced strain hardening of the material and partly increased the failure load in consequence to changes to the concrete matrix.

Finally, Naaman and Hammoud (1998) described the fatigue characteristics of high early strength fibre reinforced concrete (HESFRC). 14 specimens were tested under 4-point bending fatigue. Two mixes containing 2% (vol) of hooked steel fibres were selected, and for each mix three different target load ranges were applied: 10-70%, 10-80% and 10-90% of the ultimate flexural capacity, as obtained from the corresponding control static tests. All specimens tested in this study were pre-cracked before cyclic loading, with two to three visible cracks in the constant moment region. This was an essential characteristic of these tests compared with other studies on fatigue of fibre reinforced concrete. As observed for all specimens, one major crack propagated in the constant moment region, until final failure of specimen occurred. It was suggested that for all practical purposes, a stress range of 65% of the static flexural strength can be taken as the endurance limit in design. Moreover, the

experimental work revealed that two mixes reinforced with 2% (vol) hooked-end steel fibres, with aspect ratios of either 60 or 100, showed essentially similar behaviour under fatigue loading. This may imply that the influence of aspect ratio on fatigue life was not as significant as the volume fraction of fibres. However, a more realistic explanation is that, with hooked-end fibres, the fibre pull-out resistance after debonding is primarily controlled by the end hook and not by the fibre length.

4.2.4 Discussion

The fatigue life of a specimen is defined as the number of cycles to failure at the given loading range. Although there is no standard procedure for carrying out fatigue tests, fatigue testing is assumed to be of high difficulty, and great care must be exercised. However, even in the most carefully planned tests, a large scatter is usually observed in fatigue life. This is because a small error in the estimate of the ultimate strength induces an error in the loading range, which in turn can have an enormous effect on the number of cycles to failure.

Generally, it is well known that the fatigue strain gradually increases with an increase in the number of cycles. The fatigue strain development consists of three stages: stage 1 is the rapid increase up to about 10% of the total life, stage 2 is the uniform increase from 10 to 80% of total life, and stage 3 is the rapid increase until failure. The same behaviour is observed also in other materials, such as carbon fibre reinforced composites under impact fatigue, in a research made by Sarkar and Roy (2001).

It is mainly accepted that the concrete damage under fatigue loading mainly occurs in the fracture process zone (FPZ) present at the crack tip. It was shown that after applying comparatively high pre-peak loads to concrete wedge splitting specimens, during the following cyclic loading the crack propagation rate remarkably increased. This rate increase was attributed to the presence of a larger FPZ after the application of some "spikes" in the loading history. The fatigue behaviour of concrete structures can be correctly studied only when the material behaviour in the FPZ is known. Some researchers suggest that this can be determined by performing cyclic direct tension tests on cracked specimens.

Some experimental results available in the literature have evidenced that the ultimate displacements of specimens subjected to cyclic loading are very close to the load-displacement curve (envelope curve) obtained in corresponding static tests (Cangiano et al., 1997). This aspect may be particularly meaningful for fibre reinforced concrete characterised by high post-cracking stresses and deformations. The use of fibres can prove to be even more effective in high strength concrete, which on account of the intragranular nature of the cracking phenomenon, is characterised by comparatively brittle fracture behaviour. There are, however, many arguments about this observation.

The observed lack of clear tendency of the G_F values with increasing number of load cycles (Kessler and Muller, 1997) may result from different, sometimes contrary influences. The energy-supply by each load cycle results in a continuous separation of the aggregates from the matrix and therefore in an enlargement of the FPZ and in a further crack propagation, respectively. In the unloading case, a crack cannot close completely because of the unlocked or pulled out aggregates. This phenomenon leads to tensile stresses, especially in the vicinity of the crack tip, and reduces the maximum load F_m with increasing number of load cycles. However, the contribution of the second part of the descending branch to the value of the fracture energy G_F is higher for high cycle fatigue tests (Kessler and Muller, 1997). As a result of these effects, the shape of the envelope curves changes with increasing number of load cycles, as was found by many researchers. This observation clearly shows that the assumption of a unique envelope curve for the fatigue behaviour of concrete is correct only for low and medium cycle fatigue, but cannot be maintained for high cycle fatigue. This might be the reason why no clear tendency for the influence of the number of load cycles on the fracture energy G_F could be observed.

The feature of crack growth under static tests is found to be similar in fatigue tests, but with some differences. Indeed, most of the investigations carried out on lateral surfaces, showed a complex crack growth process. Generally, a unique crack propagates in the matrix and skirts around the aggregates along the well-known interfacial transition zone. This mechanism, which results in the deterioration of the bond between the coarse aggregate and the matrix, is dominant. Sometimes, a crack runs across an aggregate with a branching phenomenon within this aggregate.

However, in this case the observations of the initial state showed a pre-existing damage within the aggregate before the crack tip reached it. The crack sometimes is composed of two branches. Nevertheless only one of them is on the future main crack path. Due to stress redistribution, the opening of other microcracks decreases but never closes completely and remains observable. When the crack stops in the matrix, two branches can be observed in the area of the crack end. When it stops in an aggregate, there are no diffuse microcracks. The observation of the crack propagation inside the material is similar to the one on the lateral surfaces. This point differs from static tests, where previous investigations showed discontinuous microcracks distributed ahead of the main path inside the specimens. This distribution is not observed in the case of fatigue tests. This phenomenon can be related to the residual crack opening observed at the unloading state, which induces tensile stresses in the area of the crack tip. These stresses interconnect the discontinuous microcracks.

A possible mechanism of fatigue crack growth in concrete is proposed by Horii et al. (1992). It is seen from Figure 4.4 that the cyclic tension-softening behaviour is complex and includes many characteristics, one of which may be the mechanism responsible for fatigue crack growth. One of the noticeable features of the cyclic behaviour is the residual crack opening displacement. At a point that undergoes tension-softening during loading, there exists residual opening displacement at an unloaded state. This works to resist the elastic constraint, which acts to close the crack faces, resulting in compressive stress at the point and tensile stress at the crack tip. This may be the mechanism of fatigue growth. Horii et al. (1992) also concentrated on another feature of this curve, which is the material behaviour on reloading. The opening displacement and transmitted stress in the reloading process are almost proportional, with a reduced slope. It should be noticed that the maximum stress during reloading is decreased to about 85% of the stress before unloading. This degradation in the reloading process is considered to be the main source of the fatigue crack growth.

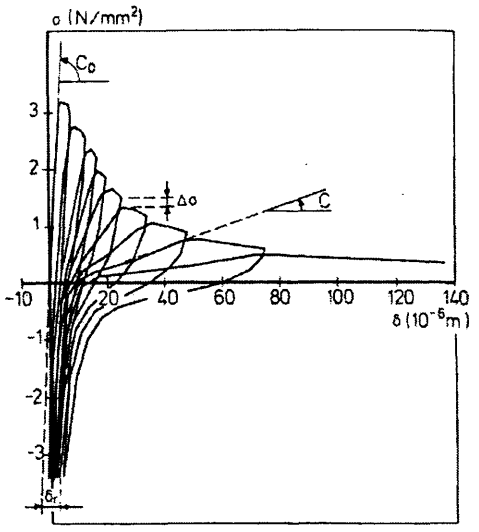

Figure 4.4: Stress-deformation relation under cyclic loading (After Horii et al., 1992).

A paper of Yan et al. (1999), which refers to the effect of silica fume and steel fibre on the dynamic mechanical performance of high strength concrete, reveals the mechanisms by which silica fume and steel fibre reduce the damage under fatigue. At the crack tip, steel fibres can restrain the extension of the crack, reduce the extent of stress concentration at the tip of crack, change the direction of crack growth, and delay the growth rate of the crack. The incorporation of silica fume into the matrix brings the strengthening, toughening and crack resisting effects of the steel fibres into full play (filler, crystallising and pozzolanic effects). The extent of improvement in the fatigue capacity of FRC can be expected to depend upon the fibre volume content, fibre type and geometry. However, the main fibre parameter influencing the fatigue performance of FRCs seems to be the fibre content, whereas the aspect ratio and fibre type is secondary in importance (Lee and Barr, 2004). Although most researchers agree that FRC has better fatigue behaviour compared to plain concrete, there is conflicting evidence based on the work of Cachim et al. (2002), discussed above. This contradiction, however, does not undervalue the contribution of fibres, but only brings to light the importance of fibre distribution in the fatigue response of concrete. Finally, the presence of fibres does not seem to enhance the fatigue life of concrete under compressive fatigue loading. On the other hand, fibre addition benefits the fatigue performance under flexural fatigue loading. A possible explanation is that under tensile forces, the fibres are able to bridge cracks and prolong fatigue life. On the contrary, the presence of fibres cannot display their true effectiveness under compressive loading, as the mode of failure is different (Lee and Barr, 2004).

Crack growth curve has been observed to show three stages: initial deccelerated growth, steady state growth, and final accelerated growth. It is seen that most of fatigue life is spent in the second stage of steady state crack growth. If the crack growth rate during the steady state stage can be lowered, the total fatigue life can be made longer. With fibre bridging, it appears plausible to realise fatigue crack arrest during cyclic loading. This can be achieved by minimising the degradation rate of interfacial bond strength. Also, other microstructural parameters have the same influence on crack growth (e.g. increasing the fibre volume fraction can lead to a slower growth rate in the steady state stage and eventually to crack arrest). It is also known in many materials that fatigue crack growth rate becomes negligible when the net crack-tip stress intensity factor amplitude, K_{tip}, is below a threshold value, K_{th}, so the above discussion on achieving negligible crack growth rate is equivalent to achieving K_{tip} below K_{th}. This can be achieved with the addition of closely spaced and randomly dispersed fibres as reinforcements. The action of fibre bridging and fibre pullout dissipates energy in the wake of the crack tip. This means that a properly designed FRC can arrest the fatigue crack even after the crack starts to grow, showing an advantage of FRCs. By contrast, concrete has no means to lower K_{th}, once a fatigue crack starts to grow. This is the fracture mechanics approach on the fatigue problem which will be introduced in the next section, where a micromechanics based model by Li and Matsumoto (1998, 1999) will be described.

4.2.5 Fatigue modelling

4.2.5.1 Introduction

The addition of fibres to the concrete matrix can dramatically improve the fatigue performance of the composite as well as its resistance to impulsive and dynamic loads. Secondly they impart additional strength in tension, shear and flexure. The degree of improvement of the mechanical characteristics of FRCs is influenced by the specimen size, loading configuration, size and type of fibres. A better understanding of these improvements and also of the bridging activity of fibres is necessary in order to develop an appropriate model for the fatigue response of FRCs. Moreover, to design structures economically against fatigue loading, the relationship between load and fatigue life must be established.

4.2.5.2 Models for fatigue strength and fatigue life prediction

A simple relationship between applied stress and fatigue life is difficult to obtain. Fatigue is a progressive fracture of a material. To predict the average life of a structural component, a number of specimens have to be tested at various stress levels until failure. Since the average life is generally the best estimate, it is commonly used to describe the fatigue characteristics of the specimens. The test results can be plotted either on log-normal or log-log paper, with the stress on the ordinate and corresponding fatigue life on the abscissa. A straight line representing the average life is then fitted to the test data. The two most common models for best fit are the following (Ramakrishnan et al., 1996):

1. The logarithmic equation (log-normal plot): $Y = a + b * ln(X)$
2. The power equation (log-log plot): $Y = a * X^b$

The selection of the model to predict the fatigue life is based on the correlation coefficient. Also the assumption of normality of the data must be checked. This is done by producing a normal probability plot of the residuals and checking whether the data form approximately a straight line. Several researchers suggest that a power equation gives the best fit. Earlier studies showed that the total fatigue life should be expressed by two straight-line segments, one for the high-cycle and one for the low-cycle fatigue range.

This separation into high- and low-cycle regions can be avoided with the power equation:

$$Y = a * X^b$$

or taking logarithms of both sides,

$$ln(Y) = ln(a) + b * ln(X)$$

The proposed expression to determine the fatigue life of FRC is:

$$S = f_{max} / f_r = C_0 (N)^{C_1}$$

in which C_0 and C_1 are coefficients and f_{max} / f_r is the fatigue stress ratio (fatigue strength/flexural strength). This expression is valid only in the range from 10^3 to $2*10^6$ cycles.

4.2.5.3 Cyclic behaviour

When concrete with a sufficiently large fibre content cracks in response to monotonically applied load, the cracks are bridged by fibres whose presence retards crack growth and increases the fracture energy. A strength increase is observed only for relatively large fibre volumes, because otherwise the strength increment due to fibres is small compared with the concrete strength. In contrast, ductility and toughness increases can be noted for very low fibre volumes. The same is true in the case of cyclic load response. The fibres contribute a disproportionate share to the energy absorption capacity of the composite, because they possess considerable ductility, whereas the concrete matrix does not. Frictional effects on the fibre-matrix interface account for another major contribution. Both of these phenomena greatly retard the damage accumulation in the composite and lengthen its fatigue life. It is not clear whether the failure mechanisms for monotonic and cyclic load are fundamentally different. Although the experimental evidence so far seems to support the hypothesis that they are not, it is not clear at all that the actual degradation processes in the two cases are identical (Ramakrishnan et al., 1996).

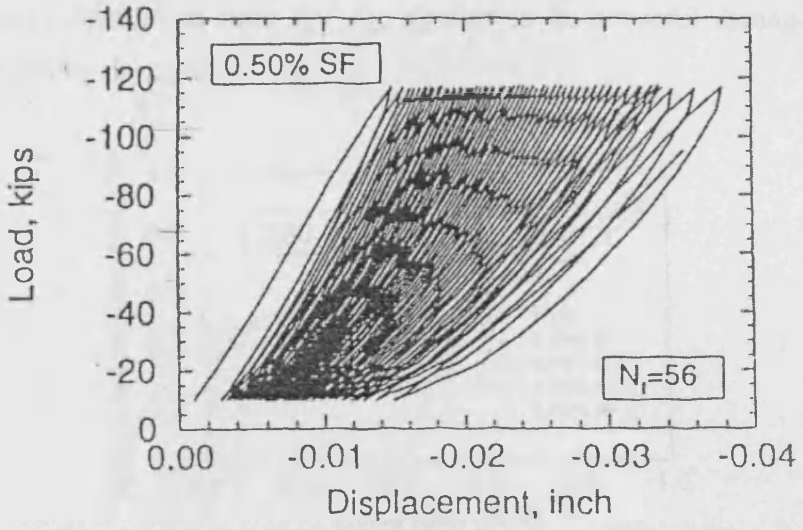

Figure 4.5: Load-deformation histogram for specimen with 0.5% steel fibre content (After Ramakrishnan et al., 1996).

Several important characteristics of FRC response to uniaxial cyclic compression are illustrated in the load-deformation plot of Figure 4.5. The following observations can be made (Ramakrishnan et al., 1996):

1. Damage causes a gradual degradation of the elastic stiffness properties, which expresses itself in the form of a reduced secant modulus and a large increase in irrecoverable elastic strain.
2. A considerable increase in permanent strains that are not recoverable upon unloading can be interpreted as plastic deformation. Experts are still at a loss to explain exactly what micromechanical processes are responsible for this apparent plastic deformation and whether it is correct to call it such.
3. Individual hysteresis loops are changing their shape throughout the fatigue life. Loading branches are initially convex, but soon turn concave. The degree of nonlinearity of both loading and unloading branches increases considerably with cycling, reflecting the complex mechanism of crack opening and closing.
4. The total strain accumulation history (Figure 4.6) can be categorised into the three phases of fatigue life. However, only phases two and three can rightly be associated with damage.
5. The areas of the enclosed hysteresis loops, a measure of progressive energy dissipation (Figure 4.7), increase gradually and in most cases rather slowly. The total energy dissipation capacity E_{tot} has been found to correlate strongly with the fatigue life and because of its integral nature has the advantage of less statistical scatter than the number of cycles to failure. Therefore, the energy dissipation ratio E / E_{tot} appears to be a useful damage index for modelling purposes.

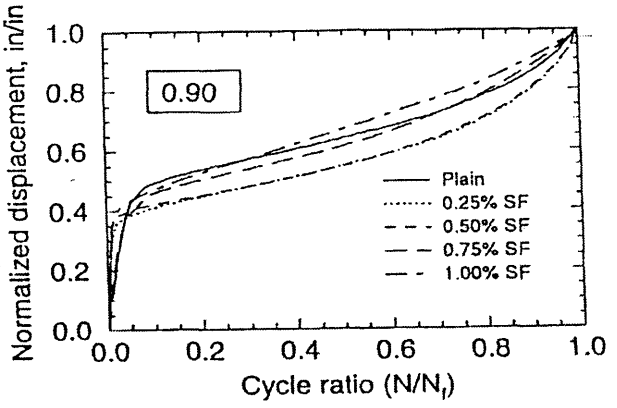

Figure 4.6: Strain accumulation histogram for SFRC at stress-strength ratio 0.90 (After Ramakrishnan et al., 1996).

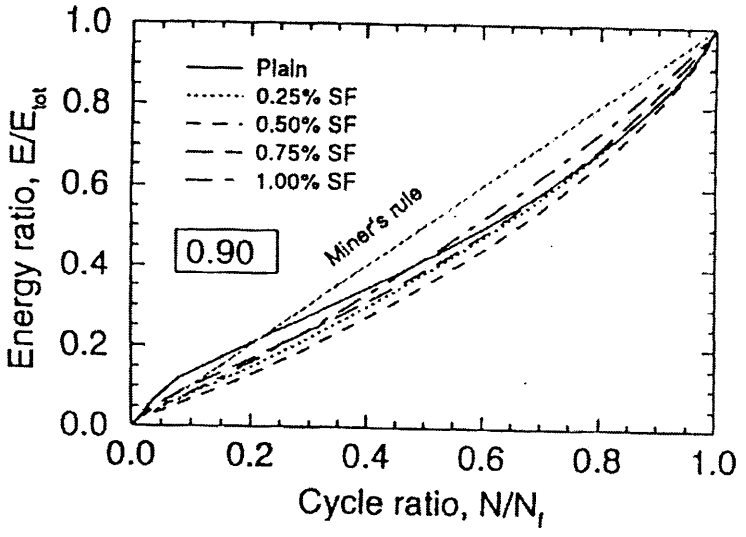

Figure 4.7: Damage accumulation histogram (measured by energy ratio) for SFRC at stress-strength 0.90 (After Ramakrishnan et al., 1996).

These are some of the observations that define the objectives of a mathematical model for reproducing the cyclic behaviour of FRC. In modelling FRC material behaviour under cyclic load, two fundamentally different approaches can be followed – the micromechanics and the macromechanics approach. In the micromechanics approach, the constitutive behaviour of the fibres, the concrete matrix, and the interface are modelled separately and then combined by some suitable method. In the macromechanics approach the composite is treated as if it were a single material, having properties which are derived either empirically from tests of the composite, or the properties of the matrix are modified to account for the effect of the fibres. At the time of writing this there exist very few models capable of simulating the cyclic response of FRC. Some models can reproduce the response of FRC to only monotonic load, while others address only plain concrete subjected to either monotonic or cyclic load. The following section shall review some of the models that are believed to be most promising.

4.2.5.4 Macromechanics based models

These models are generally based on continuum damage mechanics and plasticity theory, because FRC exhibits both strength and stiffness deterioration under cyclic load as well as residual deformations which can be interpreted as plastic strains.

An interesting mechanism of fatigue crack growth in concrete is the one proposed by Horii et al. (1990, 1992). It is strongly believed that a fracture theory capable of describing the behaviour of concrete must include in it a description of the material softening taking place in the fracture process zone (FPZ). The Dugdale-Barenblatt-type model of the bridging zone is modified for fatigue crack growth. The bridging zone is modelled as an extended part of a semi-infinite crack along which stresses are transmitted due to bridging by aggregate. First, let us consider the initial loading (Figure 4.8a). The crack opening displacement and transmitted stress satisfy a tension-softening relation. Here a linear tension-softening relation AB in Figure 4.9 is assumed for simplicity. The stress is bounded at the end of the bridging zone. The problem is reduced to integral equations for transmitted stress (Horii et al., 1989). By solving them numerically, the relationships between the applied load and bridging zone length and distribution of transmitted stress (and accordingly crack opening displacement) are obtained. Next let us consider the unloading and reloading by an amount to be determined (Figure 4.8b). Along some part of bridging zone (loading part), the same tension-softening curve AB is satisfied. Along the other part of the bridging zone (unloading part), the transmitted stress is assumed to be proportional to the crack opening displacement. The stress at point E is set to be $\alpha\sigma_0$, where σ_0 is the stress before unloading at point C and α is a constant called the degradation parameter. A different position in the unloading part satisfies a proportional relation with a different slope, depending on the stress state before unloading. The degradation parameter α is assumed to be constant independent of the stress before unloading. With those conditions and the condition that the stress is bounded at the tip of the bridging zone, the problem is formulated and solved numerically. The unloading part in which the proportional relation is satisfied is determined so that the solution along OD does not exceed point D. An iterative solution procedure is employed to satisfy this condition. For the following cycles a similar procedure is repeated. In the present model the cyclic effect in the unloading part (the proportional relation with reduced slope) is not taken into account unless the point reaches the tension-softening curve. This effect should be clarified and included in the model. Moreover, the present model predicts arrest of crack extension after several cycles when the load level is low. Hence the model cannot be applied to high-cycle fatigue.

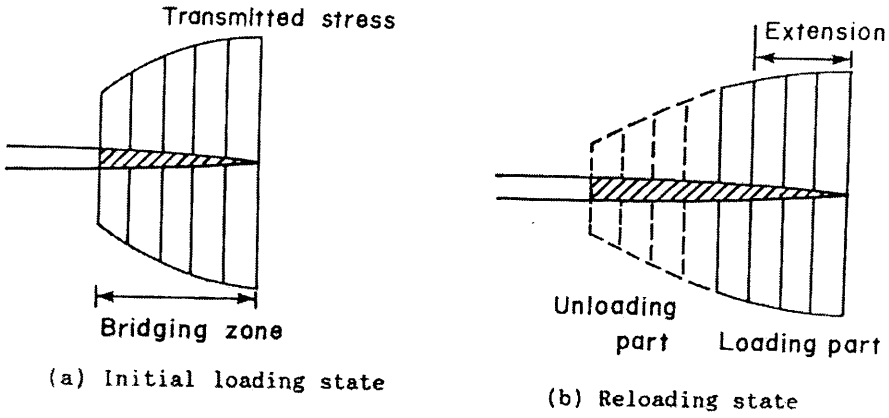

Figure 4.8: Model of fatigue crack growth (After Horii et al., 1990, 1992).

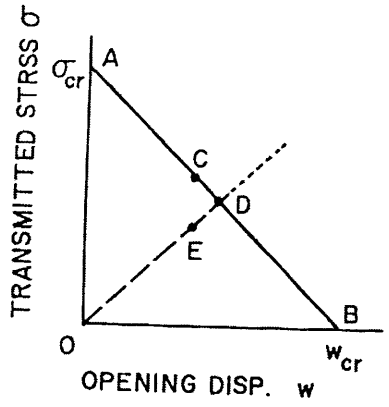

Figure 4.9: Material behaviour in loading part and unloading part (After Horii et al., 1990, 1992).

Peng and Meyer (2000) have developed a very promising macro-model within the framework of continuum damage mechanics and plasticity theory. The model describes the inelastic behaviour of concrete reinforced with randomly distributed fibres. Assuming the material to be an initially homogeneous and isotropic continuum, the inelastic behaviour can be represented by the model shown in Figure 4.10, which consists of a series of n Maxwell-type chains arranged in parallel together with one additional dashpot-like block element and one spring element in series. The elastic response of the material is represented by spring E and the inelastic response by the various parallel elements. Concrete is represented by a thermodynamically consistent mechanical model. For the r^{th} spring element, the spring stiffness C_r relates the generalised force $Q^{(r)}$ to an internal variable, $p^{(r)}$ as $Q^{(r)} = C_r : (e^i - p^{(r)})$. The generalised frictional force $Q^{(r)}$ is assumed to be related to the rate of the corresponding internal variable $p^{(r)}$ through the dashpot-like block α_r by $Q^{(r)} = \alpha_r :$

$dp^{(r)} / d\zeta_D$, where $d\zeta_D^2 = de^i : de^i$ is a generalised time measure. From this basic formulation a stress-strain relationship has been derived. Damage is assumed to occur at the beginning of any load history due to initial defects in the material. A second order damage tensor is introduced, and the damage evolution is assumed to be associated with the current state of stress and damage accumulation. To represent the stress-induced anisotropy, a fourth order damage tensor is constructed on the basis of the second order damage tensors. The material constants a_r and C_r reflect the damage accumulation. An elasto-plastic stress-strain relationship is then established which includes the anisotropic damage accumulation in plain and fibre reinforced concrete. The model is capable to simulate the response of plain and fibre reinforced concrete subjected to triaxial stress histories and strain-controlled cyclic loading.

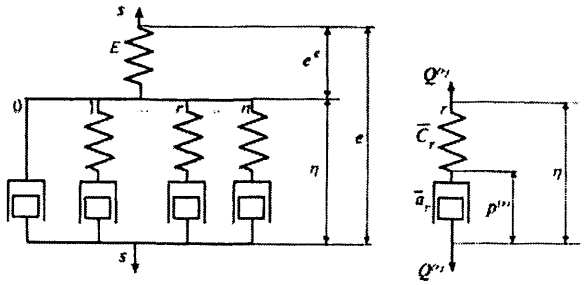

Figure 4.10: Mechanical model for thermodynamically consistent constitutive equation (After Peng and Meyer, 2000).

A numerical model for the analysis of concrete under fatigue loading has been developed by Cachim et al. (2002). It is based on viscoplasticity theory, replacing time-dependent with cycle-dependent behaviour. The analysis is performed in a two-step procedure. Initially, loads are monotonically increased until they reach their maximum level of the cyclic process, which is done with a standard non-linear analysis. Then, with the load fixed at the maximum level, the cycles are applied to the structure and a cycle-dependent analysis is executed. Only the evolution of inelastic part of the deformation is considered in each cycle. An exponential law, characterised by two parameters, ζ and m, controls the evolution of the permanent deformation per cycle. These parameters must be determined from the test results by a trial-and-error approach. Permanent deformations are governed by a surface similar to the plasticity load surface, with their direction defined by a non-associated law. The constitutive equations of the model are formed considering that in the presence of relatively small deformations, the change in deformation per cycle, $\partial\varepsilon/\partial N$, may be divided into an

elastic part, $\partial\varepsilon^e/\partial N$, and into a plastic part, $\partial\varepsilon^p/\partial N$, according to $(\partial\varepsilon/\partial N) = (\partial\varepsilon^e/\partial N) + (\partial\varepsilon^p/\partial N)$. The integration of the constitutive equations leads to the following system of non-linear equations in which the unknowns are the state of stress and the plastic multiplier: $\Delta\varepsilon_{n+1} - \Delta\varepsilon^e_{n+1} - \Delta\lambda_{n+1}(\partial g/\partial\sigma_{n+1}) = 0$ and $(1/\zeta\Delta N)\Delta\lambda_{n+1} - \varphi(\sigma_{n+1}, \kappa_{n+1}) = 0$. σ is the stress vector, $\partial g/\partial\sigma$ defines the direction of permanent deformation, κ is the hardening parameter and ζ represents a measure of the deformation per cycle. The iterative procedure is continued with increasing deformations until the stress state reaches the fatigue envelope or until reaching the monotonic envelope, which will lead to fatigue failure (Figures 4.11 and 4.12). Regardless of the simplicity of the model, it can identify the main characteristics of the flexural fatigue tests.

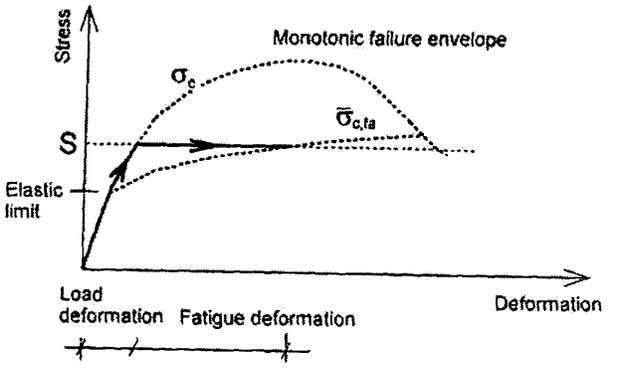

Figure 4.11: Strain evolution for a stable process (After Cachim et al., 2002).

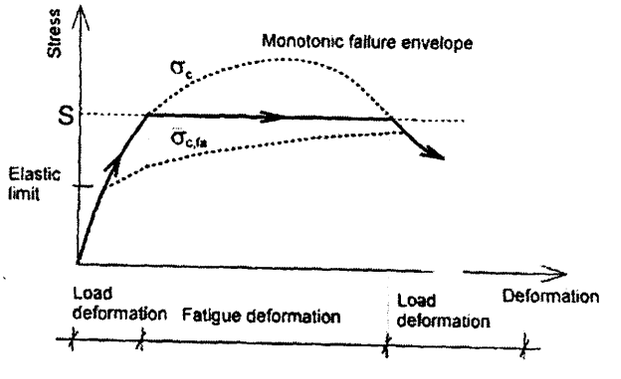

Figure 4.12: Strain evolution for an unstable process (After Cachim et al., 2002).

One of the most important models representing the growth of discrete cracks in concrete under fatigue loading is the one developed by Hordijk and Reinhardt (1991). The model is based on the post-peak cyclic tensile behaviour of concrete and shows how a crack or softening zone propagates under repeated loading. From fatigue tests, it appears that after an unloading-reloading cycle, the curve will not return to the same

point of the envelope curve where it started from, but to a point that belongs to a lower stress. This phenomenon is due to the damage which is caused in such an unloading-reloading loop. It is clear that some mismatch of the crack surfaces will occur at unloading, resulting in a propagation of existing microcracks. From these experiments it was furthermore concluded that the envelope curve was not significantly affected by the cyclic loading. The particular model is based on non-linear fracture mechanics. The three basic equations are, respectively, empirical expressions for the unloading curve (I), the gap in the envelope curve (II) and the reloading curve (III) (Figure 4.13). It has been chosen to use only characteristic points in the σ-w relation (f_t, w_c, w_{eu}, σ_{eu}, σ_L) as variables in the expressions, while w_c is defined as $5.14G_F / f_t$. The expressions that were chosen are based on a close inspection of the experimental results. The model represents the actual material behaviour, including the relation between stress drop and the lower stress level of the loading cycle very well. In addition, by numerical simulation it has been demonstrated that the softening zone will propagate under repeated loading and finally the numerical analysis resembled the cyclic creep curve, as usually found in fatigue experiments, very well. However, the proposed approach applies only for the fatigue behaviour of plain concrete (Hordijk and Reinhardt, 1991).

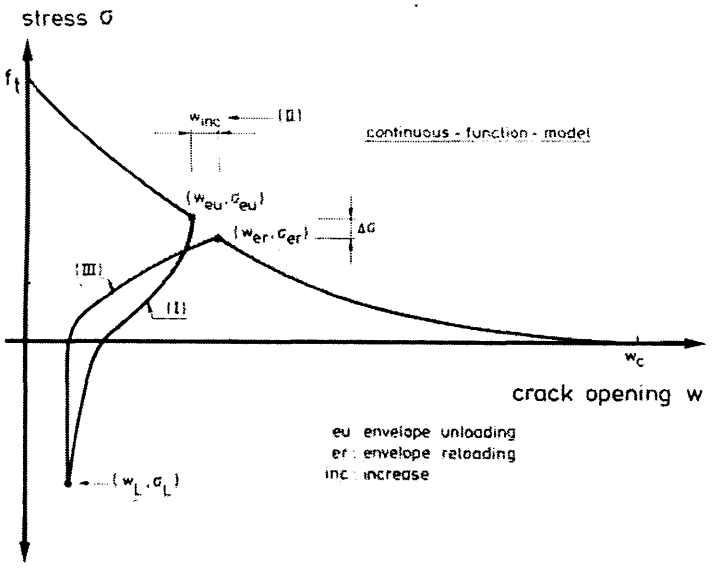

Figure 4.13: Setup for the crack cyclic behaviour model (After Hordijk and Reinhardt, 1991).

Several macromechanics theories have been developed for the fatigue response of FRC and many discussions have been made. In addition, several reviews have been

made of the models developed so far, which discuss their advantages and weaknesses (Ramakrishnan et al., 1996; Francois, 1991).

4.2.5.5 Micromechanics based models

According to micromechanics approach, the mechanism of fatigue crack growth of fibre reinforced concretes is governed by three factors: matrix fatigue crack growth, crack bridging by fibres, and cycle-dependent degradation of crack bridging (Figure 4.14). Several investigators have made experiments involving the pullout of individual fibres to measure their modification of the fracture behaviour of concrete and also to shed some more light on the mechanisms that govern the cyclic behaviour of FRC. Here we present some of the most important works on fatigue modelling, based on the micromechanics approach.

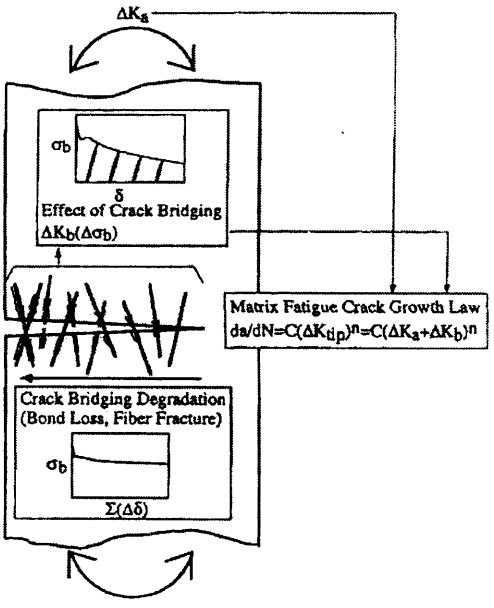

Figure 4.14: Fatigue damage on material constituents (After Matsumoto and Li, 1998 and 1999).

Matsumoto and Li (1998 and 1999) developed a fracture mechanics based fatigue model of randomly distributed fibre composites, which considers the aforementioned factors. The authors used the experimental data obtained by Jun and Stang (1998) who performed flexure fatigue tests of fibre reinforced concretes. The authors believe that the progressive fatigue damage on material constituents is responsible for fatigue life of a material. Here, material constituents include matrix, fibres and fibre-matrix interface, and these undergo microscopic changes during fatigue loading. Some of

these microscopic changes in turn cause a detrimental change in macroscopic material properties. Among a number of microscopic changes during fatigue loading, fatigue crack growth can be considered the damage most responsible for fatigue life of FRCs. FRCs fail in fatigue when a fracture propagates unstably, subsequent to stable crack growth under fatigue loading. Thus, fatigue life of FRCs is controlled by stable fatigue crack growth behaviour.

Stable fatigue crack growth in FRCs is affected by 3 main factors:

1. Matrix fatigue crack growth law specific to a matrix (this is quantified with the Paris law, which relates the crack growth rate to the crack-tip stress intensity factor amplitude)
2. Crack bridging of fibres (a cyclic constitutive law between the crack bridging stress amplitude and the crack opening displacement amplitude due to fibres and aggregates is described)
3. Fatigue damage in the fibre-matrix interface and/or bridging fibres (the interfacial frictional bond degradation under cyclic sliding is quantified assuming that the bond degradation is governed by the accumulated crack opening displacement change)

Fatigue damage on matrix: stable matrix fatigue crack growth

The stable fatigue crack growth in the matrix has been observed to obey a Paris law type equation. This law gives the relation between the crack growth rate and the crack-tip stress intensity factor amplitude, namely:

$$\frac{da}{dN} = C(\Delta K_{tip})^n \tag{4.1}$$

where a = crack length, N = number of load cycles, C = Paris constant, ΔK_{tip} = crack-tip stress intensity factor amplitude and n = Paris exponent. Hence the fatigue life N_f can be computed if ΔK_{tip} is known:

$$N_f = \int_{a_i}^{a_f} \frac{1}{C(\Delta K_{tip})^n} da \tag{4.2}$$

where a_i = initial crack length and a_f = final crack length.

In the present model of fatigue crack bridging, the aggregates are viewed as bridging elements co-existing with the fibres, so that the cement paste serves as the brittle matrix in FRC composites. Assuming linear elastic fracture mechanics for simplicity, a_f is related to the cement matrix fracture toughness, K_c, by:

$$K_c = \sigma_{\max} F \sqrt{\pi a_f} \tag{4.3}$$

where σ_{max} = maximum applied stress in a given load amplitude and F = dimensionless geometry factor. For the present problem formulation, the cracked body is treated as a homogeneous cement matrix, while the aggregates and fibres are treated as applying negative loading or closing pressure on the fatigue crack. Therefore the problem reduces to obtaining ΔK_{tip} of FRCs.

$$\Delta K_{tip} = \Delta K_a + \Delta K_b \tag{4.4}$$

where ΔK_a=stress intensity factor amplitude due to external applied loading and ΔK_b= stress intensity factor amplitude due to crack bridging (Figure 4.14).

For a beam in flexural bending that has a crack on the tension face ΔK_a, is given by:

$$\Delta K_a = 2\int_0^a G(x,a,w)\Delta\sigma_a(x)dx \tag{4.5}$$

where w = full beam depth, $\Delta\sigma_a(x) = \Delta\sigma_0(1 - 2x/w)$ (linear gradient for bending), $\Delta\sigma_0$ = applied external stress amplitude, and x is measured from the tension face of the beam. $\Delta\sigma_0$ is related to applied external moment amplitude, ΔM, through:

$$\Delta\sigma_0 = \frac{6\Delta M}{bw^2} \tag{4.6}$$

$G(x, a, w)$ is a weight function that represents a unit force contribution to the crack-tip stress intensity factor, as follows:

$$G(x,a,w) = \frac{1}{\sqrt{\pi a}} \frac{h_1(x/a, a/w)}{\left(1 - x^2/a^2\right)^{1/2}} \tag{4.7}$$

where h_1 is found in Tada (1985).

Similarly, ΔK_b is a function of the relation between the crack bridging stress amplitude, $\Delta\sigma_b$, and the crack opening displacement amplitude, $\Delta\delta$, (hereafter refered to as the cyclic constitutive law) and is given by:

$$\Delta K_b = -2\int_0^a G(x,a,w)\Delta\sigma_b(\Delta\delta(x))dx \tag{4.8}$$

where, $\Delta\sigma_b(\Delta\delta)$ = cyclic constitutive law and $\Delta\delta(x)$ = crack opening displacement amplitude at a point, x, on the crack surface.

ΔK_{tip} can be calculated as described above, if the crack opening displacement amplitude at a point, x, on the crack surface, $\Delta\delta(x)$, is known *a priori*. This can be obtained by solving an integral equation:

$$\frac{\Delta\delta(x)}{2} = \frac{4}{E}\int_x^a \left\{ \int_0^{a'} G(x',a',w)\left[\Delta\sigma_a(x') - \Delta\sigma_b(\Delta\delta(x'))\right]dx' \right\} G(x,a',w)da' \tag{4.9}$$

where E = matrix elastic modulus.

Effect of crack bridging: cyclic constitutive law

Crack bridging stress in FRCs is exerted by fibres and aggregates, so the cyclic bridging law, $\Delta\sigma_b$, is given by the superposition of crack-bridging stress-crack opening displacement relation due to fibres and aggregates under cyclic loading:

$$\Delta\sigma_b = \Delta\sigma_f + \Delta\sigma_m \tag{4.10}$$

where $\Delta\sigma_f$ = fibre bridging stress change under cyclic loading and $\Delta\sigma_m$ = aggregate bridging stress change under cyclic loading.

Cyclic bridging law due to fibres, $\Delta\sigma_f(\Delta\delta)$, is based on the micromechanics of fibre bridging under cyclic loading. Expressions for $\Delta\sigma_f(\Delta\delta)$ are summarised in Li and Matsumoto (1998 and 1999). The normalised cyclic bridging law due to fibres can be represented by:

$$\Delta\tilde{\sigma}_f = function\left(\Delta\tilde{\delta}, \tilde{\delta}_{\max}, \tilde{\delta}^*\right) \tag{4.11}$$

where $\Delta\tilde{\sigma}_f = \Delta\sigma_f / \sigma_0$, $\sigma_0 = V_f \tau (L_f d_f) 2$, V_f= fibre volume fraction, τ = interfacial frictional bond strength, L_f = fibre length, d_f = fibre diameter, $\Delta\tilde{\delta} = \Delta\delta / (L_f / 2)$, $\tilde{\delta}_{\max} = \delta_{\max} / (L_f / 2)$, $\tilde{\delta}^* = \delta^* / (L_f / 2) = (2\tau L_f)(E_f d_f)$, and E_f= fibre elastic modulus. The complete form of the above equation is given by Li and Matsumoto (1998, 1999).

The law shows that the fibre bridging stress amplitude, $\Delta\sigma_f$, is a function of the maximum bridging strength, σ_0, the crack opening displacement amplitude, $\Delta\delta$, the maximum crack opening displacement experienced in the preceding load cycle, δ_{max}, and the fibre composite system parameter, δ^*. The dependence on the maximum crack opening displacement, δ_{max}, appears because the debonded length of the fibre-matrix interface and the reduced number of bridging fibres are determined by δ_{max}, or in other words the pull-out load.

The monotonic constitutive law due to fibres is required for the evaluation of the cyclic constitutive law, since δ_{max} is related to the maximum bridging stress, $\sigma_{f\,max}$, experienced in the preceding cycle. Expressions for the monotonic constitutive law due to fibres are summarised in Li and Matsumoto (1998, 1999).

Fatigue damage on fibres: interfacial bond degradation

Finally, the interfacial degradation under cyclic loading is derived from experimental observations in fibre reinforced ceramics and fibre reinforced concrete. The authors suggested a bilinear function for interfacial frictional bond strength, τ:

$$\tau = max\ \{(\tau_i + D \sum_{i=1}^{N} \Delta\delta_i),\ \tau_f\} \qquad (4.12)$$

where τ_i = initial bond strength, D = degradation coefficient (negative for degradation), N = number of load cycles, $\Delta\delta_i$ = crack opening displacement change at i^{th} cycle, and τ_f= final or steady state bond strength.

Here, the interfacial bond degradation is measured with:

$$\sum_{i=1}^{N} \Delta\delta_i = \text{accumulated crack opening displacement change} \qquad (4.13)$$

The interfacial frictional bond strength then degrades (D is negative) with the accumulated crack opening displacement change. This degraded friction influences fatigue crack growth behaviour by modifying the fibre cyclic constitutive law in response to both the number of cycles and the crack opening displacement changes experienced at each point on the bridged crack surface. Interfacial degradation also directly influences the maximum fibre bridging strength attainable in a given load cycle via the monotonic constitutive law, $\sigma_f(\delta)$.

The interfacial bond degradation is a function of the position on the crack surface. The bond strength degrades more near the crack mouth, since fibres are subjected to a large number of cycles and crack opening displacement changes, whereas the undegraded bond strength is exerted in the newly created crack surface near the crack tip.

$$\sum_{i=1}^{N} \Delta\delta_i(x) = \text{accumulated crack opening displacement change at } x \qquad (4.14)$$

A semi-analytical method to predict fatigue behaviour of FRC based on the equilibrium of force in the critical cracked section has been developed by Jun et al. (1999). The model relies on the cyclic bridging law, the so-called stress-crack width relationship under cyclic tensile load, as the fundamental constitutive relationship in tension, and focuses on the fatigue life prediction in the case that the maximum load is larger than the first crack load.

The basic assumptions behind this model can be stated as follows:

1. After a dominant fatigue crack is created, the bridging behaviour within the fracture zone governs the rate of fatigue crack advancement.
2. The stress at the crack tip remains constant and is equal to the material tensile strength.
3. Material properties outside the fracture zone are unchanged during fatigue loading.

The cyclic stress-crack width relationship was determined experimentally, by deformation controlled fatigue tensile tests on notched specimens. Thereafter, the

analysis is performed considering a simply supported rectangular beam that is subjected to an external bending moment. The behaviour of the beam is assumed to be elastic until the maximum principal tensile stress reaches the tensile strength of the material. After that it is assumed that a single crack has formed with a maximum tensile strength at the crack tip. Using the equilibrium conditions and the stress-crack width relationship, a complete solution of external load and *CMOD* and crack length is obtained. The authors claim that there is good correlation between the experiments and the model predictions.

Li et al. (1993) have developed a micromechanic-based theoretical model, which captures the essential features of the stress-crack width relationships at small crack widths (less than 0.3 mm). Micromechanisms included are the bridging actions due to aggregates and fibres, Cook-Gordon interface debonding and fibre prestress. The fibre bridging action involves interface slip-dependent friction as well as snubbing friction for fibres bridging at inclined angles. The aggregate bridging action is modelled using an empirical expression, which fits a wide range of experimental data extremely well. In this model the aggregate bridging stress σ_a is expressed as a function of the crack opening w. Based on the concept of debonding against a frictional strength of τ and on the concept of an inclined fibre acting as a flexible rope passing over a frictional pulley against a snubbing coefficient f, the fibre bridging stress, σ_f, was derived by integrating the individual contribution of fibres located at various centroidal distances (z) from the matrix crack and at various orientations (φ) relative to the tensile loading direction. Subsequently, the additional bridging compliance was considered as a result of the Cook-Gordon effect. Cook and Gordon predicted that a crack of finite root radius in an elastic solid under remote tensile load will create a crack tip stress field with a crack-plane-parallel tensile component which reaches a maximum at a distance of the radius of the crack tip (Li et al., 1993). Thus, a matrix crack approaching an isolated fibre can cause interface debonding before the crack tip reaches the fibre-matrix interface, if the interfacial strength is adequately weak. As a consequence, it is expected an additional displacement δ_{cg} related to the elastic stretching of the debonded length a, labelled as the Cook-Gordon parameter. Therefore, the total crack width, w, is approximately given as the sum of ($\delta_{cg} + \delta$), where both δ_{cg} and δ are related to the fibre bridging stress, σ_f. This procedure allows the calculation of the fibre bridging stress, σ_f, indirectly as a function of the total crack width, w. Finally, it

was recognised that at the formation of a matrix crack, and prior to any crack opening, the fibre is already in a stressed state. The level of prestressing, σ_{ps}, may be estimated from the load-sharing between fibre and matrix at the matrix cracking strain. It is suggested that in a FRC, and especially for a small crack opening, the aggregate bridging effect and the fibre bridging effect may be assumed to operate simultaneously. When the prestressing effect is included, the total composite bridging stress $\sigma_c(w)$ is then given by $\sigma_c(w) = \sigma_a(w) + \sigma_f(w) + \sigma_{ps}(w)$.

4.2.5.6 Models originally developed for ceramic composites

Ceramic composites, reinforced with several types of discontinuous fibre, have many similarities to High Performance Fibre Reinforced Cementitious Composites (HPFRCCs). The elimination of coarse aggregates, the presence of microsilica and water-soluble polymers and also the application of high pressure and temperature lead to materials with enhanced density and homogeneity. Therefore, models originally developed to describe the behaviour of ceramic composites, might be appropriate to depict the performance of HPFRCCs. Since there is no plasticity in most ceramic composites, the only possible mechanism for experimentally observed fatigue to proceed is through damage in the form of cracks. A decrease in the interfacial friction stress with fatigue cycling has been suggested as the most significant phenomenon responsible for fatigue in Ceramic Matrix Composites (CMCs). It has been suggested that frictional wear of the interface results in a decrease in clamping stress and thus the shear stress, τ, of the interface. A possible consequence of the lowering of τ is that the modulus of the CMC is lowered. The modulus changes are suggested to provide a measure of damage in composite. Two sources of radial clamping stress are residual stresses from differential thermal expansion, and misfit from roughness at the debonding interface. Several models have been proposed for the progressive interface debonding, which is the key parameter in the fatigue response of these materials (Parthasarathy and Kerans, 2001).

4.3 HIGH STRAIN OR STRESS RATE

4.3.1 Introduction

Strain-rate effects on the behaviour and on the failure of concrete under dynamic loading have received significant attention during last decades and are investigated from both experimental testing and modelling point of views. Several modern concrete structures for special applications may be subjected to loading at very high rate of stress or high strain rates. Under highly dynamic conditions, the strain-rate dependence of material response causes the material behaviour to be significantly different from what is observed under quasi-static conditions. Since compression tests are much easier to perform than the tensile ones, most results on rate sensitivity at high strain rates, which can be found in the open literature concerns compression.

4.3.2 High strain rate testing configurations

Experimental data have shown that a rate effect exists which can increase strength and deformation of concrete. A variety of testing methods have been used to show the rate effect. There are several questions concerning loading rate effects with respect to testing. First, the testing method must be clear and physically sound so that the quantity, which has to be determined, can be measured. Second, testing methods should be described or developed which are suited to investigate the reason for the rate effect found (e.g. whether the increase of fracture energy at high loading rates is caused by an increase of the size of the fracture process zone or by the forced fracture of aggregates or other causes should be investigated by other techniques). Several testing approaches have been used and the most important of them are described below:

- Dynamic tensile testing of brittle materials is one of the most difficult to perform. The difficulties originate from the boundary and initial conditions concerning the specimen shape and wave propagation, which is always present before and after fracture. The standard configuration, that is a tensile specimen attached at both ends and loaded from one active end, is not recommended, because of the stress

and strain gradients present due to the elastic wave propagation (Klepaczko and Brara, 2001).

- The Split Hopkinson Pressure Bar (SHPB) system, also called Kolsky's apparatus is a commonly used experimental technique in the study of constitutive laws of materials at high strain rates. The first use of a long thin bar to measure stresses in impact conditions has been reported by Hopkinson (1914). The experimental setting with two long bars widely used today was pioneered by Kolsky (1949). This ingenious technique for a compression test has been extended to the tensile and torsional loading with no significant changes in the concepts. A typical SHPB test is shown in Figure 4.15. It is composed of the long input and output bars with a short specimen placed between them. With the impact of a projectile at the free end of the input bar, a compressive longitudinal "incident" wave $\varepsilon_I(t)$ is created in the input bar. Once the incident wave reaches the interface of the specimen bar, a reflected pulse $\varepsilon_R(t)$ in the input bar and a transmitted pulse $\varepsilon_T(t)$ in the output bar are developed. With gauges glued on the input and output bars, these three basic waves are recorded. Their treatment allows calculation of forces and particle velocities at both faces of the specimen. According to the wave propagation theory, stress and particle velocity associated with a wave are simply related to the strain measured by the gauges. Thanks to the superposition principle and the shifting of waves (propagation theory), these values are known not only at the measured points but everywhere in the bar and in particular at bar-specimen interfaces (Gary and Bailly, 1998). Details of the equations and principles of the bar are widely documented for a variety of test types (Klepaczko and Brara, 2001; Gary and Bailly, 1998).

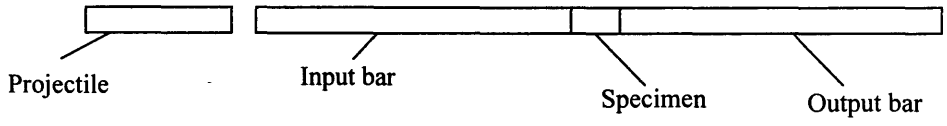

Figure 4.15: Typical SHPB setup.

- The use of an input bar in the SHPB test leads to a limitation of the maximum force for a given impact velocity because of the linear relation between the stress and the particle velocity associated with the same wave. The SHPB fails to smash concrete specimens at medium strain rates. Low strain rates need low input

velocities that will produce low input forces. A current solution to overcome this problem is to strike directly the specimen with a heavy striker. This arrangement is the so-called Direct Impact Hopkinson Bar (DIHB) test, which is a modification of the original SHPB test (Zhao and Gary, 1997) (Figure 4.16).

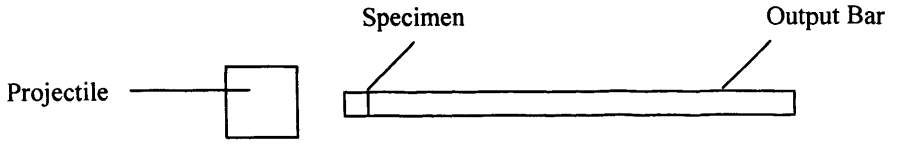

Figure 4.16: Direct Impact Hopkinson Bar (DIHB) test (After Zhao and Gary, 1997).

- Another use of the SHPB to test concrete in tension is the so-called Splitting Tensile test. In this configuration the SHPB is operated in the compression wave mode and the disk specimen is rotated 90^0, so that the load is applied along the specimen diameter. This is the so-called "Brazilian Test" applied in dynamics. With this experimental technique the maximum strain reached is ~20 s^{-1}.
- To pass into higher strain rates other experimental techniques must be developed. One of the most promising directions to test brittle materials in dynamic tension is to apply the principle of spalling. Spalling is a specific form of fracture, which occurs near free surfaces of a solid remote from a source of plane compressive wave. A new experimental technique, based on the Hopkinson Bar principle combined with the spalling phenomenon has been developed (Brara et al., 2001), to test concrete loaded at high strain rates in tension. The setup was equipped with a high-speed camera for the recording of the fracture process. This original technique allowed for determination of the tensile strength of wet concrete at high strain rates varying from 20 to 130 s^{-1}. The setup consists of a concrete specimen in the form of round bar, which is loaded by a compressive incident wave through the Hopkinson Pressure Bar, made of hard aluminium alloy (Figure 4.17). A short Al-alloy projectile launched by an air gun produces the incident compression wave. In order to assure a good wave transmission, the concrete specimen is in tight contact with the Hopkinson Bar before loading. After projectile impact, the incident wave generated in the Hopkinson Bar is transmitted into the concrete specimen, and a small part is reflected back to the Hopkinson bar due to the difference of impedances. The compression wave, which is transmitted into the

specimen, is reflected by the specimen free end as a tensile wave. The superposition of the incident compression wave and the reflected tensile one generates a tensile stress, which grows rapidly in time along the concrete specimen. Due to the wave superposition, the net tensile wave leads to spalling (tensile fracture) of the specimen at a certain distance from the free end, where the tensile stress reaches the critical value. The use of relatively short projectile permits to reach very high loading rates. The whole process of wave propagation is recorded via the three strain gauges cemented to the Hopkinson Bar surface at three specified distances. This arrangement allows for determination of the fracture stress caused by spalling, the stress history in the specimen, the critical time of loading, and the loading rate or strain rate (Klepaczko and Brara, 2001).

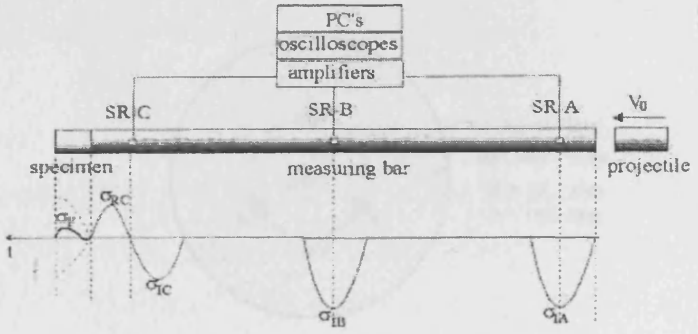

Figure 4.17: Experimental technique based on Hopkinson Bar principle combined with the spalling phenomenon (After Brara et al., 2001).

- Plate impact provides a unique means to generate extremely high strain rates and high pressures under well-controlled conditions (Grote et al., 2001) (Figure 4.18). This method can be used to produce data for the extreme conditions not yet fully simulated in laboratory or analysed in modelling. Average strain rates achieved are of the order of 10^4 s^{-1} and confining pressures in the experiments are of the order of 1-1.5 GPa. The specimen is placed at the front of the projectile assembly. A gap between the disk specimen and the projectile tube is provided to allow a traction-free end condition for the back surface of the specimen during the impact process. The specimen impacts against an anvil plate made of hardened tool steel. The impact occurs in a vacuum chamber. The velocity of the projectile V_0 is measured immediately prior to impact. Upon impact, compression stress waves are generated in both the specimen and the anvil plate. These waves propagate

from the impact face toward the rear surface of the specimen and the rear surface of the anvil plate. Upon arriving at the rear free surfaces, these compression waves are reflected as tensile waves. The reflected tensile waves then interfere destructively with the on-going incident compression waves, reducing the compressive stress in the specimen.

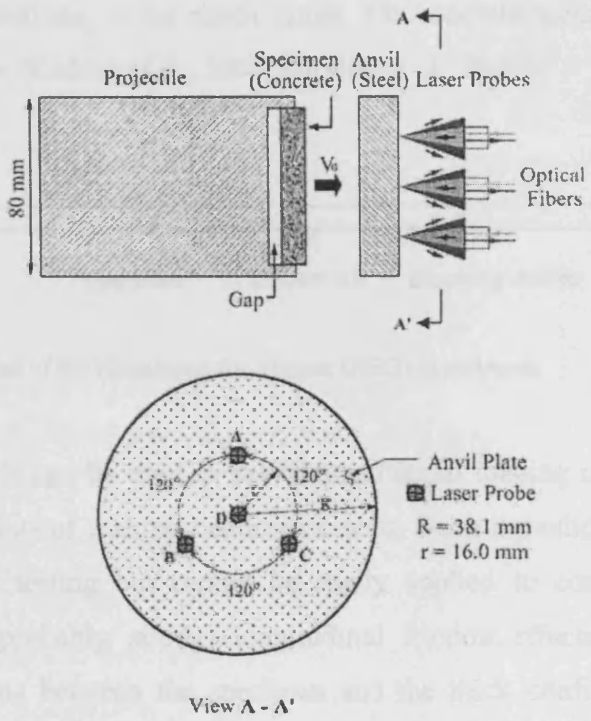

Figure 4.18: Configuration of the plate impact experiment (After Grote et al., 2001).

- The Hopkinson Bar Bundle (HBB) technique is a variation of the SHPB. It is a special equipment that enables precise measurement of the stress-strain diagram, including the softening branch, which is important for the correct evaluation of the energy absorption capability of concrete. The test rig consists of five parts connected in a serial system. A preloading bar, a blocking device, an aluminium bar (the incident bar), then follows the specimen. Finally another aluminium bar, identical to the first one (the transmission bar) (Figure 4.19). The two bundles (transmission and incident bars) consist of smaller aluminium bars, to each of which the concrete test specimen is glued using an epoxy resin. Strain gauges on each individual bar in the bundles enables measurement of the incident, reflected and transmitted pulses on each portion of the concrete specimen cross-section. During an experiment the pre-loading bar is initially pulled in tension in the elastic range, while the two aluminium bars and the specimen are unloaded. This

can be done by activation of the blocking device. The elastic energy stored in the pre-tensioned bar is then suddenly released, as a brittle fracture occurs of a notched bolt in the blocking device. This generates a tensile pulse, which propagates along the incident bar, loads the specimen and propagates along the transmission bar. During the entire test the pre-loading bar and the two aluminium bars will stay in the elastic range. The concrete specimen, on the other hand will fracture (Cadoni et al., 2001; Ulfkjær et al., 2001).

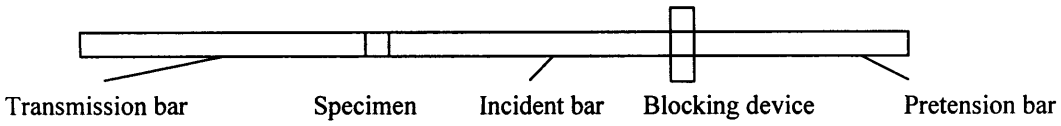

Figure 4.19: Configuration of the Hopkinson Bar Bundle (HBB) experiment.

- Different methods can be used to provide multiaxial loading conditions. A very simple one consists of making oedometric tests. Such a method has given good results for sand testing but cannot be easily applied to concrete because of unknown (and probably strong) longitudinal friction effects induced by the differential strains between the specimen and the thick confining cylinder. To avoid longitudinal friction, another method exists using a thin metallic ring compressed with the specimen. This method needs special specimen preparation and the use of a strain gauge on the ring. It allows for simultaneous measurement of the radial pressure and strain of the specimen, but without the ability of an easy control of the lateral pressure. For the sake of simplicity, the specimen is put into a cylindrical quasi-static pressure cell. The bars are acting as pistons and are introduced into the cell through seal rings. The lateral pressure can be applied with oil (up to 50 MPa), or with air (up to 10 MPa). The use of air as fluid seems to be the most accurate technique. It is not sure that a measurement of the oil pressure during the test, at a point in the chamber, would give an exact measure of the pressure applied to the specimen, because of transient effects in the fluid (Gary and Bailly, 1998; Zhao and Gary, 1997).
- Early tests on concrete under dynamic loading were performed with pendulum and drop weights. These are the so-called impact tests, which will be discussed

separately in section 4.4. The lack of precision of these tests does not allow for an accurate determination of the material behaviour.

4.3.3 High strain rate testing problems

Experimental problems are encountered in the testing of concrete with techniques using bars, and one should be cautious in interpreting experimental results. The reason arises from the fact that these techniques have been initially developed for the testing of metals. The commonly used SHPB, the DIHB and the test under confined pressure are of most significance; therefore several studies have been conducted for the investigation of the specific problems. A recent study by Zhao and Gary (1997) noticed these problems and suggested methods to obtain accurate measurements in those tests. The main difficulty of the measurement in the techniques using bars lies in the fact that the three basic waves have to be shifted from the strain gauges to the specimen faces, in time and distance. This shifting leads to two different perturbations. First, waves change in their shapes (wave dispersion) on propagating along the bar. Second, one has to find the exact time shift for the three waves so that the shifted waves at the bar-specimen interfaces correspond to the same time origin. To avoid shifting errors, the correction of the so-called wave dispersion effect should be made at first (Klepaczko and Brara, 2001; Zhao and Gary, 1997). An accurate determination of time shifts is obtained by a method based on the simulation of the specimen response (Zhao and Gary, 1996). One can simulate numerically, for an elastic specimen, the fictitious reflected and transmitted waves where the exact origins are known. If the specimen is supposed to behave elastically at the early stage of the test, the comparison between simulated and real waves allows for a precise determination of their origins. The application of those improvements in the data processing gives more accurate results. They are particularly important for the accuracy in the range of small strains.

Finally, the selection of the specimen length is of crucial importance in a SHPB test. The specimen must be short enough for a uniform state of stress along the length of the specimen to be rapidly achieved during loading. On the other hand, when very short specimens are used, friction between the specimen ends and the bars can play a significant role and lead to an apparent increase in strength. The diameter of the

specimen also needs to be small relative to the wavelength of the applied load pulse for the one-dimensional wave theory to be valid.

4.3.4 Experimental works

The tensile failure of normal concrete and steel fibre reinforced concrete at high strain rates was studied by Ulfkjær et al. (2001). Four very different kinds of concrete (a normal strength concrete and three high strength steel fibre reinforced concretes) have been tested at high strain rates using the Hopkinson Bar Bundle. The load-displacement curves obtained from the experiments were converted into stress-strain curves by dividing by the length of the specimen. The uniaxial tensile strength and the fracture energy were the two fracture parameters that have been calculated from the measured load-displacement curves. The uniaxial tensile strength was assumed to be the maximum stress measured during the loading process and the specific fracture energy was calculated as the area under the load-displacement curve (the elastic part of the deformation had been subtracted). The tensile strength was seen to increase both for normal and high performance concretes with increasing strain rate, while there was no clear picture regarding the energy absorption. The fracture energy of the normal strength concrete showed an increase compared to the static value, whereas this was not the case for the high performance concrete. This was probably due to fact that the fracture energy for the static experiments was determined on beams in three-point bending, where a significant amount of energy dissipates in zones away from the fracture zone.

Lambert and Ross (1997) investigated the dynamic fracture, crack velocity and strength response of cementitious materials. The research concentrated on obtaining crack velocity data for calibrating a model proposed by Grady (1988) and the subsequent prediction of strength response. The authors have obtained crack propagation speeds in mortar for a spectrum of strain rates. The splitting tension cylinder geometry (Brazilian) and cylinders with known central pre-notches were the specimen geometries for this effort. The cylinders subjected to a range of strain rates from 10^{-7} to 10 s^{-1}. All quasi-static tests were conducted on a closed loop servo-hydraulic machine. All crack velocities from the quasi-static tests are the maximum pre-peak values. The stress loading history of the specimen was obtained via strain

gauges mounted on the transmitted bar of the SHPB. Therefore, the stress magnitude and the average strain rate were determined from appropriate formulae. Crack velocity was measured through the use of thin foil resistive gauges and ultra-high speed digital photography to validate the foil gauge data. The foil gauges were glued directly on the surface near the crack tip and their resistance changed in direct proportion to the crack length. A constant current was supplied and the change in resistance (i.e. crack length) was measured as a corresponding change in potential. Additional velocity information was obtained from the notched cylinders by time-of-failure analysis of the transmitted signal. The time from the beginning of the transmitted signal to its peak was taken as the maximum time for the crack to propagate from the pre-existing notch tip to the outer tensile domain radius (approximately 80% of the physical radius, and it delineated the region under constant tensile stress, i.e. the region which is required to fail for catastrophic tensile failure). Thereafter, the model calibration was performed and predicted the increase in tensile stress as a function of strain rate. The uniqueness of this application is that the model accurately replicates experimentally obtained strength data, even though the model constants were obtained from an entirely separate analysis, using crack propagation data from the same experiment set. The use of the notched, splitting tension fracture specimens and the SHPB was believed to be the first in documented literature, at the time the tests were done.

Okada and Horii (1997) focused their attention on the effect of specimen-size and loading rate on the tension-softening curve, which represents the relationship between transfer stress and crack width in a crack growth region (a material characteristic of tensile crack growth in concrete). The tension-softening curve of the material was obtained by two back analysis programs, after wedge-splitting tests were carried out. Specimens of three sizes were tested with four different loading (CMOD) rates (0.1 mm/min, 1.0 mm/min, 10 mm/min, and 340 mm/min). The maximum value of fracture energy was calculated by dividing the area enclosed by the load (F) versus loading point displacement curve up to the final measuring point (a measurement was finished when the load dropped to about 5-7% of the maximum load) by the area of the ligament. The tension-softening curve was estimated from the actually measured load F versus $CMOD$ curve by two methods: back analysis program 1 (Uchida et al., 1995) and back analysis program 2 (Nanakorn and Horii, 1997). These back analysis

programs use a piecewise-linear function for the tension-softening curve. There was a relatively good agreement between tension-softening curves calculated by the two programs, both in the stress when softening starts and the shape of the curve. The most important findings of this study were the following: the maximum load and the specific fracture energy tended to increase with the loading rates, but no noticeable effect of specimen size on the specific fracture energy was seen. The average crack velocities of small-sized specimens, at the different strain-rates, were similar to the velocities obtained from medium and large-sized specimens. It was observed that crack velocities were roughly proportional to *CMOD* rates. It was observed that the estimated tensile strength tended to increase with an increase in the loading rate. With increasing loading rate, the fracture energy tended to increase. The rate of increase was small when the rate of *CMOD* was less than 10 mm/min. Finally, while the values of the fracture energy scattered more in the small specimen, the average values of the fracture energy did not show any clear dependency on the specimen size.

The general behaviour of quasi-brittle materials at high-strain rate was examined Gary and Bailly (1998). Dynamic loadings under compression were performed with a SHPB apparatus. Moreover, the response of concrete under multiaxial loading was investigated, using a specific device, which was specially built to produce dynamic compression under various controlled lateral confinement pressures, allowing for an independent evaluation of radial inertia and lateral pressure effects. Concrete shows an asymmetric ultimate behaviour (with failure strength in tension much lower than in compression) under quasi-static loading and a strong sensitivity to the triaxiality of the loading. The same asymmetry was found for the strain-rate sensitivity, which for concrete, remains small in tension and strongly increases in compression. Such an effect is often attributed to the lateral confinement induced by inertia effects. It is thus important to take into account those effects in the physical analysis of the dynamic behaviour of concrete. A model was proposed in which local inertia effects were introduced in the constitutive law through the strain acceleration. The validity of the model was checked by the results obtained by the special device for multiaxial loading. Results found in the literature show an increase of the maximum stress with the average strain rate, under dynamic compression loading. Experimental results presented in this study showed a change in the strain-rate sensitivity of the maximum stress, for a strain-rate about 10 s^{-1}, which could be due to inertial effects. Below this

value, only a strain rate effect due to the viscosity may be observed. This viscous effect is small and is attributed to the presence of free water in the concrete. For high strain rates (>100 s^{-1}), the structural effect is very important and becomes the major contributor to the apparent increase of the maximum strength. Finally, experimental results from the dynamic compression tests under lateral pressure showed that the strain rate has an influence on the maximum stress (apparent strength), as in the unconfined compression tests. It seems that the residual stress (post-peak phase) only depends on the confinement.

The strain-rate sensitivity and pressure dependence were believed to be two of the most important factors influencing the behaviour of concrete under dynamic conditions. Grote et al. (2001) studied the dynamic behaviour of concrete and mortar at high strain rates of the order of 10^4 s^{-1} and pressures up to 1.5 GPa. This investigation used SHPB and plate impact to achieve a range of loading rates and hydrostatic pressures. The SHPB experiments involved strain rates between 250 and 1700 s^{-1} without lateral confinement and the plate impact experiments subjected the materials to deformation at strain rates of the order of 10^4 s^{-1} with confining pressures of 1-1.5 GPa. Experiments indicated that the load-carrying capacities of the concrete and mortar increased significantly with strain-rate and hydrostatic pressure. The behaviour of mortar was significantly rate-sensitive in the strain-rate range of 10^{-3} - 1700 s^{-1}. The rate-dependence was weaker for strain rates above this transition rate. The stress-strain curves of mortar had similar shapes at different rates and showed strain softening after the peak stress, reflecting fragmentation and granular flow. Under the conditions of plate impact, significantly higher stresses were carried by concrete and mortar than what was observed for the materials under conditions of quasi-static, uniaxial compression. The marked increase in stress-carrying capacities under plate impact conditions was attributed to the effects of strain-rate hardening and the strong pressure dependence of the response of the materials. Approximately 42% of the strength enhancement was due to rate sensitivity and 58% was attributed to the effect of hydrostatic pressures. The average stress carried by concrete in plate impact experiment was approximately 30% higher than that of mortar, indicating the hardening effects of aggregate in concrete under impact loading. In contrast, the strength of concrete was found to be lower than that of pure mortar under conditions of quasi-static, uniaxial stress. The different trends reflect the effects of different

deformation and failure mechanisms in concrete under the quasi-static and impact loading. The key is the presence or lack of hydrostatic pressure. Finally, due to material heterogeneity inherent in the concrete and mortar specimens, the stress and deformation were non-uniform in general.

Brara et al. (2001) carried out an experimental and numerical study of concrete at high-strain rates in tension, using a new experimental technique based on the Hopkinson Bar principle combined with the spalling phenomenon. The experimental setup was described above. The results demonstrated a high rate sensitivity of tensile strength. The tensile strength increased from 4 up to about 12 times when compared to quasi-static values. A considerable increase in strength was confirmed by the analysis of digital images, obtained by means of a high speed CCD arrangement. In this case, the tensile strength was evaluated via velocity of the ejected parts of specimens, using again the one-dimensional wave analysis. In parallel with experiments, an attempt was made to model the failure of concrete for use in a computer program based on Discrete Element Method (DEM). The DEM, adapted for cohesive materials, approximated the concrete as an assembly of rigid particles connected by interaction laws. Thus, by taking into account the coherent nature of concrete, the fragmentation process could be implicitly described by breaking the bonds. In this approach, the experiments and simulations complement each other. In case of simulation, experiments allow to demonstrate the level of prediction of the fragmentation process obtained by the numerical code. In case of experiment, numerical simulation may indicate, for example, that a new method is needed to determine the fracture stress, or to introduce a new failure criterion. The numerical method proposed predicted exactly the experimental results. Klepaczko and Brara (2001) in another study used the same testing configuration to test wet and dry concrete at high strain rates. The results showed that the absolute value of the failure stress for wet and dry concrete was almost the same for a particular strain rate, which is not the case at low strain rates in tension or compression, when the wet concrete shows higher rate sensitivity than the dry one, under both tension and compression.

An analytical and experimental investigation of mode *I* fracture of concrete was conducted by Lambert and Ross (2000), under dynamic loading of a SHPB, using notched-cavity splitting tension cylinders (Brazilian test). The fracture parameters

were extracted by the application of the two-parameter fracture model. This is an equivalent elastic crack theory that characterises failure using the critical stress intensity factor K_{Ic} and the critical crack tip opening displacement $CTOD_c$ parameters (Karihaloo, 1995). Moreover, ultra-high speed digital photography was synchronised with the fracture process, to provide additional validation. The results showed that the effective fracture toughness and specimen strength both increased significantly continuously with loading rate. In addition, $CTOD_c$ was observed to increase with strain rate before reaching an asymptotic value.

Cadoni et al. (2001) investigated the behaviour of plain concrete subjected to tensile loading at high strain-rate. The tests had been performed on cube specimens and they used the Hopkinson Bar Bundle equipment. An increase of tensile strength with increase of relative humidity inside the concrete was clearly observed for impact loads. On the other hand, a slight decrease of tensile strength was noticed for saturated concrete specimens under quasi-static loads. Different levels of free water inside the specimen had an important influence on the sensitivity of the concrete response to the strain-rate. Plain concrete showed strain-rate dependence: increase of strength, ductility and energy absorption capability with increasing strain-rate. The increase of strength, ductility and energy absorption was non-linear and became remarkable at strain-rates > 1 s^{-1}.

4.3.5 Discussion and conclusions

Experimental data have shown that a rate effect exists which can increase the strength and deformation of concrete. A variety of testing methods have been used to demonstrate the rate effect, however one should be cautious in interpreting experimental results since other effects may also have significant influence, and also specific experimental problems are encountered. Since compression tests are much easier to perform than the tensile ones, most results on rate sensitivity at high strain rates, which can be found in the open literature concerns compression. Dynamic tensile testing of brittle materials is one of the most difficult to perform. The difficulties originate from the boundary and initial conditions concerning the specimen shape and wave propagation, which always present before and after fracture. The review presented above and the observation of the current trends in

testing of concrete, ceramics and rocks in dynamic tension leads to the conclusion that the best configuration to reach high strain rates in tension is the arrangement of bar projectile, Hopkinson bar and a cylindrical, relatively long specimen. Such an arrangement permits for many different variations in geometry and measurements. For example, the incident bar can be instrumented using a Hopkinson bar, or not instrumented at all. Also the specimen can be instrumented, or both the incident bar and the specimen can be simultaneously instrumented. The level of the wave analysis may be also very different.

Several theories have been developed in order to explain the strength increase due to high loading rates based on thermodynamic or statistical grounds. Inertia forces in the vicinity of a running crack have also been taken into account, as well as the influence of a limited crack propagation velocity on the behaviour. The most important of them are believed to be the so-called fracture theories, which include a rate effect. Weerheijm and Reinhardt (1989) have stated that the partition between the various types of energy changes during crack extension. This causes a decreasing crack propagation velocity resulting in a strength increase. The available energy to form new crack surfaces in the region around the crack tip decreases. Mihashi and Wittmann (1980) used this approach to predict the influence of loading rate on strength of concrete. They state that fracture is caused by a series of local failure processes in the hydrated cement paste and in the interfaces between cement and aggregate. As soon as a failure criterion is reached, a crack is initiated at a material defect. The same theories explain also the rate effect during an impact loading.

Looking at the inhomogeneous structure of concrete, there is a secondary effect, which depends on inertia: it is the exact fracture path which is forced through aggregate particles rather than around the particles. Since strength and fracture energy of the aggregate particles are larger than those of the matrix, this effect increases the total fracture energy of concrete and the tensile strength as well.

The quasi-static compressive strength of the mortar is higher than that of the concrete, which has the same mortar phase. This difference is related to different deformation and failure mechanisms in these materials. In concrete, microcracks readily develop and grow along the aggregate-matrix interfaces due to high stress concentrations at

these interfaces and due to weak interfacial bonding. These microcracks coalesce and develop into macrocracks under increased loading, leading to a premature failure of concrete compared to mortar. However, under the high strain rate experiments, the stress carried by concrete is significantly higher than that carried by the mortar. In the dynamic case, the cracks propagate also through the hard aggregate, which has as a result the apparent increase of the total fracture energy and tensile strength of concrete, as it was stated above. Moreover, in the case of dynamic loading under confining pressure, the confining stresses tend to keep the interfaces under overall compressive loading, retarding the initiation and growth of cracks. The closure effect of the high hydrostatic stresses causes deformation to occur in both the mortar phase and the aggregate in concrete, allowing the strengthening effect of the aggregate to manifest. Consequently, the overall strength of concrete appears to be higher than that of mortar. Another aspect is that in the dynamic case it is normally not a unique crack starting and growing from a single point but there are many macrocracks starting simultaneously and propagating from many points; in other words the multi-activation of cracks is present. The multi-activation of fracture is an effect of the impact loading. Cracks are growing so rapidly and are so well distributed over the specimen cross-section that the pulse accelerates all material particles and there is no time to concentrate the load on the weakest place; many weak points are simultaneously brought to fracture by the load wave.

In the case of High Performance Fibre Reinforced Concrete (HPFRC), the presence of silica fume and steel fibres has a significant effect on the dynamic mechanical performance of the material (Karihaloo, 1995; Yan et al., 1999). It is indicated that steel fibres effectively restrain the initiation and propagation of cracks during the failure of a HPFRC structure, mitigate the stress concentrations at the tips of the cracks and delay the damage process under dynamic loading. Silica fume effectively improves the structure of the interface, eliminates the weakness of the interfacial zone, reduces the number and size of cracks and enhances the ability of steel fibres to resist cracking and restrain damage. As a result, the incorporation of steel fibres and silica fume can increase greatly the performance of HPFRC subjected to dynamic loading, by increasing its cracking resistance. The mechanisms of the combined effect of silica fume and steel fibres are well analysed in the fracture mechanics literature (Karihaloo, 1995; Shah et al., 1995).

4.4 IMPACT LOADING

4.4.1 Introduction

Impact occurs when one object strikes another, such that large forces are developed between the objects during a very short period of time. Therefore, impact strength is of importance when concrete is subjected to a repeated falling object, or a single impact of a large mass at a high velocity. The principal criteria are the ability of a specimen to withstand repeated blows and to absorb energy (Neville, 1995). This is particularly the case when the consequences of local damage or possible penetration of a structural member are deemed to be sufficiently serious.

4.4.2 Impact testing configurations

In concrete structures such as road facilities, harbour facilities, sediment control dams, and others, impact loads sometimes act directly on members. Load bearing capacity, toughness and displacement recovery properties are important, and should be evaluated appropriately.

Several testing approaches have been used and the most important of them are described below:

- The simplest of the impact tests is the "repeated impact drop-weight test" (ACI Committee, 1988), in which the number of blows necessary to cause prescribed levels of distress in the test specimen is the main parameter and the drop-height is kept constant. Relative impact resistance of different materials can be evaluated by using this testing method. However, the method cannot be applied to the evaluation of relative impact resistance of different structural types. Moreover, it is not possible using such a test, to quantify the energy absorbed or obtain any of the fundamental material properties necessary for design.
- The repeated impact drop-weight test with increasing drop-height is a later modification of the original test proposed by ACI 1988 (Figure 4.20). The drop-weight is lifted using a hoist, and released by controlling electromagnetic force in the loading. The drop-height is initially set and increments are given at each

impact. The acceleration of drop-weight, reaction force at supporting point and displacement at several points of the span are measured at time intervals, using a dynamic strain gauge and a waveform recorder. When the displacement of the beam specimen after striking of the drop-height (residual displacement) exceeds a certain value, the loading is terminated. This testing method is efficient for the study of the global response of the concrete specimen (drop-height and load-displacement relations) and also for the local damaged concrete (cracks, spalling of concrete portions). The impact force can be calculated by the mass of drop-weight times the measured acceleration of drop-weight. The impact reaction force is equal to the double of the reaction force measured at one of the supports. However, inertia effects of the beams produce differences in the obtained values of reaction forces and therefore great consideration must be given to the interpretation of the test measurements (Rokugo et al., 2001).

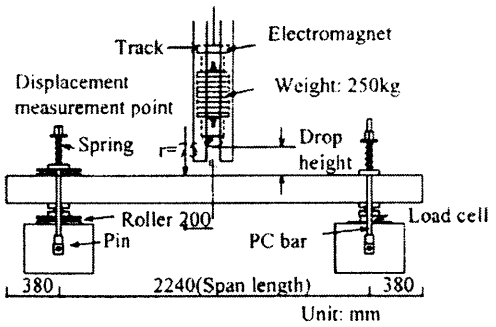

Figure 4.20: Test setup for impact tests (After Rokugo et al., 2001).

- The instrumentation of drop-weight impact machines is a complicated task, to which careful consideration must be given. The most common instrumentation techniques used with impact machines consist of the following components: (i) In order to measure the acceleration of the impact hammer as it drops, a series of precisely spaced holes are drilled in a metal strip along the side of the machine. A photocell is attached to the hammer in such a way that its circuit is completed whenever it passes one of these holes. By determining the transit time between successive holes, the acceleration of the hammer can be determined. However, there is unavoidable friction between the hammer and the steel guide, which has a slight effect on the final acceleration value. (ii) Load measurements are obtained by using electric resistance strain gauges mounted on the tup. Some gauges are mounted around the circumference of each of the holes drilled on the tup. The

purpose of these holes is to produce stress concentration in the steel tup, thus increasing the sensitivity of the resulting "load cell". The gauges are calibrated by loading the tup in static loading in a calibrated universal testing machine. Careful consideration must be given to the response of gauges. Some researchers found that the response is linear within the load range of the instrumented tup. (iii) In order to measure the acceleration of the beam itself, either one or more small accelerometers are attached to the upper surface of the beam. (iv) All of the data can be recorded using a high-speed scanning oscilloscope (e.g. Nicollet). The user selects the scan time between successive load and acceleration reading, so that the entire impact event can be captured on the oscilloscope. After each test, the data are plotted automatically on an X-Y recorder and these curves are then digitised, and any further analysis is carried out using a computer.

It must be said, however, that the aforementioned techniques are nothing more than general approaches to the instrumentation problem. Some of them are already regarded as old and new solutions are proposed. Nevertheless, the concept of these new solutions is very similar to the initial adopted methods.

- A traditional configuration for the determination of the magnitude of the maximum value of crack velocity in concrete is presented in Figure 4.21. The impact equipment is very simple and mainly consists of a vertical tube to guide a steel cylinder with a mass. The impact cylinder hits a steel beam, which causes a tensile stress wave in the notched concrete specimen. Due to tensile loading an unstable crack growth is initiated. The principle of the technique consists of the destruction of barriers by the propagating crack and the registration of this process with time. These barriers are made of liquid silver and are connected with one electrical circuit together with electrical resistances. During the propagation of the crack the barriers are destroyed, the electrical resistances activated, and the change of electrical voltage recorded. The behaviour of voltage vs. time shows the moments of barrier destruction and the crack velocity can be calculated (Curbach et al., 1989).

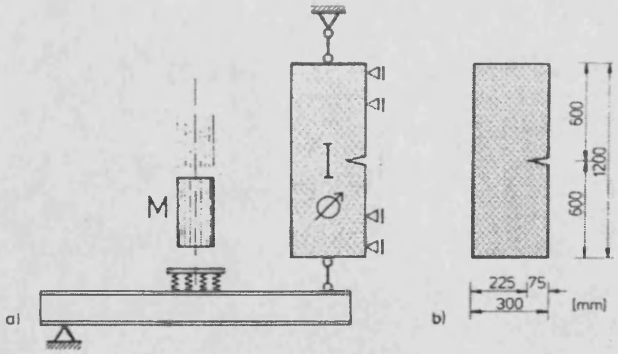

Figure 4.21: a) Test setup for the determination of crack velocity, b) Dimensions of specimen (After Curbach et al., 1989).

- Another popular test for such materials is the Charpy test, which is recommended for impact testing of metals. Therefore, this test has to be modified in order to overcome the problems associated with the instrumentation of the Charpy impact tester. Gopalaratnam et al. (1984) have designed a modified instrumented Charpy test, with a view to shed more light on the parasitic effects of inertia and to provide some general guidelines on the selection of the various test parameters. The conventional Charpy tester was modified and instrumented to facilitate tests on concrete specimens at different impact velocities. Among the three primary modifications were: (a) instrumentation of the striker and the two supporting anvils (it was felt that recording of anvil and striker loads simultaneously was essential both to a proper interpretation of inertial loads, and to assess the influence of parameters like test-system compliance, specimen size and impact velocity on the test results. The anvil and the striker were designed to serve as compression load cells capable of recording dynamic loads transmitted through them during an impact event), (b) seating arrangement to accommodate large-sized specimens (commonly recommended sizes for impact testing of metal specimens are 10x10x50 mm. The heterogeneity of cement-based composites necessitates use of larger specimens), and (c) low-blow fixture to enable tests at different impact velocities (this allowed impact velocities in the range of 0.5 – 3.0 m/s). A 4-channel digital oscilloscope with two 2-channel differential amplifier plug-in units of high resolution and frequency response were used for storing the load, strain and deflection histories. Strains were measured by directly bonding foil gauges at quarter point (or midpoint in some tests) on the tension face of the specimen. A bridge-completion network, using dummy gauges, was used to

provide temperature compensation. A bridge amplifier provided for bridge excitation and signal amplification. Load outputs from the supports and the striker, beam deflection and strain were all monitored using a digital oscilloscope. Triggering of the scope sweep was accomplished externally using the signal from a fibre-optic block and flag assembly (Gopalaratnam et al., 1984) (Figure 4.22).

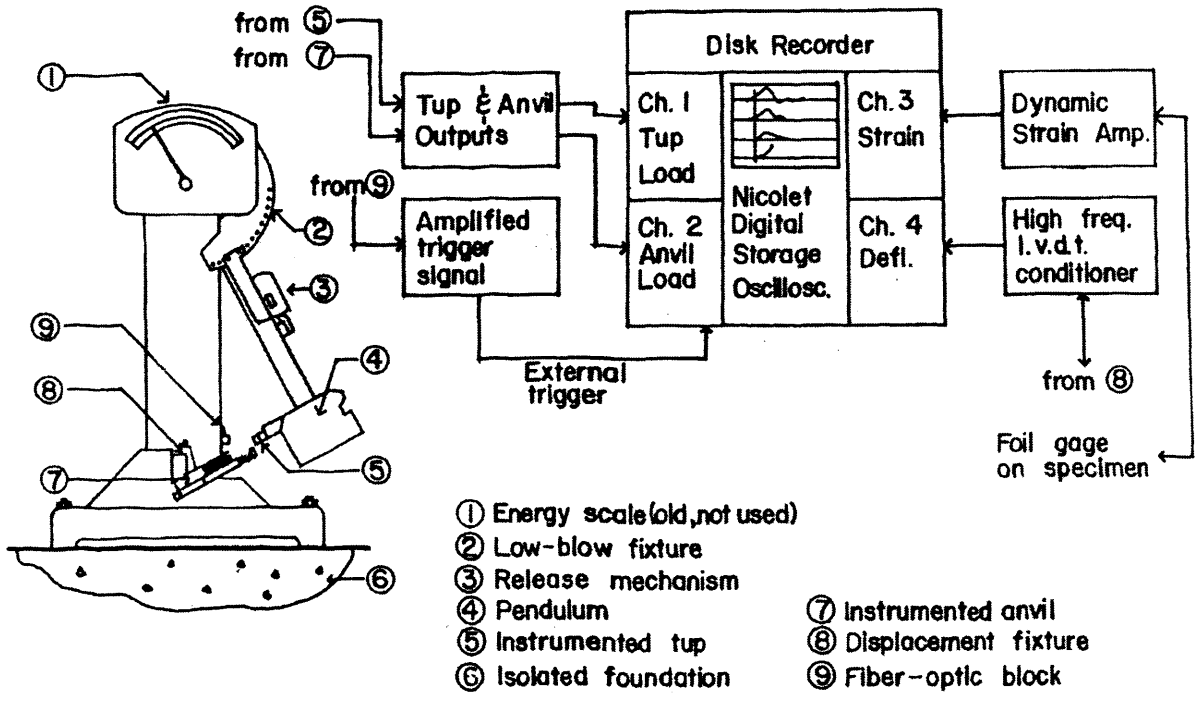

Figure 4.22: General features of the modified Charpy test (After Gopalaratnam et al., 1984).

4.4.3 Impact testing problems

There are many difficulties associated with the instrumented impact testing of concrete. In particular, as indicated in detail by Suaris and Shah (1981), the effects of specimen inertia must be considered, which manifest themselves as oscillations on the load-time records. Impact loading will create inertial oscillations in the contact zone between the tup and the specimen. The time required for this inertial load to be dissipated is about three times the period of the apparent specimen oscillation, t. Thus, for any time less than about $3t$, it is not possible to use the tup signal directly to measure the specimen load; in the time range from 0 to $3t$, adjustments for the inertial load must be made. Since for the relatively brittle concrete specimens the time to fracture is significantly less than $3t$, some procedure must be adopted to eliminate, as much as possible, inertial effects.

The procedure chosen by Suaris and Shah (1981) was to introduce a soft pad between the tup and the specimen, in order to reduce the amplitude of the inertial oscillations; an analytical model was then developed which could predict both the amplitude and the period of the inertial oscillations. Other investigations also proved experimentally that the introduction of an aluminium-damping pad effectively reduced the peak load recorded by the striker. Server et al. (1977) have recommended that errors due to inertial oscillations can be neglected after three half-periods of oscillations. While this guideline had been accepted more or less as a standard practice for metal testing, this was shown to be insufficient for impact testing of asbestos cement composites. Suaris and Shah (1983) instrumented the support anvil in addition to the tup in order to obtain valid load values. Gopalaratnam et al. (1984) have proposed guidelines regarding specimen dimensions, impact velocity and tup weight which were devised to reduce the inertial oscillations during an instrumented Charpy-type of impact test. By using a two-degree-of-freedom model, it was possible to estimate the period of inertial oscillation as well as its amplitude. Simple and approximate expressions were proposed to evaluate the frequency of oscillation, and the maximum difference between the recorded tup and anvil loads. In general, it was found that the larger the ratio of the (hammer) tup mass to the beam mass and the beam stiffness to the effective stiffness of the contact zone, the lower is the adverse effect due to inertial oscillation. Bentur et al. (1986) used a different procedure: they attached accelerometers directly to the impacted specimens, so that the acceleration history of the specimens during the impact event could be measured directly. This permitted a calculation of the inertial loads, as well as specimen velocities and accelerations. Therefore, load-deflection curves for impact loading could be generated. It was also found that at the peak load measured by the instrumented tup, the inertia load may account for more than 2/3 of the total load.

Failure to account for the inertial load may result in misleading conclusions. Consequently, it can be said that in order to analyse the results of an impact test, one must be able to separate the inertial loading effect from the total load measured by the instrumented tup. During the initial stages of the impact of brittle materials like concrete the values of the inertial load (i.e. the load required to accelerate the specimen) can be much greater than the load necessary for the stressing and straining of the beam. As a result, the total load sensed by the tup is very sensitive to the inertia

effect; in many instances, only a small fraction of the total load is involved in beam bending itself.

Another effect that may have significant influence on the interpretation of the experimental results in impact tests is the local damage of concrete. Local damage occurs during an impact by a hammer on a concrete beam, when concentrated stresses occur in the contact area. These can lead to damage of the concrete by which a certain amount of energy is dissipated. This amount depends on the hardness of the hammer, its shape and flatness, on the mechanical properties of the beam, its geometry and flatness, and on the measure of coincidence of the hammer and the beam surface. In order to avoid arbitrary influences on the results, the contact surfaces should fit as well and reproducibly as possible and/or a pad, always of the same material as the hammer, should cover the contact surface of the beam (Reinhardt, 1990).

4.4.4 Improvement of performance of concrete against impact loading

The improvement of performance of concrete beams against impact loading is of significant importance, as on many occasions impact loads act directly on members. Experimental results have shown that using a buffer layer is an effective method to improve impact resistance. For the buffer layers, however, it is also important to prevent the spalling of concrete. One of the effective approaches to improve the spalling resistance is the use of cement-based materials with micro-fibres having good mechanical properties, such as strain hardening. A study of Rokugo et al. (2001) presented the results of repeated impact drop-weight test with gradually increasing drop-height on reinforced concrete beams, prestressed concrete beams, concrete beams reinforced with short steel fibres and prestressed concrete beams reinforced with short steel-fibres. In addition, the concrete beam with a buffer layer made of a cement-based material with micro-fibres has been developed for improving the impact resistance. The micro-fibre reinforced mortar, which was used as a buffer layer in this study was based on ECC mixture (Li, 1998). This is a high performance mortar, showing strain-hardening behaviour. Some of the most important results obtained were that prestressing and reinforcing with short steel-fibres imparted impact resistance to concrete beams. Moreover, prestressing improved the performance for the restoration of deflection of the members under impact load. In the specimen with

no short steel fibres, prestressing gave only the ductility with higher restoration of deflection. For FRC beams, the prestressing gave higher impact reaction force at each impact. In the case of steel-fibre prestressed concrete beam with higher prestress, the effect of prestressing was not evident. It seems that too much prestressing increased the local damage in concrete. There would be a best combination between the steel-fibre content and the amount of prestressing, for the optimisation of the impact performance of the beam. Finally, the buffer layer made of cement-based material with micro-fibres improved the impact resistance of concrete beams and the spalling of concrete reduced. Nevertheless, the bond properties at interface between the buffer layer and substrate should be improved in order to utilise the high-performance of the buffer layer, e.g. strain-hardening behaviour. This resulted from the observed delamination of the buffer layer in the case of some prestressed concrete beams reinforced with short steel fibres.

4.4.5 Experimental works

The behaviour of concrete beams under impact loading was studied by Bentur et al. (1986), using an instrumented drop-weight impact apparatus. Both plain and conventionally reinforced beams were tested, with the impact load applied at mid-span. The load on the instrumented striking tup and the acceleration of the beam itself were measured as a function of time; the entire impact events had duration of 10 to 70 ms. Typical load vs. time curves for both plain and reinforced concrete were created, using the load obtained from the instrumented tup (total load). For both specimens, the peak load occurred at slightly less than 1 ms after contact between the tup and the specimen. Beyond the peak, the load declined to zero, over a period of about 70 ms for the reinforced concrete, but much more rapidly for plain concrete (more brittle). Typical acceleration vs. time curves for the same plain and reinforced concrete specimens were also created, from the data obtained from an accelerometer. For both specimens, there is a peak in the acceleration vs. time curve, which occurs at the same time as the peak in the load vs. time curves. In the case of the reinforced concrete, the acceleration diminished rapidly after the peak. A somewhat slower decay in acceleration was noted for the plain concrete. The analysis of the results was concentrated on the separation of the inertial loading effect from the total load measured by the instrumented tup and the evaluation of the actual bending load on the

beam. Therefore the flexural behaviour of the material could be investigated by its actual bending load vs. deflection curves, under impact loading. The conclusion drawn by the authors was that for the reinforced concrete the curve was insensitive to any assumption made regarding the distribution of acceleration along the beam; both the linear and sinusoidal assumptions resulted in similar curves. This was not the case for the plain concrete, where the shape of the curve is considerably affected by the assumption regarding the distribution of accelerations. Finally, estimations of energy from the instrumented tup loadings do not agree well with the sum of the calculated kinetic energy and the energy expended in deflecting and fracturing the beam. This difference is the "unaccounted energy" and is probably dissipated in the machine itself. This energy can, unfortunately, constitute a large proportion of the total energy measured in the tup, particularly during the initial stages of the impact, when the peak load occurs. The value of the "unaccounted energy" is sensitive to the structure and rigidity of both the testing machine and the specimen. Therefore, different systems may yield different proportions of unaccounted energy.

Gopalaratnam et al. (1984) have used the modified instrumented Charpy test at four different velocities to enable impact testing of cement-based composites. The tests were performed with and without a rubber pad between the striker and the specimen. The pad was used to reduce the stiffness of the contact zone and thereby minimise possible inertial oscillations. It was observed that loads recorded by the tup and the striker are within acceptable limits of each other at all times. Peak loads recorded by these two load cells are almost identical (within 3%), indicating that the effects due to inertial loading are virtually eliminated. The ascending part of the load-time curves had a "knee", due to the presence of the damping pad of rubber. The descending portion (which should be vertical for an elastic, ideally brittle material) had a steep negative slope. This is attributed to the strain softening post-ultimate behaviour of concrete and also to loads associated with kinetic energy imparted to the fractured halves of the specimen. The assumption of elastic beam behaviour seemed justified because the quarter-point strains recorded were almost half of the midpoint strains until peak loads. This also indicated that the failure was predominantly due to pure bending. For tests conducted without the rubber pad, inertial oscillations and, as a result, the differences in anvil and tup loads were, in general, higher. Moreover, the tests conducted without the damping pad yielded higher rates of straining than those

conducted with it when identical drop-heights were used. Consequently, higher peak loads and shorter fracture times were observed in these tests. Finally, it was observed that concrete exhibited increased flexural strengths at the higher rates of loading. This is the so-called "rate effect". An increase of about 60% was observed when the strain rate was increased from 10^{-6} /s to 0.3 /s. At the higher rates of loading, there is a decrease in the amount of microcracking, which can be inferred from the increase in the secant modulus at peak loads. Additionally, a weaker mix was more rate sensitive than a stronger one.

Hughes and Beeby (1982) tested pin-ended and simply supported beams by dropping a nominally rigid striker onto the beam at midspan. For each test the impact force history and the beam displacements (maximum and residual) were measured. Two strikers of different masses were used and also various pads were positioned at the impact zone to vary its stiffness. Test results showed that beams remained elastic during the first impact and, in most cases, failed subsequently in flexure at midspan. Moreover, there was an apparent increase in recovery with increasing impact velocity. This could be a consequence of an increased yield stress due to strain-rate effects. Numerous investigators have noted this phenomenon. The authors used a relatively simple elastic impact solution using the "simple beam" theory, which has been shown to describe adequately the test results for the beam impact tests. The type of analysis is not without reason called the "simple beam", since amongst others it neglects shear and rotary inertia. The bounds of applicability can really be found only by experimentation and this is a severe limitation of the method. In addition, it was suggested that an equivalent static force approach had very limited applicability for an impact design, since it could not adequately describe impact phenomena like reverse moment, reverse reactions, etc., caused by the excitation of higher modes. The authors also recognised the importance of two parameters, the mass ratio ($\alpha = m_{beam} / m_{striker}$) and the pulse ratio ($\beta$). The pulse ratio measures the stiffness of the impact and basic mobility of the beam. The results of the analysis showed an increasing influence of inertia oscillations on the measured results with decreasing stiffness of the specimen and increasing stiffness of the contact area. The stiffer the impact zone, the more mobile the beam because of the higher modes. Finally, an upper bound to the impact force was obtained by assuming that all the kinetic energy of the striker was

transferred to the impact zone. The instrumentation used by the authors in this study was very poor. All that could therefore be done was to relate the energy available in the impact to the final state of the beam after impact (i.e. the residual deflection).

CHAPTER 5: DETERMINATION OF THE SIZE-INDEPENDENT SPECIFIC FRACTURE ENERGY OF CARDIFRC® FROM THREE-POINT BEND TESTS

5.1 INTRODUCTION

The true specific fracture energy of any type of concrete G_F is the most useful material parameter in the analysis of cracked concrete structures (Karihaloo, 1995). The test method for the determination of G_F and even its precise definition has been a subject of intense debate among researchers because it has been found to vary with the size and shape of the test specimen and with the test method used. Guinea et al. (1992) identified several sources of energy dissipation that may influence the measurement of G_F, for example the influence of curtailing the P-δ tail in a bend test (Elices et al., 1992). They concluded that when all factors are taken into account, an almost size-independent specific fracture energy G_F can be obtained. Hu and Wittmann (1992) have addressed the possibility that the local specific fracture energy itself may not be constant along the crack path in a test specimen.

The specific fracture energy G_F according to the RILEM recommendation (1985) is the average energy given by dividing the total work of fracture by the projected fracture area (i.e. the area of the initially uncracked ligament). Therefore, for a specimen of depth W and initial notch length a, the fracture energy is given by:

$$G_F = \frac{1}{(W-a)B}\int P d\delta \tag{5.1}$$

where B is the specimen thickness, P is the applied load, and δ is the displacement of the load point.

In the case that the concrete fracture is modelled by a fictitious crack (Hillerborg, 1985), then the energy dissipation for the crack propagation can be described by the cohesive stress $\sigma(w)$. More precisely, the specific fracture energy corresponds to the area under the $\sigma(w)$ curve

$$G_F = \int_0^{w_c} \sigma(w) dw \tag{5.2}$$

where w_c is the critical crack opening.

The fracture process zone (FPZ) around the propagating crack can be considered as consisting of two regions, an inner softening zone, w_{sf}, and an outer micro-fracture zone, w_f, as shown in Figure 5.1 (Hu and Wittmann, 1992). During crack propagation the inner and the outer zone widths may vary substantially, depending on the crack tip stress field. It is clear that the critical crack opening w_c is restricted by the inner and the outer zone widths. This restriction becomes more obvious when a FPZ approaches the free boundary of a specimen. Therefore, a smaller w_c and a smaller fracture energy are calculated if Equation (5.2) is used. These variations in w_{sf}, w_f and w_c lead to the conclusion that the fracture energy G_F defined by Equation (5.2) can be dependent on the location of FPZ in relation to the free boundary of the specimen. To distinguish the fracture energy G_F defined by the two equations, Duan et al. (2001) use symbol g_f for the local fracture energy defined by Equation (5.2).

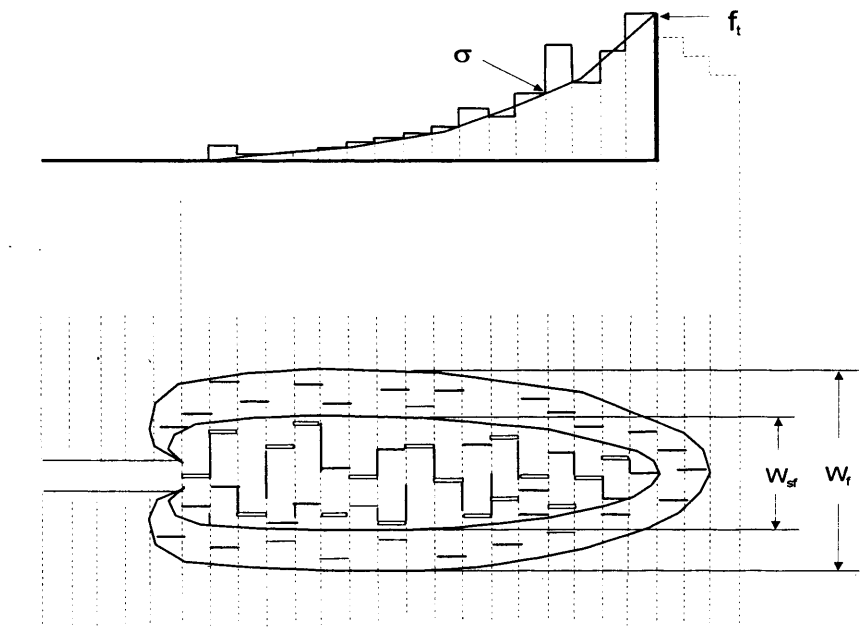

Figure 5.1: The fracture process zone and discreet bridging stresses. The FPZ is divided into the inner softening zone and the outer micro-fracture zone. w_c is related to the width of the inner softening zone w_{sf} (After Hu and Wittmann, 1992).

Hu (1995), and Hu and Wittmann (2000) have made the following assumptions:

$$\begin{aligned} w_{sf}(x) &\propto w_f(x) \\ w_c(x) &\propto w_{sf}(x) \\ g_f(x) &\propto w_c(x) \end{aligned} \tag{5.3}$$

where x denotes a position along a fracture ligament in the FPZ and $g_f(x)$ represents the local fracture energy. The fracture energy defined by Equation (5.1), which may be size- or ligament-dependent, is denoted by $G_f(\alpha)$, to distinguish it from the size-independent G_F, with $\alpha=a/W$.

According to the energy conservation principle, the specific fracture energy $G_f(\alpha)$ defined by Equation (5.1) can be determined as follows:

$$G_f(\alpha) = \frac{1}{(W-a)} \int_0^{W-a} g_f(x) dx \tag{5.4}$$

Differentiating Equation (5.4) with respect to the crack length a gives the local fracture energy $g_f(x)$ at the crack tip:

$$g_f(x) = G_f(\alpha) - (W-a)\frac{dG_f(\alpha)}{d\alpha} \tag{5.5}$$

Equations (5.4) and (5.5) above imply that $G_f(\alpha)$ = constant, if $g_f(x)$ = constant. If $g_f(x)$ $\neq$ constant then $G_f(\alpha) \neq$ constant, i.e. size or ligament effects are observed. Figure 5.2 shows schematically that if $g_f(x)$ decreases when approaching the boundary of the specimen at later stages of fracture, $G_f(x)$ is indeed dependent on the ligament or initial crack length.

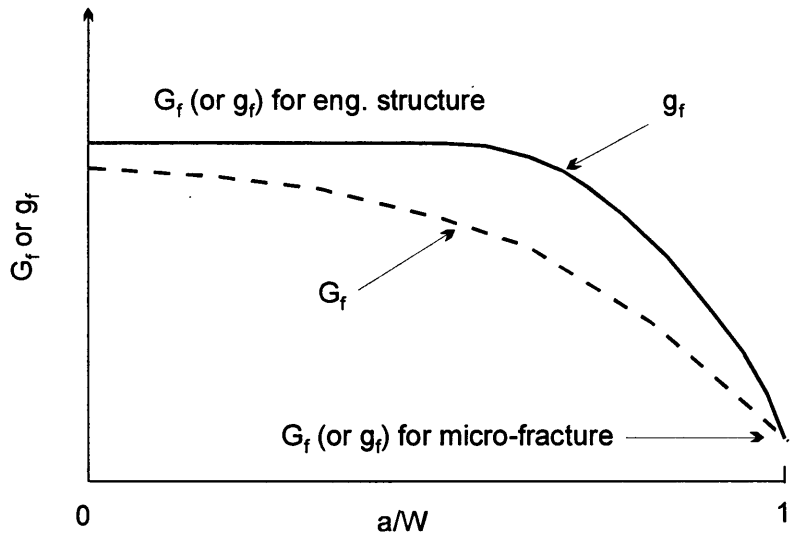

Figure 5.2: If g_f decreases monotonically along the ligament, G_f has to be dependent on the a/W ratio, as observed in many experiments.

Duan et al. (2001) argued that the effect of the free boundary is felt in the fracture process zone (FPZ) so that the energy required to create a fresh crack decreases as the crack grows. Initially, when the crack grows from a pre-existing notch, the rate of decrease is moderate but it accelerates as the crack approaches the free boundary (Figure 5.2). Therefore, the change in the specific fracture energy can be represented by a bi-linear approximation (Figure 5.3). The transition from the moderate to the rapid decrease occurs at the so-called transition ligament length (Hu, 2000) that depends on both the material properties and specimen size and shape. In general the transition ligament length a_l is smaller than the unnotched specimen ligament (W-a). On the basis of the bilinear approximation, the size independent specific fracture energy G_F can be back calculated from the measured specific fracture energy $G_f(a/W)$ from

$$G_f(a/W)= \begin{cases} G_F\left[1-\dfrac{a_l/W}{2(1-a/W)}\right]; & 1\text{-}a/W > a_l/W \\ G_F\cdot\dfrac{(1-a/W)}{2(a_l/W)}; & 1-a/W \le a_l/W \end{cases} \tag{5.6}$$

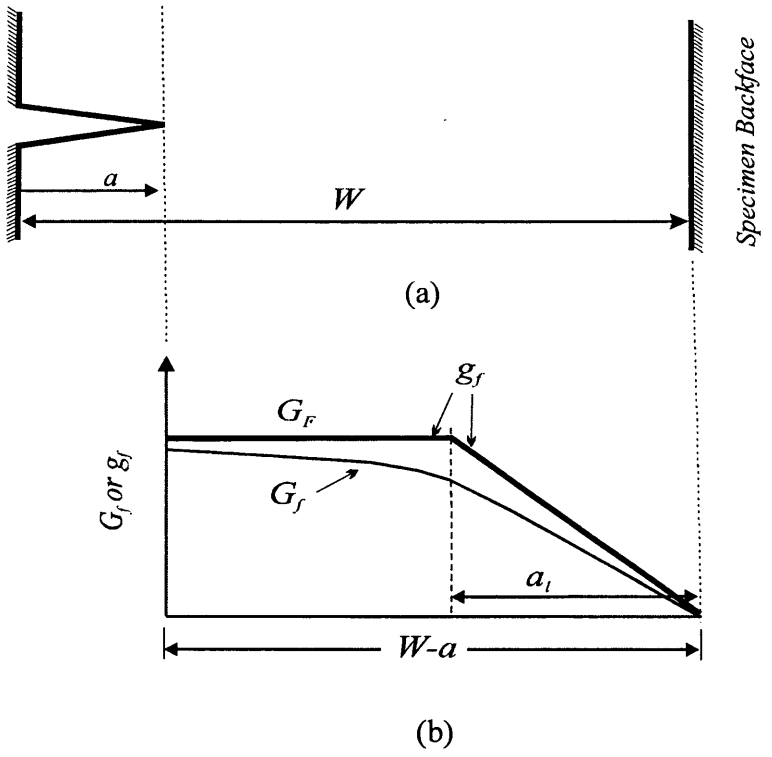

Figure 5.3: The distribution of fracture energy (G_f and g_f) along the un-notched ligament, W-a (b) of a notched test specimen of depth W and notch depth a (a).

The size-independent G_F of a concrete mix can be obtained from Equation (5.6), once the size-dependent $G_f(a/W, W)$ for a specimen of given size W is known. The test results for $G_f(a/W, W)$ from TPB and WS specimens are substituted into Equation (5.6) in order to determine the size-independent specific fracture energy G_F and the transition ligament length a_l. It is customary to test specimens of varying size W and several notch to depth ratios a/W, but to keep the span to depth ratio constant. The number of the measured $G_f(a/W, W)$ is therefore much larger than the two unknowns G_F and a_l in Equation (5.6). For this reason, the over-determined system of equations so obtained is solved by least squares method to get the best estimate of G_F and a_l.

Abdalla and Karihaloo (2003) observed that a size-independent specific fracture energy G_F of concrete could be obtained by testing very few three point bend (TPB) or wedge splitting (WS) specimens of the same dimensions and shape, one half of which contain a very shallow and the other half a deep starter notch. This observation is very important, since the determination of the true specific fracture energy becomes

a simple and straightforward task. It requires testing of just a few specimens of any one overall size and shape, with two notch to depth ratios and the solution of two simultaneous Equations (5.6) in two unknowns G_F and a_l using the mean values of $G_f(a/W)$ for the two a/W values. This not only eliminates the use of least squares method for the solution of an over-determined system of simultaneous equations but, more importantly, eliminate the time consuming and often cumbersome (when large specimens are required for testing) testing of a large number of specimens with different W and a/W.

5.2 EXPERIMENTAL RESULTS

Three-point bend (TPB) tests have been conducted on the two different mixes (I and II) of CARDIFRC® and G_F determined on the basis of the concept of local fracture energy, as it was explained above. Six beams of Mix I (100x100x500 mm) and eight beams of Mix II (100x100x500 mm) were used for this experimental program. The beams were cast in summer 2002 and were stored in the laboratory in ambient conditions until the time of testing. For each mix two notch to depth ratios were used (a/W=0.05 and a/W=0.50) (Figure 5.4).

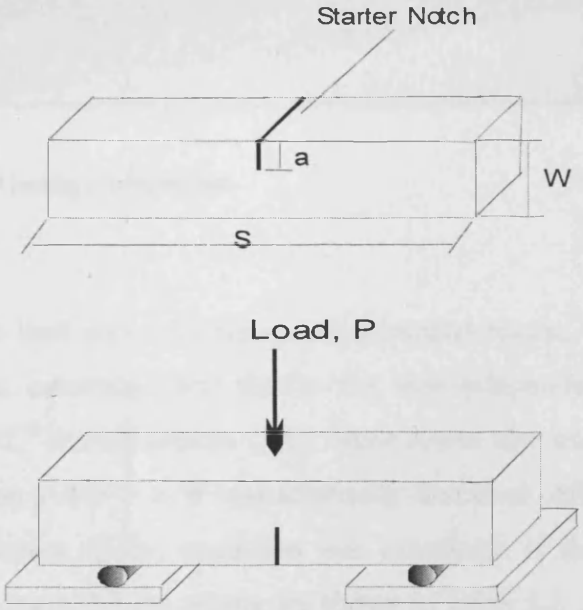

Figure 5.4: Specimen shapes and dimensions.

All specimens were tested in deformation control. Three types of measurement were recorded for each beam: (1) the load from the load cell of the testing machine; (2) the vertical deflection at one side of the specimen and (3) the crack mouth opening displacement (CMOD), using a clip gauge. The vertical deflection was measured by a single LVDT. The tests were performed in a stiff self-straining testing frame, fitted with a DARTEC 2500 kN dynamic-static actuator. The machine was powered by a 23 lit/min DARTEC hydraulic pump and was connected with a DARTEC 9600 Digital Feedback Controller.

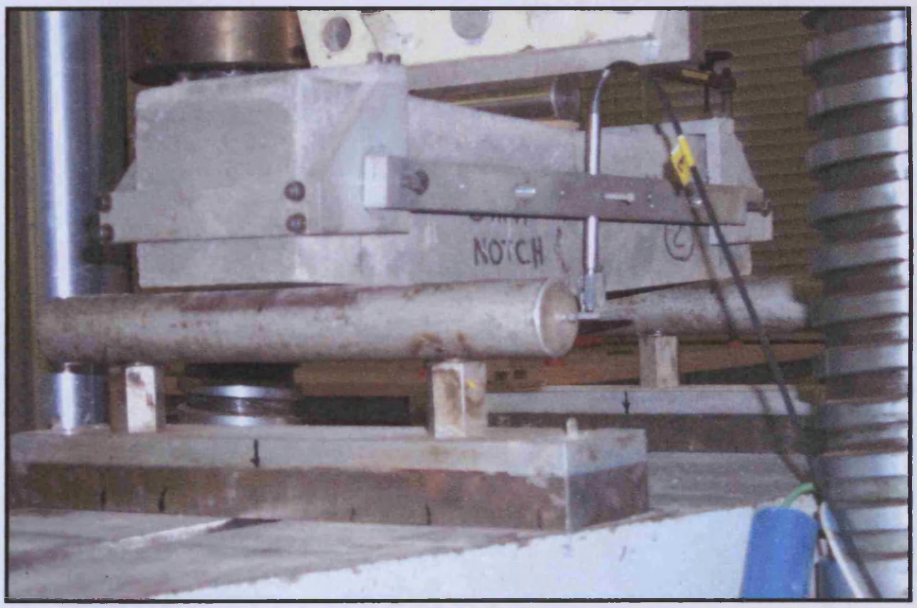

Figure 5.5: 3-point bend testing configuration.

Thereafter, using the load and deformation experimental results, the specific fracture energy $G_f(a/W)$ was calculated and finally the size-independent specific fracture energy of CARDIFRC® from Equation (5.6). Since a_l was also unknown, the equation that satisfies condition $1\text{-}a/W > a_l/W$ was arbitrarily first used. After the calculation of G_F and a_l, the fulfilment of this condition was examined. If this was not met, the second equation was used. All the results are shown in Table 5.1.

Table 5.1: Experimental results.

		TEST NO.	$G_f(a/W)$ (N/m)	$Avg.G_f(a/W)$ (N/m)	G_F (N/m)
CARDIFRC® MIX I	a/W = 0.05	1	28403.0	23927.2	37615 (a_l=69 mm)
		2	23288.3		
		3	20090.2		
	a/W = 0.50	1	12950.6	13601.0	
		2	12719.0		
		3	15133.5		
CARDIFRC® MIX II	a/W = 0.05	1	28789.9	25009.1	34525 (a_l=52 mm)
		2	22484.9		
		3	23860.6		
		4	24901.0		
	a/W = 0.50	1	15326.6	16479.3	
		2	16939.2		
		3	14191.7		
		4	19459.7		

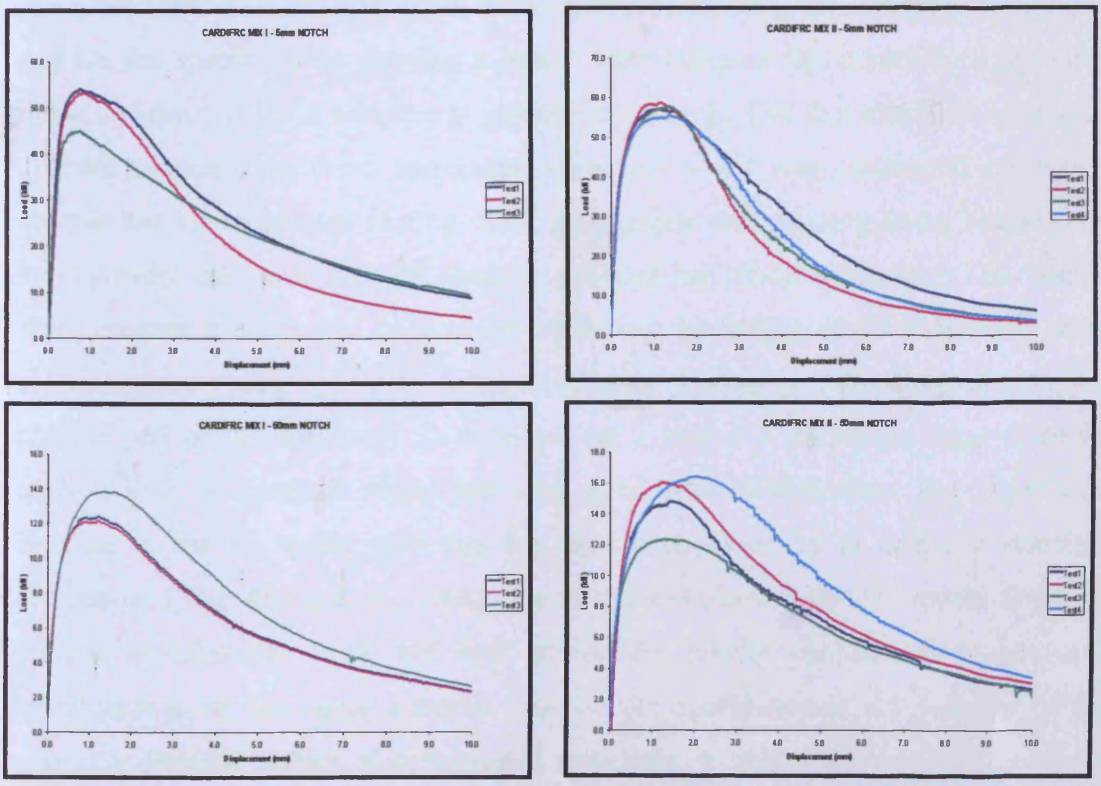

Figure 5.6: 3-point bend test graphs for CARDIFRC mixes I and II, notches 5 and 50 mm.

The above experimental results were compared with corresponding results obtained on CARDIFRC® specimens, in three-point bending (Lyons, 2002) and in direct tension (Benson, 2003). These tests gave the following values of the specific fracture energy for the two mixes of CARDIFRC®:

Table 5.2: Experimental results.

	G_F(N/m) (3-PBT)	G_F(N/m) (D.T)
CARDIFRC® MIX I	22909	20411
CARDIFRC® MIX II	17875	17412

5.3 DISCUSSION

The true fracture energy obtained from the current experimental work is substantially higher than that obtained by Lyons (2002), and by Benson (2003). This is mainly attributed to the fact that the specimens tested in this experimental work were cast almost two years prior to testing. During that time the specimens were stored in the concrete laboratory, in ambient conditions. Therefore, there was plenty of time for the unreacted material in the specimens to react chemically with the environmental water and for the specimens to develop a better bond between the randomly distributed fibres and the matrix, in addition to gaining in strength. The fact that little unreacted material remained in these specimens after two years was confirmed by visual observation during testing. During crack propagation and opening under loading, no loose powder was noticed to fall from the cracked part of the specimens. This was in sharp contrast to what had been observed during the testing of CARDIFRC® beam specimens at a young age (9-28 days), when a lot of loose powder dropped from the cracked part of the specimen. In addition, the 2-year old specimens were of better quality, with no obvious voids and very good fibre distribution. The significant increase in the G_F value with age has also been observed in ordinary concrete (Petersson, 1980; Zhang et al., 2000). However, it is obvious that the results from the current experimental work are well above the results obtained from previous investigations on the same material. Despite the confidence in the validity of the currently obtained values, it is suggested that these be treated as upper limits on the CARDIFRC® size-independent specific fracture energy.

In order to verify the increase in strength with age, six cubes (100x100x100 mm) were cut from the edges of the tested beams of Mix I and six from the edges of the tested beams of Mix II. These specimens were tested in compression; experimental results revealed an increase of the order of 5% in the average compressive strength, in comparison with the average compressive strength obtained at early age, and a remarkably low standard deviation (1.82% for Mix I and 2.82% for Mix II). The low scatter in the compressive strength again attests to the improvement in the material with age. The results are shown in Table 5.3.

Table 5.3: Experimental results.

	Compressive Strength (MPa) (At early age)	Compressive Strength (MPa) (After 2 years)	Change
CARDIFRC® Mix I	193.6	205.30	+6%
CARDIFRC® Mix II	207.0	217.30	+5%

It can be observed that the increase of the specific fracture energy, G_F, with aging is substantially higher than the increase of the compressive strength. This can be explained theoretically by the constitutive relations of CARDIFRC®, where it can be seen that an improved bond between fibre and matrix has a greater effect on the specific fracture energy of the material, than on its compressive strength. The relation between the crack opening w and the stress transmitted across the crack, the specific fracture energy and the compressive strength of the material are given by the following expressions (Karihaloo and Lange-Kornbak, 2001):

$$\sigma(w) \approx 2hLV_f \tau_g K_{Ic,m} \sqrt{\frac{1}{d}\frac{E_f}{E_b}} \left\{ \frac{1}{8} - \frac{w^2}{2L^2} \right\} \tag{5.7}$$

$$G_F = \int_{w=0}^{L/2} \sigma(w) dw \approx \frac{h}{24} L^2 V_f \tau_g K_{Ic,m} \sqrt{\frac{1}{d}\frac{E_f}{E_b}} \tag{5.8}$$

$$f_c^{'} = \frac{f_{t,b}^{'} \sqrt{\frac{\pi a_o b}{c^2}} + \sqrt{2}\tau_B}{1-\mu} \tag{5.9}$$

where τ_v is the fibre pull-out strength, τ_g is the residual frictional strength, E_f is the Young modulus of the fibre, E_b is the Young modulus of the unreinforced and uncracked matrix, L is the embedded length of fibres, V_f is the volume fraction of fibres, h is the snubbing factor, d is the fibre diameter, f'_{tb} is the tensile strength of the matrix, a_o is the half crack length at f'_{tb}, μ is the coefficient of friction between crack faces, and τ_B is the contribution to shear stresses from the fibres.

It can be clearly observed that an increase in the residual frictional pull out strength, τ_g, which is achieved by an improvement in the bond between the randomly distributed fibres and the matrix, contributes dramatically to the increase of the specific fracture energy G_F of the specimen. During the period that the specimens were stored in the concrete laboratory, in ambient conditions, the unreacted material in the specimens reacts chemically with the environmental water as a result of which the contact area between the fibre and the surrounding material increases leading to an improvement in the bond between the randomly distributed fibres and the matrix. However, when the specimen is tested in compression, the better cohesion between fibres and matrix is not of great importance. The improved bond plays only an indirect role, through the factor τ_B which represents the contribution of the fibres to shear stresses, increasing only by a small amount the compressive strength of the material.

CHAPTER 6: STATIC AND FATIGUE RESPONSE OF CARDIFRC® - EXPERIMENTAL RESULTS

6.1 INTRODUCTION

CARDIFRC® is an Ultra High Performance Fibre Reinforced Concrete (UHPFRC) developed in recent years in Cardiff University. CARDIFRC® consists of two base mixes designated Mix I and Mix II. Each mix consists of Portland cement commercially available from Blue Circle, Elkem Refractory microsilica U983 Grade, fine sand, superplasticiser commercially available from Adomast, water and two kinds of fibre – short having length 6 mm and long having length 13 mm – commercially available from Bekaert.

6.2 MIX PREPARATION

The mixes were prepared according to the most effective regime, determined from past experimentations. The procedure is described in the patent application GB 0109686.6.

The first step in the mix procedure was to evaluate the mould volume, adding about 15% to take into account any waste. Then the constituents were scaled down to the desired volume and weighed. The volume of casting material did not exceed 0.035 m^3, in order to achieve better mixing of the constituents.

6.2.1 Mix I

The coarsest and the finest of the ingredients, i.e. the 250-600 μm sand and the microsilica were placed into the mixer. Initially, they were mixed by hand and then by the mixer for at least two minutes. It has to be noted at this stage that special care has to be taken during mixing in order to avoid spillage of the powder from the mixer, since the latter operates at a speed that can cause the powder to spill.

After the first two minutes of mixing the rest of the constituents were added one at a time followed by two minutes of mixing to ensure uniformity. The sequence of the ingredient addition was as follows: the 2nd coarsest (sand 9-300 μm), then the 2nd finest (cement). All the ingredient additions were followed by more than 2 minutes of mixing. After the addition and mixing of the last grade of sand the next ingredient to be added are the steel fibres.

The short (6 mm) fibres were added first while the long (13 mm) ones were added afterwards. Both short and long fibres were added in four instalments i.e. 25% of the total quantity each time. It has to be mentioned that as the fibres were added into the mix, they were passing through a vibrating sieve. The reason was to separate the fibres, which were stuck together due to the electrostatic forces between them. Each instalment of fibres was followed by two minutes of mixing to ensure even distribution of the fibres into the mix. After the last instalment was added and mixed for the required time, water and superplasticiser were added. Two thirds of the measured volume of superplasticiser was added to the water volume. The liquid mixture in turn was poured into the dry mix in increments of 50%, 25%, 12.5% and 12.5%. This procedure had to be precise for the microstructure to become densely packed. Each increment of the superplasticiser – water mixture was followed by two minutes of mixing.

6.2.2 Mix II

The mixing sequence is mainly the same for Mix II as for Mix I. The main differences between the two mixes are the 3rd grade of fine sand used in Mix II, the larger amount of long fibres used in Mix II and as a consequence of the last two the larger amount of superplasticiser incorporated in Mix II.

Again, the coarsest and the finest of the ingredients, i.e. the 1-2 mm sand and the microsilica were placed into the mixer. Initially, they were mixed by hand – in order to ensure better dispersion of particles - and then by the mixer for at least two minutes. The sequence remained the same as earlier, i.e.: the 2nd coarsest (sand 212 – 1000 μm), then the 2nd finest (cement) and the last grade of sand (9 – 300 μm). After

the last instalment of the sand and the adequate mixing time the steel fibres added in the mix in exactly the same way as described for Mix I earlier. Once again it has to be mentioned that special care has to be taken when mixing the fibres in order the mix to be very homogeneous and the fibres well distributed. After the last instalment of fibres was added and mixed for the required time, water and superplasticiser were added into the mix again exactly as described earlier for Mix I. It has to be mentioned that earlier research in this field revealed that the superplasticiser (*sp*) is active for about 15 minutes having as a starting point the last inclusion of *sp* and water in the mix. In other words the mixing of that last instalment and the casting have to be completed within 15 minutes in order for the *sp* to be fully effective. This implies that casting has to be quick and precise. Another important factor for such a material is adequate vibration. Especially for this material an electric vibration table is used (the vibration is triggered by two electric motors), since the magnetic vibration table can affect the orientation of the fibres in the matrix. The maximum vibration frequency applied on the electric vibration table was 95 Hz.

Thereafter, the moulds are left in environmental conditions for 24 hours and then, the demoulded specimens are placed into a hot curing tank, filled with water controlled at 90^0 C. The specimens are left in the tank for 9 days. The first day the temperature of the curing tank is increased (20-90^0 C) and on the ninth day is decreased (90-20^0 C) gradually, in order to prevent the thermal shock of the specimens. The hot curing regime is applied in order to minimise the curing period of the material.

At the beginning of this experimental work, several problems were encountered with the workability of the original mix, which in turn affected the quality of the external surfaces of the specimens. After several trial and error attempts, it was decided to increase the superplasticiser/water ratios of the two mixes of CARDIFRC®. For Mix I this ratio was increased from 0.15 to 0.18 and for Mix II from 0.37 to 0.40. For the new ratios, tests were performed on cubes and cylinders, which showed that the strengths of the modified materials were slightly increased in comparison to the original mixes. These higher *sp/w* ratios are likely to have produced denser and stiffer mixes. Besides, the quality of the external surfaces of the specimens was increased dramatically, due to the increased workability of the mixes. Another factor that

affected the quality of the external surfaces was the insufficient vibration provided by the vibration table, at the beginning of this experimental work.

6.3 CONTROL TESTS

To determine the mechanical properties of CARDIFRC®, compressive and tensile splitting strength tests have been conducted, as well as tests towards the evaluation of the Modulus of Rupture (MOR) and the Young Modulus of the material.

6.3.1 Compressive strength tests

For the determination of the compressive strength of the two mixes of CARDIFRC®, cubes of each mix were tested according to BS 1881-116:1983. At this point it has to be mentioned that for both mixes some trial castings have been done, after it was found that the original superplasticiser/water ratios (0.15 for Mix I and 0.37 for Mix II) did not give sufficiently wet mixes, resulting in poor compaction and finally in specimens with large voids on their surface. For Mix I two trial *sp/w* ratios – from which only the one was selected to be the *sp/w* ratio for the whole experimental work – were used (0.18 and 0.21), whereas in Mix II *sp/w* ratio of 0.40 was used. In all cases the *sp/w* ratios were increased only by increasing the *sp* quantity and keeping the amount of water the same as for the base mixes. For Mix I 6 cubes with *sp/w* = 0.18 and 6 cubes with *sp/w* = 0.21 were tested. For Mix II 12 cubes with *sp/w* = 0.40 were tested. The tests were performed in a FARNELL Compression Testing Machine, with a load capacity of 2500 kN (Figure 6.1). The compressive strength for Mix I, *sp/w* = 0.18 is f_c = 193.6 MPa (Standard Deviation = 8.20 MPa), for Mix I, *sp/w* = 0.21 is f_c = 179.6 MPa (Standard Deviation = 5.40 MPa) and for Mix II, *sp/w* = 0.40 is f_c = 207.0 MPa (Standard Deviation = 7.98 MPa). The results of all the tests are presented in Tables 6.1, 6.2 and 6.3.

Figure 6.1: FARNELL compression testing machine.

Table 6.1: Compressive strength results for CARDIFRC® Mix I – $sp/w = 0.18$.

Cube Number	Weight (kg)	F_c (kN)	Compressive Strength (MPa)
1	2.68	1841	184.10
2	2.67	2076	207.60
3	2.71	1963	196.30
4	2.79	1915	191.50
5	2.70	1875	187.50
6	2.70	1946	194.60
		Mean f_c	**193.60**

Table 6.2: Compressive strength results for CARDIFRC® Mix I – $sp/w = 0.21$.

Cube Number	Weight (kg)	F_c (kN)	Compressive Strength (MPa)
1	2.60	1843	184.30
2	2.59	1877	187.70
3	2.64	1774	177.40
4	2.61	1729	172.29
5	2.65	1774	177.40
6	2.67	1776	177.60
		Mean f_c	**179.60**

Table 6.3: Compressive strength results for CARDIFRC® Mix II – *sp/w* = 0.40.

Cube Number	Weight (kg)	F_c (kN)	Compressive Strength (MPa)
1	2.64	1914	191.40
2	2.70	2146	214.60
3	2.70	2068	206.80
4	2.68	2093	209.30
5	2.70	2187	218.70
6	2.67	2027	202.70
7	2.70	1956	195.60
8	2.64	2116	211.60
9	2.67	2113	211.30
10	2.70	2054	205.40
11	2.64	2138	213.80
12	2.69	2025	202.50
		Mean f_c	**206.98**

6.3.2 Tensile splitting tests

For the determination of the indirect tensile strength of the two mixes of CARDIFRC®, cylinders of each mix were tested according to BS 1881-117:1983 (Figure 6.2). For Mix I 5 cylinders with *sp/w* = 0.18 and 5 cylinders with *sp/w* = 0.21 were tested. For Mix II 11 cylinders with *sp/w* = 0.40 were tested. The tests were performed on a FARNELL Compression Testing Machine, with a load capacity of 2500 kN. The indirect tensile strength for Mix I, *sp/w* = 0.18 is f_t = 28.64 MPa (Standard Deviation = 3.07 MPa), for Mix I, *sp/w* = 0.21 is f_t = 24.73 MPa (Standard Deviation = 1.34 MPa) and for Mix II, *sp/w* = 0.40 is f_t = 21.36 MPa (Standard Deviation = 3.56 MPa). The results obtained for Mix I are remarkable, with indirect tensile strength values reaching up to 33.26 MPa. Again the highest values are observed in the mix with the lower *sp/w* ratio (0.18), as expected. The tensile values obtained for Mix II are also quite exceptional, reaching up to 27.37 MPa. The results of all the tests are presented in Tables 6.4, 6.5 and 6.6.

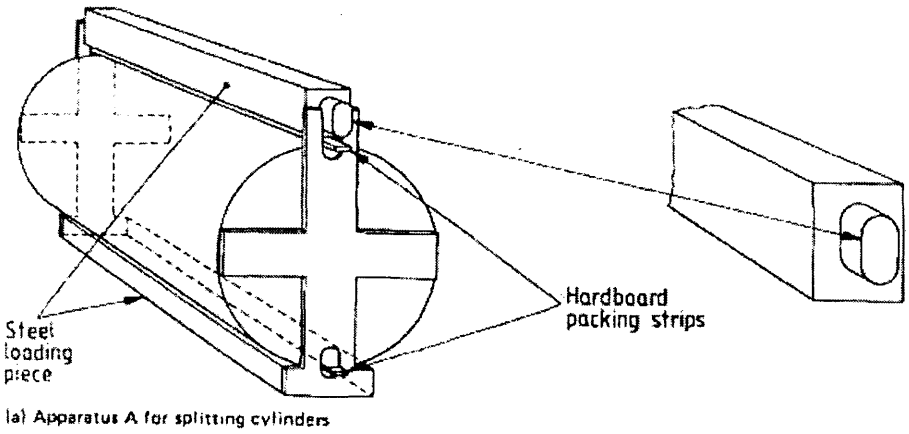

Figure 6.2: The jig used for the tensile splitting test (BS1881-117:1983).

It has to be mentioned that during the tests, the bolts at the base of the jig, which is designed for normal strength concrete mainly, in one case failed due to shear. That was the reason for the lost specimen mentioned in Table 6.5. It is obvious that the material was very strong and the applied load very large and hence the steel loading piece at the top at some point instead of being vertical had a very small inclination, large enough though to cause shear failure of the bolts at the base. The following tables show the results obtained by the tensile splitting tests.

Table 6.4: Tensile splitting strength results for CARDIFRC® Mix I – $sp/w = 0.18$.

Cylinder Number	Weight (kg)	Applied Load (kN)	Indirect Tensile Strength (MPa)
1	4.20	889	28.30
2	4.22	784	24.96
3	4.22	855	27.22
4	4.21	1045	33.26
5	4.21	925	29.44
		Mean f_t	**28.64**

Table 6.5: Tensile splitting strength results for CARDIFRC® Mix I – $sp/w = 0.21$.

Cylinder Number	Weight (kg)	Applied Load (kN)	Indirect Tensile Strength (MPa)
1	4.04	Specimen Lost	Specimen Lost
2	4.06	795	25.30
3	4.08	790	25.15
4	4.08	715	22.76
5	4.06	808	25.72
		Mean f_t	**24.73**

Table 6.6: Tensile splitting strength results for CARDIFRC® Mix II – *sp/w* = 0.40.

Cube Number	Weight (kg)	Applied Load (kN)	Indirect Tensile Strength (MPa)
1	4.19	860	27.37
2	4.22	571	18.18
3	4.19	794	25.27
4	4.22	635	20.21
5	4.20	535	17.03
6	4.20	641	20.40
7	4.15	507	16.14
8	4.19	694	22.10
9	4.19	764	24.32
10	4.20	748	23.81
11	4.15	631	20.08
		Mean f_t	**21.36**

6.3.3 Modulus of elasticity (*E*)

For the determination of the modulus of elasticity of the two mixes of CARDIFRC®, cylinders of each mix were tested according to BS 1881-121:1983. For Mix I, one cylinder with *sp/w* = 0.18 was tested. For Mix II, one cylinder with *sp/w* = 0.40 was tested. The specimens were taken from the same group of specimens that were tested for tensile splitting strength. The tests were performed in an AVERY-DENISON Type 7152, Servo-Hydraulic Testing Machine, with a load capacity of 600 kN. The machine was fitted with a DARTEC 9600 Digital Feedback Controller. On each cylinder 2 gauges, 30 mm long, were placed, after a very careful surface preparation, for the measurement of the specimen strains. For comparison purposes LVDTs were also used in order to obtain a second value of the elastic modulus. The specimens were loaded up to the one third of their compressive strength (approximately 455 kN) and then unloaded. The value of 455 kN was calculated by transforming the average compressive load measured on CARDIFRC® cubes into a circular surface (100 mm diameter). The loading-unloading procedure was repeated two times. The load was applied in 50 kN load increments, starting at 5 kN. The modulus of elasticity for Mix I, *sp/w* = 0.18 is *E* = 48.0 GPa and for Mix II, *sp/w* = 0.40 is *E* = 50.0 GPa. The results were very satisfactory since both values are very close to the theoretical modulus of elasticity, according to the Rule of Mixtures (50 GPa) in which allowance has been

made for the random orientation of fibres (see for example (3.14)). The *E*-value of Mix II is slightly higher than Mix I, since Mix II contains coarser sand than Mix I.

6.3.4 Modulus of rupture (MOR)

For the determination of the modulus of rupture of Mix I of CARDIFRC®, 100x100x500 mm beams were tested according to BS 1881-118:1983, in 4-point bend tests (Figure 6.3). For Mix I 8 beams with sp/w = 0.18 were tested in deformation control. Two types of measurement were recorded for each beam: (1) the load from the load cell of the testing machine; (2) the vertical deflection at the midspan. The vertical deflection was measured by two LVDTs placed at the middle points on opposite sides of the test beam. The average of the two LVDTs was used as a final value of deformation. The intention of these tests was to determine the flexural strength of the material, in order to define the load amplitudes of the fatigue tests, as a percentage of this flexural strength and also the static load-displacement envelope curve. The tests were performed in an AVERY-DENISON Type 7152, Servo-Hydraulic Testing Machine, with a load capacity of 600 kN. The machine was fitted with a DARTEC 9600 Digital Feedback Controller. The initial displacement rate was 0.002 mm/s and after the peak load the rate was increased to 0.005 mm/s. The failure was nominally defined at a fixed midspan displacement of 10 mm.

The modulus of rupture f_{cf} is given by the equation:

$$f_{cf} = (F \,.\, L) / (d_1 \,.\, d_2^2)$$

F: breaking load (N)

d_1, d_2: lateral dimensions of the cross section (mm)

L: distance between supporting rollers (mm)

For Mix I, sp/w = 0.18, f_{cf} = 31.60 MPa (Standard Deviation = 2.20 MPa). The results of all the tests are presented in Table 6.7.

From the mean value of the flexural strength measured from the above tests (f_{cf} = 31.60 MPa), the corresponding value of the ultimate load (P_u) in 3-Point Bending was calculated, by applying the following formula:

$$f_{cf} = \frac{M \times y}{I} = \frac{P_u \times L}{4 \times \left(\frac{b \times h^3}{12}\right)} \times \frac{h}{2} = \frac{12 \times P_u \times L \times h}{8 \times b \times h^3} = \frac{3 \times P_u \times L}{2 \times b \times h^2}$$

$$\Rightarrow \quad P_u = \frac{2 \times f_{cf} \times b \times h^2}{3 \times L} \quad \Rightarrow \quad P_u = \frac{2 \times 31.60 \times 100 \times 100^2}{3 \times 400} \quad \Rightarrow \quad \underline{P_u = 52.67 \text{ kN}}$$

where I is the second moment of area, y is the distance of the centroid of the beam from the extreme fibre, and b and h are the width and height of the beam, respectively.

Table 6.7: MOR results for CARDIFRC® Mix I – $sp/w = 0.18$.

Beam Number	Peak Load (kN)	MOR (MPa)
1	84.06	33.63
2	42.91	17.17
3	72.35	28.94
4	83.93	33.57
5	83.04	33.21
6	74.18	29.67
7	82.42	32.97
8	72.98	29.19
	Mean f_{cf}	**31.60**

Note: The flexural strength of the specimen No.2 was substantially lower than the flexural strengths of the rest specimens, therefore it was not included in the calculation of the mean value of the flexural strength and its standard deviation.

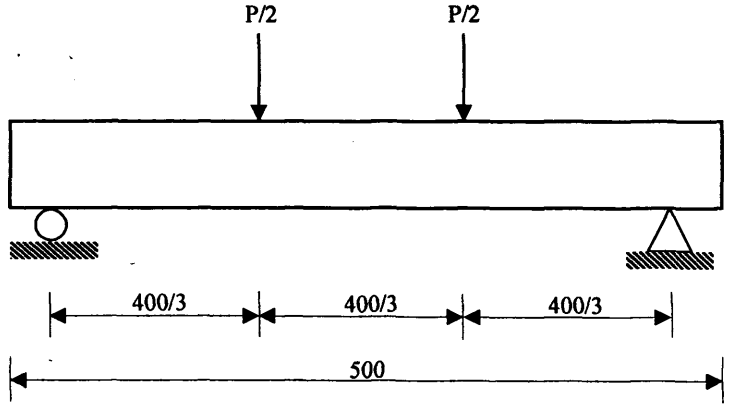

Figure 6.3: Schematical presentation of the modulus of rupture (MOR) test.

6.3.5 Three-point bend tests (100x100x500 mm)

For the determination of the tensile/flexural strength of Mix I of CARDIFRC®, 100x100x500 mm beams were tested in three-point bending (Figure 6.4). For Mix I 8 beams with *sp/w* = 0.18 were tested in deformation control. Two types of measurement were recorded for each beam: (1) the load from the load cell of the testing machine; (2) the vertical deflection at the centre point. The vertical deflection was measured by a single LVDT placed underneath the testing beam, at the centre point. The intention of these tests was to determine the tensile/flexural strength of the material, in order to define the load amplitudes of the fatigue tests, as a percentage of this flexural strength and also the static load-displacement envelope curve. The tests were performed in a stiff self-straining testing frame, fitted with a DARTEC 2500 kN dynamic-static actuator. The machine was powered by a 23 lit/min DARTEC hydraulic pump and was connected with a DARTEC 9600 Digital Feedback Controller. The failure was arbitrarily defined at a fixed displacement of 10 mm.

The tensile/flexural strength σ_t is given by the equation:

$$\sigma_t = (M.\ y) / I$$

M = bending moment (N.mm)

I = moment of inertia (mm^4)

y = distance of the centroid from the extreme fibre (mm)

For Mix I, *sp/w* = 0.18, the average peak load is P_u = 60.22 kN (Standard Deviation = 2.56 kN) and the average flexural strength is σ_t = 36.14 MPa (Standard Deviation = 1.54 MPa). The results of all the tests are presented in Table 6.8 and graphically in Figures 6.5 and 6.6.

Table 6.8: Tensile/flexural strength results for CARDIFRC® Mix I – $sp/w = 0.18$.

Beam Number	Peak Load (kN)	Tensile/Flexural Strength (MPa)	Notes
1	62.68	37.61	Tests 1-5 were performed using a displacement rate equals to 0.002 mm/s. In order to check the rate effect on the tensile/flexural strength of CARDIFRC®, specimen No.6 was tested at 0.02 mm/s and specimens No.7, 8 were tested at 0.2 mm/s.
2	58.30	34.98	
3	56.75	34.05	
4	61.48	36.89	
5	61.91	37.15	
6	64.31	38.59	
7	64.14	38.48	
8	61.46	36.88	
	Mean σ_{tf} (1-5)	**36.14**	

Note: The mean value of the tensile/flexural strength in Table 6.8 was calculated based on the results of specimens 1-5, all tested at the same rate, equal to 0.002 mm/s.

As it is noted in Table 6.8, 3 beams were tested at higher rates of applied deformation/time, in order to examine the rate effect on the beam response. Beam No.6 was tested at a rate of 0.02 mm/s and beams No.7, 8 were tested at a rate of 0.20 mm/s. Although these testing rates are not as high as the rates applied in dynamic tests, an increase of the flexural strength of the material was observed, while the increase of the energy absorption was more pronounced for the beams tested at a rate of 0.20 mm/s. This can be observed from the load – displacement curves of tests 6-8, comparing with the average curve of the tests performed at a rate of 0.002 mm/s (Figure 6.6). These increases are attributed to the so-called "rate-effect", discussed in Chapter 4. Although the mechanisms behind the increase of the flexural strength and the energy absorption due to rate effect in HPFRCCs are still under investigation, a reasonable explanation seems to be the one given by Jeng and Shah (1985). Because of inertia effects, the exact path of the crack propagation is affected, which is forced to develop along the shortest possible path lengths in a very short time, generally through stronger matrix zones, resulting in higher material strength. Fracture theories, which include a rate effect, also include the partition between the various types of energy changes during crack extension. This causes a decreasing crack propagation velocity resulting in a strength increase. The available energy to form new crack surfaces in the region around the crack tip decreases (Weerheijm and Reinhardt, 1989). In addition, Suaris and Shah (1982) claimed that the bond strength between deformed fibres and concrete matrix was expected to increase with strain rate,

resulting in a higher percentage increase in energy absorption by deformed fibres than by smooth fibres.

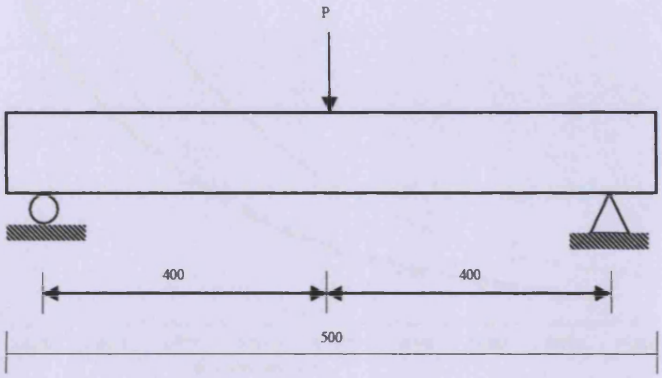

Figure 6.4: Schematical presentation of the 3 – point bending test.

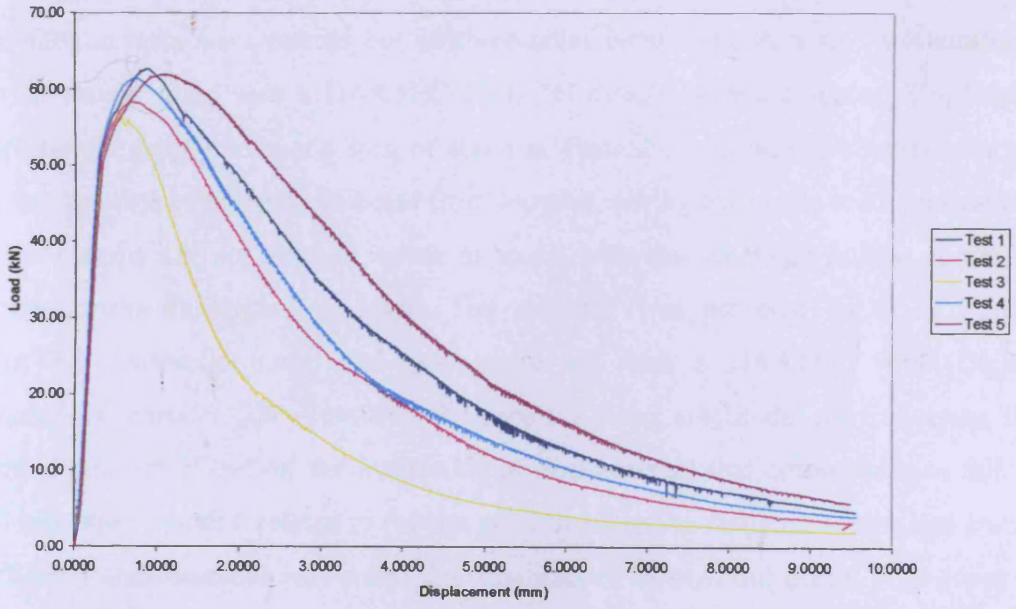

Figure 6.5: Load – displacement response of CARDIFRC® - Mix I beams tested in 3 – point bending.

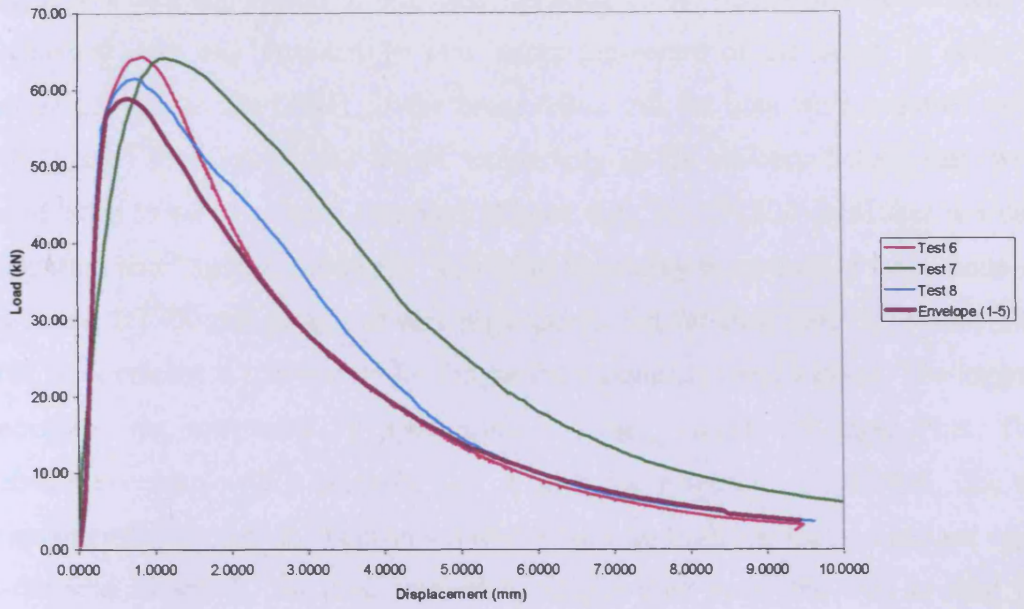

Figure 6.6: Load – displacement response of CARDIFRC® - Mix I beams tested in 3 – point bending at higher strain rates.

6.4 FATIGUE TESTS (100x100x500 mm)

The fatigue tests were carried out as three-point bend tests, in a stiff self-straining testing frame, fitted with a DARTEC 2500 kN dynamic-static actuator. The beams were simply supported over a span of 400 mm. Four short cylindrical clamps were set on the supports to prevent the beam from moving, during the cyclic load application. These clamps did not actually come in touch with the specimen, unless it started moving from its original position. The machine was powered by a 23 lit/min DARTEC hydraulic pump and was connected with a DARTEC 9600 Digital Feedback Controller. This controller directed the stress amplitude, the frequency, the applied number of cycles, the magnitude of displacement that corresponds to failure and any other function related to the test performance. The testing machine had a very stiff setup and therefore only small deformations of its own can occur. Four types of measurement were recorded for each beam: (1) the load from the load cell of the testing machine; (2) the vertical deflection at the centre point; (3) the time parameter; and (4) the number of cycles to failure. The vertical deflection was measured by a single LVDT placed underneath the testing beam, at the centre point. The specific LVDT was calibrated for a very narrow range of deformation (±2.5 mm), because the deformation of the beam during its fatigue life was expected to be very small. In this

way, it was also anticipated to minimise the noise of the particular measurement. A mechanical stop was installed 10 mm below the centre of the beam, in order to prevent damage to the LVDT, if the beam failed. All the data were acquired using DT800 dataTaker logger and stored temporarily in its memory before they were downloaded to the connected computer (Figure 6.7). The DT800 dataTaker is a data acquisition and logging instrument, which has the ability to operate in burst mode. In this mode, DT800 can sample at very high speeds, but for short periods of time. This mode of operation is appropriate for fatigue data acquisition and logging. The logging procedure was controlled by appropriate software, called DeLogger Plus. This software provides with a powerful set of tools for working with DT800, like the programme builder option. This option allows the user to define the number and types of the scan channels, the time interval to trigger each scan, the way to read the channel (e.g. voltage) and how to convert the reading into appropriate engineering units. Many more options are available, which are beyond the requirements of this test configuration.

The tests were carried out with load control between two limits (with a sinusoidal force variation in time). The minimum stress level, S_{min}, was 10% of the monotonic strength and the maximum stress level, S_{max}, ranged from 70% to 85% of the monotonic strength. Before the cyclic process started, the beams were preloaded with 3 static cycles of loading and unloading between 2 kN and 28 kN, which corresponded to 50% of the monotonic flexural strength of the material. The specimens were preloaded for stabilisation purposes. The frequency of loading used was 6 Hz. The tests stopped after the specimen failure (as conventionally defined above) or after one million cycles, whichever occurred first.

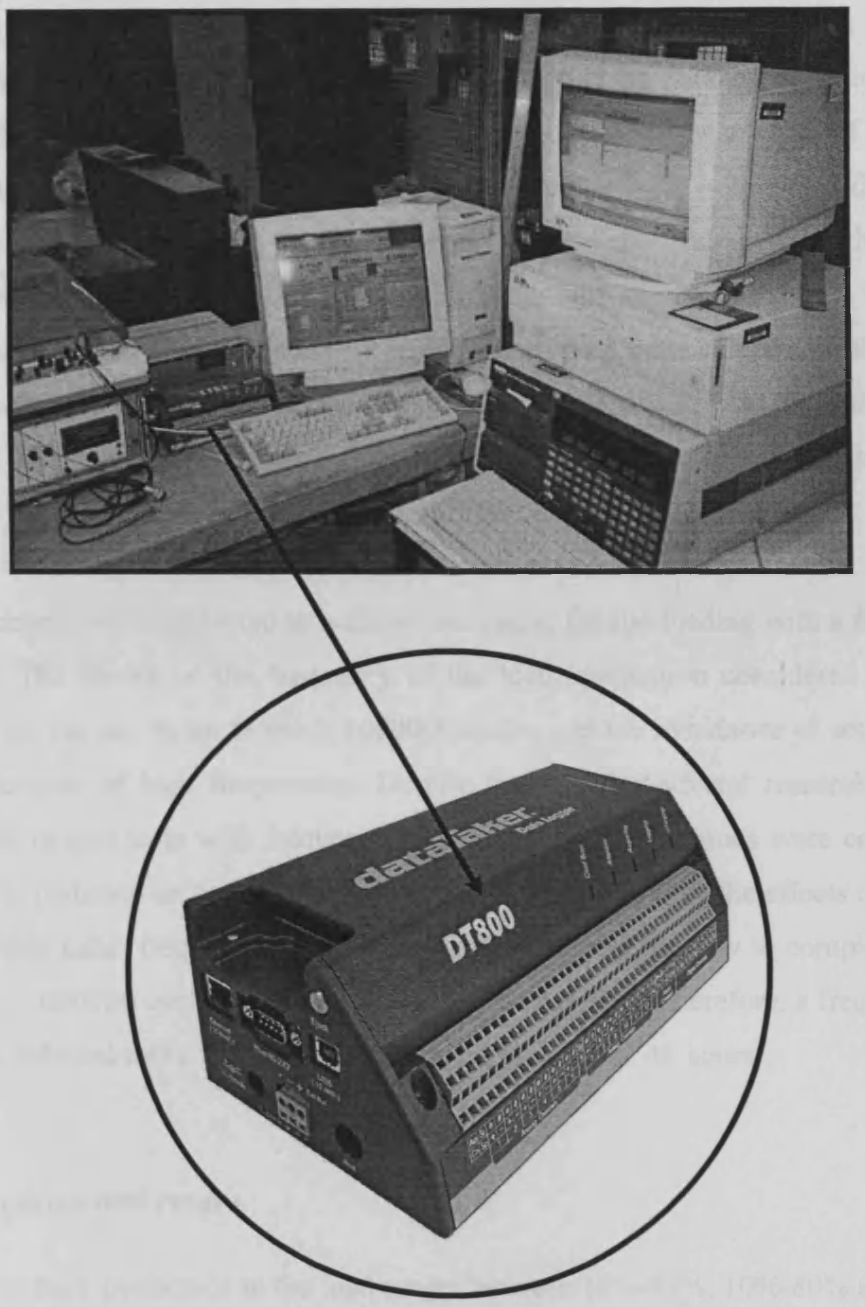

Figure 6.7: Logging system of the fatigue response of CARDIFRC® specimens.

6.4.1 Test variables

Generally, fatigue tests have been carried out for a given constant minimum stress or for a constant ratio between the minimum and maximum stress level. In this study, a constant minimum stress level of 10% of the static flexural strength was maintained. The cyclic tests were carried out at maximum stress levels ranging from 70% to 85% of the monotonic strength.

The fatigue tests were performed in load control. It was decided to use a value of ultimate load equal to P_u = 57 kN. This value resulted if the standard deviation of the peak load measured in the 3-PB tests was subtracted from the mean value of the peak load obtained from the experiments, i.e. $P_u = P_{avg} - S.D$ (60.2 – 2.6 ≈ 57 kN). Each specimen was first subjected to three slow cycles between 2 kN and 28 kN, which corresponded to a stress level of 50% of the monotonic strength. It should be noted that specimens tested in this study were not pre-cracked before cyclic loading. This concept supports the selection of the stress level of 50%, which lies within the elastic range of the material response. This is an essential characteristic of this study compared with previous studies on fatigue of fibre reinforced concrete.

The specimens were subjected to a sinusoidal cyclic fatigue loading with a frequency of 6 Hz. The choice of the frequency of the load application considered the time required for the test beam to reach 1000000 cycles and the avoidance of several side effects because of high frequencies. Despite the fact that several researchers have conducted fatigue tests with frequencies up to 20 Hz, these values were considered too high to maintain an accurate load range and also to minimise the effects of inertia. On the other hand, frequencies of 1-2 Hz were considered too low to complete a full test (up to 1000000 cycles) within a reasonable time period. Therefore, a frequency of 6 Hz was selected and a full test was completed in less than 48 hours.

6.4.2 Experimental results

Tests have been performed in the load ranges between 10%-85%, 10%-80% and 10%-70% of the ultimate flexural strength. In Table 6.9 and Figure 6.8 are presented the results of the fatigue life of specimens (i.e. number of cycles to failure, *N*). It is observable that there is a large scatter in the experimental fatigue life, which is a characteristic of the fatigue tests. This is attributed to the nature of the material and also to errors in test variables, which are repeated in a large number of cycles. The large scatter in the experimental results did not give the opportunity to estimate the trend of the fatigue life of the particular beams, not even after the large number of tests performed.

Table 6.9: Number of cycles sustained by CARDIFRC® - Mix I beams (100x100x500 mm).

Fatigue Tests - CARDIFRC® - Mix I Beams (100x100x500 mm)			
Beam Number	**10% - 85% Pu**	**10% - 80% Pu**	**10% - 70% Pu**
1	706	9918	5910
2	181738	2144	18
3	18	14	437
4	2510	4036	1000000
5	41539	28733	279
6	169279	911453	4
7	1000000	195703	1000000
8	6174	9337	3
9	4918	131237	527988
10	161839	78940	110999
11	493	-	-
12	54977	-	-

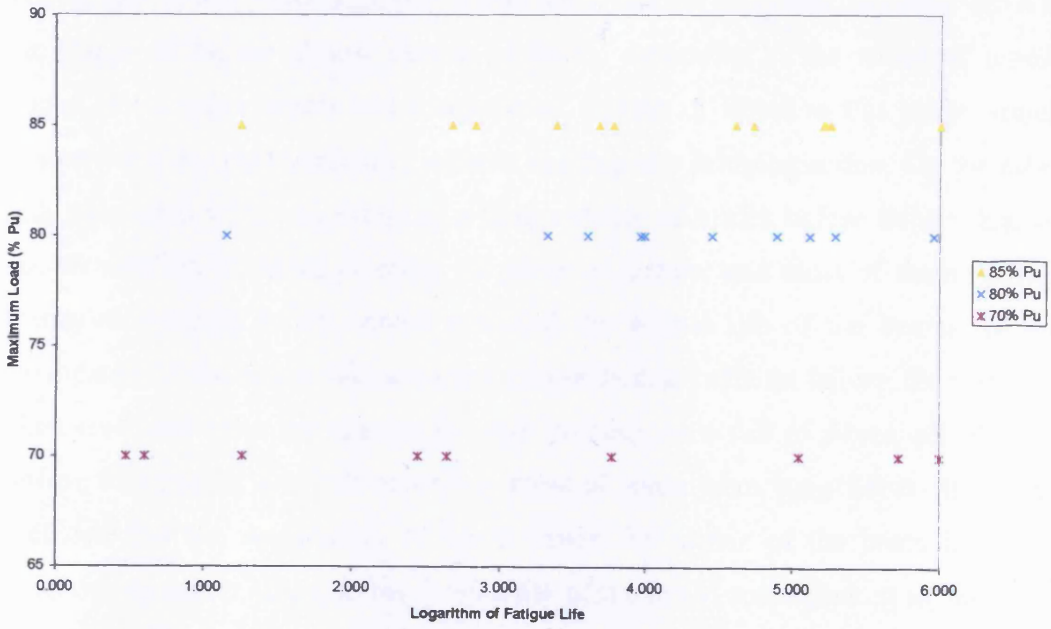

Figure 6.8: Fatigue life of CARDIFRC® - Mix I beams (100x100x500 mm).

6.4.3 Analysis of experimental results

The large scatter of the experimental fatigue life of the tested beams is mainly attributed to the inhomogeneous nature of the material. The addition of fibres to the concrete matrix can dramatically improve the fatigue performance of the composite and also they impart additional strength in tension, shear and flexure. Therefore, the material attains improved strength characteristics. It is, however, extremely difficult to achieve an even distribution of fibres within the mix, because of the large quantity of fibres used. This has the effect that some internal vertical planes of the specimen under flexure will be devoid of fibres. In the worst case scenario that these devoid planes are located in the central area of the beam, where the maximum bending moment is applied, they become failure planes, after very few cycles. Another important aspect is the orientation of the fibres in this area of the maximum bending moment.

The failure surfaces of the tested beams were thoroughly examined visually. It was observed that beams which sustained a very small number of cycles, had large areas in their planes of failure almost devoid of fibres, especially in the zones of tensile stresses. Some other beams had a significant number of fibres in this plane, which however were oriented vertically, without exerting any bridging action. On the other hand, specimens which experienced a large number of cycles before failure, had an even distribution of fibres crossing the plane of failure, and most of them applied substantial bridging action, which extended the fatigue life of the beams. In the extreme case of the beams that sustained 1000000 cycles without failure, the planes of failure (revealed after the specimens were broken) were full of fibres, all of them exerting bridging action and moreover most of them were long fibres. It can be concluded that the distribution of fibres within the matrix of the beam is a very important parameter affecting the fatigue life of the tested specimens. It is, however, extremely difficult to achieve an even distribution of fibres in the mix. For the improvement of fibre distribution, the adding of fibres in the mix is performed using two different sieves, for short (4 mm sieve) and long fibres (11 mm sieve). Many interesting observations regarding the fibre distribution in CARDIFRC® were made by the image analysis of specimens, which will be explained in Chapter 7.

There was a suspicion that the poor distribution of the fibres within the specimen was also a result of the high frequency applied on the electric vibration table, used during the casting procedure. A thorough examination of the distribution of the fibres within the specimens was performed by Benson (2003), who investigated this distribution using x-ray tomography. This investigation revealed that there were more fibres at the sides and the bottom of the specimen and fewer fibres in the central area of the beam. It is strongly believed that the high frequency of almost 100 Hz used during casting of specimens had as a consequence a spinning action on the fibres forcing them to the sides of the beams.

6.5 THREE-POINT BEND TESTS

6.5.1 Cut specimens (250x100x33 mm)

In order to verify the images taken by the CT scanner, it was decided to cut some of the existing 100x100x500 mm specimens into six smaller specimens. More precisely, each of the 100x100x500 mm beams gave two top, two middle and two bottom specimens, each one of dimensions 250x100x33 mm (Figure 6.9).

(1) TOP	(2) TOP
(3) MIDDLE	(4) MIDDLE
(5) BOTTOM	(6) BOTTOM

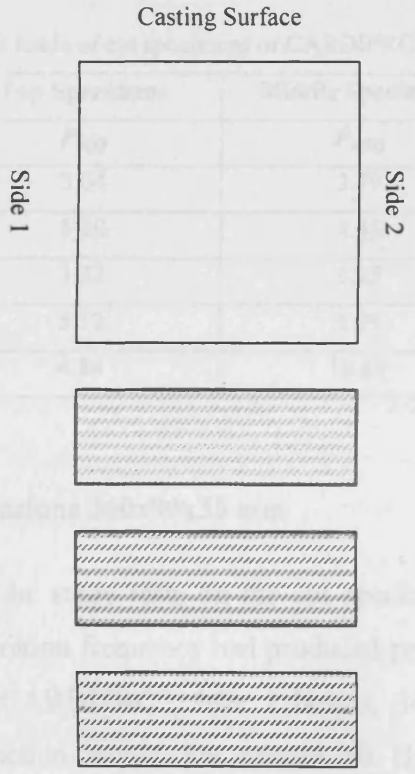

Figure 6.9: Schematical presentation of the cut specimens and the fibres density in top, middle and bottom specimens.

The cut specimens were tested statically in three-point bending, with displacement control, and the peak loads were noted. The experimental results of the average peak loads for top, middle and bottom specimens are presented below, whereas the results of the peak loads are all summarised in Table 6.10.

Top Specimens: $P_{u,top} = 4.30$ kN

Middle Specimens: $P_{u,mid} = 6.09$ kN

Bottom Specimens: $P_{u,bot} = 11.31$ kN

It can be clearly observed that the ultimate load from the flexural static tests is much lower at the top, and is significantly increased when moving to middle and finally bottom specimens. The bottom specimens give the highest value of peak load, which is a clear indication that these specimens had more fibres, in comparison to the top and middle specimens. These experimental results undoubtedly confirm the suspicion of the poor distribution of fibres within the original specimens, as a result of the high frequency of almost 100 Hz used during the compaction of the cast specimens.

Table 6.10: Experimental peak loads of cut specimens of CARDIFRC® - Mix I.

Beam Number	Top Specimens	Middle Specimens	Bottom Specimens
	$P_{u(T)}$	$P_{u(M)}$	$P_{u(B)}$
1	3.04	3.79	8.11
2	5.20	4.43	10.89
3	3.32	5.25	13.48
4	5.12	6.09	11.35
5	4.84	10.89	12.74

6.5.2 Specimens of dimensions 360x90x35 mm

After the completion of the static tests on the cut specimens, where it was clearly revealed that the high vibration frequency had produced poor distribution of the fibres, it was decided to cast CARDIFRC®, Mix I beams, 360x90x35 mm, where the frequency during compaction would not exceed 50 Hz. Moreover, the selected dimensions were regarded to be more realistic, in the sense that CARDIFRC® is a material that is mainly used for repairing, in thin strips of about 20 mm thickness. For static and fatigue tests 50 specimens were cast.

The beams were tested in three-point bending, with a testing span of 280 mm. The tests were performed in displacement control, and the peak load and the load-displacement curves obtained. For Mix I, the average peak load was P_u = 12.20 kN (Standard Deviation = 1.02 kN) and the average flexural strength was σ_{ct} = 48.98 MPa (Standard Deviation = 3.88 MPa). The flexural strength of CARDIFRC® determined from these specimens was well above the strength obtained from the initial large beams used, i.e. 100x100x500 mm. However, this increase of the flexural strength can

be attributed to the size effect. All the results are shown in Table 6.11 and graphically in Figure 6.10.

Table 6.11: Tensile/flexural strength results for CARDIFRC® - Mix I (360x90x35 mm).

Beam Number	Peak Load (kN)	Tensile/Flexural Strength (MPa)
1	11.27	42.93
2	12.63	48.11
3	13.07	49.79
4	13.72	52.27
5	13.24	50.44
6	13.22	50.36
	Mean σ_{cf}	**48.98**

For the fatigue tests, it was decided to use a value of ultimate load equal to P_u = 10 kN. This value was obtained if two standard deviations was subtracted from the mean value of the peak load obtained from the experiments, i.e. $P_u = P_{avg} - 2S.D$ (12.2 – 2.0 ≈ 10 kN). The concept behind the subtraction of two standard deviations from the average peak load was to increase the probability that the ultimate monotonic load of all specimens tested in fatigue would be lower than the applied P_u, to about 95.5% (Figure 6.11). This practice was aiming to minimise the factors that caused the huge scatter in fatigue life of the 100x100x500 mm beams, and to eventually obtain more consistent results.

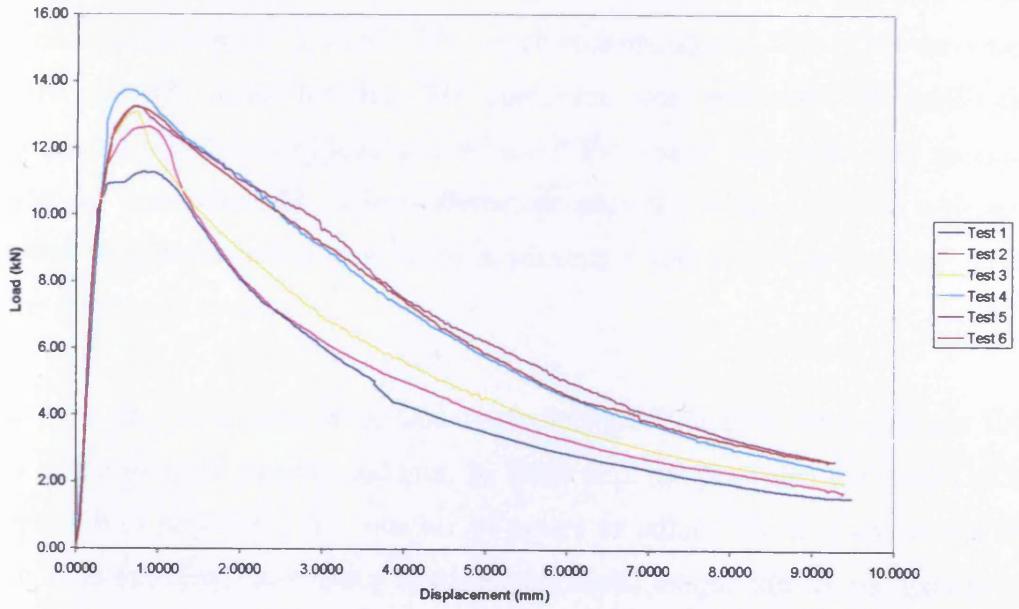

Figure 6.10: Load – displacement response of CARDIFRC® - Mix I beams (360x90x35 mm) tested in 3 – point bending.

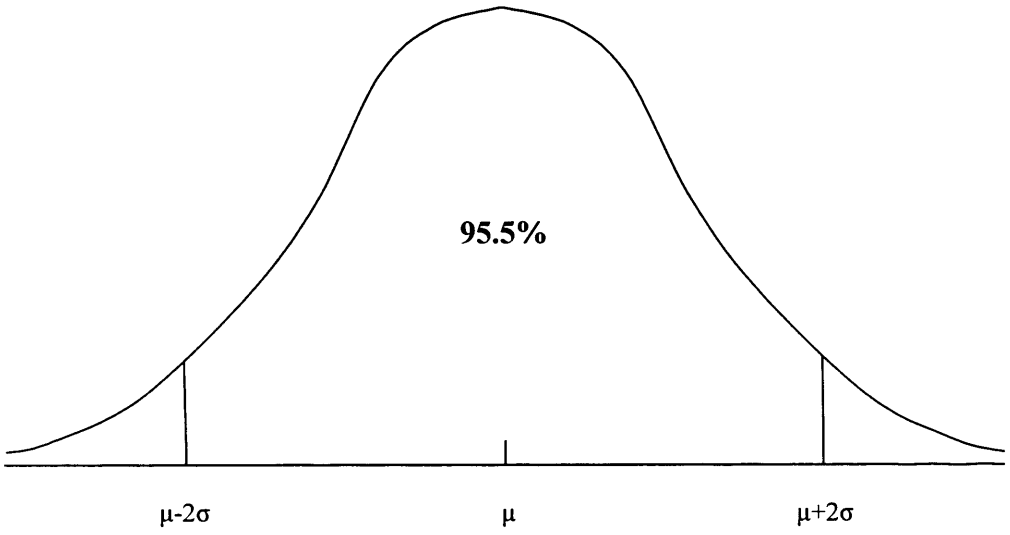

Figure 6.11: Distribution of probability ultimate load P_u be lower than μ-2σ.

6.6 FATIGUE TESTS (360x90x35 mm)

The fatigue tests were carried out as three-point bend tests, in the same way as was described earlier for the 100x100x500 mm beams. The tests were carried out with load control between two limits (with a sinusoidal force variation in time). The minimum stress level, S_{min}, was 10% of the monotonic strength and the maximum stress level, S_{max}, ranged from 80% to 90% of the monotonic strength. Before the cyclic process was started, the beams were preloaded with 3 static cycles of loading and unloading between 1 kN and 5 kN, which corresponded to 50% of the monotonic flexural strength of the material. The specimens were preloaded for stabilisation purposes. The frequency of loading used was 6 Hz. The tests stopped after specimen failure (as conventionally defined above) or after one million cycles, whichever occurred first. In the special case of two specimens, it was decided to test them up to a higher number of cycles.

Tests have been performed in the load ranges between 10%-80%, 10%-85% and 10%-90% of the ultimate flexural strength. In Table 6.12 are presented the results of the fatigue life of specimens (i.e. number of cycles to failure, N). It is observable that there is an excellent consistency in the experimental fatigue life for the load ranges between 10%-80% and 10%-85%, since all of the eight specimens sustained 1000000

or more cycles without failing. This is attributed to the lower frequency used during the vibration of these specimens, which had as a result a more even distribution of the fibres within the specimen and also to the definition of P_u as equal to P_{avg}-2SD, as it was explained in previous paragraph.

An important observation from the tests performed at maximum load levels of 80% and 85% P_u, is the fact that none of the eight tested specimens developed any visible cracks during the fatigue loading of the 1000000 cycles. This is another confirmation of the improved distribution of the fibres within these specimens, but it also implies that probably no failure of specimen will occur at lower maximum stress levels. From the above experimental results, it can be concluded that the endurance limit of the material is approximately at 85% of its flexural strength. Below this limit none of the tested specimens failed, not even after a very high number of cycles (e.g. 20000000 cycles). Slightly above this load limit, some specimens did not fail after 1000000 cycles, whereas some other specimens failed after a relatively small number of cycles. This scatter is reasonable, since on one hand 90% P_u is slightly above the fatigue limit (therefore some specimens do not fail), and on the other hand the limit of 90% P_u is very high for fatigue testing, therefore some specimens fail very early. Another remark about the observed fatigue limit is that this limit is very high, not very often observed in the relevant literature. This is an indication that CARDIFRC® has an extensive elastic zone, which is also confirmed by direct tension tests performed by Benson (2003).

Table 6.12: Flexural fatigue tests experimental results (CARDIFRC® - Mix I, 360x90x35 mm).

Load Amplitude (% P_u)	**Fatigue Life (N)**				
	N_1	N_2	N_3	N_4	**Average Fatigue Life (N)**
10-90%	1000000	21564	9315	1000000	-
10-85%	1000000	1000000	1000000	20000000	1000000(*1)
10-80%	1000000	1000000	1000000	2000000	1000000(*1)

*1: The average fatigue life considers only the first 1000000 cycles sustained by specimen No.4.

In order to check whether internal cracks had developed in the specimens that sustained 1000000 or more cycles without failure, they were tested afterwards in static three-point bending. The purpose of this static testing was to compare the post-fatigue flexural strengths and static envelope curves with the pre-fatigue test results. None of the specimens had any visible external cracks, after the end of the fatigue testing. The specimens tested at 80%, 85% and 90% P_u in fatigue, showed a small increase in their flexural strength (Table 6.13). This increase seemed to be higher than could be attributed to the increase due to age alone. This increase in flexural strength was believed to depend on the maximum flexural fatigue stress (S_{max}) to which the specimens were subjected earlier. Based on the fatigue literature review, it was anticipated that with lower S_{max} values the increase in flexural strength will be higher. This, however, was not confirmed experimentally, since the increase of the flexural strength for specimens tested earlier up to 80%, 85% and 90% P_u was about of the same order of magnitude. A remarkable observation was that the specimens which did not fail after 1000000 cycles up to 90% P_u, showed the highest increase (7%), whereas the lowest increase (5%) was observed for specimens tested earlier up to 80% P_u. The increase observed for specimens tested earlier up to 85% P_u was about 6%. Although it seems that there exists a linear correlation between the fatigue loading stress and the corresponding after-fatigue static flexural strength, no certain conclusions can be drawn. The difference is believed to be very small; therefore the increase in the flexural strength is assumed to be of the same order of magnitude for the three groups. Moreover, the result of the average strength for specimens tested up to 90% P_u, was based only on two specimen results, which did not fail after fatigue. It is believed that the increase in flexural strength is approximately constant for specimens subjected to fatigue stress close to the fatigue limit of the material. This result confirms previously noted results in the literature, that prior cycling may lead to an improvement in strength (Naaman and Hammoud, 1998; Ramakrishnan et al., 1996; Naaman and Harajli, 1990). It was suggested that this increase in strength is due to densification of the material, caused by stress cycling. It is also known that most FRCs are linearly elastic up to about 80% or more of the matrix tensile strength and that the microcracking process starts beyond this point. This leads to the conclusion that beam specimens subjected to cyclic flexural stress below this level are not likely to have decreased first crack flexural strength (Ramakrishnan and Lokvik, 1992).

However, the mechanisms behind the increase of the post-fatigue flexural strength in HPFRCCs are still unclear.

From the comparison of the static flexural curves before and after the fatigue loading (Figures 6.12-6.14), it can be observed that all specimens subjected to fatigue exhibit a reduced stiffness. This is an indication that there is a small internal damage in the specimens, due to the prior fatigue loading. However, this internal damage is very small and also can be considered as a distributed damage, which does not lead to the formation of a single localised crack. The reduction of the stiffness is more prominent in the case of the specimen tested up to 20000000 cycles, which is an extremely high number of cycles. On the other hand, no certain conclusion can be drawn regarding the effect of fatigue loading on the fracture energy, since the area under the curves pre- and post-fatigue loading are approximately the same. The same lack of consistency in the results is also reported in the literature.

Table 6.13: Experimental peak loads and tensile/flexural strengths of CARDIFRC® - Mix I beams (360x90x35 mm), tested in 3 – point bending, after they have been subjected fatigue loading.

Beam Number	10%-90% Pu		10%-85% Pu		10%-80% Pu	
	P_u (kN)	f_t (MPa)	P_u (kN)	f_t (MPa)	P_u (kN)	f_t (MPa)
1	14.65	55.81	12.65	48.19	14.30	54.48
2	-	-	14.64	55.77	13.70	52.19
3	-	-	14.30	54.48	12.40	47.24
4	12.88	49.07	13.33	50.78	13.60	51.81
Average Strength		52.44		52.30		51.43

It can be conclusively said that the fatigue performance of steel fibre reinforced concrete is strongly related to the fibre distribution within the specimens. It is believed that the stress concentration is restricted by the matrix and the fibre-matrix bonding strengths. Several researchers concluded in their investigation that the specimens failed if the fibres could not prevent the crack growth. A proper and even fibre distribution can lead to an extremely long fatigue life, especially in the case of HPFRCCs, where the interfacial bond between the fibres and the matrix is particularly strong, due to the dense structure of the material. On the other hand, in the case of specimens with poor fibre distribution in the possible planes of failure, their fatigue life may be exhausted after a few cycles, as it will be shown in Chapter 7. Especially for CARDIFRC®, the better fibre distribution achieved in specimens of dimensions 360x90x35 mm revealed that it can have an excellent fatigue response, extended up to

an extremely high number of cycles, without significant internal damage. All the figures of the fatigue response of CARDIFRC® specimens – Mix I (360x90x35 mm) are presented in Appendix A.

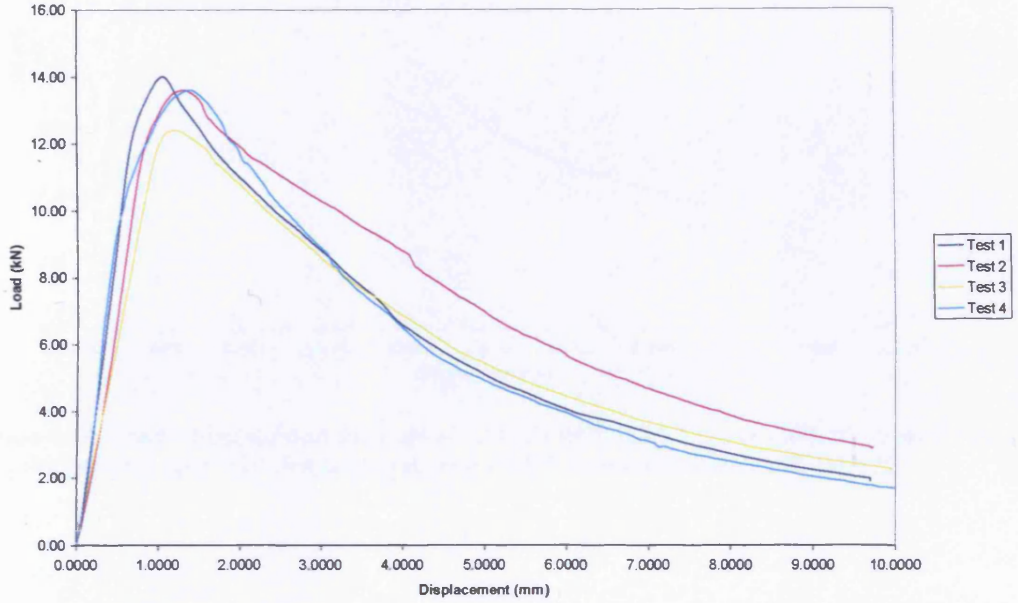

Figure 6.12: Load – displacement response of CARDIFRC® - Mix I beams (360x90x35 mm) tested in 3 – point bending, after subjected fatigue loading (1000000 cycles) between 10%-80% P_u.

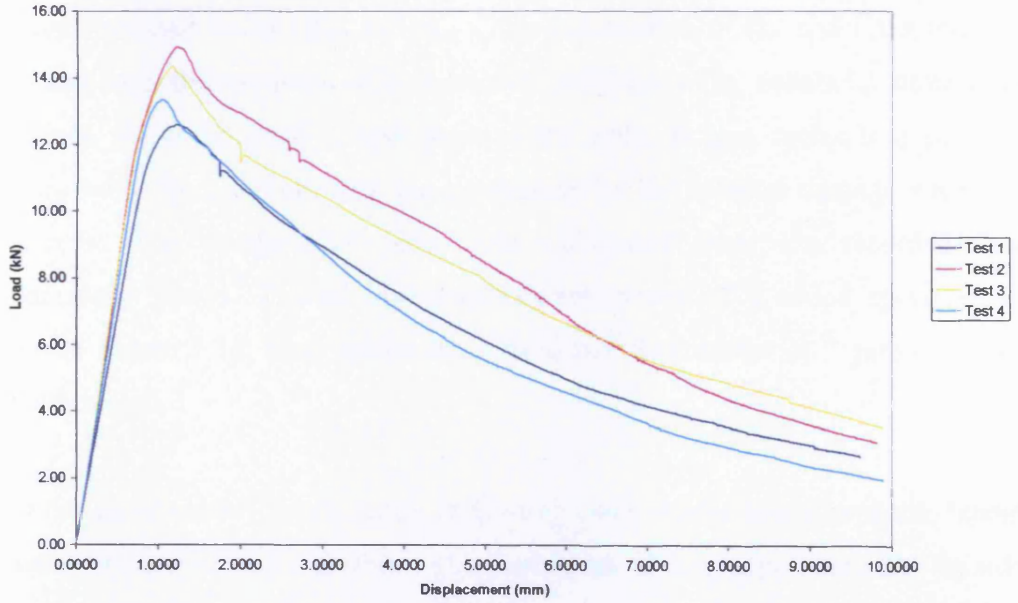

Figure 6.13: Load – displacement response of CARDIFRC® - Mix I beams (360x90x35 mm) tested in 3 – point bending, after subjected fatigue loading (1000000 cycles) between 10%-85% P_u.

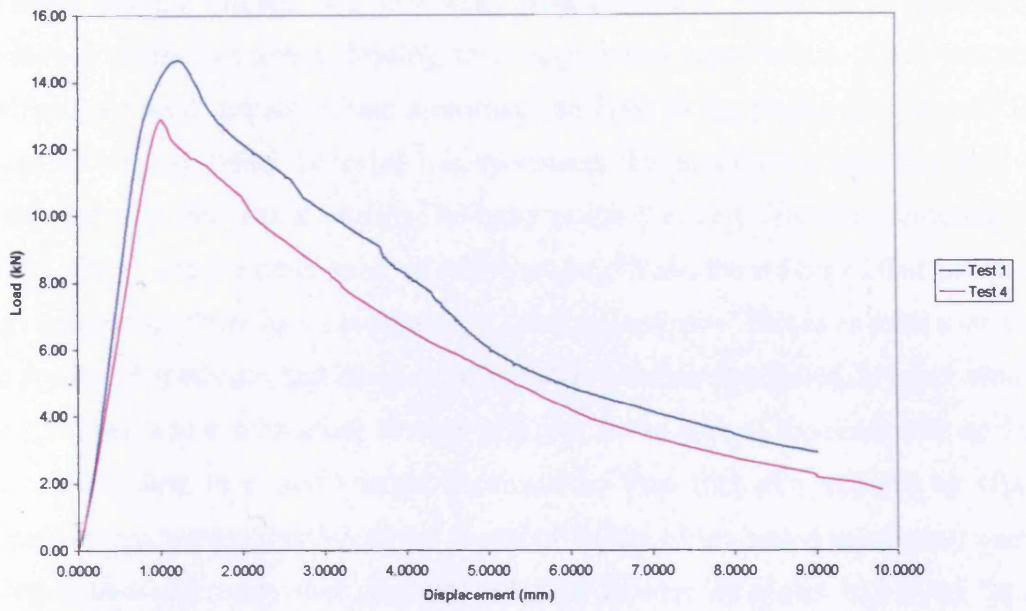

Figure 6.14: Load – displacement response of CARDIFRC® - Mix I beams (360x90x35 mm) tested in 3 – point bending, after subjected fatigue loading (1000000 cycles) between 10%-90% P_u.

6.7 EXAMINATION OF THE COMPLIANCE OF FATIGUE SPECIMENS

The compliance of a test specimen is defined as the ratio of displacement to load; therefore the units are in mm/kN. Since the fatigue tests are performed in load control between two load limits (S_{min} and S_{max}), the deformation of the specimen increases with time, until the specimen fails or reaches 1000000 cycles, whichever occurs first. Therefore, the compliance of specimens tested under fatigue cycles is expected to increase with time, representing the progression of the internal damage within the specimens. The compliances have been calculated from the recorded load-displacement curves. Typical load-displacement curves of a tested specimen are shown in Figure 6.15, from which the compliance data shown in Figure 6.16 have been calculated.

From the experimental results many interesting observations could be made, leading to some certain conclusions about the usefulness of the experimentally recorded compliance evolution. It was clearly observed that at each load amplitude, the CARDIFRC® specimen that sustained low number of cycles had high value of initial compliance (Figure 6.16). This is a clear indication that the particular specimen had

an initial internal damage or a very weak plane (devoid of fibres) in the area of the maximum applied moment, leading to a large initial deformation. That was also verified by visual inspection and also image analysis of the planes of failure of the tested specimens, which revealed that specimens that sustained a small number of cycles had very few fibres exerting bridging action (i.e. very few fibres crossing the failure plane). On the other hand, at each load amplitude, the specimen that sustained high number of cycles had a low value of initial compliance. This is an indication that the particular specimen had much smaller initial internal damage or, in other words, the specimen had a substantial number of fibres in the area of the maximum applied moment, leading to a small initial deformation. That was also verified by visual inspection and image analysis of the planes of failure of the tested specimens, which revealed that specimens that sustained a higher number of cycles had many fibres exerting bridging action (Chapter 7). In addition, it was observed that the compliance during loading of a particular specimen was slightly higher than the corresponding compliance during unloading (Figure 6.17), but the difference was too small to attribute to any residual damage in the material.

In some cases, however, it was observed that specimens that had similar fatigue lives, although they had very close values of final compliances, their initial values differed substantially. This could probably be attributed to a small initial internal damage leading to a high value of initial compliance, but thereafter a sufficient number of fibres within the specimen restrained the evolution of the damage, leading to a high number of cycles to failure.

CARDIFRC® specimens of dimensions 360x90x35 mm had a more consistent fatigue response, as it was shown above. The compliances of the specimens tested between the same stress levels were of the same order of magnitude, having minor differences between them, verifying this consistent behaviour. The compliance curves are almost parallel for specimens tested up to the same maximum stress level, having a small ascending trend, which corresponds to the small internal distributed damage taking place within the specimens due to load cycling (Figure 6.17). This was also confirmed from the post-fatigue flexural tests, as it was explained above.

From the plot of the Number of Cycles to Failure against Compliance, it can be clearly observed that the fatigue life can be separated into three stages: stage 1 represents a rapid increase of the compliance up to a small percentage (5%-10%) of the total fatigue life, stage 2 is the gradual increase from (5%-10%) up to (80%-90%) of the total fatigue life, and finally stage 3 corresponds to a rapid increase until failure. The shape of these curves is very similar to the creep curves of the specimens. The specimens that failed after a small number of cycles (i.e. have a short fatigue life) have only the third branch of this curve (i.e. rapid increase until failure). In contrast, in the case of specimens which did not fail after the completion of 1000000 or more loading cycles, only the first and second stages of the typical fatigue life curve were developed, indicating that the failure point due to fatigue for these specimens was far away (Figures 6.16 and 6.17). This is an additional verification of the extremely good fatigue behaviour of CARDIFRC®, as long as a proper and even distribution of fibres is achieved.

It can be said that the compliance of a specimen is an indicator of the internal damage progress due to fatigue loading. Therefore, it can be used to obtain a rough estimate of the total fatigue life of the particular specimen, only after a relatively small number of cycles. The compliance method cannot give accurate predictions of the number of cycles that can be sustained by the specimen; however it can give a rough idea of the order of magnitude of the fatigue life of the specific specimen. This may provide a quick means of controlling the quality of CARDIFRC® strips manufactured on a mass scale in a factory.

Figure 6.15 shows a typical load-displacement curve of a fatigue test, whereas Figures 6.16 and 6.17 show typical relations between the compliance and the corresponding fatigue life of CARDIFRC© Mix I beams (360x90x25 mm) tested in fatigue between several load limits. The graphs for all the tested specimens are given in Appendix A.

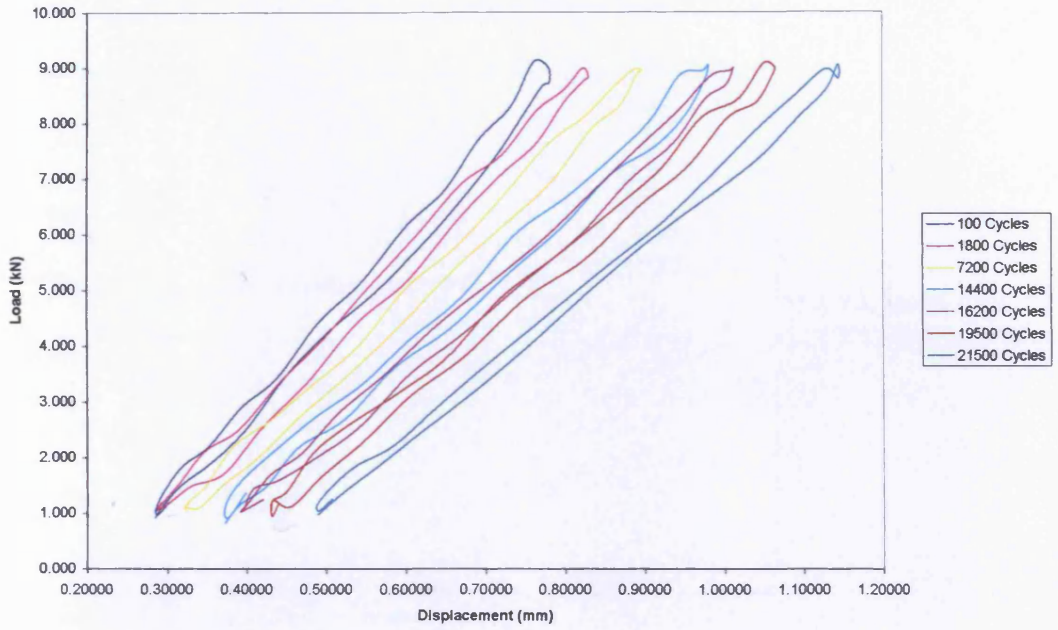

Figure 6.15: Typical load-displacement curve of CARDIFRC® - Mix I specimen (360x90x35 mm) tested in fatigue (load amplitude 10%-90% P_u, specimen failed after 21564 cycles).

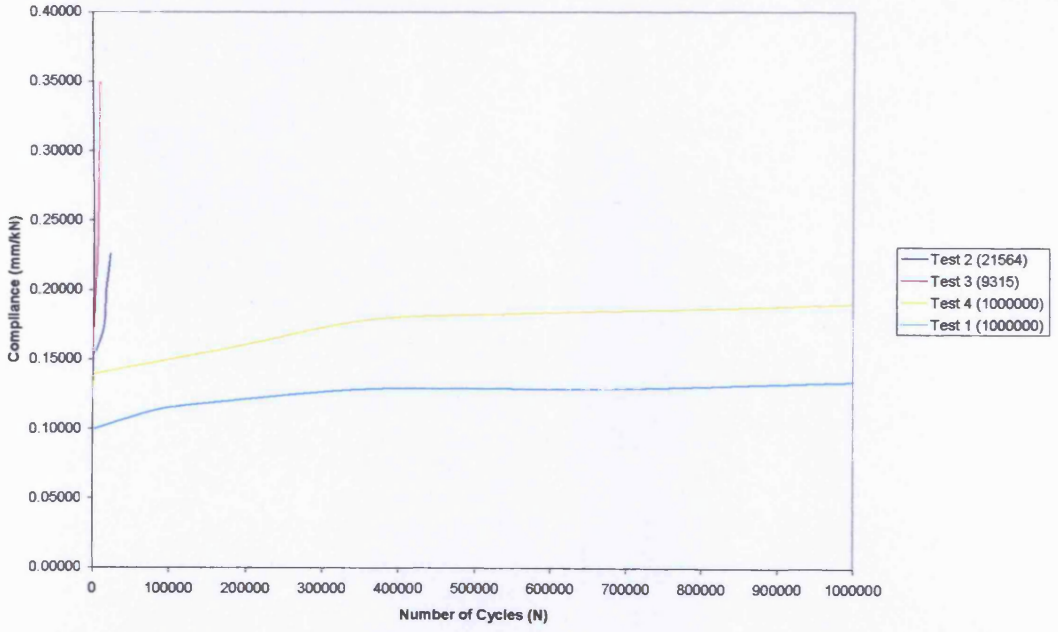

Figure 6.16: Compliances of the loading branch of fatigue cycles (360x90x35 mm CARDIFRC® beams, load amplitude 10%-90% P_u).

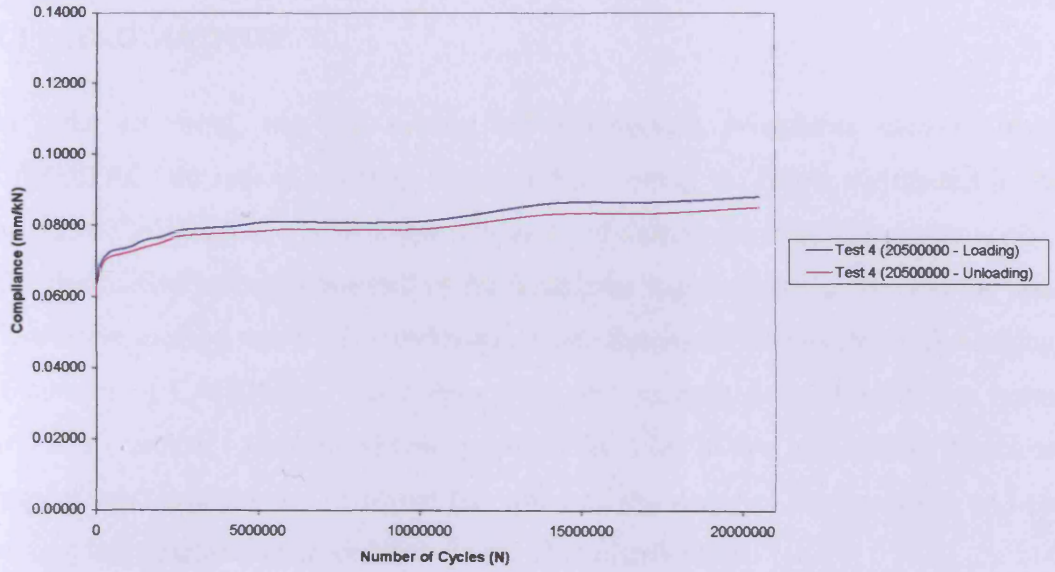

Figure 6.17: Compliances of the loading and unloading branches of fatigue cycles (360x90x35 mm CARDIFRC® beams, load amplitude 10%-85% P_u).

CHAPTER 7: FIBRE DISTRIBUTION

7.1 INTRODUCTION

In order to verify that the mixing and compaction procedures used to make CARDIFRC® do indeed result in the steel fibres being uniformly distributed in the hardened CARDIFRC®, both destructive and non-destructive techniques were applied. The destructive method consisted of the traditional image analysis, whereas the non-destructive method was a novel technique of computerised tomography (CT) imaging. A number of CARDIFRC® specimens were cast (namely, 100x100x500 mm beam, 100 mm diameter cylinder and two types of thin strip, 20 mm and 16 mm thickness, respectively) and studied to reveal the effect of the shape of the specimen and the mixing and compaction procedures on the fibre distribution.

The non-destructive technique of CT imaging has been used first. A series of CT scans was undertaken in a General Electric CTi Helical Scanner at Velindre Hospital, Cardiff, in order to image the specimens under consideration in predetermined sections along their length, and to log the X-ray absorption density along the depth of the section. This part of work was performed completely by Benson (2003). Subsequently, the specimens were cut along these predetermined sections and the cross sections investigated under an optical microscope, with two different mesh grids applied on them. Firstly, a 20x20 mm mesh grid was applied by Benson (2003) and thereafter a 10x10 mm mesh grid was applied, in order to achieve the best possible correlation between the image analysis data on fibre distribution in the cross-section with the X-ray absorption density data. Such a correlation would open a route for fast and non-destructive evaluation of the fibre distribution in a factory environment. The correlation achieved between the CT scanner imaging technique and the 10x10 mm mesh grid applied is found to be reasonably good.

7.2 CT IMAGING

CT imaging is a technique whereby cross-sectional images are generated by computer software from multiple X-ray readings. In the latest generation helical scanners, the X-ray tube and detector are continuously rotated in a stator around the object being

scanned, and the object is moved forward continuously through the centre of the stator. The amount of the X-ray beam transmitted through the object is measured, in all directions around the 360^0 stator, and the X-ray attenuation, measured in Hounsfield units, calculated. The images are compiled from thousands of readings taken in the different directions using a computer program based upon an image reconstruction algorithm (Benson, 2003).

The CT images are produced by mapping the X-ray absorption density in Hounsfield units on to a grey scale, such that air appears black (-1000 Hounsfield units) and the densest particles in the specimen appear white (3017 Hounsfield units) with water being calibrated at 0 Hounsfield units. The resolution of detail in a medical CT scanner depends upon the selected field of view and image matrix size shown, as well as how finely the views are sampled. In the present case, a 512x512 matrix was used for a 150 mm wide field of view, giving an in-plane resolution of 0.29 mm. Thus as even the latest CT helical scanners are unable to resolve individual steel fibres because of their small diameter, it was decided to produce contour plots of the X-ray absorption density at 2 or 3 sections along the length of each specimen. The specimen could subsequently be cut along these sections and the fibre distribution analysed by image analysis. In this way, the X-ray absorption density contours can be correlated to the actual fibre distribution (Benson, 2003). The casting surface of the specimens under examination was identified before scanning, in order to check the uniformity of the fibres over the depth of the specimen normal to the casting direction, and therefore make more definite conclusions about the mixing and compaction procedures applied. Figure 7.1 shows the direction and orientation in which the specimens were scanned, and the cast (float finished) face.

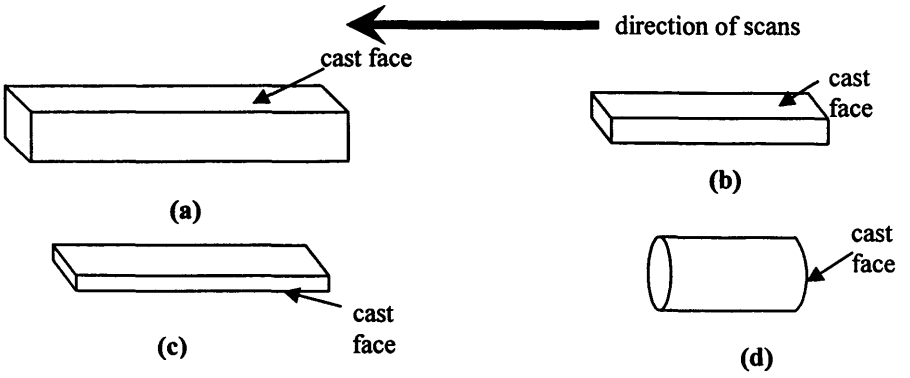

Figure 7.1: Figures showing the cast face (i.e. the surface finished with the trowel during casting) in relation to the orientation of the scans. (a) beam, (b) 20 mm thick strip, (c) 16 mm thick strip and (d) cylinder (After Benson, 2003).

In order to produce the contour plots non-destructively, a 10 mm x 10 mm grid was overlaid on the selected scanned sections on the computer screen and a probe was used to measure the X-ray absorption density at each grid intersection point, whose exact coordinates along the cross-section were also recorded. From these measurements contour plots of X-ray absorption density along the selected cross-sections were constructed. Results demonstrated that the fibre distribution is generally uniform, irrespective of the shape of the specimen made from CARDIFRC®.

This idea was first introduced for plain concrete by Karihaloo and Jefferson (2001) and has been extended to study the influence of mixing and compaction procedures on the distribution of fibres in various specimens (namely tensile specimens, retrofit strips, small beams, cylinders and cubes). Particular emphasis is being placed on the influence of the combined volume fraction of short and long fibres. This research is still in early stages, but it has already confirmed that the fibre mixing procedure indeed ensures their uniform distribution in the mixes (Benson, 2003).

7.3 IMAGE ANALYSIS

The above observations had to be further confirmed by image analysis performed on the same sections of the specimens, after cutting them with a diamond saw at these sections. This is the corresponding destructive method for examining the fibre distribution within a fibre reinforced concrete specimen.

Initially a 20 mm x 20 mm mesh grid was overlaid on the selected sections, for the image analysis procedure. However, the contour plots produced from the CT scans did not entirely agree with the image analysis of the selected sections, and the achieved correlation between the destructive and non-destructive technique was not very encouraging. Therefore, it was decided to apply a finer mesh grid over the selected sections and repeat the procedure under the image analyser.

A 10 mm x 10 mm grid was overlaid on the selected sections under the optical microscope. Each square of the grid was numbered and examined thoroughly under the microscope. After positioning the section to capture the selected square for fibre

counting, the grid was removed. The light intensity and the position of the microscope lens were adjusted in order to achieve the most vivid image of the examined square of the grid, marking with white spots all the points where fibres appeared in the square. The rest of the area of the examined square without any fibres was painted black on the obtained image. A CCD camera coupled with a 80 mm optical lens was used to acquire the image. This image was processed by appropriate image analysis software (Leica Quantimet 500), which finally categorised the fibres by taking an average of four measurements to determine their equivalent diameter and this value was placed in the appropriate range. The ranges selected were based on the fibre diameter (0.16 mm) and were set as 0.16-0.32 mm, 0.32-0.48 mm, etc. The range between 0-0.16 mm was omitted. The smallest possible fibre image that can be seen after cutting (which corresponds to a fibre that is perpendicular to the cutting section) is 0.16 mm, irrespective of the angle at which the fibre is embedded in the matrix. Therefore, whatever is captured as having an equivalent diameter smaller than 0.16 mm does not correspond to a fibre; and the inclusion of the range 0-0.16 mm would lead to a significant overestimation of the counted number of fibres. For this reason, there is no point in increasing the resolution of the image. This procedure was repeated for the whole grid overlaid on each selected section. Thereafter, the number of fibres per cm^2 was calculated and appropriate contour plot software (MATLAB 6.5) used for the creation of the contour plots for each section, for comparison with the corresponding contour plots obtained from the CT scanner.

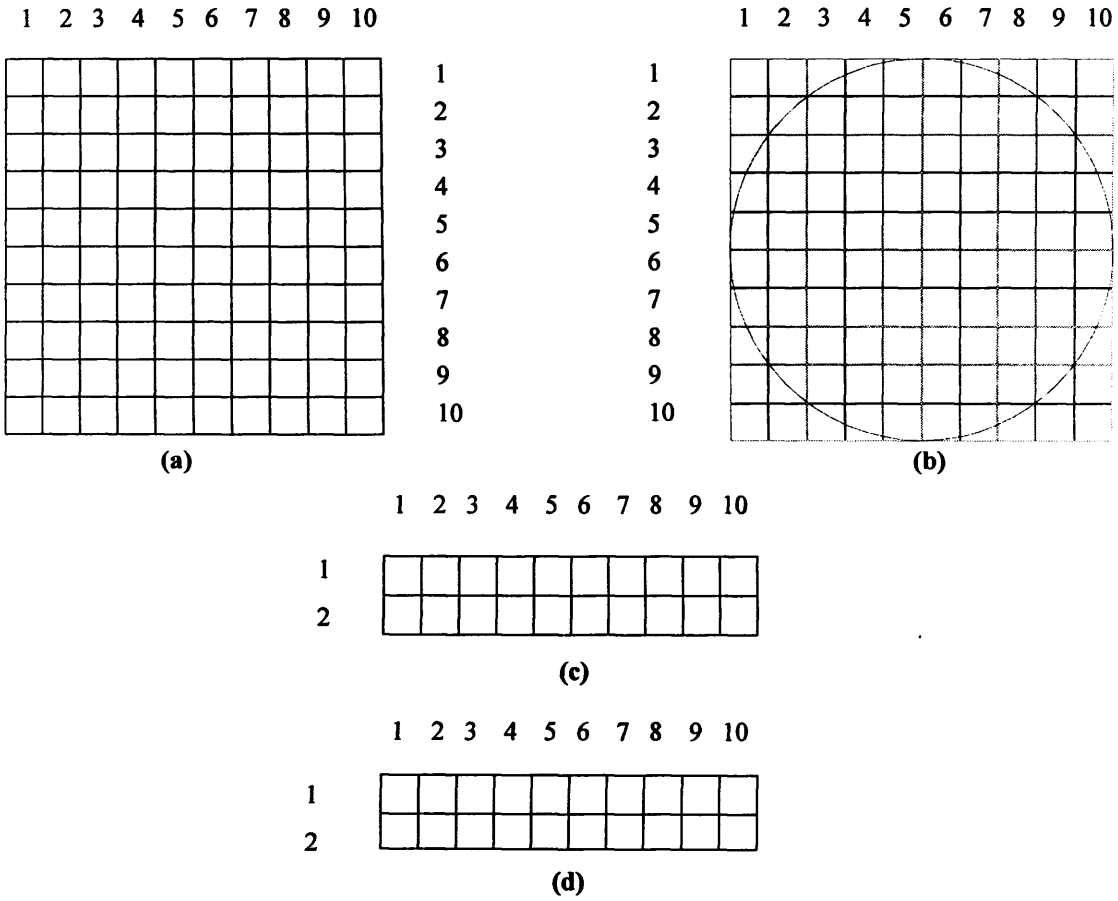

Figure 7.2: 10 mm x 10 mm grids used for image analysis. (a) 100 mm x 100 mm beam, (b) 100 mm diameter cylinder, (c) 20 mm thin strip and (d) 16 mm thin strip (grid in row 2 is only 6 mm x 10 mm).

7.3.1 Optical microscope results

Table 7.1 summarises the average numbers of fibres (/cm^2) that were counted under the optical microscope, for the several specimen configurations and sections under consideration. The number of fibres is calculated by multiplying the number of recorded events in the 0.16-0.32 range by one, the number of events recorded in the next higher range (0.32-0.48) by two (two fibre diameters), and so on. From the number of fibres so calculated the average number of fibres per cm^2 for each section was calculated.

Table 7.1: Average number of fibres resulting from image analysis of specimen sections.

	Average Number of Fibres (/cm^2)
16mm Strip – Slice 2	132
16mm Strip – Slice 22	157
20mm Strip – Slice 3	128
20mm Strip – Slice 20	178
100x100mm Beam – Slice 2	173
100x100mm Beam – Slice 18	172
100mm Cylinder – Slice 3	125
100mm Cylinder – Slice 10	134
Average	**150**

7.3.2 Analysis of optical microscope results

From the known volume fractions of short (L = 6 mm) and long (L = 13 mm) fibres within CARDIFRC® Mix I, (4.5% and 1.5%, respectively), it is easy to work out the number of short and long fibres in a certain volume of the material. The diameter of both types of fibre is equal to d = 0.16 mm. Thus, the

Volume of 6 mm long fibre = $(\pi / 4) \times d^2 \times L = (\pi / 4) \times (0.16)^2 \times 6 = 0.1206$ mm^3
Volume of 13 mm long fibre = $(\pi / 4) \times d^2 \times L = (\pi / 4) \times (0.16)^2 \times 13 = 0.2614$ mm^3

Number of 6 mm long fibres in 1000 mm^3 = (1000 x 4.5) / (100 x 0.1206) = 373
Number of 13 mm long fibres in 1000 mm^3 = (1000 x 1.5) / (100 x 0.2614) = 57

The number of short and long fibres that will theoretically be seen in one cut section (10 x 10 mm) of the particular volume of 1000 mm^3 is given by the theory of geometric probability or more precisely by the solution of the so-called *Buffon* problem in three dimensions (Solomon, 1978). Although the proof of the particular problem is beyond the scope of the current work, some basic points are described below. The original problem called "*the Buffon needle problem*" and is about the probability of a needle (line segment) of length l that is dropped "at random" on a set of equidistant parallel lines in a plane that are d units apart, $l \leq d$, intersecting a line. The problem is solved by considering a finite number of possible positions for the

needle as equally likely outcomes and then treating the limiting case as a representation of the problem. This includes a definition of randomness for the distance x of the needle's midpoint to the nearest line and the acute angle φ formed by the needle and a perpendicular from the midpoint to the line. The solution is obtained by computing the ratio of favourable outcomes to the total set of outcomes and passing to the limit.

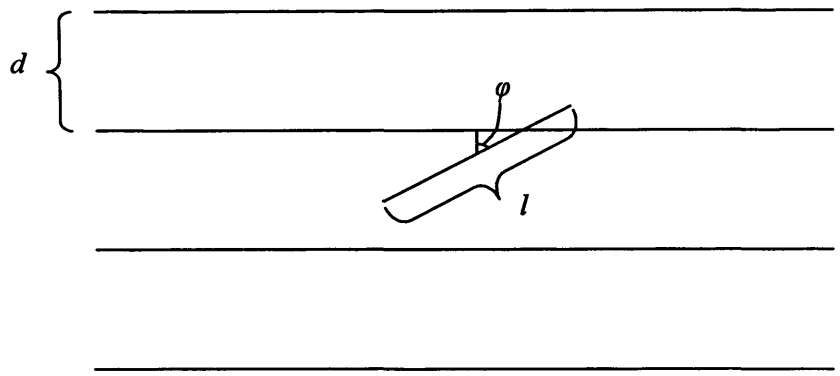

Figure 7.3: Buffon needle problem in two-dimensions.

Buffon's problem is also extended to those situations where the needle is larger than the shortest distance between grid lines, and therefore multiple intersections can be seen. However, a more general extension of the problem is the one provided by Morton (1966), who proved an important and remarkable result on the expected number of intersections and distribution of angles of intersections for a random set of rectifiable curves in the plane.

The three dimensional situation is the estimation of the volume–surface ratio of cells and this is very important since it can also serve to delineate some pathology, for example, cancerous versus non-cancerous cells. The method takes as its point of departure a result by Crofton (1885) which shows that if a line is repeatedly placed at random over a plane containing a closed figure, the average length of the chord $E(c)$ intersected by the figure will be:

$$\mathrm{E}(c) = \pi \frac{area}{perimeter}$$

no matter what the shape of the figure, as long as its boundary is a convex curve.

However, before this result could be employed for estimating volume-surface area ratios it required the following modifications:

1. it had to be made applicable to line segments;
2. a simple procedure for measuring chord length had to be found;
3. it had to be extended to cover non-convex figures (e.g. figures with re-entrant corners);
4. it had to be extended to provide an estimate not only of the area-perimeter ratio in the focal plane under observation but the volume-surface ratio in the three dimensions of which the observed focal plane is a two-dimensional representation.

The first three of these modifications were accomplished by a single device. A line of finite length, say r, was considered and the number of times each of the two end points fell in the interior of a plane figure was counted. This number was denoted by $E(h)$ for hits and the number of times the line intersected the perimeter of the figure was denoted by $E(c)$ for cuts. Then, in a very large number of throws it will be found that

$$r\frac{E(h)}{E(c)} = \pi\frac{area}{perimeter}$$

for all closed figures including the non-convex ones.

The fourth and important modification was provided by a mathematical result. When a line of length r is placed at random in three-dimensional space containing a closed figure, for a very large number of throws it may be shown that

$$r\frac{E(h)}{E(c)} = 4\frac{volume}{surface \cdot area}$$

This result satisfied condition 4. Since placing a line at random in three dimensions could be shown to be formally equivalent to placing a plane at random in three dimensions and placing the line at random on the resulting two-dimensional plane section.

If the space contains a series of figures of different volumes and surfaces, then

$$r\frac{E(h)}{E(c)} = 4\frac{sum \cdot of \cdot volumes}{sum \cdot of \cdot surface \cdot areas}$$

Here *E(h)* is the number of hits, i.e. the number of times each of the two end points of the line fall in the interior of the plane closed figure and *E(c)* is the number of times the line intersects the perimeter of the figure. As in two dimensions, this result applies irrespective of whether the closed figure is convex or not.

We shall use the above theoretical result to calculate how many fibres of 6 mm and 13 mm length would be cut by a plane section if we considered three different cubes of side 5, 10 and 20 mm:

1. 5x5x5 mm Cube

According to the *Buffon's* problem solution: $r\frac{E(h)}{E(c)} = 4\frac{volume}{surface \cdot area}$

For 6 mm fibres: $6\frac{E(h)}{E(c)} = 4\frac{125}{6\times 25} = \frac{10}{3}$ Therefore, $E(h) = \frac{5}{9}E(c)$

As the total number of 6 mm fibres in a 5 mm cube = 373/8, i.e. $E(h) + E(c) = 47$

We have that the total number of 6 mm fibres cut by a 5x5 mm section is $E(c) = 30$.

For 13 mm fibres: $13\frac{E(h)}{E(c)} = 4\frac{125}{6\times 25} = \frac{10}{3}$ Therefore, $E(h) = \frac{10}{39}E(c)$

As the total number of 13 mm fibres in a 5 mm cube = 57/8, i.e. $E(h) + E(c) = 7$

We have that the total number of 13 mm fibres cut by a 5x5 mm section is $E(c) = 6$

Thus, the total number of fibres cut by a 5x5 mm grid in a 5 mm cube is $E(c) = 30 + 6 = 36$

Giving the **Total Number Cut = 144/cm^2**

2. 10x10x10 mm Cube

According to the *Buffon's* problem solution: $r\frac{E(h)}{E(c)} = 4\frac{volume}{surface \cdot area}$

For 6 mm fibres: $6\frac{E(h)}{E(c)} = 4\frac{1000}{6\times100} = \frac{40}{6}$ Therefore, $E(h) = \frac{10}{9}E(c)$

As the total number of 6 mm fibres in a 10 mm cube = 373, i.e. $E(h) + E(c) = 373$

We have that the total number of 6 mm fibres cut by a 10x10 mm section is $E(c) = 177$.

For 13 mm fibres: $13\frac{E(h)}{E(c)} = 4\frac{1000}{6\times100} = \frac{40}{6}$ Therefore, $E(h) = \frac{20}{39}E(c)$

As the total number of 13 mm fibres in a 10 mm cube = 57, i.e. $E(h) + E(c) = 57$

We have that the total number of 13 mm fibres cut by a 10x10 mm section is $E(c) = 38$

Thus, the total number of fibres cut by a 10x10 mm grid in a 10 mm cube is $E(c) = 177 + 38 = 215$

Giving the **Total Number Cut = 215/cm^2**

3. 20x20x20 mm Cube

According to the *Buffon's* problem solution: $r\frac{E(h)}{E(c)} = 4\frac{volume}{surface \cdot area}$

For 6 mm fibres: $6\frac{E(h)}{E(c)} = 4\frac{8000}{6\times400} = \frac{40}{3}$ Therefore, $E(h) = \frac{20}{9}E(c)$

As the total number of 6 mm fibres in a 20 mm cube = 2984, i.e. $E(h) + E(c) = 2984$

We have that the total number of 6 mm fibres cut by a 20x20 mm section is $E(c) = 926$.

For 13mm fibres: $13\frac{E(h)}{E(c)} = 4\frac{8000}{6\times 400} = \frac{40}{3}$ Therefore, $E(h) = \frac{40}{39}E(c)$

As the total number of 13 mm fibres in a 20 mm cube = 456, i.e. $E(h) + E(c) = 456$

We have that the total number of 13 mm fibres cut by a 20x20 mm section is $E(c) = 225$

Thus, the total number of fibres cut by a 20x20 mm grid in a 20 mm cube is $E(c) = 926 + 225 = 1151$

Giving the **Total Number Cut = 288/cm^2**

According to the calculations made above, the number of fibres that are expected to be cut per cm^2 increases with the increase of the dimensions of the sample specimen. In the special cases examined here, where the sample specimens are cubes, the increase seems to be relatively constant. More specifically, while the number of fibres cut per cm^2 is 144 for a 5x5x5 mm cube, the corresponding numbers are 215 and 288 for 10x10x10 mm and 20x20x20 mm cubes respectively. It can be noticed that the number of cuts per cm^2 increases approximately by 70 when the volume of cube is increased eightfold. This conclusion, however, has to be verified both theoretically and practically with more examples, in order to be used extensively.

The average number of fibres counted under the microscope (150/cm^2) is smaller than the theoretical number of fibres that is expected to be seen in the cut surface (215/cm^2), according to the known volume fraction of fibres within the mix. This lower number is, however, reasonable and expected for several reasons. First, as the specimen sections were cut using a 3 mm thick blade, the fibres in the cut sections that were embedded less than 3 mm in the matrix would simply fall out during the

cutting process. This would particularly be the case with short fibres 6 mm long. Second, the image analyser would not account for fibres lying in the cut section or those which were in this plane prior to cutting. Third, there are uncertainties in the image analysis count. These will be discussed later.

The same sections of the same specimens mentioned above, had also been examined earlier under the same optical microscope, by Benson (2003), using a 20x20 mm grid. The average number of fibres counted was 270/cm^2, which is considerably higher than the corresponding one from the 10x10 mm grid (150/cm^2). The number derived from the 10x10 mm grid is much closer to the actual number of fibres in the section and this was verified visually by counting the number of fibres in selected, representative positions in the sections. The higher number of fibres measured using the 20x20 mm grid is attributed to the fact that features with an equivalent diameter lower than the diameter of a single fibre were also counted (the range 0-0.16 mm was included). However, these features obviously do not correspond to fibres, as was previously argued.

7.4 COMPARISON OF CT IMAGING AND IMAGE ANALYSIS RESULTS

In order to check the degree of correlation between the images produced from the non-destructive CT imaging and the results obtained from the optical microscope after the cutting of the specimens, contour plots of the fibre count in the cut sections were produced, using appropriate software. The contour plots from the CT imaging were produced using SURFER 8 and the contour plots from the image analysis (10 mm x 10 mm mesh grid) were produced using MATLAB 6.5. After a careful examination of the contours from the two methods, it can be clearly observed that a reasonable correlation exists between them. This is encouraging, since it reveals that both the destructive and non-destructive methods can be used with confidence for the fibre distribution evaluation of fibre reinforced concrete specimens. Therefore, the selected method depends only on the special characteristics of each method (destructive or non-destructive) and on general considerations (cost, time, etc.).

The CT imaging results for the beam sections (Figure 7.5) show that there is a generally uniform distribution of fibres. However, there is a lower density around the perimeter of the sections, as indicated by the light spots that correspond to lower X-ray absorption density. In slice 2, which is very close to the side wall of the mould, it is noticed that the lower part of the section, which corresponds to the part towards the mould face, has a lower density (below 2000 Hounsfield units). This is very important, since this part of the beam can be easily subjected to tension, and a lower number of fibres can be a clear reason for a crack to be effortlessly initiated. Light spots also appear in the top corners, the outer limits of the vertical sides of the section and also in the interior of the section. They are not, however, predominant (about 2500 Hounsfield units) and they do not change the general impression of uniformly distributed fibres within the section. The picture obtained from image analysis of the same section (Figure 7.9) is very similar to that from CT scanning. The darker spots at the bottom of the section contain a lower number of fibres (below160 fibres) and mostly confirm the picture obtained from CT scanning. Figure 7.9 also shows the spots with lower number of fibres appear in the top corners, the outer limits of the vertical sides of the section and also in the interior of the section, thus confirming the CT imaging data.

Slice 18 is closer to the centre of the beam, far away from the side walls of the mould. A careful examination of both the CT imaging and the image analysis contours reveals that the top part of the section, which corresponds to the part near the cast face, has a lower density (below 2000 Hounsfield units). This is the predominant patch with a lower density in the particular section, and it seems to be almost identical to the picture seen in lower part of slice 2 of the same beam, which corresponds to the part towards the mould face. As it was noticed for the lower part of slice 2, it also applies here that this is of high significance, since this part of the beam can be subjected to tension and a crack to be straightforwardly initiated. The correlation between the two techniques (i.e. between the two contours) is also validated in the other parts of slice 18. Spots of lower fibre density also appear in the bottom corners, the outer limits of the vertical sides of the section and also in the interior of the section. The general impression of uniformly distributed fibres within the section is however undiminished.

Both of the cylindrical slices (3 and 10) have very similar pictures which indicate that the distribution of fibres in those two sections is not fairly uniform. This is evidently supported by the major yellow patches (lower density) in the interior of the cylindrical sections, as it can be seen from the CT imaging contours. This is additionally confirmed by visual inspection of the sections after cutting, where it appears that at these patches correspond areas with very low number of fibres and some voids. According to Benson (2003) who cut the specimens right after their CT scanning, at these areas was also observed unhydrated material, which implies poor compaction during the casting process. All these remarks were also made on the corresponding contour plots produced from the image analysis of the two cylindrical slices. As it can be visibly noticed, the positions and the areas covered by the dark patches that correspond to areas with fewer fibres are reasonably correlated to the regions with low X-ray absorption (yellow patches). This is a proof of the reasonable link between the destructive and non-destructive methods used.

The contour plots for the 16 mm thick strips (Figure 7.7) produced from the CT imaging of the sections point out a lower concentration of fibres near the cast faces of the sections, especially in the case of slice 2, which is very close to the side wall of the mould. These sections are clearly marked by the yellow patches (low density), which start from the cast face of the sections and run through the interior. The image of fibre distribution is slightly improved in the case of slice 22, which is closer to the centre of the strip and is far from the side wall of the mould. The contour plots for the 16 mm thick strips produced from the image analysis of the two slices (Figure 7.11) illustrate clearly the poor distribution of fibres and the lower fibre concentration near the cast faces of the strip and the progressive running of these areas through the interior of the sections.

In the case of the 20 mm thick strips, it is also observed that the fibre distribution is not uniform. Both slices have a low fibre density in the middle (large yellow patches), which are extended in large areas in the interior of the sections. The contour plots for the 20 mm thick strips produced from the image analysis of the two slices illustrate clearly the poor distribution of the fibres within these sections. However, the correlation achieved between the two methods in the case of the 20 mm thin strips is

not the best possible. Nevertheless, there are explanations for this discrepancy, which will be discussed in following section.

16mm Strip Slice 22

20mm Strip Slice 20

Beam Slice 2

Beam Slice 18

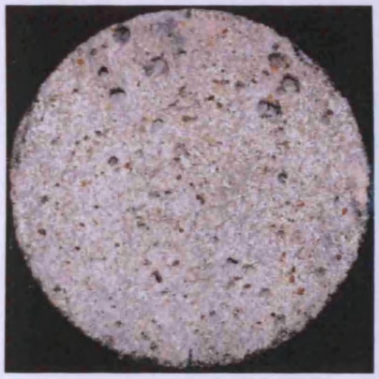

Cylinder Slice 3

Cylinder Slice 10

Figure 7.4: Pictures of CARDIFRC® specimen sections used for image analysis.

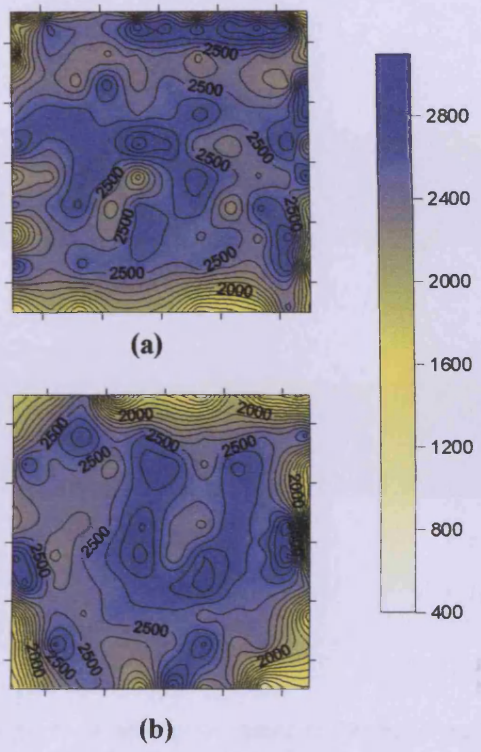

Figure 7.5: Contour plots showing the X-ray absorption densities for the beam cross-section (100 mm x 100 mm) for (a) slice 2 and (b) slice 18 (After Benson, 2003).

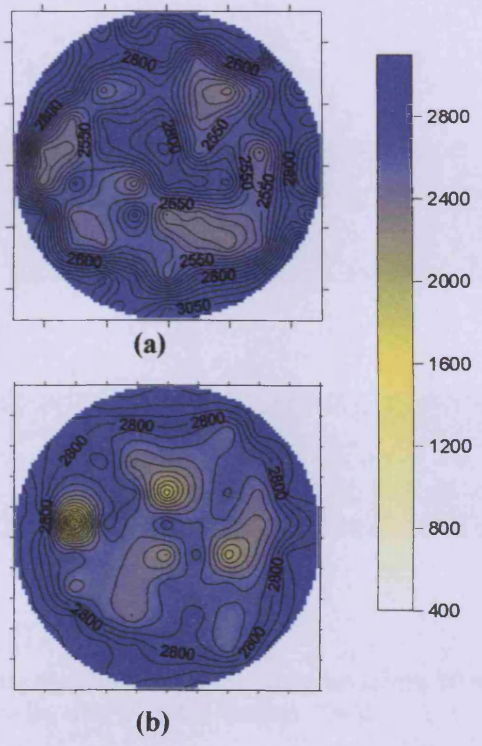

Figure 7.6: Contour plots showing the X-ray absorption densities for the cylinder (100 mm diameter) for (a) slice 3 and (b) slice 10 (After Benson, 2003).

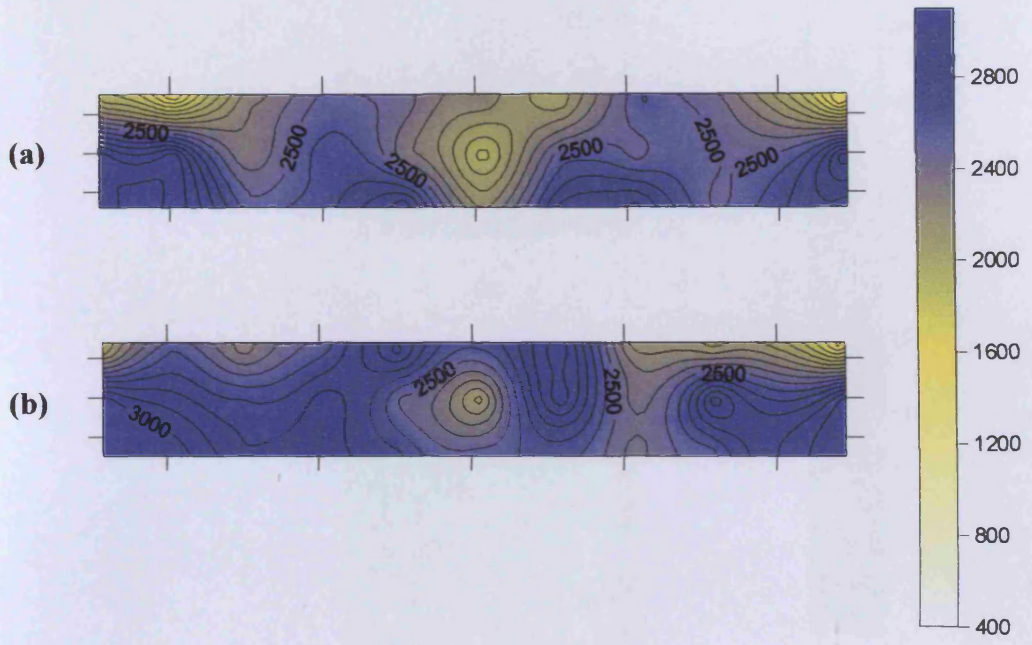

Figure 7.7: Contour plots showing the X-ray absorption densities for the 16 mm strip cross-section (100 mm width) for (a) slice 2 and (b) slice 22 (After Benson, 2003).

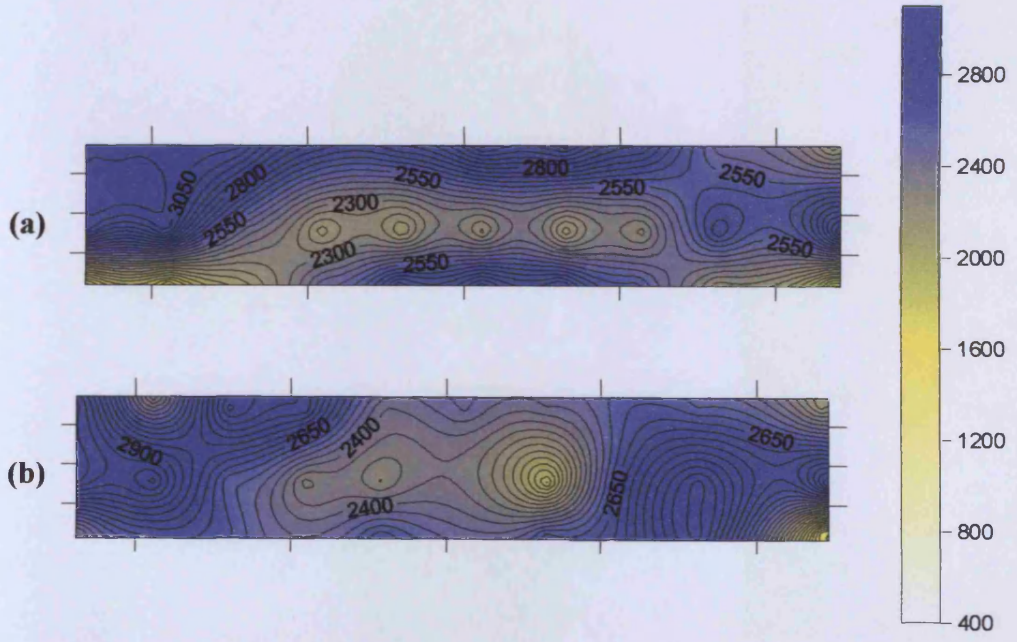

Figure 7.8: Contour plots showing the X-ray absorption densities for the 20 mm strip cross-section (100 mm width) for (a) slice 3 and (b) slice 20 (After Benson, 2003).

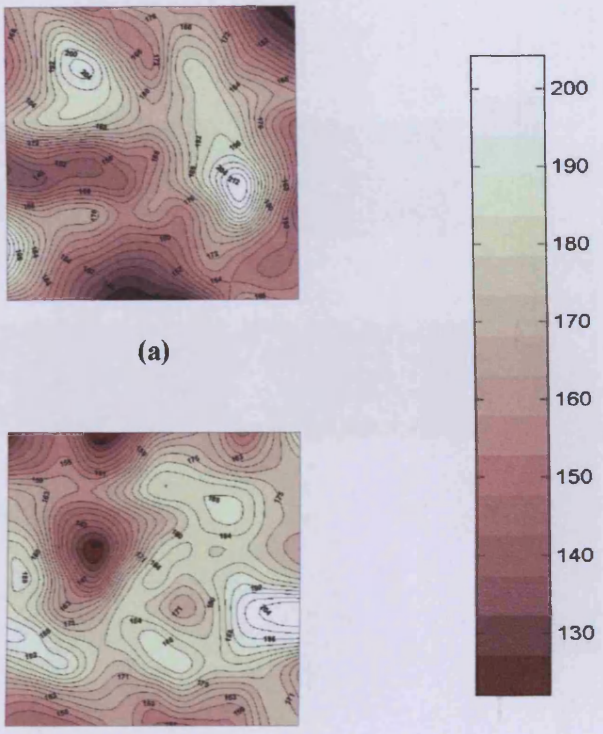

Figure 7.9: Contour plots showing the fibre distribution for the 100x100 mm beam cross-section for (a) slice 2 and (b) slice 18.

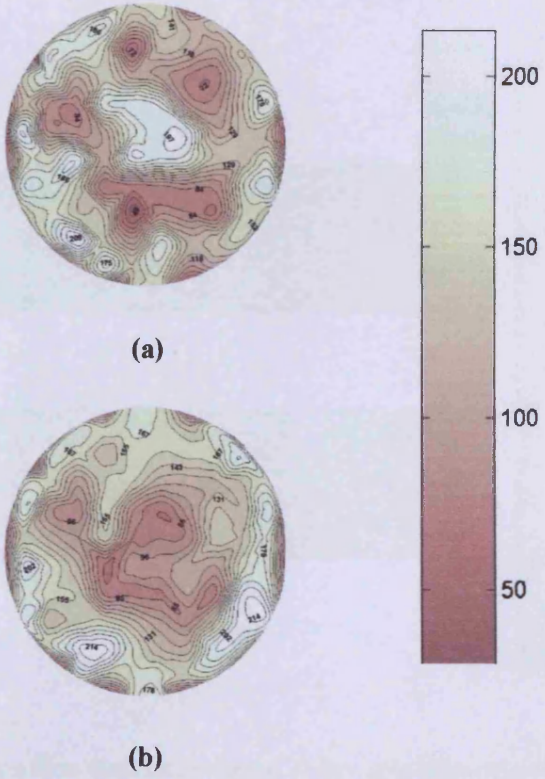

Figure 7.10: Contour plots showing the fibre distribution for the cylinder (100 mm diameter) cross-section for (a) slice 3 and (b) slice 10.

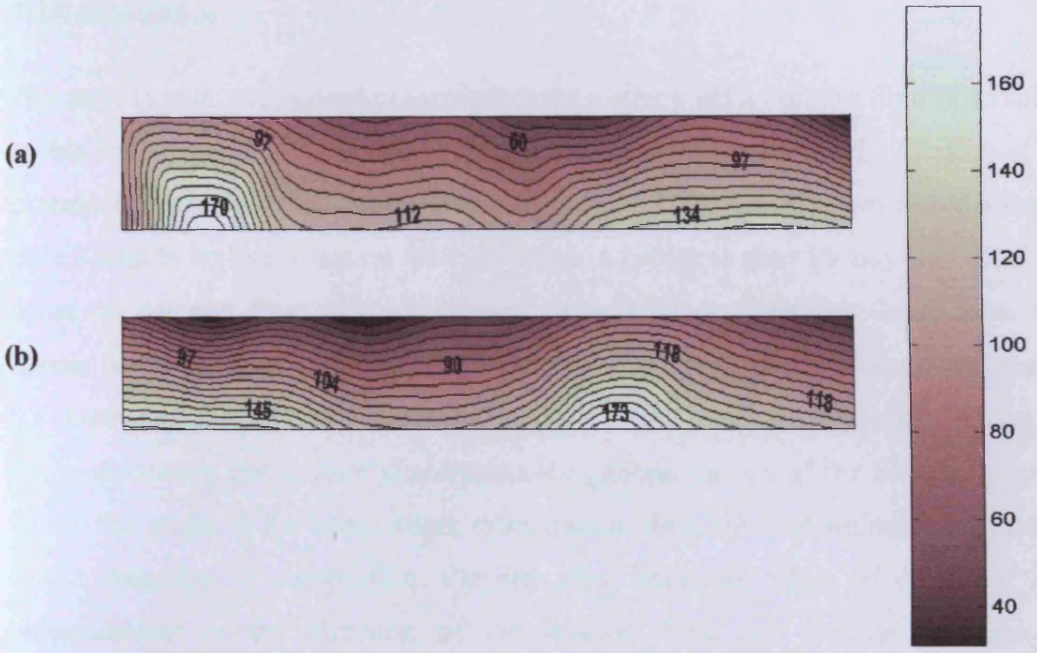

Figure 7.11: Contour plots showing the fibre distribution for the 16 mm strip cross-section (100 mm width) for (a) slice 2 and (b) slice 22.

Figure 7.12: Contour plots showing the fibre distribution for the 20 mm strip cross-section (100 mm width) for (a) slice 3 and (b) slice 20.

7.4.1 Discussion

The casting and compaction procedures have a strong effect on the fibre distribution within specimens. Furthermore, fibre distribution is influenced by the location of the examined section in the specimen. In the case of 100x100x500 mm beam fibres in slice 2 tend to be less dense on the mould face, whereas in slice 18 they tend to be less dense on the cast face of the specimen. In both beam slices less dense spots also appear in the corners, near the edges of the vertical sides of the sections and also in the interior of the section. However, the spots in the interior of the cross section are not predominant and cannot characterise the general picture of the fibre distribution within the slices of the beam under examination. Both slices examined were parallel to the direction of compaction. On the other hand, the slices of cylinders were perpendicular to the direction of compaction. This can provide a reasonable explanation for the significantly different pictures of the fibre distribution between the two types of specimen.

In the case of 100 mm diameter cylindrical specimen, the fibre distribution in the two slices is quite similar. In both slices the least dense spots appear in the centre of the sections, whereas the areas near the perimeter of each slice have a fairly high number of fibres. The inconsistency in the uniformity of the fibre distribution in cylindrical slices does not seem to be affected significantly by the distance from the cast or the mould face. One is given the impression that during compaction of cylindrical specimens fibres move towards the circumference of the circular sections. On the other hand, in the case of beams, it seems that fibres move in the opposite direction (i.e. towards the centre of the beam sections). However, this fibre movement is not as apparent, as in the case of cylindrical specimens. The smaller dimensions of the cylindrical specimens, in comparison to beams, might be a reason for the convenience of this migration.

Strips of 16 mm thickness reveal a lower concentration of fibres near the cast faces of the sections, which at some points runs progressively through the middle of the sections. It could be claimed that this is due to the fact that these slices are parallel to the direction of compaction, as it is argued above in connection with beams. However, it is believed that the very small thickness of these strips makes such a correlation

extremely uncertain and risky and other factors are involved, such as the float used to smooth the surface during casting. This may have the result the pushing the fibres, oriented perpendicular to the trowel, to the mould face of the specimen. In the case of the 20 mm thick strips, it is also observed that the fibre distribution is not uniform. Both slices have a low fibre density over a large area in the middle. The small thickness of the 16 mm strips gives rise to uncertainties regarding the reasons of poor fibre distribution.

As mentioned by Benson (2003), clustering of fibres (Figure 7.14) may result in a higher X-ray absorption reading relative to uniformly distributed fibres (Figure 7.13). Cluster is a set of points in the feature space where the local X-ray absorption density is large compared to the density at feature points in the surrounding region. When clustering is present in the fibres distribution, most fibres have at least one closest neighbour. Consequently, the nearest-neighbour distance is greatly reduced. In most cases, the variance as a measure of the uniformity of the spacing between clustered fibres is also reduced. This clustering phenomenon supports the suggestion that clustered set of fibres may result in a higher X-ray absorption reading, relative to uniformly distributed fibres. This, however, does not mean that the total number of fibres is higher.

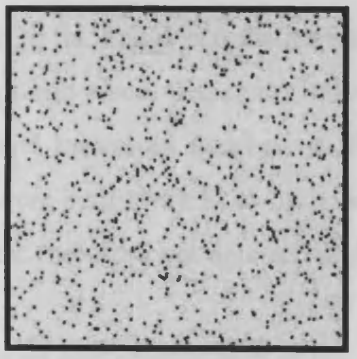

Figure 7.13: Uniform distribution of fibres.

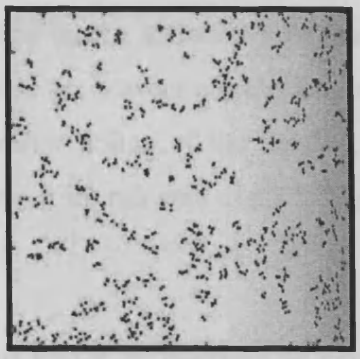

Figure 7.14: Clustered distribution of fibres.

In contrast to CT imaging, image analysis is concerned with making quantitative measurements of recognisable features in an image. The image analysis techniques require extraction of certain features that aid in the processing of the image under

consideration. Segmentation techniques are used to isolate the desired object features from the scene so that measurements can be made on it subsequently. Quantitative measurements of object features allow classification and description of the image. In the particular case under consideration, the image analysis was performed on cut sections of CARDIFRC® specimens, in order to quantify the number of fibres within each section. There are, nevertheless, many problems and uncertainties in this process, although it is a reliable, tried and tested procedure. In addition to the general problems and drawbacks of image analysis (e.g. noise), pointed out in the literature, some other problems were encountered during this project, which may to some extend have reduced the correlation between the destructive and non-destructive methods. These problems are now addressed.

Depending upon the shape of the fibre cluster, the object detected may be incorrectly interpreted by the software, leading to a wrong number of fibres. For instance, a batch of ten fibres oriented perpendicular to the section under examination will be correctly estimated, since the software will detect the equivalent of ten unit diameters of 0.16 mm. At the same time, a single fibre that lies parallel to or at a severe acute angle to the examined section, may be considered incorrectly as the equivalent of more than one fibres perpendicular to the section, leading to an overestimation of the actual number of fibres. This happened particularly near the edges of the specimen, where single fibres were bent away from the mortar matrix after cutting. Therefore, in addition to the image acquisition and its interpretation by the software used, a regular and thorough visual inspection was required to ensure the correct correlation between actual and measured number of fibres. In some other points of the section, fibres which were bent away from the mortar matrix were not illuminated at all by the light; they were therefore not detected and counted.

The perfect and precise shift of the specimen section under the microscope lens, from one measured grid to the next, without the fibres being double counted by the software is of crucial importance (Figure 7.15). Otherwise, the total number of fibres will be an overestimation of the actual or an underestimation in the case that a part of the section is not covered at all.

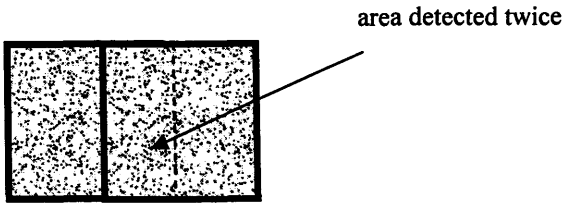

Figure 7.15: Specimen area detected twice during image analysis.

The light illumination over the section is one of the most sensitive parameters affecting the correct and reliable image detection. Even for grid boxes next to each other in the section, the light source has to be positioned carefully, in order to highlight all the fibres but not features (e.g. sand grains) which are not of interest to the study.

The sections of specimens used for image analysis were not identical to the sections scanned by CT scanner, since certain amount of material was lost during cutting. The thickness of the cutting blade was 3 mm, and therefore the loss of material was inevitable. As a result, the sections examined by the two techniques were not completely identical. This is one of the major reasons for some discrepancies between the obtained images from the two methods, although, as mentioned and proved earlier, the correlation is rather good. Moreover, during the cutting of specimens a large number of fibres are lost, since many short fibres are very likely to have small embedment lengths. At the same time, fibres lying in the direction of cutting will be detached from the plane and lost. In addition, more fibres are lost during cutting from the edges of specimen than from its centre, thus reducing the fibre count near the edges.

Cutting also loosened unhydrated cement-silica from the section together with any fibres. This was particularly evident near the centre of the specimens.

The last but not the least objective of this project was a possible correlation between the local X-ray absorption density, as it can be seen from contours produced after CT scanning of specimens, with the corresponding number of fibres as it is measured from the image analyser. For this purpose, contour plots of two beam and two cylinder sections have been plotted side by side in Figures 7.16-7.17. Moreover, the actual X-ray absorption densities at grid centres have been plotted against the fibre counts per grid for these sections in Figures 7.18-7.19. It is clear from these figures

that the X-ray absorption density correlates reasonably linearly with the fibre count in the thicker specimens, irrespective of their shapes.

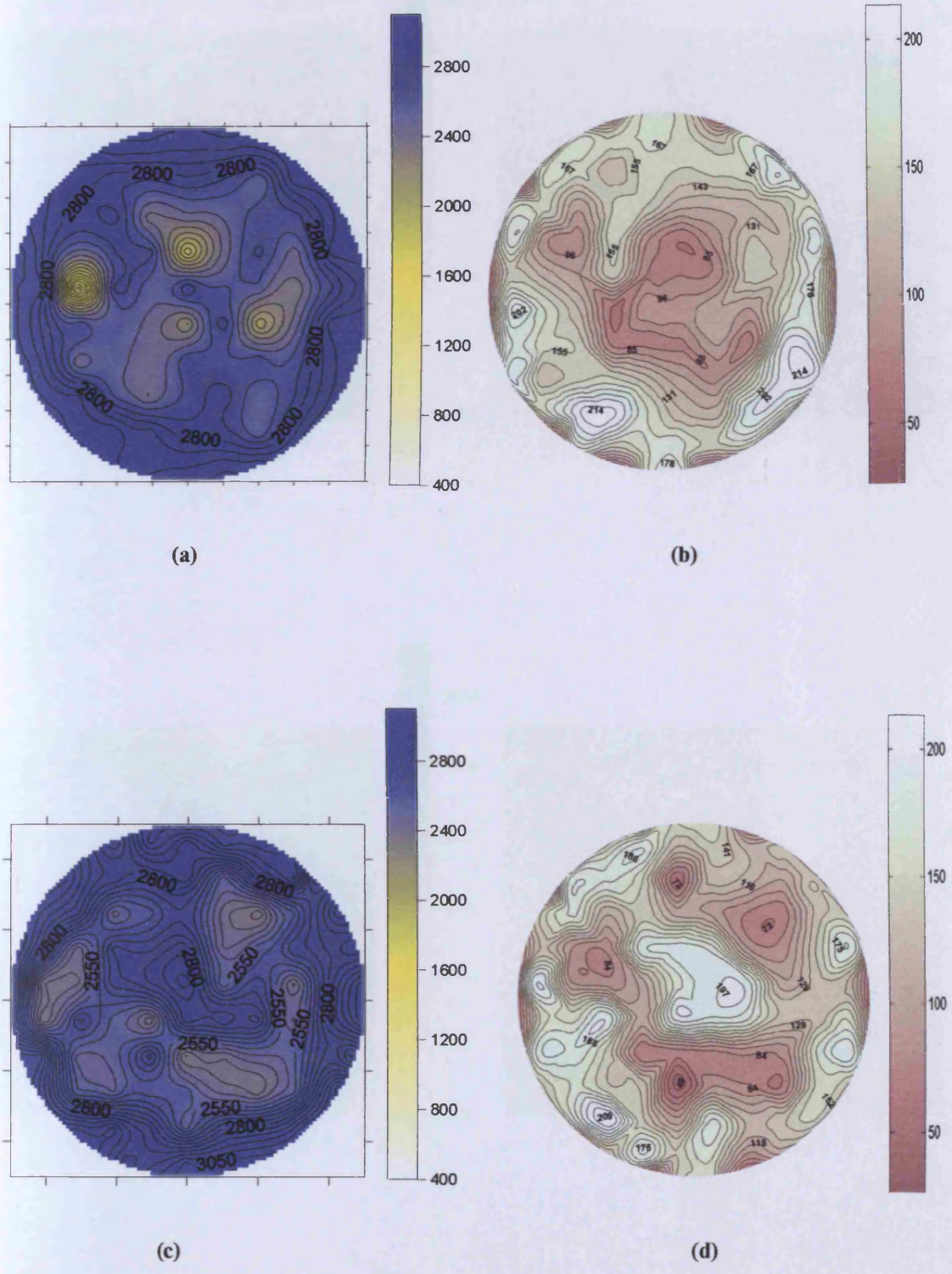

Figure 7.16: Contour plots showing the X-ray absorption densities (a) and (c), and the fibre count (b) and (d) for the cylinder slices 10 and 3, respectively.

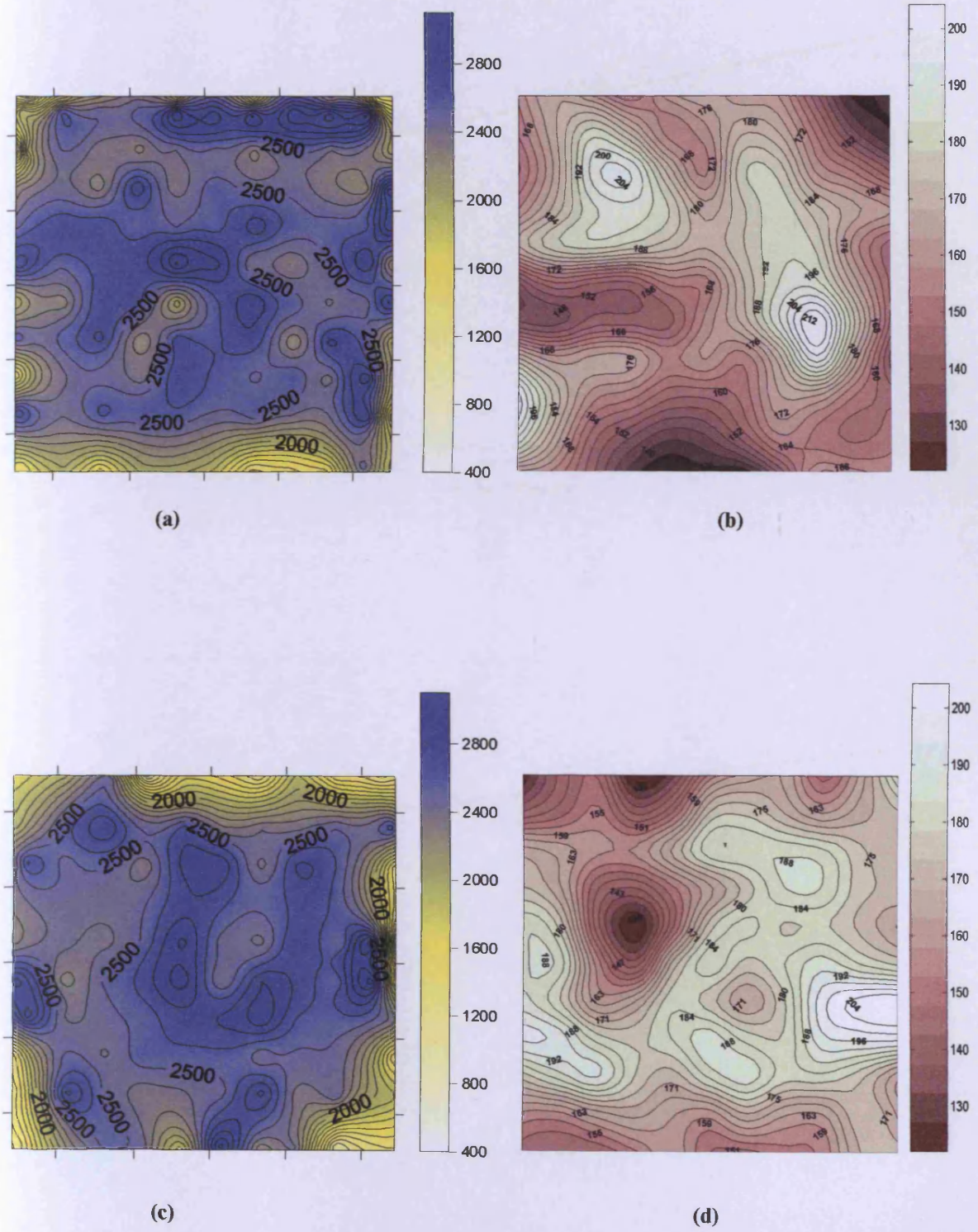

Figure 7.17: Contour plots showing the X-ray absorption densities (a) and (c), and the fibre count (b) and (d) for the beam slices 2 and 18, respectively.

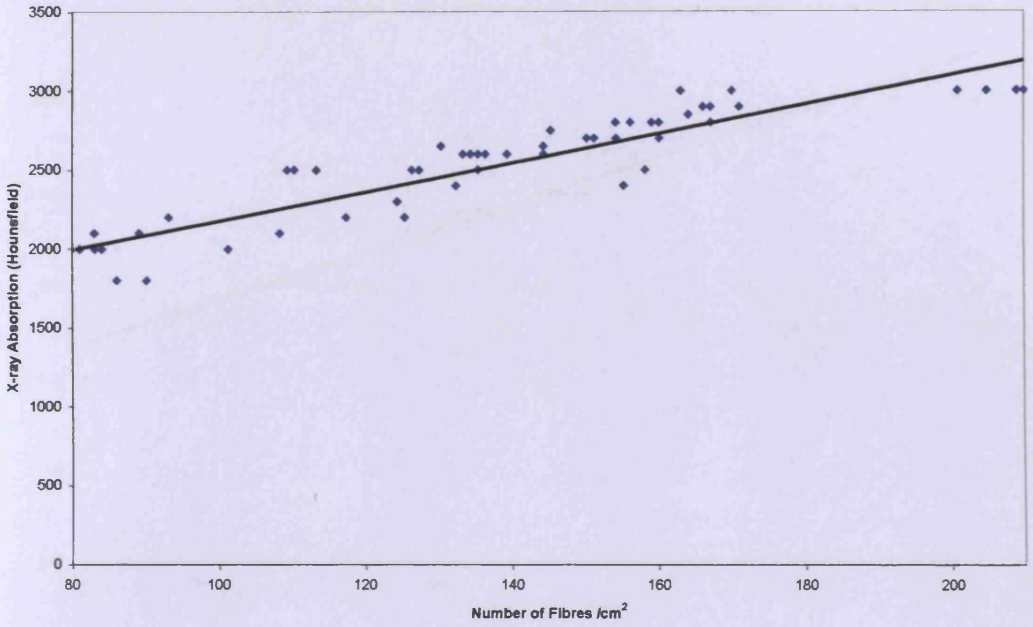

(a)

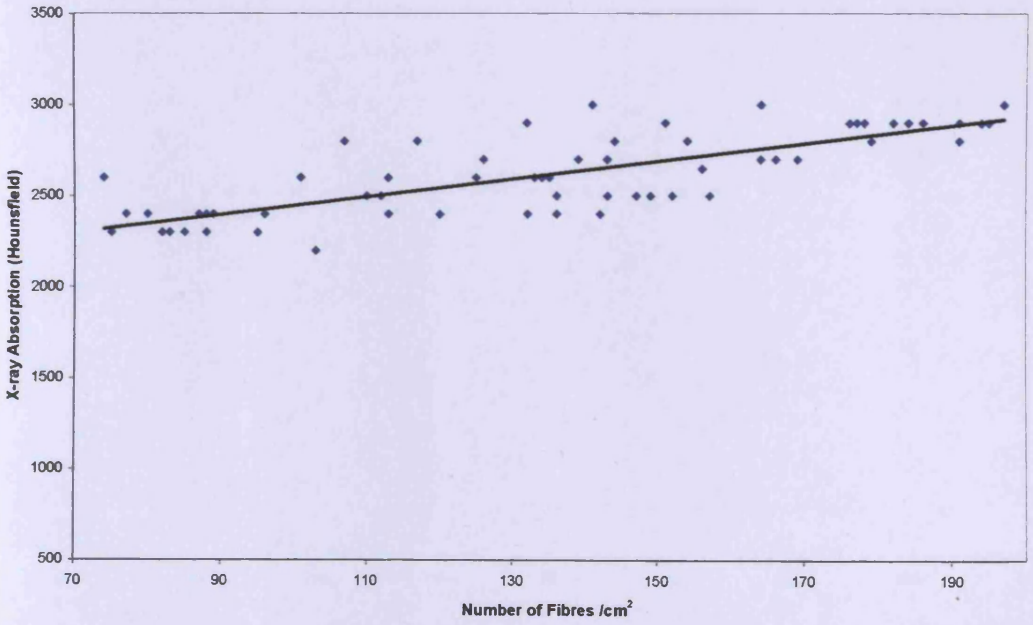

(b)

Figure 7.18: X-ray absorption density vs. number of fibres per cm^2 in (a) cylinder slice 10 and (b) cylinder slice 3.

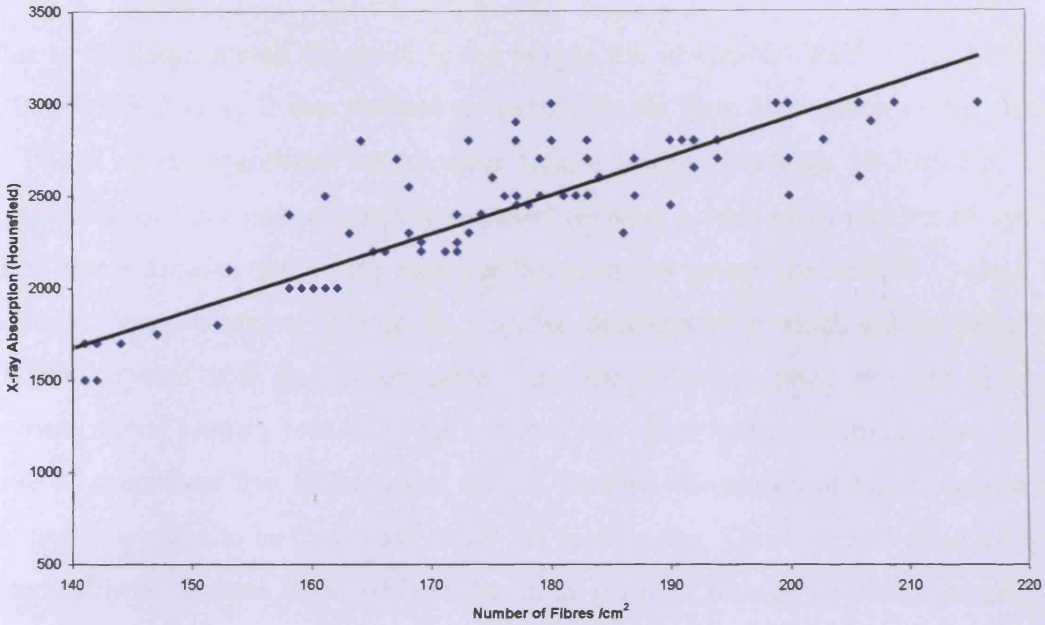

(a)

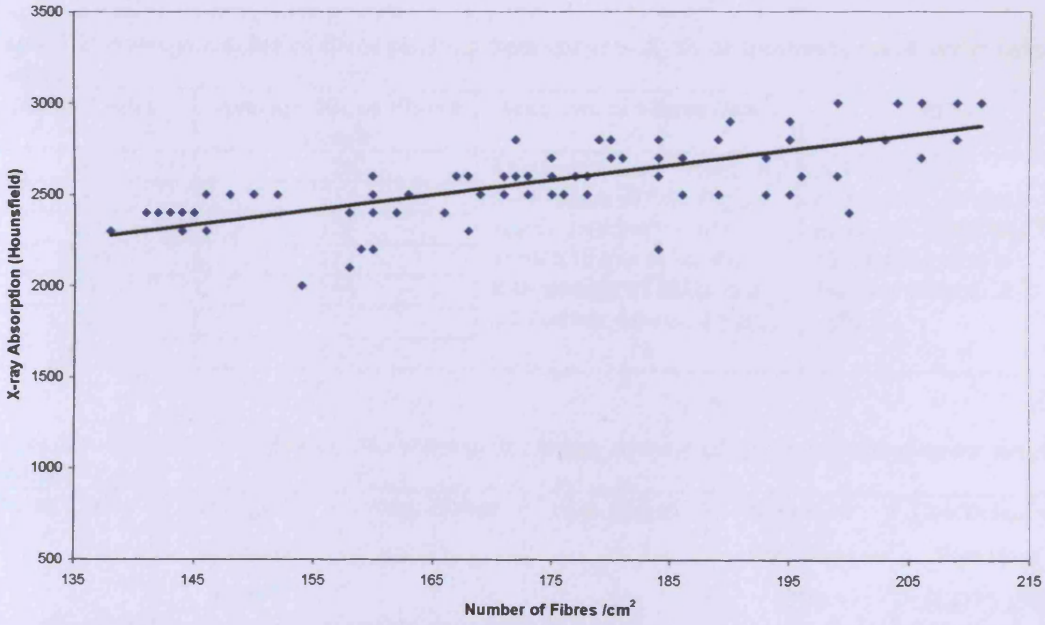

(b)

Figure 7.19: X-ray absorption density vs. number of fibres per cm^2 in (a) beam slice 2 and (b) beam slice 18.

7.5 FATIGUE SPECIMENS

Due to the large scatter observed in the fatigue life of CARDIFRC® - Mix I beams (100x100x500 mm), it was decided to investigate the fibre distribution in the planes of failure of six specimens tested under fatigue loading (between 10-70% P_u). The fatigue life of the selected specimens varied between a very small number of cycles (less than a decade) and a very high number of cycles (more than 500000 cycles). In addition, the distribution of fibres in a section of a specimen which did not fail after 1000000 cycles was also investigated. This particular specimen was cut along a predetermined section, located in the centre of the beam, using a diamond saw. In the case of specimens that failed under fatigue loading, the planes of failure had to be flattened in order to be examined under the microscope. This was also done using a diamond saw, as close as possible to the actual plane of failure. The exact number of cycles sustained by each of the selected specimens and the average number of fibres (/cm^2) resulting from the image analysis of their planes of failure are shown in Table 7.2. Other statistical measures are given in Table 7.3.

Table 7.2: Average number of fibres resulting from image analysis of specimens tested under fatigue loading.

No. of Cycles	Average No. of Fibres (/cm^2)	Max. No. of Fibres (/cm^2)	Notes
3	120	Theoretical result based on the solution of "*the Buffon needle problem*". For a 10x10x10 mm cube, the total number of fibres in a cut section, equals 215/cm^2.	All specimens (100x100x500 mm) made of CARDIFRC® - Mix I and tested in fatigue between 10-70% P_u.
4	116		
437	125		
5910	131		
110999	159		
527988	174		
>1000000	194		

Table 7.3: Statistical analysis of the results of the image analysis of specimens tested under fatigue loading.

No. of Cycles	Average No. of Fibres (/cm^2)	Max. Count	Min. Count	Standard Deviation (SD)	Coefficient of Variation (COV) (%)
3	120	215	5	70.30	61
4	116	215	5	66.02	55
437	125	215	28	58.89	47
5910	131	202	27	37.73	29
110999	159	212	72	28.32	18
527988	174	213	127	20.82	12
>1000000	194	215	138	14.54	7

The deduction from this investigation is that higher average number of fibres in the plane of failure result in an extended fatigue life of the specimen. The case of the specimen that sustained 4 cycles is an exception, since the average number of fibres is lower than the specimen sustained 3 cycles. It is, however, important that both specimens have an average number of fibres lower than that in the specimens that sustained higher number of cycles. All planes of failure examined have at least one grid where the maximum counted number of fibres is equal or very close to the theoretical maximum (resulting from the *"Buffon needle problem"*). On the other hand, the minimum count varies significantly between the selected specimens. This discrepancy is pictured clearly in the values of standard deviation and coefficients of variation. It is apparent that the decreased standard deviation, which means a more even distribution of fibres within the matrix, leads to a higher number of fatigue cycles. The same conclusion is also supported by the coefficients of variation, which also decrease as the fatigue life increases.

Specimens that sustained a very small number of cycles (3 and 4 cycles) have a very heterogeneous distribution of fibres in their planes of failure. It is easily recognisable that large areas of these sections have a significantly lower density of fibres, as indicated in Figures 7.20-7.23. The areas with lower density of fibres are located in both cases in the bottoms of the specimens. This is very important, since these parts of the beams were subjected to tension, and a lower number of fibres was a clear reason for a crack to be effortlessly initiated, resulting in extremely low fatigue life. Although the upper parts of these sections have a higher number of fibres, this was not sufficient to prevent the fast failure of these specimens. It has to be mentioned, that in some points the number of counted fibres was extremely small, less than ten (Table 7.3). The average number of fibres in these two sections is 118 (/cm^2).

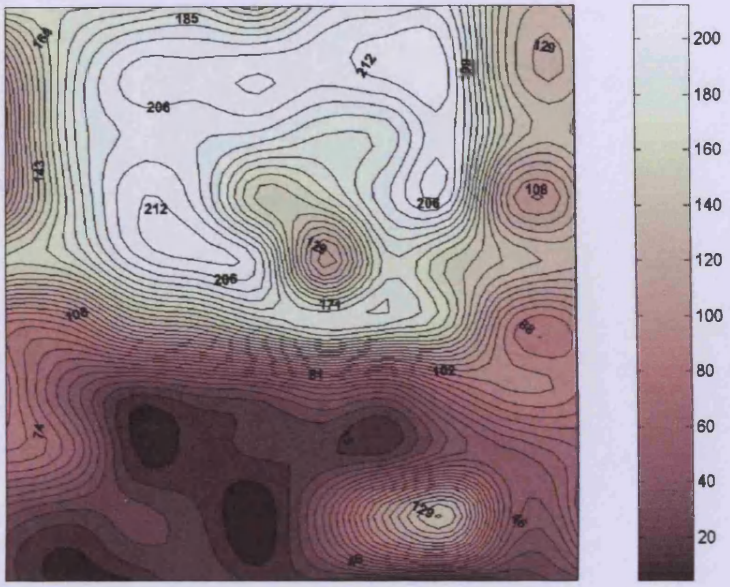

Figure 7.20: Contour plot showing the fibre distribution for the 100x100 mm beam plane of failure, after fatigue testing between 10-70% P_u (failure after 4 cycles).

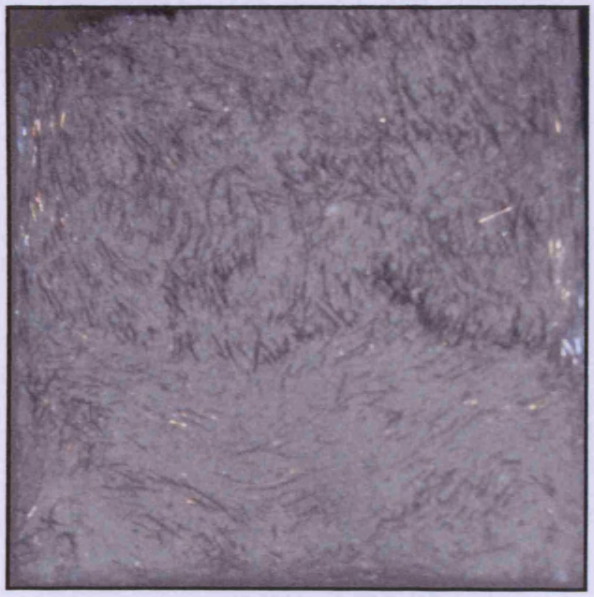

Figure 7.21: Plane of failure of the 100x100 mm beam after fatigue testing between 10-70% P_u (failure after 4 cycles).

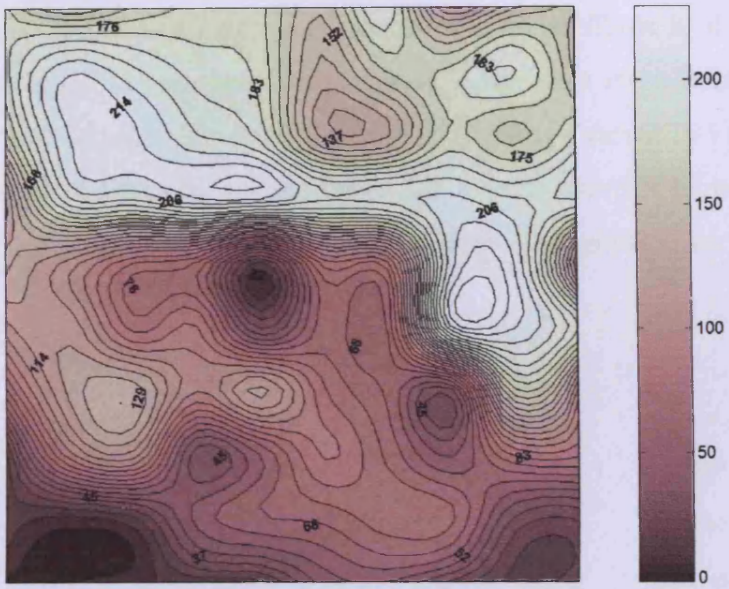

Figure 7.22: Contour plot showing the fibre distribution for the 100x100 mm beam plane of failure, after fatigue testing between 10-70% P_u (failure after 3 cycles).

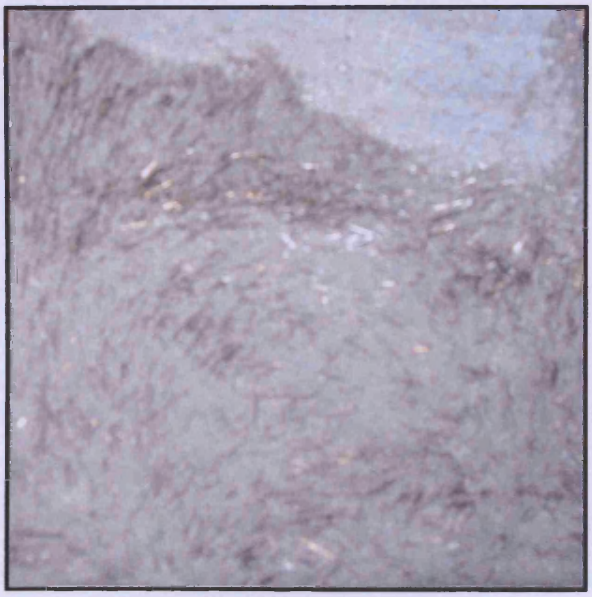

Figure 7.23: Plane of failure of the 100x100 mm beam after fatigue testing between 10-70% P_u (failure after 3 cycles).

The third specimen under investigation that sustained a slightly higher number of cycles (437 cycles) has also a heterogeneous distribution of fibres in the plane of failure. It is very apparent that three main regions, covering a large fraction of the total section, have a considerably lower density of fibres, as shown in Figure 7.24. The average number of fibres in this section is 125 (/cm^2), which is higher than the number of fibres counted in the sections of specimens that sustained lower number of cycles.

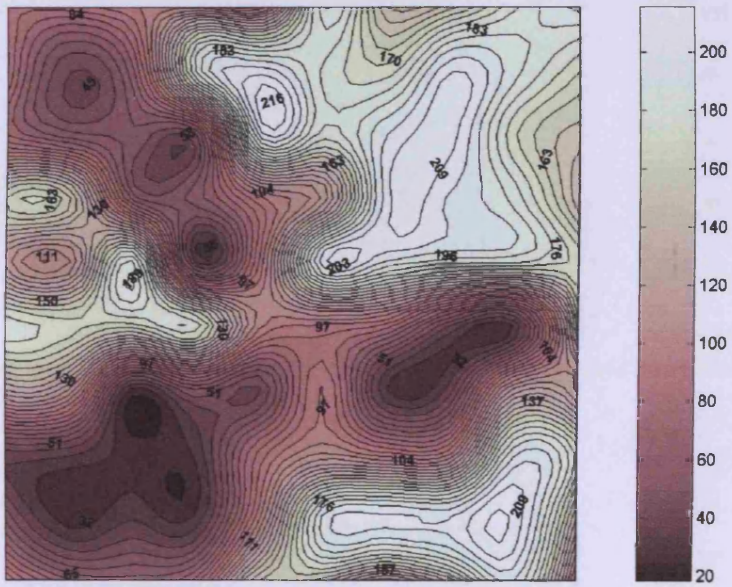

Figure 7.24: Contour plot showing the fibre distribution for the 100x100 mm beam plane of failure, after fatigue testing between 10-70% P_u (failure after 437 cycles).

The fourth specimen under investigation, which failed after 5910 cycles, has a generally uniform distribution of fibres in the plane of failure, apart from an area starting from the bottom of the beam and extending up to the centre, where the fibre concentration is noticeably lower (Figure 7.25). The average number of fibres in this section is 131 (/cm^2), which is higher than the number of fibres counted in the sections of specimens that sustained lower number of cycles.

Specimens that sustained significantly higher number of cycles (110999 and 527988), have a considerably higher number of fibres in their planes of failure (159/cm^2 and 174/cm^2, respectively) (Figures 7.26, 7.27). The distribution of fibres is also generally

even, with the exception of some areas with lower fibre concentration. It is believed that these areas facilitated the crack initiation and propagation within these sections.

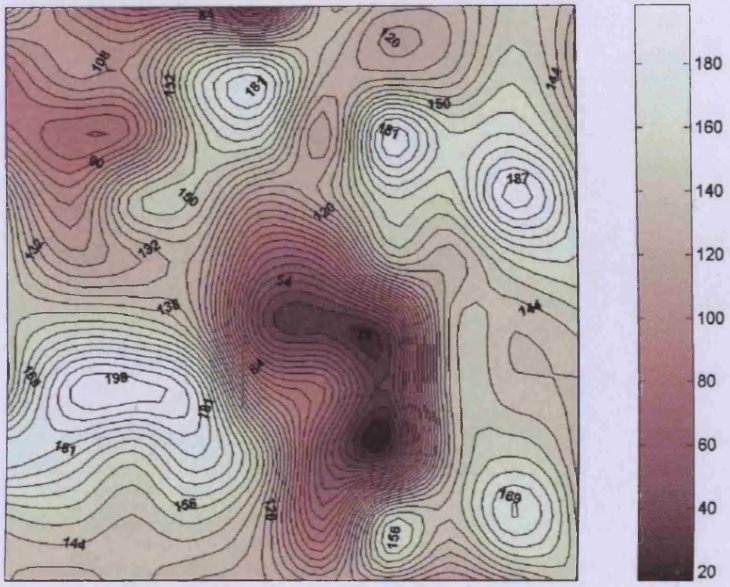

Figure 7.25: Contour plot showing the fibre distribution for the 100x100 mm beam plane of failure, after fatigue testing between 10-70% P_u (failure after 5910 cycles).

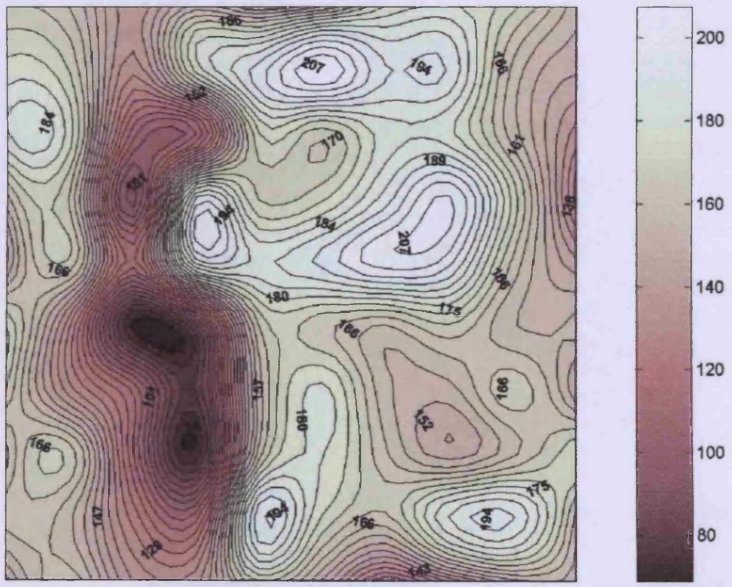

Figure 7.26: Contour plot showing the fibre distribution for the 100x100mm beam plane of failure, after fatigue testing between 10-70% P_u (failure after 110999 cycles).

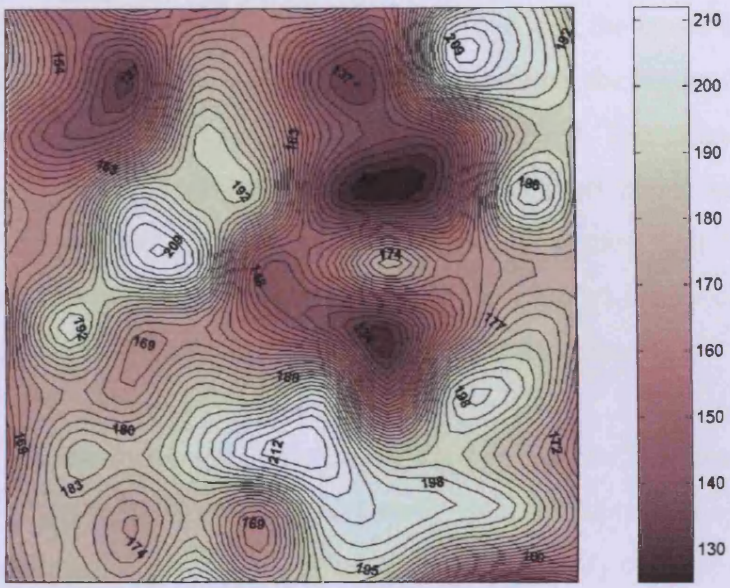

Figure 7.27: Contour plot showing the fibre distribution for the 100x100 mm beam plane of failure, after fatigue testing between 10-70% P_u (failure after 527988 cycles).

Finally, in the case of the specimen that did not fail after the application of 1000000 cycles, the even distribution of fibres is very characteristic, which in combination with the noticeably higher average number of fibres (194/cm^2), satisfactorily explains why the specimen did not fail during testing (Figure 7.28).

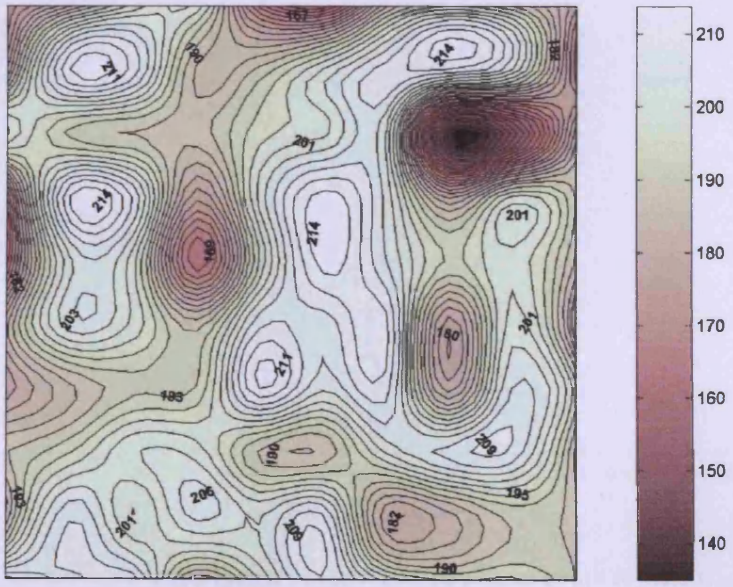

Figure 7.28: Contour plot showing the fibre distribution for the 100x100 mm beam plane of failure, after fatigue testing between 10-70% P_u (no failure after 1000000 cycles).

Considering that the theoretical maximum number of fibres per cm^2 (resulting from the *"Buffon needle problem"*) is 215, it can be concluded that the closer the number of fibres in the plane of failure is to the theoretical maximum, the higher the number of cycles will be sustained by the specimen (Figure 7.29). Theoretically, if the specimen is covered by the maximum number of fibres in every single section, then the fatigue life of the particular specimen will exceed 10^6 cycles. This conclusion, however, needs more investigation, since many other parameters are involved in the problem (e.g. fatigue life of fibres, bond between fibres and matrix, etc.).

This result is very important considering the existing correlation between the image analysis and CT-scanning analysis, presented earlier in this chapter. By applying the non-destructive method, the maps of the X-ray absorption density of the specimen can be produced. The magnitude of the X-ray absorption in the several areas of the section can lead to an estimate of the corresponding numbers of fibres in those areas (based on the correlation between X-ray absorption density and corresponding number of fibres), and therefore to an estimation of the expected fatigue life of the specimen.

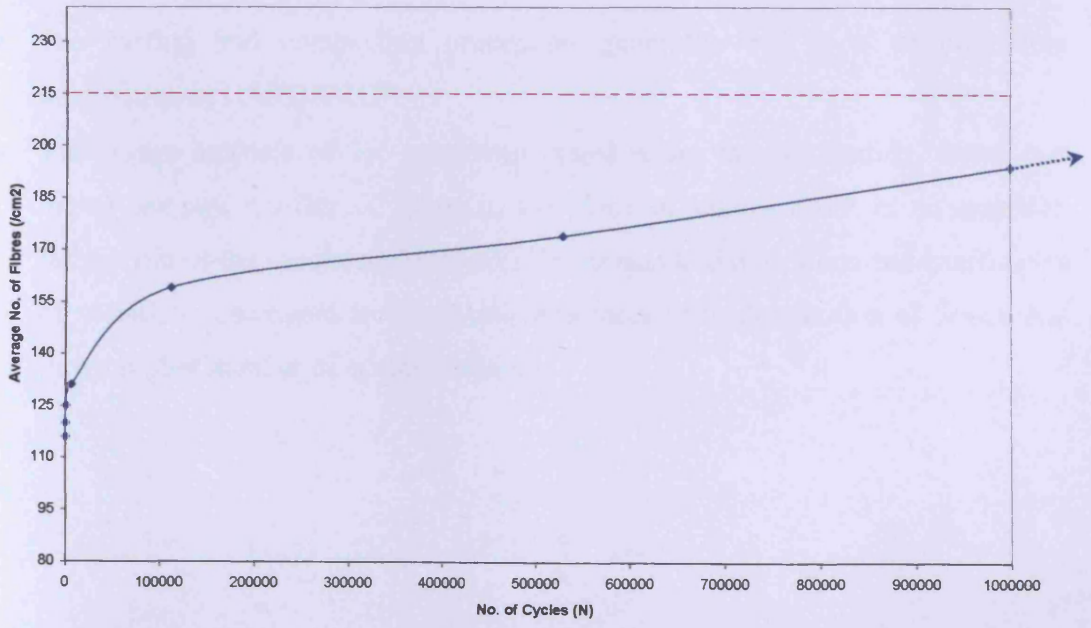

Figure 7.29: Relation between average number of fibres and number of cycles to failure.

7.6 CONCLUSIONS

From the image analysis work conducted in this project and from the CT imaging work done previously by Benson (2003), the following conclusions can be drawn:

- The contour plots of CARDIFRC® specimens obtained after applying the destructive and non-destructive techniques are in good agreement, revealing the section areas of higher and lower fibre densities.
- The achieved correlation for beams and cylinders is better than the one achieved for thinner strips. Possible reasons have been provided for this.
- Image analysis is a powerful tool. Despite its many deficiencies and the fact that is a destructive method, it can rapidly give objective results. It is strongly believed that the chosen grid of 10 mm x 10 mm is the optimum, since a finer mesh may not capture the larger features. However, the results of a 5 mm x 5 mm mesh grid would be interesting to study.
- In thicker sections the X-ray absorption density plots are reasonably linearly related to the actual fibre concentration. Thus the non-destructive CT imaging technique can be used to control the quality of products in a factory without the need of destructive testing.
- The casting and compaction procedures generally lead to a uniform fibre distribution in CARDIFRC®.
- The image analysis of the specimens tested under fatigue loading shows that higher average number of fibres in the plane of failure result in an extended fatigue life of the specimen. Moreover, lower standard deviations and coefficients of variation correspond to specimens with more even distribution of fibres, and thus a higher number of cycles to failure.

CHAPTER 8: MODELLING OF THE STATIC FLEXURAL RESPONSE OF CARDIFRC® BEAMS

8.1 FICTITIOUS CRACK PROPAGATION IN FIBRE-REINFORCED CONCRETE BEAMS

8.1.1 Introduction

The fictitious crack model proposed by Hillerborg et al. (1976) (Chapter 2) for the description of the softening behaviour of plain concrete has been widely accepted and used in the research community in the last two decades. This is due to the fact that this model is able to closely describe the fracture behaviour of concrete and because it gives a good explanation of many previously unexplained phenomena like e.g. the size effect. In recent years it has become widely recognised that the tensile behaviour of fibre-reinforced concrete (FRC) may be also described with the concepts of the fictitious crack model (Hillerborg, 1980). In the fictitious crack model it is assumed that, prior to crack initiation, the material exhibits linear elastic behaviour. After crack initiation it is assumed that stresses may be transmitted across the crack. The crack-bridging stresses are taken to be a function of the crack opening given by the stress-crack opening relationship. When the fictitious crack model is applied to plain concrete the stress-crack opening relationship is often modelled as a linear function. This is, however, too crude a model if the concrete has been reinforced by fibres. In order to capture the characteristics of the tensile behaviour of FRC the stress-crack opening relationship must be at least a bilinear function (Olesen, 2001).

The flexural failure of concrete beams may be modelled by the development of a fictitious crack in an elastic layer with a thickness proportional to the beam depth. This idea was presented by Ulfkjær et al. (1995) in the case of a linear stress-crack opening relationship. Olesen (2001) modelled the bending failure in the same way, using however a bilinear stress-crack opening relationship, in order to allow the modelling of FRC beams. Moreover, the analysis carried out by Olesen (2001) includes the effect of a normal force. Including a normal force in the analysis permits the application of the solution to, for example, column problems and problems characterised by built-in eigenstresses due, for instance, to a change of temperature.

The analysis of the crack propagation through the elastic layer is made without considering the overall beam behaviour. The elastic layer may be regarded as a nonlinear hinge for which the solution may be expressed in terms of the overall hinge deformation. Once the hinge behaviour has been established the hinge may be applied to different kinds of beam-bending problems, e.g., the three-point bending test or the transversely loaded beam on an elastic foundation (Olesen, 2001).

8.1.2 Cracked hinge model

The basic idea of the non-linear cracked hinge model is to isolate the part of the beam close to the propagating crack and model it as a short beam segment subjected to a bending moment and a normal force. Figures 8.1 and 8.2 show the typical three-point bend beam, geometry and deformation of the hinge element. The concept of the hinge views the crack as a local change in the overall stress and strain field. Therefore, the disturbance of the strain field, caused by the presence of the crack, is confined to take place between rigid boundaries and is assumed to vanish outside a certain band width, s (Figures 8.1 and 8.2). Each rigid boundary may translate and rotate such that it may be joined with an uncracked beam. Thus, outside of this band the structural element is modelled using the elastic beam theory.

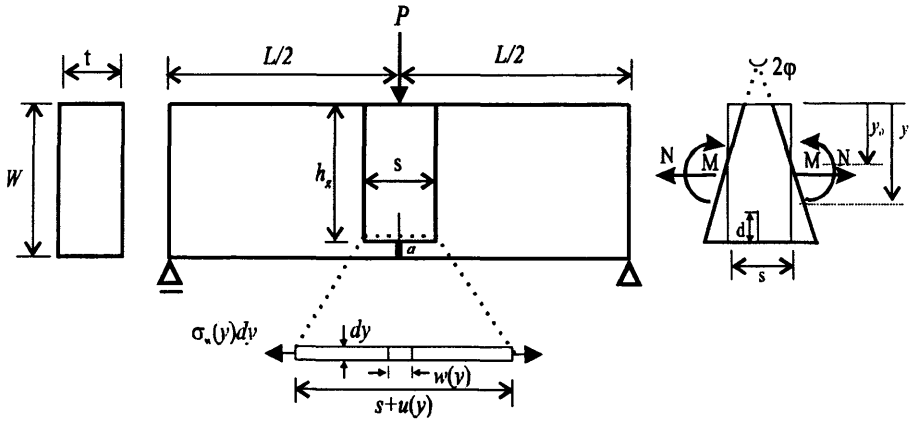

Figure 8.1: Three-point notched bend beam with a non-linear hinge modelling the propagation of a crack at mid-section, with the illustration of an incremental horizontal layer of the hinge shown below the beam. To the right: geometry of the hinge deformation.

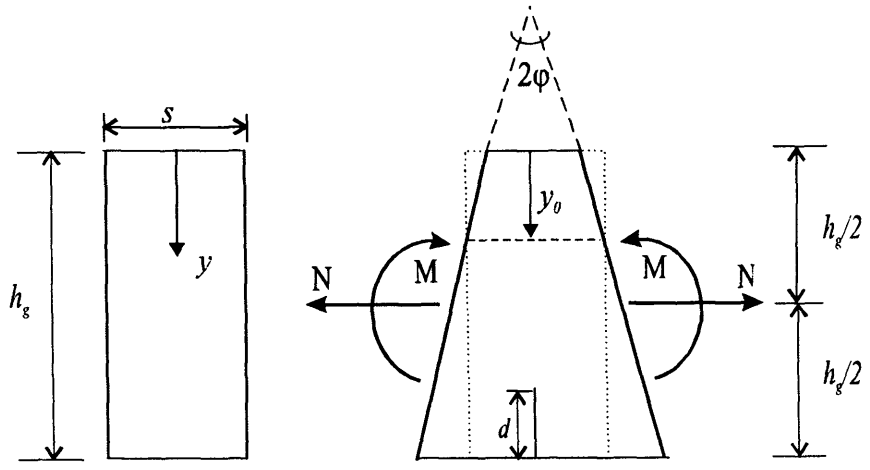

Figure 8.2: Geometry, loading and deformation of cracked hinge (After Olesen, 2001).

The constitutive relation for each segment inside the hinge is assumed to be linear elastic in the pre-cracked state, while the cracked state is approximated by a bilinear softening curve (Figure 8.3):

$$\sigma = \begin{cases} E\varepsilon & \text{pre-cracked state} \\ \sigma_w(w) = g(w)f_t & \text{cracked state} \end{cases} \tag{8.1}$$

where E = elastic modulus; ε = elastic strain; $\sigma_w(w)$ = stress-crack opening relationship; and f_t = uniaxial tensile strength.

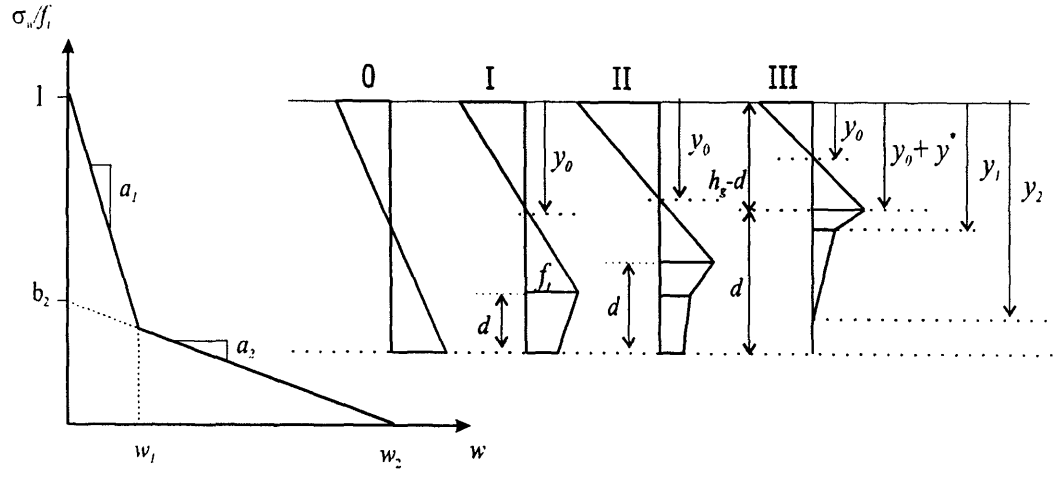

Figure 8.3: Definition of a bi-linear stress-crack opening relationship and the four different phases of crack propagation. Phase 0 = State of stress prior to cracking; Phases I-III = States of stress during crack propagation.

The shape of the stress-crack opening relationship is defined by the function $g(w)$ of the crack opening w, normalised so that $g(0) = 1$.

$$g(w) = b_i - a_i w = \begin{cases} b_1 - a_1 w & 0 \le w < w_1 \\ b_2 - a_2 w & w_1 \le w < w_2 \end{cases} \tag{8.2}$$

where $b_1 \equiv 1$, and the limits w_1 and w_2 are given by the intersection of the two line segments, and the intersection of the second line segment and the abscissa, respectively. a_1 and a_2 represent the slopes of the first and the second line segments of the bilinear curve, respectively (Figure 8.3).

$$w_1 = \frac{1 - b_2}{a_1 - a_2}; w_2 = \frac{b_2}{a_2} \tag{8.3}$$

The deformation of the hinge is described by half the angular deformation φ and the depth of the neutral incremental strip y_0 (Figures 8.1 and 8.2). The mean values of the curvature κ^* and the distribution of longitudinal strains ε^* at a depth y are introduced as:

$$\kappa^* = 2\frac{\varphi}{s};\ \varepsilon^*(y) = (y - y_0)\kappa^* \tag{8.4}$$

The deformation of an incremental strip is given by $u(y) = s.\ \varepsilon^*(y)$, where s is the width of the hinge. In the case when the strip has cracked the deformation, $u(y)$ may also be obtained as the sum of the elastic deformation of the strip and the crack opening

$$u(y) = s\varepsilon^*(y) = s\frac{\sigma(w(y))}{E} + w(y) \tag{8.5}$$

By combining Equations (8.4) and (8.5), the following solution for the crack opening in the cracked incremental segment at depth y, $w(y)$ and the associated crack bridging stress, $\sigma_w\{w(y)\} = f_t\, g\{w(y)\}$ (Olesen, 2001) is obtained:

$$\sigma_w(w(y)) = (2(y - y_0)\varphi - w(y))\frac{E}{s} \tag{8.6}$$

By using Equation (8.2) it may also be written as

$$\sigma_w(w(y)) = f_t(b_i - a_i w(y)) \quad i \in [1,2] \tag{8.7}$$

If Equations (8.6) and (8.7) are solved with respect to $w(y)$ and $\sigma_w(w)$ for each value of i, the following solutions are obtained:

$$w(y) = \frac{2(y - y_0)\varphi - \zeta_i}{1 - \beta_i} \tag{8.8a}$$

$$\sigma_w(w(y)) = \frac{\zeta_i - 2(y - y_0)\varphi\beta_i}{1 - \beta_i}\frac{E}{s} \quad i \in [1,2] \tag{8.8b}$$

where the dimensionless parameters β_i and ζ_i are defined by:

$$\beta_i = \frac{f_t a_i s}{E} \qquad \zeta_i = \frac{f_t b_i s}{E} \qquad i \in [1,2] \tag{8.9}$$

The solutions given in Equation (8.8) establish in an analytical form the crack opening profile $w(y)$ and the stress distribution in the cracked part of the hinge $\sigma_w(w)$ as functions of the hinge deformation φ, and y_0. This is an essential result that makes it possible to obtain closed-form solutions to the nonlinear constitutive behaviour of the cracked hinge as a whole. It is observed that the crack opening profile $w(y)$ is linear within each segment of the stress-crack opening relationship but the inclination with respect to the crack face is not the same in the two segments.

As a crack forms and then propagates from the bottom of the hinge, the stress distribution changes through three distinct phases (Figure 8.3). The crack-opening profile is divided into different intervals that are governed by the solutions in Equation (8.8) corresponding to different values of i. Besides y_0, these intervals are determined by the parameters y^*, y_1, and y_2 (Figure 8.3). An expression for y^* may be found from

$$y^* = \frac{sf_t}{2\varphi E} \tag{8.10}$$

Expressions for y_1 and y_2 are obtained from Equation (8.8a)

$$y_i = y_0 + \frac{1}{2\varphi}(\zeta_i - (\beta_i - 1)w_i) \quad i \in [1,2] \tag{8.11}$$

Analysis of the hinge element allows for the determination of the axial load N and the bending moment M for any given hinge rotation 2φ. The problem now is solved in four phases, one for each state of crack propagation. Phase 0 represents the elastic state, when no crack is formed, while phases I, II and III represent different stages of crack propagation (Figure 8.3).

The complete stress distribution is now established in all phases of the crack propagation, and by balancing the sectional stresses with the external longitudinal force N and the bending moment M (Figures 8.1 and 8.2) a relationship between N, M, and φ may be obtained in each phase. The following normalisations are introduced:

$$\mu = \frac{6}{f_t h^2 t} M \qquad \rho = \frac{1}{f_t h t} N \qquad \theta = \frac{hE}{s f_t} \varphi \qquad \alpha = \frac{d}{h} \tag{8.12a-d}$$

where t = width of the hinge in the direction normal to the paper; and d = depth of the fictitious crack. Given these normalisations the pre-crack elastic behaviour of the hinge is described by $\alpha_h = 0$ and $\mu = \theta$, where $0 \leq \theta \leq 1\text{-}\rho$, and where the onset of cracking is given by $\theta = 1 - \rho$. The solutions covering each of the cracked Phases I, II, and III are given in (8.13), (8.14), and (8.15) respectively. Full derivations of the solutions for the particular case $\rho = 0$ are given in Appendix B1.

Phase I

$$\alpha = 1 - \beta_1 - \sqrt{(1-\beta_1)(\frac{1-\rho}{\theta} - \beta_1)} \tag{8.13a}$$

$$\mu = 4(1 - 3\alpha + 3\alpha^2 - \frac{\alpha^3}{1-\beta_1})\theta + (6\alpha - 3)(1-\rho) \tag{8.13b}$$

Phase II

$$\alpha = 1 - \beta_2 - \frac{1-b_2}{2\theta} - \sqrt{(1-\beta_2)\left(\frac{(1-b_2)^2}{4\theta^2(\beta_1-\beta_2)} - \beta_2 + \frac{b_2-\rho}{\theta}\right)} \tag{8.14a}$$

$$\mu = 4\left(1 - 3\alpha + 3\alpha^2 - \frac{\alpha^3}{1-\beta_2}\right)\theta + (6\alpha - 3)(1-\rho) - \frac{(1-b_2)\left(3\alpha^2 - \left(\frac{c}{2\theta}\right)^2\right)}{1-\beta_2} \tag{8.14b}$$

Phase III

$$\alpha = 1 - \frac{1}{2\theta}\left(1 + \sqrt{\frac{(1-b_2)^2}{\beta_1 - \beta_2} + \frac{b_2^{\,2}}{\beta_2} - 4\rho\theta}\right) \tag{8.15a}$$

$$\mu = 4(1-3\alpha+3\alpha^2-\alpha^3)\theta + (6\alpha-3)(1-\rho) - 3\alpha^2 + \frac{1}{4\theta^2}\left(1-\frac{b_2}{\beta_2}\right)\left(1-\frac{b_2}{\beta_2}+c\right)\left(1+\frac{\beta_1 c}{1-\beta_1}\right) + \left(\frac{c}{2\theta}\right)^2 \tag{8.15b}$$

Here the constant c has been introduced as $c = (1 - b_2)(1 - \beta_1)/(\beta_2 - \beta_1)$.

In terms of θ the point of transition from Phase I to Phase II, $\theta_{I\text{-}II}$, may be found from the condition that $y_1 = h_g$, and the point of transition from Phase II to Phase III, $\theta_{II\text{-}III}$, may similarly be found from $y_2 = h_g$. These transition points, together with the point of transition between Phase 0 and Phase I, $\theta_{0\text{-}I}$ are given by:

$$\theta_{0-I} = 1 - \rho \tag{8.16a}$$

$$\theta_{I-II} = \frac{1}{2}\left(1 - \rho - c + \sqrt{(1-\rho-c)^2 + \frac{c^2}{\beta_1 - 1}}\right) \tag{8.16b}$$

$$\theta_{II-III} = \frac{1}{2}\left(\rho(\beta_2 - 1) + \frac{b_2}{\beta_2} + \sqrt{\rho^2(\beta_2-1)^2 + 2\rho(\beta_2-1)\frac{b_2}{\beta_2} + \frac{(1-b_2)^2}{\beta_1 - \beta_2} + \frac{b_2^{\,2}}{\beta_2}}\right) \tag{8.16c}$$

8.1.3 Application to a three-point bend beam

The three-point bend beam is a simply supported beam with a span length L, loaded at midspan by a transverse concentrated load of magnitude P. The nonlinear cracked hinge is incorporated into the beam at midspan, and the load-deflection relationship of the beam is established. The midspan deflection, v, of the beam may be determined as the sum of the elastic beam deflection, v_e and the deflection due to the crack, v_c. The non-dimensional midspan deflection, δ, is introduced by the normalisation

$$\delta = \frac{2v}{L}\frac{hE}{sf_t} = \frac{2v}{L}\frac{\theta}{\varphi} \tag{8.17}$$

thus the normalised elastic deflection may be found from

$$\delta_e = \frac{L}{3s}\mu(\theta) \tag{8.18}$$

The deformation of the hinge is the sum of the elastic deformation of the hinge and the deformation due to crack. The normalised deformation due to the crack only, θ_c, is found by subtracting the normalised elastic deformation, θ_e, from the total deformation of the hinge, θ. The normalised elastic deformation of the hinge is given by $\theta_e = \mu(\theta)$. Since the normalised deflection due to hinge deformation is equal to the normalised hinge deformation, θ, the normalised deflection due to the crack, δ_c, is given by:

$$\delta_c = \theta_c = \theta - \mu(\theta) \tag{8.19}$$

The total normalised midspan deflection may then be found from:

$$\delta = \delta_e + \delta_c = \theta + \left(\frac{L}{3s} - 1\right)\mu(\theta) \tag{8.20}$$

The load on the beam is related to the normalised moment through

$$P(\theta) = \frac{2}{3}\frac{f_t h^2 t}{L}\mu(\theta) \tag{8.21}$$

where L is the total length of the beam.

Equations (8.20) and (8.21), together with the relevant expressions for the normalised moment $\mu(\theta)$ (8.13-8.15) establish the load-deflection relationship of the beam, using θ as the controlling parameter.

The crack-mouth opening displacement (CMOD) in a three-point bend test depends also on two contributions. These are the opening due to the presence of the crack, δ_{COD}, and the opening due to elastic deformation, δ_e.

$$CMOD = \delta_{COD} + \delta_e \tag{8.22}$$

The value δ_{COD} is the crack opening at the bottom of the hinge, i.e. at $y = h_g$, and may be determined from Equation (8.8a)

$$\delta_{COD} = w(h) = \frac{sf_t}{E}\frac{1-b_i+2\alpha\theta}{1-\beta_i} \tag{8.23}$$

$$(b_i,\beta_i) = \begin{cases} (1,\beta_i) & for\ \theta_{0-I} < \theta \le \theta_{I-II} \\ (b_2,\beta_2) & for\ \theta_{I-II} < \theta \le \theta_{II-III} \\ (0,0) & for\ \theta_{II-III} < \theta \end{cases} \tag{8.24}$$

δ_e can be found from handbooks, e.g. Tada et al. (1985) and is given by:

$$\delta_e = \frac{4\sigma\alpha}{E}\left(0.76-2.28\alpha+2.87\alpha^2-2.04\alpha^3+\frac{0.66}{(1-\alpha)^2}\right) \tag{8.25}$$

where, $\sigma = 6M/(W^2t)$, $M = PL/4$, and a is the initial crack length such that $\alpha = a/W$.

8.1.4 Modelling of the static response of CARDIFRC® beams tested in 3-point bending

The nonlinear cracked hinge model proposed by Olesen (2001) and described above has been used for the simulation of the static response of CARDIFRC® beams, under three point bending. The model is based on the fracture mechanics concepts of the fictitious crack model, with a bilinear stress-crack opening relationship. The constitutive behaviour of CARDIFRC® is presented analytically in Chapter 3, where the numerical expressions describing the three stages of the pre- and post-peak response of the material are given. As it is shown in Figure 8.4, the post-peak response (i.e. stress-crack mouth opening) is approximated by two alternative bilinear relationships. The first linear branch of the two relations is identical, whereas the second linear branch is modified slightly in the two cases, in order to achieve the best possible fit. Thereafter, parameters w_1 and b_2 for the two alternative curves are estimated graphically (Figure 8.4). For normalisation purposes, the value of b_1 is set equal to 1, such that $g(0)=1$ and $w_2=6.5$, which corresponds to half length of the long fibres (13 mm) embedded in CARDIFRC®. From Equation (8.3), the slopes a_1 (initial) and a_2 (secondary) of the two branches of the bilinear curve which enter the hinge

model are calculated. Table 8.1 summarises the values of the parameters a_1, a_2, b_1, b_2, w_1 and w_2 used in the hinge model, for the two alternative bilinear approximations.

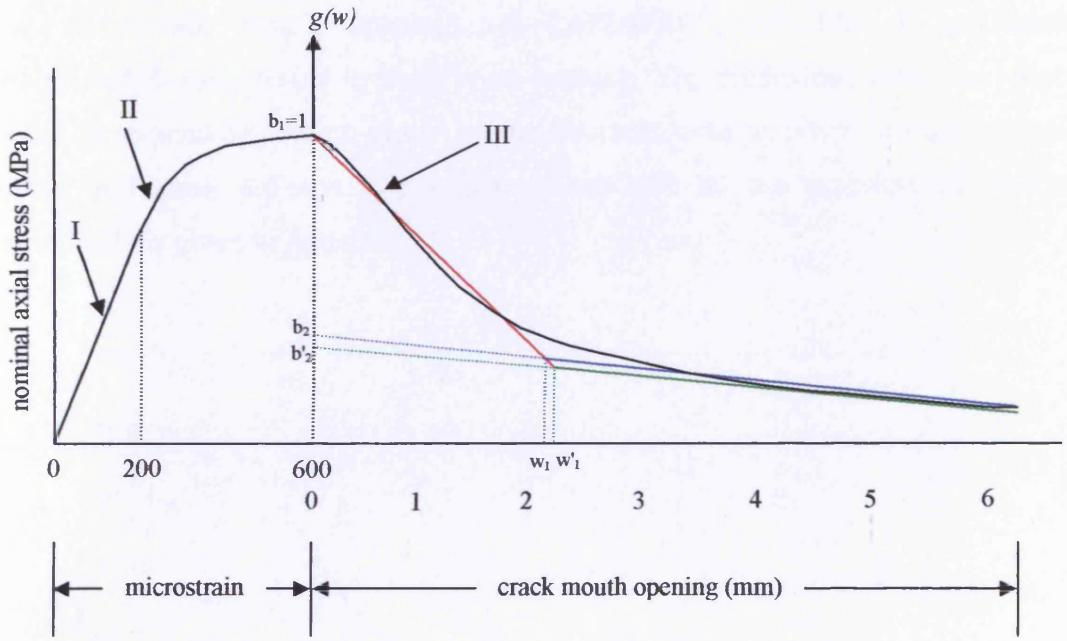

Figure 8.4: Definition of parameters of bilinear stress-crack opening relationship for CARDIFRC®.

The two additional material parameters entering the hinge model are the Young Modulus, E and the uniaxial tensile strength, f_t. The value used for the first parameter was 48 GPa which is in accordance with the experimental values for CARDIFRC®, Mix I, whereas the uniaxial tensile strength, f_t, was set equal to 16 MPa and derived as an average value of the experimental results of Alaee (2002) and Benson (2003).

Table 8.1: Parameters of bilinear stress-crack opening relationship for CARDIFRC®.

	a_1	a_2	b_1	b_2	w_1	w_2
Bilinear Curve 1	0.33	0.06	1.00	0.39	2.29	6.50
Bilinear Curve 2	0.33	0.05	1.00	0.33	2.36	6.50

The computer program for the calculation of the load-deflection curve is written in FORTRAN language and is given in Appendix B2.

8.1.5 Results and discussion

Figure 8.5 shows the load-deformation curves generated by the hinge model, for the two bilinear approximations (HM1 and HM2, Table 8.1) of the post-peak response (i.e. stress-crack mouth opening) of CARDIFRC®, for Mix I specimens (100x100x500 mm) tested in three-point bending. The predictions from the hinge model corresponding to these approximations are compared with typical experimental curves in Figures 8.6 and 8.7. A comparison with all the experimental results individually is given in Appendix C.

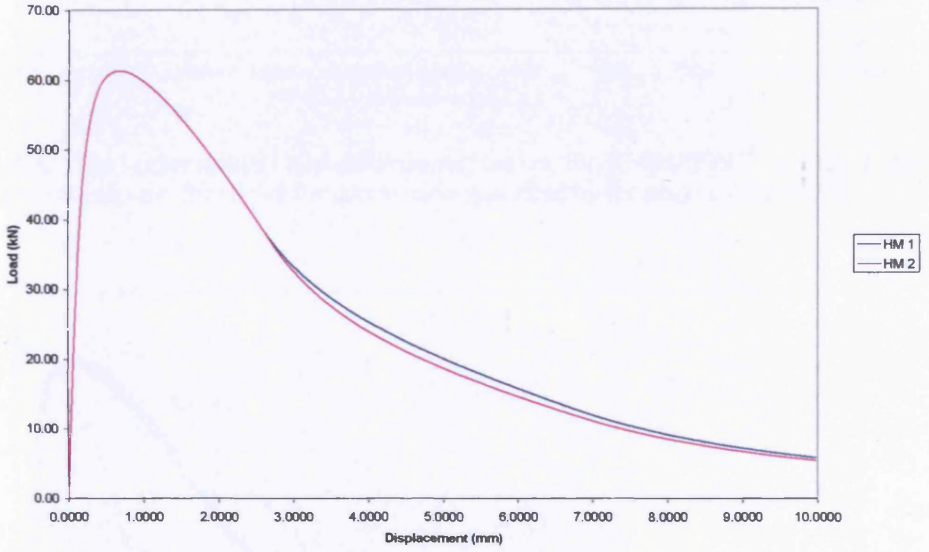

Figure 8.5: The load-deformation curves generated by the hinge model for the two bilinear approximations (HM1 and HM2) of the softening branch of CARDIFRC®, for Mix I specimens (100x100x500 mm) tested in three-point bending.

As expected and as can be seen from Figure 8.5, the two bilinear approximations of the stress-crack mouth opening behaviour give identical results for the initial branch of the flexural post-peak response of CARDIFRC®. Thereafter, the tail of the curve resulting from HM2 is slightly below the corresponding from HM1, since the slope a_2 of the secondary part of the bilinear curve 2 is less stiff (Table 8.1).

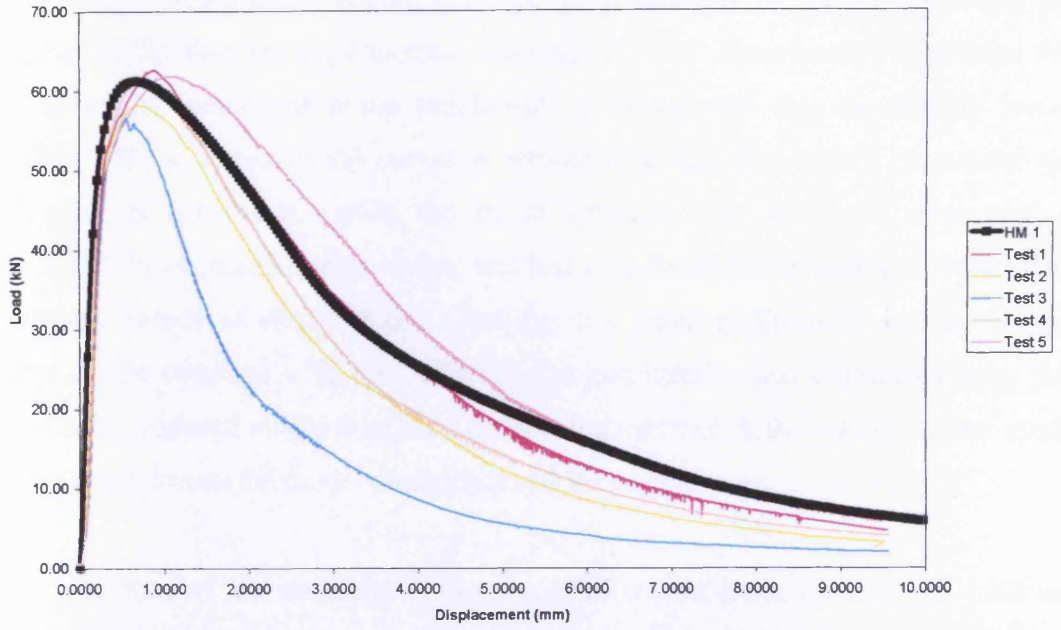

Figure 8.6: The experimental load-deformation curves for CARDIFRC® - Mix I specimens (100x100x500 mm) and the load-deformation curve generated by the hinge model (HM1).

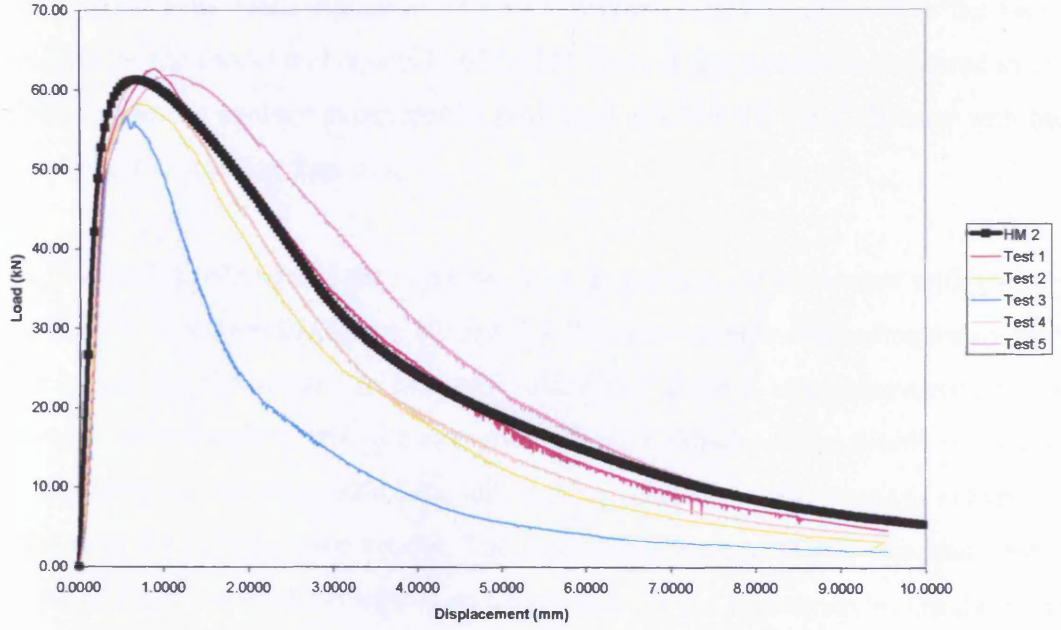

Figure 8.7: The experimental load-deformation curves for CARDIFRC® - Mix I specimens (100x100x500 mm) and the load-deformation curve generated by the hinge model (HM2).

Figures 8.6 and 8.7 demonstrate the performance of the model and compare the load-deformation curves predicted by the model with typical test results. It can be clearly seen that the trend of the model results is generally in a good agreement with the test

results. The model gives in both cases pre-peak branches of the curves which are slightly stiffer than the experimental. Although the difference is very small and the simulation is considered to be satisfactory, it is believed that the slightly lower stiffness of the experimental curves is attributed to the abnormality caused by the vibration of the beam during the initial application of the load. This was a phenomenon observed during testing and had as a result the recording of somewhat increased values of displacement, resulting in a small nonlinearity and a reduced value of the recorded stiffness. Although the nonlinearity was eliminated from the graphs, the reduced stiffness of the beams still exists and is the reason for the small difference between the model predictions and the experiments.

The peak load of the model prediction is based on the input value of the uniaxial tensile strength (f_t) of the material and is also very close to the experimental peak loads. The only inconsistency is the result of test 3, which is a special case that will be discussed separately later. If test 3 is ignored, then the average value of the experimental peak loads equals to 61.10 kN, which is almost identical to the value predicted by the model and equals to 61.28 kN. Even if test 3 is also considered in the calculation of the average experimental peak load (60.22 kN), the difference with the model result is still less than 2%.

The post-peak prediction of the hinge model is in a very good agreement with the test results, as can be seen in Figures 8.6 and 8.7. The two bilinear approximations which are based on the constitutive relation of CARDIFRC® seem to reproduce satisfactorily the experimental curves, with the exception of test 3, which will be discussed below. An argument can be made about the tail of the predicted curves, which is somewhat stiffer than the experimental results. The simulation, though, is still adequate and it can be said that the model results is an upper limit for the experimental. On the other hand, the branch of the curve right after the peak load, which corresponds to the initial part of the bilinear curve with slope a_1, represents an average of the experimental curves. The good agreement of the model predictions with the experimental results is a verification of the proposed constitutive relation for the tension softening part of CARDIFRC® (Benson, 2003).

Test No.3 is the only discrepancy in the fitting of the model predictions. The experimental curve is significantly lower than both curves resulting from the predictions of the hinge model. A thorough investigation of the plane of failure of this particular CARDIFRC® specimen revealed a very poor distribution of fibres, which is the major reason for its poor flexural behaviour. Although the number of fibres in this plane of failure was not low, most of the fibres were short and their orientation was such that they did not exert any bridging action, resulting in the poor post-peak response of the specimen (Figure 8.8). The importance of the even fibre distribution in specimens is discussed and highlighted in Chapters 6 and 7.

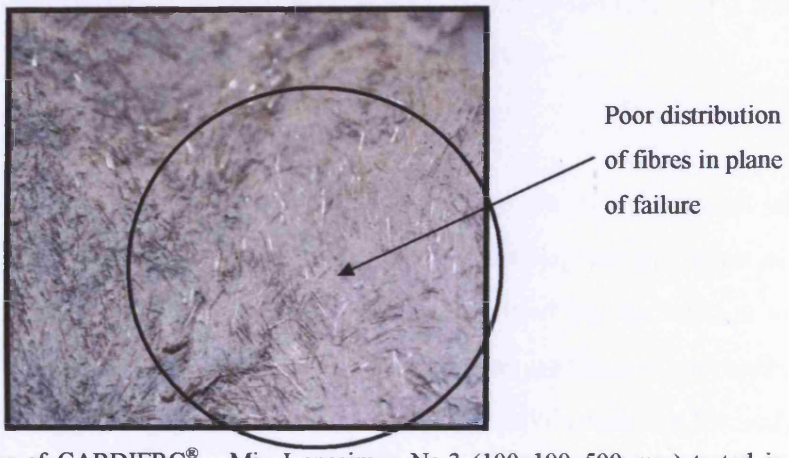

Figure 8.8: Plane of failure of CARDIFRC® - Mix I specimen No.3 (100x100x500 mm) tested in three-point bending.

The hinge size, s, which plays an essential role in the hinge model, may be a function of the specimen geometry. The dependency of the model solution on the hinge size, i.e. s/h_g ratio was studied by Ulfkjær et al. (1995), who concluded that for three-point bend test the optimal value of s/h_g ratio is 0.5. This result has been confirmed by Olesen (2001) and is used in the present simulation.

8.1.6 Conclusions

The nonlinear cracked hinge model permits the stress-crack opening relationship to be modelled by a bilinear curve, allowing for the modelling of a broad range of FRC materials. An essential requirement is the careful choice of the appropriate bilinear approximation, which should be representative of the tension softening behaviour of the material.

In the case of CARDIFRC®, two bilinear approximations were selected, which were based on the constitutive behaviour of the material in tension (Benson, 2003). The predictions of the hinge model based on these bilinear approximations are in a very good agreement with the experimental results. This is an additional verification of the proposed constitutive relation for the tension softening part of CARDIFRC®. Finally, the ability of the hinge model to simulate accurately the nonlinear behaviour of FRC highlights the importance and uniqueness of fracture mechanics approach, in contrast to the conventional design codes.

8.2 COMBINED DAMAGE/FRACTURE MECHANICS APPROACH TO THE DESCRIPTION OF CONCRETE FLEXURAL BEHAVIOUR

8.2.1 Introduction

A description of the nonlinear tensile response of concrete before the attainment of the tensile strength of the material f_t' can be given by considering the evolution of distributed damage (i.e. of microcracks) in the material under load and its relation to the microstructural parameters. In combination with a fracture mechanics approach, the post-peak behaviour, when damage has localised and a cohesive crack has formed, can also be predicted, resulting in a complete description of concrete flexural behaviour.

8.2.2 Continuum damage mechanics approach

Concrete contains pores and microcracks even in its virgin, unstressed state. Under low tensile stresses, however their influence on its mechanical response is not noticeable, which is therefore accepted to be linear elastic. With an increase in applied tensile stress, microcracks form at the interfaces between matrix and fibres (in a fibre reinforced concrete), leading to the pre-peak (i.e. prior to the ultimate tensile strength) nonlinearity. The transition from linear elastic to strain hardening behaviour is governed by the tensile strength of the cementitious matrix but is mostly unaffected by the fibre parameters (i.e. fibre aspect ratio, volume fraction, bond strength). The threshold strain for concrete was accurately measured by several researchers, under different loading configurations. For CARDIFRC®, this threshold strain in uniaxial

tension is $\varepsilon_{th} = 1.44 \times 10^{-4}$ and the corresponding threshold stress $\sigma_{th} = f_{tp} = 7.40$ MPa (Alaee, 2002).

In order to describe this progressive reduction in the stiffness of the material, it is necessary to know when the microcracks will form and also how many of them will form at a particular stress level. The density of interfacial microcracks, C_d, increases with an increase in tensile/flexural loading, until it reaches a saturation level. It is assumed that the microcracks will form when the tensile strain attains the threshold value ε_{th}. It is also assumed that the degradation of the material stiffness is uniform in all directions, i.e. the damage is isotropic. This isotropic damage evolution is quantified by the scalar damage parameter ω, such that the stiffness of the damaged material $E^*(\sigma)$ at a particular stress level σ is:

$$E^*(\sigma) = E_{secant}(\sigma) = E(1 - \omega) \tag{8.26}$$

where E is Young modulus of the undamaged material and for CARDIFRC® this value is found from experimental results to range between 48 GPa (Chapter 6) and 50 GPa (Alaee, 2002). Although in paragraph 8.1.4 the value of 48 GPa was used, in the following calculations the value of 50 GPa will be applied, consistent with the stress and strain threshold values.

The scalar damage parameter ω ranges between $0 \leq \omega \leq 1$ and is a function of the applied tensile/flexural loading on the specimen, $\omega(\sigma)$. More specifically, at $\sigma = \sigma_{th}$, $\omega = 0$ and at $\sigma = 0$ (after complete softening), $\omega = 1$(Karihaloo, 1995) (Figure 8.9).

If the effect of Poisson's ratio on ω is assumed to be negligible (and there is ample evidence in support of this assumption) then under uniaxial tension σ_{11}, the stress-strain (σ- ε) relationship can be written using (8.26):

$$\sigma_{11} = E(1 - \omega)\varepsilon_{11} \tag{8.27}$$

The pre-peak nonlinear part of the load-deformation curve of CARDIFRC® is the part corresponding to stresses between $\sigma_{th} < \sigma \leq \sigma_{max}$, where the value of ω is greater than zero, however the damage is distributed, without a localised crack having formed (Figure 8.10). For a given value of load, P, greater than P_{th}, the corresponding stress level in flexure can be defined:

$$\sigma = \frac{M}{I}\frac{D}{2} = \frac{3PL}{2BD^2} \tag{8.28}$$

According to Neville (1995), the uniaxial tensile strength f_t is approximately the 50% of the corresponding flexural strength. For this uniaxial tensile stress level, the value of strain ε can be calculated from the following pre-peak constitutive relation in tension for CARDIFRC® (Alaee, 2002):

$$\sigma = 3.944 \times 10^{10}\varepsilon^3 - 9.357 \times 10^{7}\varepsilon^2 + 73880\varepsilon - 1.417 \tag{8.29}$$

Although in paragraph 8.1.4 we used the constitutive relation proposed by Benson (2003) in order to describe the post-peak behaviour of CARDIFRC®, the corresponding proposed pre-peak equation significantly underestimates the material response in flexure.

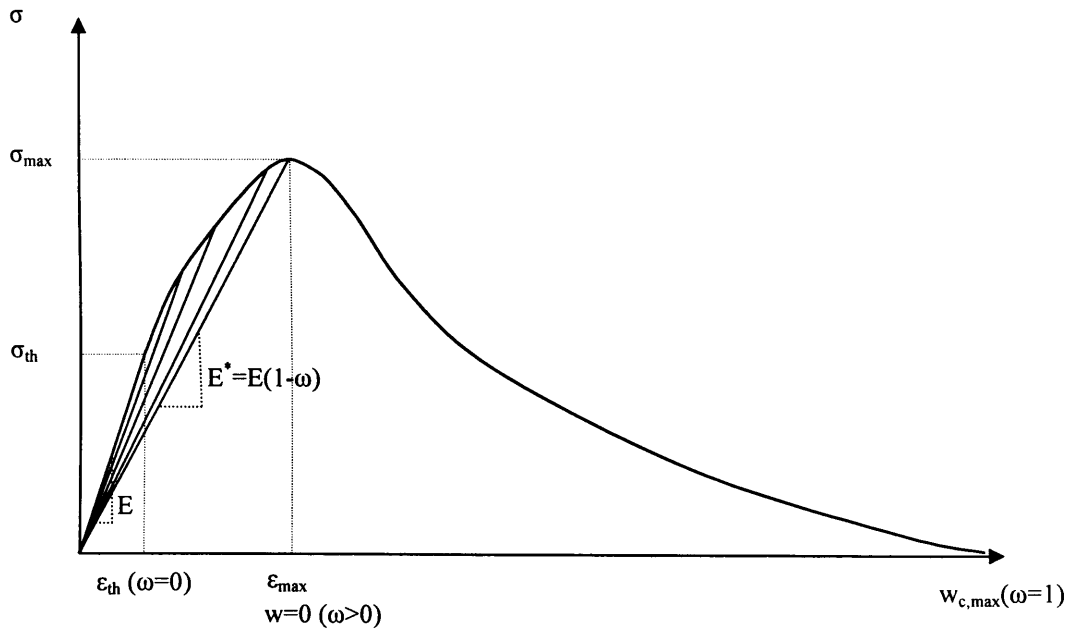

Figure 8.9: Schematical explanation of the damage evolution, quantified by the scalar damage parameter ω.

From the constitutive relation (8.29) and for the known value of uniaxial tensile stress, the corresponding value of strain is determined. Thereafter, by making use of Equation (8.27) the value of the scalar damage parameter $\omega(\sigma)$ is calculated. The reduced stiffness $E^*(\sigma)$ can be obtained using Equation (8.26). For this value of

stiffness of the damaged material, and for the given load, P, the displacement, δ, can be found by making use of the expression:

$$\delta(\sigma) = \frac{PL^3}{48E^*(\sigma)I} \tag{8.30}$$

where L is the testing span of the beam and I is the second moment of area.

By repeating this procedure for a number of values of load P up to P_{max}, a sufficient number of points can be obtained for the generation of the nonlinear pre-peak part of P- δ curve. After the formation of a cohesive crack in the beam, for stresses ranging between $\sigma_{max} > \sigma \geq 0$ (Figure 8.9), the method described in the following, making use of the Castigliano's theorem, can be applied for the prediction of the post-peak nonlinear part of the curve.

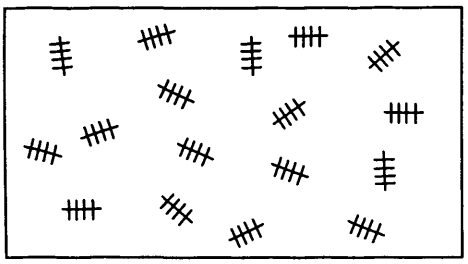

Figure 8.10: Distributed damage in the form of bridged microcracks in the material, corresponding to $\sigma_{th}<\sigma\leq\sigma_{max}$ and $\omega>0$ (pre-peak nonlinear part of the stress-strain diagram).

Figure 8.11 shows the pre-peak branch of the load-deformation curve generated based on the damage mechanics theory (DM). The prediction from the method is compared with typical experimental curves. It can be seen that the trend of the model results is generally in a good agreement with the test results.

The model gives a pre-peak branch of the curve which is slightly stiffer than the experimental. This difference, however, is very small and the simulation is considered to be satisfactory. It is believed, though, that the slightly higher stiffness of the theoretical curve may be attributed either to the initial value of E used in the calculations (50 GPa), which is higher than the experimental value obtained by the author (48 GPa) (Chapter 6), or to the abnormality caused by the vibration of the

beam during the initial application of the load, described in 8.1.5. Another possible reason is the inaccuracy in the measurement of central deflection by LVDTs during testing, especially of small values. This is an inevitable inaccuracy, since the LVDTs used for the capturing of the full load-displacement curve (up to 10 mm) were calibrated between ±5 mm. Therefore, they were not sufficiently sensitive for the accurate measurement of the very small values of deformation, during the strain hardening response of the beams.

An interesting observation made from Figure 8.12, is the relatively high value of the scalar damage parameter ω corresponding to the maximum stress σ_{max}. At this point and just before the formation of a localised cohesive crack in the beam, the value of ω is equal to 0.526, higher than 50% of its ultimate value (ω_{max}=1). This is an indication of the extension and importance of the distributed damage (Figure 8.10) in the material, which is also confirmed by careful study of specimens during testing.

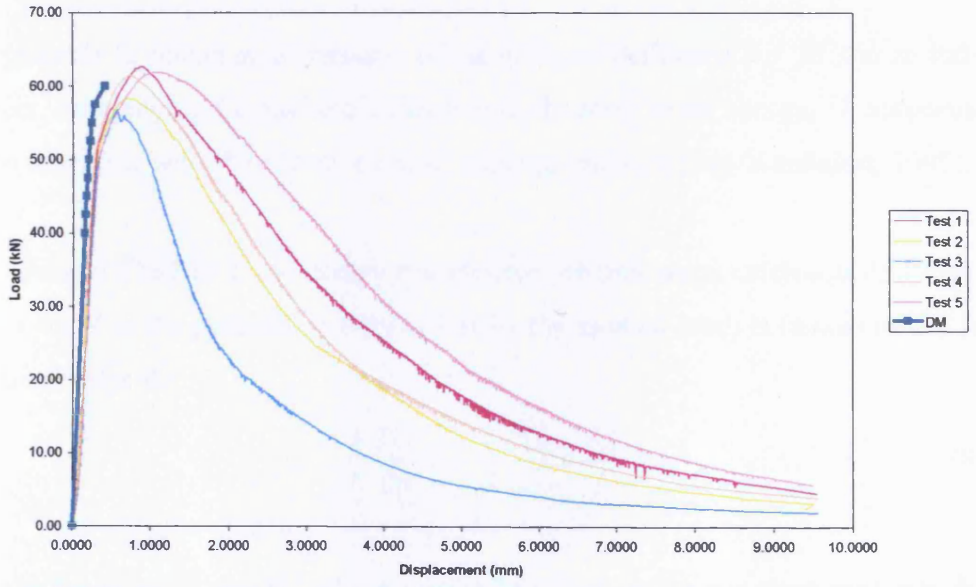

Figure 8.11: The experimental load-deformation curves for CARDIFRC® - Mix I specimens (100x100x500 mm) and the pre-peak curve generated according to damage mechanics theory (DM).

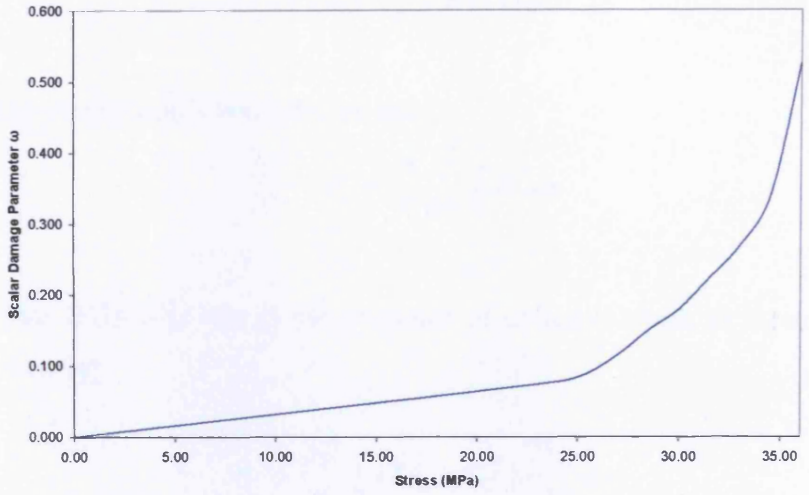

Figure 8.12: Evolution of the scalar damage parameter ω with flexural stress, in the pre-peak part.

8.2.3 Fracture mechanics approach for post-peak response

When the distributed damage has localised into the eventual fracture plane, we can consider a three-point bend beam with a cohesive crack near the midspan.

It is possible to obtain an expression of the midspan deflection $\delta = f(P)$ in an indirect manner, by applying Castigliano's theorem to the total strain energy, U, accumulated in the specimen with the cohesive crack, under gradual loading (Karihaloo, 1995).

As shown in Chapter 2, the energy release rate per unit crack extension Δa (which in turn is equal to the potential energy Π lost by the applied load) is related to the stress intensity factor K_I:

$$\frac{1}{B}\frac{\partial U}{\partial a} = -\frac{1}{B}\frac{\partial \Pi}{\partial a} = \frac{K_I^2}{E} \tag{8.31}$$

B is the beam width and E is the Young modulus. K_I is the net stress intensity factor due to load P and the closure pressure exerted by the steel fibres in CARDIFRC®:

$$K_I = K_I^P - K_I^f \tag{8.32}$$

Therefore,

$$\frac{\partial U}{\partial a} = B\frac{K_I^2}{E} \tag{8.33}$$

$$U(a) = \frac{B}{E}\int_0^a K_I^2(x)dx \tag{8.34}$$

By applying Castigliano's theorem, we have

$$\frac{\partial U}{\partial P} = \delta_P^* = \frac{B}{E}\frac{\partial}{\partial P}\int_0^a K_I^2 dx \tag{8.35}$$

The midspan deflection due to the presence of cohesive crack in three-point bend beam is given by:

$$\delta_P^* = \frac{2B}{E}\int_0^a (K_I^P - K_I^f)\frac{\partial K_I^P}{\partial P}dx \tag{8.36}$$

The total midspan deflection of a three-point bend beam in the post-peak regime is the sum of the partial deflections δ, due to the elastic and strain hardening response of the beam (pre-peak) at the maximum load P_{max} and δ^*_P, due to the cohesive crack (post-peak)

$$\delta_{tot} = \delta + \delta_P^* = \frac{P_{\max} L^3}{48E^* I} + \frac{2B}{E}\int_0^a \left(K_I^P - K_I^f\right)\frac{\partial K_I^P}{\partial P}dx \tag{8.37}$$

The partial deflection δ, due to the elastic and strain hardening response of the beam (pre-peak) was calculated above based on the damage mechanics approach.

The analytical expressions for the stress intensity factors K_I^P, and K_I^f required in the expression of $\delta = f(P)$, are calculated according to Karihaloo and Xiao (2001) and Tada et al. (1985b), respectively in the following:

Calculation of K_I^P (Karihaloo and Xiao, 2001)

$$K_I^P(x) = \frac{\sqrt{x}}{\sqrt{2\pi}(1-x)^{3/2}(1+3x)}\left\{p_\infty(x) + \frac{4}{\beta}\left[p_4(x) - p_\infty(x)\right]\right\}\sigma\sqrt{2\pi D} \tag{8.38}$$

where,

$$p_4(x) = 1.9 + 0.41x + 0.51x^2 - 0.17x^3$$
$$p_\infty(x) = 1.99 + 0.83x - 0.31x^2 + 0.14x^3$$
$$\beta = \text{span / depth} = L / D$$

$$\sigma = \frac{3}{2}\frac{PL}{D^2}$$

In case $\beta = 4$, $K_I^P(x)$ takes the following form:

$$K_I^P(x) = \frac{\sqrt{x}}{\sqrt{2\pi}(1-x)^{3/2}(1+3x)} p_4(x)\frac{6}{D}\sqrt{2\pi D}P \tag{8.39}$$

The derivative of $K_I^P(x)$ with respect to P, which appears in Equation (8.37) for the calculation of the total midspan deflection of a three-point bend beam, is given by:

$$\frac{\partial K_I^P}{\partial P} = \frac{\sqrt{x}}{\sqrt{2\pi}(1-x)^{3/2}(1+3x)} p_4(x)\frac{6}{D}\sqrt{2\pi D} \tag{8.40}$$

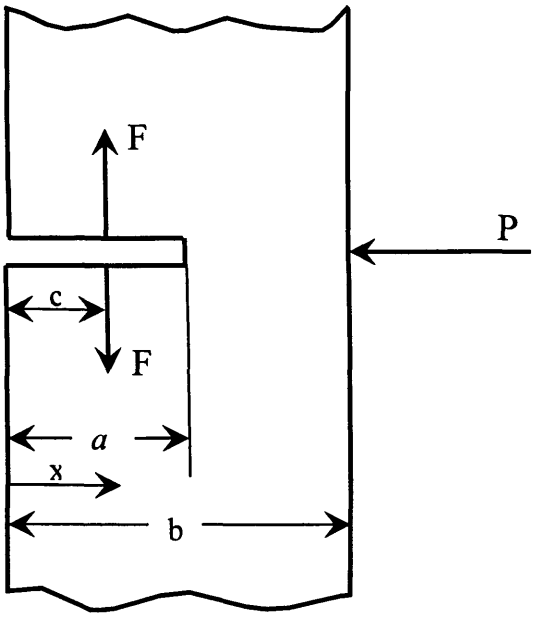

Figure 8.13: Schematical explanation of crack geometry and loading (After Tada et al., 1985).

The localised cohesive crack is assumed to be linear in profile and the continuous closure stresses exerted by fibres are discretised into infinitely many concentrated loads F, each acting on an infinitesimal crack length dc (Figure 8.14).

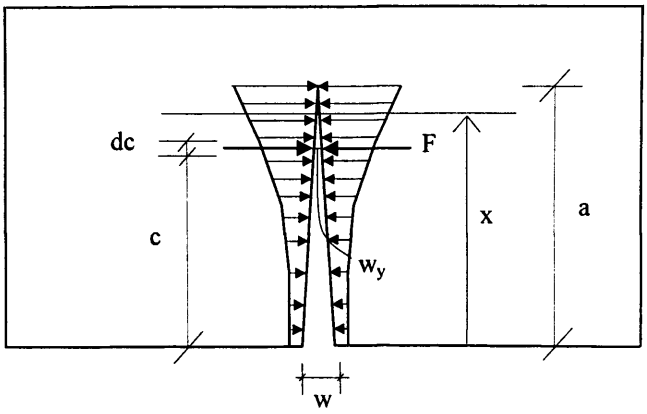

Figure 8.14: Schematical explanation of cohesive crack geometry and cohesive stress distribution.

Calculation of K_I^f (Tada et al., 1985b)

$$K_I^f = \frac{2F}{\sqrt{\pi a}} \frac{G\left(\frac{c}{a}, \frac{a}{b}\right)}{\left(1-\frac{a}{b}\right)^{3/2}\sqrt{1-\left(\frac{c}{a}\right)^2}} \tag{8.41}$$

For a generic crack of length x ($>c$) (Figure 8.13) and for a beam of depth D, the factor $G(c/a, a/b)$ which appears in the numerator of Equation (8.41) becomes $G(c/x, x/D)$ and can be calculated from the following expressions:

$$G\left(\frac{c}{x}, \frac{x}{D}\right) = g_1\left(\frac{x}{D}\right) + g_2\left(\frac{x}{D}\right)\frac{c}{x} + g_3\left(\frac{x}{D}\right)\left(\frac{c}{x}\right)^2 + g_4\left(\frac{x}{D}\right)\left(\frac{c}{x}\right)^3$$

$$g_1\left(\frac{x}{D}\right) = 0.46 + 3.06\frac{x}{D} + 0.84\left(1-\frac{x}{D}\right)^5 + 0.66\left(\frac{x}{D}\right)^2\left(1-\frac{x}{D}\right)^2$$

$$g_2\left(\frac{x}{D}\right) = -3.52\left(\frac{x}{D}\right)^2$$

$$g_3\left(\frac{x}{D}\right) = 6.17 - 28.22\frac{x}{D} + 34.54\left(\frac{x}{D}\right)^2 - 14.39\left(\frac{x}{D}\right)^3 - \left(1-\frac{x}{D}\right)^{3/2} - 5.88\left(1-\frac{x}{D}\right)^5 - 2.64\left(\frac{x}{D}\right)^2\left(1-\frac{x}{D}\right)^2$$

$$g_4\left(\frac{x}{D}\right) = -6.63 + 25.16\frac{x}{D} - 31.04\left(\frac{x}{D}\right)^2 + 14.41\left(\frac{x}{D}\right)^3 + 2\left(1-\frac{x}{D}\right)^{3/2} + 5.04\left(1-\frac{x}{D}\right)^5 + 1.98\left(\frac{x}{D}\right)^2\left(1-\frac{x}{D}\right)^2$$

Therefore, for a generic crack of length x ($>c$) and for a beam of depth D, Equation (8.41) becomes:

$$K_I^f(x,c) = \frac{2F}{\sqrt{\pi x}} \frac{G\left(\frac{c}{x}, \frac{x}{D}\right)}{\left(1-\frac{x}{D}\right)^{3/2} \sqrt{1-\left(\frac{c}{x}\right)^2}} \tag{8.42}$$

In order to find the value of K_I^f, Equation (8.42) has to be integrated along the crack length, x:

$$K_I^f(x) = \int_0^x K_I^f(x,c)dc \tag{8.43}$$

c is the location where the cohesive closure force due to fibres F is applied (Figures 8.13 and 8.14).

The magnitude of F over an infinitesimal crack length dc depends on the COD through the constitutive relation. We must, therefore, also calculate the COD, using the fracture mechanics method described in the next paragraph.

8.2.4 Fracture mechanics approach for load-COD response of CARDIFRC®

The fracture mechanics approach presented here is indispensable for the completeness of the method described above, for the determination of the complete post-peak static flexural response of CARDIFRC®. As explained earlier, the cohesive force due to fibres F, appearing in Equation (8.42) for the calculation of K_I^f, depends on the crack opening displacement at the level of its application, w_y (Figure 8.14). Therefore, displacement δ^*_P due to the cohesive crack depends on the crack opening displacement, and force F inserts the contribution of COD in δ_{tot}.

To model the flexural failure of CARDIFRC®, the free body diagram of a part of the beam made of this material, containing the dominant flexural crack is considered (Figure 8.15). This method is based on the same principle as the cracked hinge model analysed above, since both isolate a small part of the beam and thereafter use fracture mechanics concepts for the calculation of its deformation. This method, however,

assumes a linear crack profile, which is an approximation of the real situation, in contrast to the cracked hinge model.

In the case of a simple three-point bend beam, in addition to the applied load P, there is one more load which appears in the free body diagram (Figure 8.15). This is the post-peak tension softening response of CARDIFRC®, which tends to close the crack and acts against the external load which tends to open it. Two basic conditions have to be satisfied, which are described below, and the corresponding equations for CARDIFRC® beams are given.

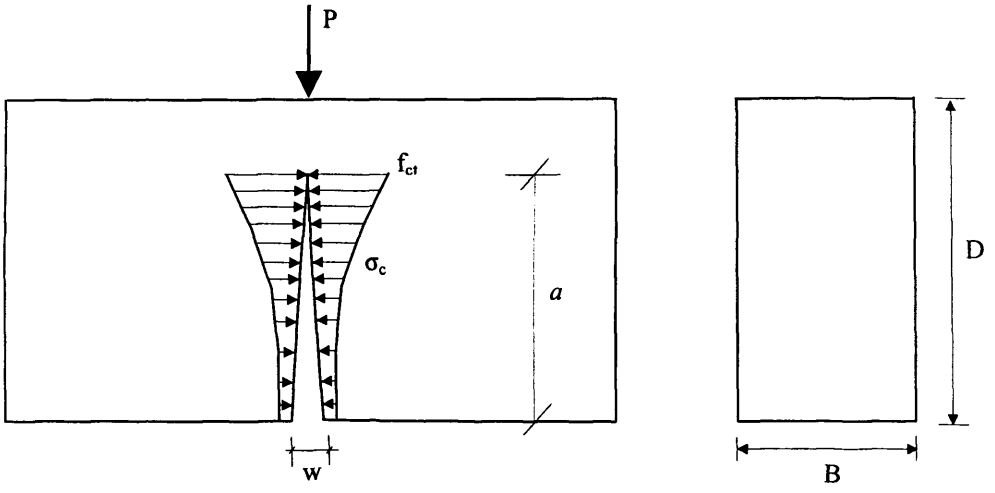

Figure 8.15: Free body diagram of the dominant flexural crack in CARDIFRC® beams.

8.2.4.1 Condition of smooth closure of crack faces

To simplify the computations, it is assumed that the crack profile is always linear, as it was also done in paragraph 8.2.3. Therefore a crack can be specified by its depth a and the opening w at its mouth. As can be seen in Figure 8.15, the stress at the crack tip is finite and equal to f_{ct}, therefore the net stress intensity factor at the crack tip must vanish (Chapter 2). However, this requires that the crack faces close smoothly near the tip. This would seem to violate the assumption of linear crack opening made earlier. Nevertheless, we shall proceed in the spirit of Barenblatt cohesive crack model (Barenblatt, 1959) and assume that the zone c near the tip of the crack where the faces close smoothly is very much smaller than the total length of the crack $c<<a$,

as shown in Figure 8.16. The net K_I at the crack tip is obtained by superimposing the stress intensity factors produced at the crack tip by the applied load (K_I^P), and the closure force exerted by the fibres (K_I^{FRC}). The condition of finite stress at crack tip, i.e. $K_I = 0$ is therefore:

$$K_I^P - K_I^{FRC} = 0 \tag{8.44}$$

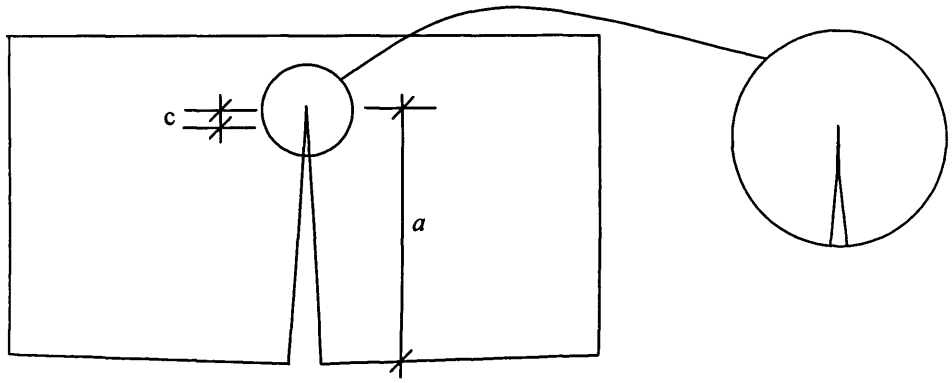

Figure 8.16: Smooth closure crack faces.

The negative sign in front of the term K_I^{FRC} indicates that the stress intensity factor produced by the applied load is reduced by the closure pressure exerted by fibres. The above formula can be written analytically by calculating K_I^P using the formula given by Guinea et al. (1998), whereas the calculation of K_I^{FRC} is made with integration from the relation proposed by Tada et al. (1985).

$$\frac{PL}{4D^{3/2}B} Y_P(\xi) - K_I^{FRC} = 0 \tag{8.45}$$

where $\xi = a/D$ and $Y_P(\xi)$ is:

$$Y_P(\xi) = \frac{6\xi^{1/2}\left(1.99 + 0.83\xi - 0.31\xi^2 + 0.14\xi^3\right)}{(1-\xi)^{3/2}(1+3\xi)} \tag{8.46}$$

This formula is the equivalent and very similar to the one proposed by Karihaloo and Xiao (2001), used in paragraph 8.2.3 for the calculation of K_I^P. ξ represents the normalised crack length.

To work out K_I^{FRC}, the closure pressure is discretised into infinitely many concentrated forces, each of magnitude *F*, as it was also done in paragraph 8.2.3. Each force is applied over small crack segments of length *dy* at a distance $y = y^*D$ from the bottom of the crack (Figure 8.17).

The magnitude of each force is:

$$F = \sigma_c(w_y)Bdy \equiv \sigma_c(w_y)BDdy^* \tag{8.47}$$

where $w_y = w(1 - y/a) = w(1 - y^*/\xi)$

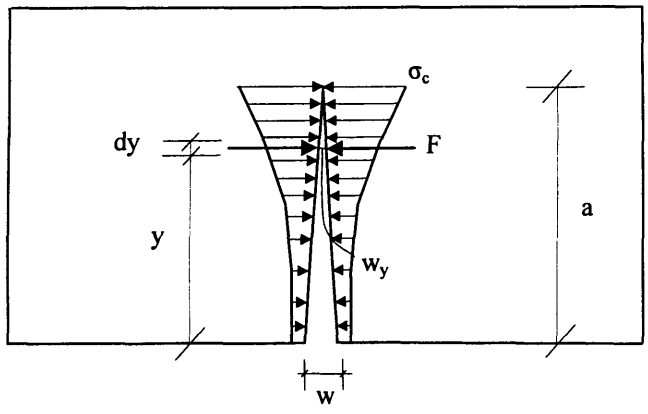

Figure 8.17: Towards the discretisation of the bridging stresses.

In the above equations, w_y is the crack opening at the level of the point load *F* (Figure 8.17). Therefore, using Tada et al. (1985), the stress intensity factor produced by this point load can be calculated

$$dK_I^{FRC} = \frac{\sigma_c(w_y)BD}{D^{1/2}B} Y(\xi, y^*)dy^* \tag{8.48}$$

By substituting the above relations into Equation (8.45), we have

$$\frac{PL}{4D^{3/2}B} \frac{6\xi^{1/2}(1.99 + 0.83\xi - 0.31\xi^2 + 0.14\xi^3)}{(1-\xi)^{3/2}(1+3\xi)} - \int_0^{\xi} \sigma_c(w_y)D^{1/2}Y(\xi, y^*)dy^* = 0 \tag{8.49}$$

$Y(\xi,y^*)$ is the compliance function at point ξ, by forces acting at point y^* and is given by:

$$Y(\xi,y^*)=\left\{\begin{array}{l}\dfrac{3.52(1-y^*/\xi)}{(1-\xi)^{3/2}}-\dfrac{4.35-5.28y^*/\xi}{(1-\xi)^{1/2}}+\\ \left[\dfrac{1.30-0.30(y^*/\xi)^{3/2}}{\left(1-(y^*/\xi)^2\right)^{1/2}}+0.83-1.76y^*/\xi\right]\left[1-(1-y^*/\xi)\xi\right]\end{array}\right\}\frac{2}{\sqrt{\pi\xi}} \qquad (8.50)$$

Formula (8.50) proposed by Tada et al. (1985) and used in this paragraph for the calculation of the stress intensity factor K_I^{FRC} is the equivalent to the formula (8.41) also proposed by Tada et al. (1985b), used in paragraph 8.2.3. ξ and y^* of Equation (8.50) represent the normalised crack length and the normalised distance of the concentrated force F from the bottom of the crack, respectively. Investigations have shown that the two formulas give almost identical results.

The final relation can be written as follows:

$$\frac{PL}{4D^{3/2}B}\frac{6\xi^{1/2}(1.99+0.83\xi-0.31\xi^2+0.14\xi^3)}{(1-\xi)^{3/2}(1+3\xi)}-$$
$$\int_0^{\xi}\sigma_c(w_y)D^{1/2}\left\{\begin{array}{l}\dfrac{3.52(1-y^*/\xi)}{(1-\xi)^{3/2}}-\dfrac{4.35-5.28y^*/\xi}{(1-\xi)^{1/2}}+\\ \left[\dfrac{1.30-0.30(y^*/\xi)^{3/2}}{\left(1-(y^*/\xi)^2\right)^{1/2}}+0.83-1.76y^*/\xi\right]\left[1-(1-y^*/\xi)\xi\right]\end{array}\right\}\frac{2}{\pi\xi}dy^*=0$$

(8.51)

The relation that gives the stress distribution with the crack opening is given (Benson, 2003):

$$\sigma_c(w_y):\ \sigma=3.07*10^{-3}w^7-0.08w^6+0.82w^5-4.42w^4+12.80w^3-18.11w^2+5.73w+12.89$$

(8.52)

This is the same constitutive equation for the post-peak response of CARDIFRC®, which was approximated by the bilinear relation for the application of the cracked hinge model.

8.2.4.2 Crack opening compatibility equation

In addition to the condition of smooth closure of crack faces at its tip, we must consider the compatibility of crack opening displacement of the beam. The crack opening displacement can again be written as the vectorial sum of the contributions from the applied load and the closure force exerted by fibres. The compatibility equation needs to be satisfied only at one level along the beam, because of the assumed known (i.e. linear) variation along the length of the crack:

$$(w)_P - (w)_{FRC} = (w) \tag{8.53}$$

Each term in the left-hand side of the above equation can be expressed in terms of the corresponding compliance coefficients. More specifically, $(w)_P = \lambda_P(PL/4)$ where λ_P is crack opening at the bottom of the beam produced by a unit applied load.

$$\lambda_P = \frac{2}{DBE}\int_{\beta}^{\xi} Y_P(x)Y(x,\beta)dx \tag{8.54}$$

where $Y_P(x)$ is the compliance function at the location of the actual load and is given by Equation (8.46) and $Y(x,\beta)$ is the geometry factor and is given by Equation (8.50).

$$\lambda_P(PL/4) - (w)_{FRC} = (w) \tag{8.55}$$

To work out the crack opening at the bottom of the beam, produced by tension softening of CARDIFRC® $(w)_{FRC}$, the continuous closure stresses exerted by fibres are discretised again into infinitely many concentrated loads F, each acting on an infinitesimal crack length dy, as previously done.

The crack opening $(w)_F$ produced by one of these concentrated loads is calculated by using the compliance method. The corresponding compliance coefficient λ_F can be computed from energy principles

$$\lambda_F = \frac{2}{BE}\int_{y}^{\xi} Y(x,\beta)Y(x,y^*)dx \tag{8.56}$$

β: location where the crack opening is to be calculated

y^*: location where the pair of wedge splitting forces are applied to the crack face

Multiplying the above compliance factor by F gives:

$$(w)_F = \frac{2\sigma_c(w_y)BDdy^*}{BE}\int_{y^*}^{\xi} Y(x,\beta)Y(x,y^*)dx \tag{8.57}$$

To calculate the crack opening at the bottom of the beam due to tension softening of CARDIFRC®, the above equation is integrated over the length of the crack:

$$(w)_{FRC} = \int_0^{\xi}\left\{\frac{2D\sigma_c(w_y)}{E}\int_{y^*}^{\xi} Y(x,\beta)Y(x,y^*)dx\right\}dy^* \tag{8.58}$$

where $Y(x,\beta)$ and $Y(x,y^*)$ are given by Equation (8.50).

The unknown parameters in the equation of smooth closure of crack faces (8.44) and the equation of the crack opening compatibility (8.53) are the crack depth a, the crack mouth opening w and the applied load P. The two equations can be solved for all the possible crack depths and crack mouth openings, and the corresponding loads can be calculated. The intersection of the solutions of the two equations can be identified as sets of a, w and P that satisfy both the required conditions. From the calculated values of P and w, the theoretical P-w curve can be drawn.

For any set of values of crack opening displacement w and crack length a from the solution of the two equations, the corresponding value of w_y at the level of the application of the cohesive force F can be calculated, using equation $w_y = w(1 - c/a)$, which is based on the assumption of a linear crack profile. For this value of crack opening displacement w_y and by making use of the constitutive equation for the post-peak response of CARDIFRC®, the magnitude of the cohesive stress at the particular level of the beam can be calculated. Thereafter, the required value of the cohesive force F is given by:

$$F = \sigma_c(w_y)Bdc \tag{8.59}$$

This can be substituted into Equation (8.42) for the calculation of stress intensity factor K_I^f. Finally, in Equation (8.36), after the estimation of the partial deflection δ due to elastic and strain hardening response of the beam (pre-peak) using continuum damage mechanics, the contribution of the cohesive crack δ^*_P to the total deflection

value can be calculated, by making use of the values of a and P corresponding to w, used for the calculation of the cohesive force F.

8.2.5 Conclusions

As a conclusion to this part of the work, it can be said that the predictions of the damage mechanics based method are in a good agreement with the experimental results. Therefore, it can be considered as a reliable and useful tool for the calculation of the pre-peak nonlinear behaviour of CARDIFRC®. The good agreement of the model with the experimental curves is an additional verification of the proposed constitutive relation for the strain hardening part of CARDIFRC®. In combination with a fracture mechanics approach, such as the one above, the post-peak behaviour, when a cohesive crack is formed can also be modelled, resulting in a complete description of concrete flexural behaviour.

Another important outcome is the high value of the scalar damage parameter ω corresponding to the maximum stress σ_{max}, just before the formation of a crack in the beam. At this point, the value of ω is about 50% of its ultimate value.

CHAPTER 9: CONCLUSIONS AND RECOMMENDATIONS FOR FUTURE WORK

9.1 CONCLUSIONS

- The true fracture energy G_F of CARDIFRC® specimens cast almost two years prior to testing is significantly higher than the corresponding value of specimens tested at a young age (9-28 days). This is mainly attributed to the fact that during that time the specimens were stored in ambient conditions. Therefore, there was plenty of time for the unreacted material in the specimens to react chemically with the environmental water and for the specimens to develop a better bond between the randomly distributed fibres and the matrix, in addition to gaining in strength. It is suggested that these results be treated as upper limits on the CARDIFRC® size-independent specific fracture energy (Chapter 5).

- At the beginning of this experimental work, problems were encountered with the workability of the original mix. After many trials, it was decided to increase the superplasticiser/water ratios of the two mixes of CARDIFRC®. For Mix I this ratio was increased from 0.15 to 0.18 and for Mix II from 0.37 to 0.40. For the new ratios, tests were performed on cubes and cylinders, which showed that the strengths of the modified materials were higher than the original mixes. These higher *sp/w* ratios are likely to have produced denser and stiffer mixes (Chapter 6).

- The results of modulus of elasticity of the two mixes of CARDIFRC® are very close to the theoretical values, according to the Rule of Mixtures (50 GPa). For Mix I, E = 48 GPa and for Mix II, E = 50 GPa. The E-value of Mix II is slightly higher than Mix I, since Mix II contains coarser sand than Mix I (Chapter 6).

- CARDIFRC® beams were tested in 3-PB at higher rates of applied deformation/time than static tests, in order to examine the rate effect on the beam response. Although the testing rates were not as high as the rates applied in dynamic tests, an increase of the flexural strength of the material was observed (Chapter 6).

- The distribution of fibres within the matrix of the beam is a critical parameter affecting the fatigue performance of steel fibre reinforced concrete. It is, however, extremely difficult to achieve an even distribution of fibres in the mix. Failure to attain this goal may result in an extremely low fatigue life, whereas a proper and even fibre distribution can lead to an extremely long fatigue life. This is more evident in the case of HPFRCCs, where the interfacial bond between the fibres and the matrix is particularly strong, due to the dense structure of the material. This is verified by image analysis of the tested CARDIFRC® specimens (Chapters 6 and 7).

- The difficulty in achieving an even distribution of fibres is more pronounced in thicker specimens (e.g. 100 mm), whereas the even distribution can be achieved without problems in specimens with a relatively small thickness (e.g. 35 mm) (Chapter 6).

- CARDIFRC® specimens of dimensions 360x90x35 mm gave an excellent and absolutely consistent fatigue response, without significant internal damage. From the experimental results, it can be concluded that the endurance limit of the material is approximately at 85% of its flexural strength. This limit is very high, not very often observed in the relevant literature. This is an indication that CARDIFRC® has excellent flaw tolerance, which is also confirmed by direct tension tests performed by Benson (2003) (Chapter 6).

- Specimens tested earlier in fatigue up to a very high number of cycles without failure, were tested afterwards statically in three point bending. All specimens showed an increase in their flexural strength compared to the average strength obtained from control tests. This result confirms previously noted results in the literature, that prior cycling may lead to an improvement in strength, which is due to densification of the material caused by stress cycling (Chapter 6).

- All CARDIFRC® specimens subjected to fatigue exhibited a reduced stiffness, which is an indication that there is small internal damage in the specimens. However, this internal damage is very small and distributed and does not lead to the formation of a single localised crack. On the other hand, no certain conclusion

can be drawn regarding the effect of fatigue loading on the fracture energy, since the areas under the pre- and post-fatigue loading curves are approximately the same. The same lack of consistency in the results is also reported in the literature (Chapter 6).

- The change in compliance of a specimen is an indicator of the internal damage evolution due to fatigue loading. Therefore, it can be used to obtain a rough estimate of the total fatigue life of the particular specimen, only after a relatively small number of cycles. This may provide a quick means of controlling the quality of CARDIFRC® strips manufactured on a mass scale in a factory (Chapter 6).

- In order to verify that the mixing and compaction procedures used to make CARDIFRC® do indeed result in the steel fibres being uniformly distributed in the hardened CARDIFRC®, both destructive and non-destructive techniques can be applied. The destructive method consists of the traditional image analysis, whereas the non-destructive method is a novel technique of computerised tomography (CT) imaging (Chapter 7).

- Despite the many potential sources of error, a careful examination of the X-ray absorption density contours and the corresponding fibre count contours reveals a reasonable correlation between the two measurements in the larger sections examined by the two techniques. From the plots of the actual X-ray absorption densities at grid centres against the fibre counts per grid, it is clear that the X-ray absorption correlates reasonably linearly with the fibre count in the thicker specimens, irrespective of their shapes. In the thin strips the correlation is poor (Chapter 7).

- The image analysis of the specimens tested under fatigue loading shows that higher average number of fibres across the plane of failure result in an extended fatigue life of the specimen. Moreover, lower standard deviations and coefficients of variation correspond to specimens with more even distribution of fibres, and thus to a higher number of cycles to failure (Chapter 7).

- The nonlinear cracked hinge model permits the stress-crack opening relationship to be modelled by a bilinear curve, allowing for the modelling of a broad range of FRC materials. In the case of CARDIFRC®, two bilinear approximations were selected, which were based on the constitutive behaviour of the material in tension. The predictions of the hinge model based on these bilinear approximations are in very good agreement with the experimental results. This is an additional verification of the proposed constitutive relation for the tension softening part of CARDIFRC® (Chapter 8).

- Damage mechanics can be considered as a reliable and useful tool for the calculation of the pre-peak nonlinear behaviour of CARDIFRC®. The good agreement of the model with the experimental results is an additional verification of the proposed constitutive relation for the strain hardening part of CARDIFRC®. In combination with a fracture mechanics approach, the post-peak behaviour, when a cohesive crack has formed can also be modelled, resulting in a complete description of the flexural behaviour (Chapter 8).

9.2 RECOMMENDATIONS FOR FUTURE WORK

- It is suggested that the true fracture energy G_F of CARDIFRC® be re-evaluated on specimens stored in ambient conditions, for more than two years. This will give an additional indication of the effect of ageing and further hydration on G_F value of CARDIFRC®.

- The dynamic response of CARDIFRC® under high strain/stress rates can be a subject of extreme interest for future work. This can be combined with the investigation of the response of structures strengthened and/or repaired with CARDIFRC® strips, under dynamic loading.

- In order to verify the experimental work, it is recommended that the fatigue behaviour of CARDIFRC® specimens be modelled, using one of the proposed models in the relevant literature.

- Although it is strongly believed that the chosen grid of 10 mm x 10 mm used in image analysis of CARDIFRC® sections is the optimum, it would be interesting to compare the results with a 5 mm x 5 mm mesh grid.

- Finally, it is suggested that a computer program should be developed for the application of the fracture mechanics method for the determination of the complete post-peak static flexural response of CARDIFRC®, analysed in Chapter 8.

LIST OF REFERENCES

Abdalla H.M and Karihaloo B.L. *Determination of size-independent specific fracture energy of concrete from three-point bend and wedge splitting tests*. Magazine of Concrete Research, 55, No.2, April, 2003, pp. 133-141.

ACI Committee 1988. *Measurements of properties of fiber reinforced concrete*. ACI Material Journal, 1988, pp. 588-589.

ACI Committee 215. *Considerations for design of concrete structures subjected to fatigue loading*. American Concrete Institute, Detroit, USA, 1986.

ACI Committee 446.1R. *Fracture mechanics of concrete: Concepts, models and determination of material properties*. American Concrete Institute, Detroit, USA, 1991.

Alaee F.J. *Retrofitting of concrete structures using high performance fibre reinforced cementitious composite (HPFRCC)*. PhD Thesis, Cardiff University, United Kingdom, 2002.

Anthony E. and Newman K. *The structure of concrete and its behaviour under load.* Proceeding of an International Conference, London, UK, 1965.

Bache H.H. *Compact reinforced composite. Basic principles*. CBL Report No.41, Aalborg Portland, Denmark, Cement-og Betonlaboratoriet, 1987.

Bache H.H. *Densified cement ultra-fine particle-based materials*. CBL Report No.40, pp. 35, Aalborg Portland, Denmark, 1981.

Balaguru P.N. and Kendzulak J. *Flexural behaviour of slurry infiltrated fibre concrete (SIFCON) made by using condensed silica fume*. In "Fly Ash, Silica Fume, Slag and natural Pozzolans in Concrete", SP-91, ACI, Detroit, 1986, pp. 1215-1229.

Balaguru P.N. and Shah S.P. *Fibre-reinforced cement composites*. McGraw-Hill, New York, 1992.

Ballatore E. and Bocca P. *Variations in the mechanical properties of concrete subjected to low cyclic loads*. Cement and Concrete Research, 27(3), 1997, pp. 453-462.

Barenblatt G.I. *On equilibrium cracks forming during brittle fracture (in Russian)*. Prikladnaya Matematica I Mekhanika (PMM), 23, 1959, pp. 434-444. (See also, *The mathematical theory of equilibrium cracks in brittle fracture*. Advances in Applied Mechanics, 7, 1962, pp. 55-129).

Bazant Z.P. and Oh B.H. *Crack band theory for fracture of concrete*. Materials and Structures, 16, 1983, pp. 155-157.

Bazant Z.P. *Size effect in blunt fracture: concrete, rock, metal*. ASCE Journal of Engineering Mechanics, 110, 1984, pp. 518-535.

Benson S.D.P. and Karihaloo B.L. *CARDIFRC® - Manufacture and constitutive behaviour*. 4th International Workshop on HPFRCC, RILEM, Naaman A. and Reinhardt H.W. (eds), Ann Arbour, USA, 2003.

Benson S.D.P. *CARDIFRC - Development and constitutive behaviour*. PhD Thesis, Cardiff University, UK, 2003.

Benson S.D.P. *Retrofitting damaged reinforced concrete flexural members with HPFRCC*. MEng Thesis, Cardiff University, UK, 1999.

Bentur A., Mindess S. and Banthia N. *The behaviour of concrete under impact loading: experimental procedures and method of analysis*. Matériaux et Constructions, Vol.19, No.113, 1986.

Bilby B.A., Cottrell A.H. and Swinden K.H. *The spread of plastic yield from a notch*. Proceedings of Royal Society, London, UK, A272, 1963, pp. 304-314.

Brara A., Camborde F., Klepaczko J.R. and Mariotti C. *Experimental and numerical study of concrete at high strain rates in tension.* Mechanics of Materials, 33, 2001, pp. 33-45.

Brown W.F. and Srawley J.E. *Plane strain crack toughness testing of high strength metallic materials.* Special Technical Publication STP410 American Society for Testing and Material (ASTM), Philadelphia, USA, 1966, p.163.

BS 1881: part 116. *Testing concrete: method for determination of compressive strength of concrete cubes.* British Standards Institution, London, UK, 1983.

BS 1881: part 117. *Testing concrete: method for determination of tensile splitting strength.* British Standards Institution, London, UK, 1983.

BS 1881: part 118. *Testing concrete: method for determination of flexural strength.* British Standards Institution, London, UK, 1983.

BS 1881: part 121. *Testing concrete: method for determination of static modulus of elasticity in compression.* British Standards Institution, London, UK, 1983.

Cachim P.B, Figueiras J.A, Pereira P.A.A. *Numerical modelling of fibre-reinforced concrete fatigue in bending.* International Journal of Fatigue, 24, 2002, pp. 381-387.

Cachim P.B., Figueiras J.A. and Pereira P.A.A. *Fatigue behaviour of fiber-reinforced concrete in compression.* Cement and Concrete Composites, 24, 2002, pp. 211-217.

Cadoni E., Albertini C., Labibes K. and Solomos G. *Behaviour of plain concrete subjected to tensile loading at high strain-rate.* Proceedings of FRAMCOS-2001 (ed. de Borst et al.), Swets & Zeitlinger, Lisse, ISBN 90 2651 825 0, France, 2001.

Cangiano S., Plizzari G.A and Slowik V. *Experimental investigation into the fatigue crack growth in concrete.* Proceedings of FRAMCOS-3, AEDIFICATIO Publishers, D-79104 Freiburg, Germany, 1997.

CARDIFRC® patent number GB 0109686.6, Karihaloo B.L., Benson S.D.P. and Alaee F.J., 2001.

Chang D. and Chai W.K. *Flexural fracture and fatigue behaviour of steel-fiber-reinforced concrete structures*. Nuclear Engineering and Design, 156, 1995, pp. 201-207.

Coster M. and Chermant J-L. *Image analysis and mathematical morphology for civil engineering material*. Cement and Concrete Composites, 23, 2001, pp. 133-151.

Crofton M.W. *Probability*, Encyclopaedia Brittanica, 9th ed., vol.19, pp. 768-788.

Curbach M., Hehn K.H. and Eibl J. *Measurement of crack velocity*. Experimental Techniques, 1989, pp. 25-27.

Duan K., Hu X.Z. and Wittmann F.H. *Boundary effect on concrete fracture induced by non-constant fracture energy distribution*. In Fracture Mechanics of Concrete Structures (R. De Borst, J. Mazars, G. Pijaudier-Cabot and J.G.M. Van Mier (Eds)), Proc. FRAMCOS-4, A.A. Balkema Publishers, Rotterdam, 2001, pp. 49-55.

Dugat J, Roux N. and Bernier G. *Mechanical properties of reactive powder concretes (RPC)*. Materials and Structures, 29, 1996, pp. 133-240.

Dugdale D.S. *Yielding of steel sheets containing slits*. Journal of the Mechanics and Physics of Solids, 8, 1960, pp. 100-104.

Elices M., Guinea G.V. and Planas J. *Measurement of the fracture energy using three-point bend tests: part 3-Influence of cutting the P-δ tails*. Materials and Structures, 1992, 25, pp. 327-334.

Francois D. *Microcracking and damage in concrete*. Toughening Mechanisms in Quasi-Brittle Materials (ed. Shah S.P.), Kluwer Academic Publishers, Netherlands, 1991, pp. 53-65.

Gary G. and Bailly P. *Behaviour of quasi-brittle material at high strain rate. Experiment and modelling.* European Journal of Mechanics and Solids, 17(3), 1998.

Gopalaratnam V.S and Shah S.P. *Properties of steel fibre reinforced concrete subjected to impact loading.* Journal of the American Concrete Institute, 83(1), 1986, pp. 117-126.

Gopalaratnam V.S., Shah S.P. and John R. *A modified instrumented Charpy test for cement-based composites.* Experimental Mechanics, 1984, pp. 102-111.

Grady D.E. *The spall strength of condensed matter.* Journal of Mechanics and Physics of Solids, 36(3), 1988, pp. 353-384.

Griffith A.A. *The phenomena of rapture and flow in solids.* Philosophical Transactions of Royal Society, London, A221, 1920, pp. 163-198.

Grote D.L., Park S.W. and Zhou M. *Dynamic behaviour of concrete at high strain rates and pressures: I. experimental characterisation.* International Journal of Impact Engineering, 25, 2001, pp. 869-886.

Guinea G.V., Pastor J.Y., Planas J. and Elices M. *Stress intensity factor, compliance and CMOD for a general three-point bend beam.* International Journal of Fracture, 89, 1998, pp. 103-116.

Guinea G.V., Planas J. and Elices M. *Measurement of the fracture energy using three-point bend tests: part 1-Influence of experimental procedures.* Materials and Structures, 25, 1992, pp. 212-218.

Hawkins N.M. *The role of fracture mechanics in conventional reinforced concrete design. Application of fracture mechanics to cementitious composites.* NATO Advanced Research Workgroup, Evanston, USA, Shah S.P., Martinus Nijhoff (editors), Dordrecht, 1985, pp. 639-666.

Hillerborg A. *Analysis of fracture by means of the fictitious crack mode, particularly for fiber-reinforced concrete.* International Journal of Cement Composites, 2(4), 1980, pp. 177-184.

Hillerborg A. *Analysis of one single crack.* In F.H. Wittmann (editor), Fracture Mechanics of Concrete, Elsevier, Amsterdam, 1983, pp. 223-249.

Hillerborg A. *The theoretical basis of a method to determine the fracture energy G_F of concrete.* Materials and Structures, 18, 1985, pp. 291-296.

Hillerborg A., Modeer M. and Petersson P.E. *Analysis of crack formation and crack growth in concrete by means of fracture mechanics and finite elements.* Cement and Concrete Research, 6(6), 1976, pp. 773-782.

Hopkinson B. *A method of measuring the pressure in the deformation of high explosive by impact of bullets.* Philosophical Transactions of the Royal Society of London, London, A213, 1914, pp. 437-452.

Hordijk D.A. and Reinhardt H.W. *Growth of discrete cracks in concrete under fatigue loading.* Toughening Mechanisms in Quasi-Brittle Materials (ed. Shah S.P.), Kluwer Academic Publishers, Netherlands, 1991, pp. 541-554.

Horii H., Hasegawa A. and Nishino F. *Fracture process and bridging zone model and influencing factors in fracture of concrete.* Fracture of Concrete and Rock (eds. Shah S.P. and Swartz S.E), Springer-Verlag, New York, 1989, pp. 205-219.

Horii H., Shin H.C. and Pallewatta T.M. *An analytical model of fatigue crack growth in concrete.* Proceedings of Japan Concrete Institute, 14, 1990, pp. 841-846.

Horii H., Shin H.C. and Pallewatta T.M. *Mechanism of fatigue crack growth in concrete.* Cement and Concrete Composites, 14, 1992, pp. 83-89.

Hoy C.W. and Bartos P.J.M. *Interaction and packing of fibers: Effects on the mixing process*. In High Performance Fiber Reinforced Cement Composites (HPFRCC3), Reinhardt H.W. and Naaman A.E. (eds), RILEM Publishers, 1999, pp. 181-191.

Hu X.Z. and Wittmann F.H. *Fracture energy and fracture process zone*. Materials and Structures, 25, 1992, pp. 319-326.

Hu X.Z. and Wittmann F.H. *Size effect on toughness induced by crack close to free surface*. Engineering Fracture Mechanics, 65, 2000, pp. 209-211.

Hu X.Z. Fracture *process zone and strain softening in cementitious materials*. ETH Building Materials Report No.1, ETH, Switzerland, AEDIFICATIO, Freiburg, 1995.

Hughes G. and Beeby A.W. *Investigation of the effect of impact loading on concrete beams*. The Structural Engineer, 60B, No.3, 1982, pp. 45-52.

Inglis C.E. *Stress in a plate due to the presence of cracks and sharp corners*. Transactions of the Institution of Naval Architects, 1913, pp. 219-241.

Irwin G.R. *Analysis of stresses and strains near the end of a crack traversing a plate*. ASME Journal of Applied Mechanics, 24, 1957, pp. 361-364.

Jain A.K. *Fundamentals of digital image processing*. Prentice Hall, USA, 1989.

Jeng Y.S. and Shah S.P. *Two parameter fracture model for concrete*. Journal of Engineering Mechanics, ASCE, Vol.111, October, 1985, pp. 1227-1241.

John V. *Testing of materials*. Macmillan, 1992.

Jun Z. and Stang H. *Fatigue performance in flexure of fiber reinforced concrete*. American Concrete Institute Materials Journal, 95(1), 1998, pp. 58-67.

Jun Z., Stang H. and Li V.C. *Fatigue life prediction of fiber reinforced concrete under flexural load*. International Journal of Fatigue, 21, 1999, pp. 1033-1049.

Karihaloo B.L. and de Vriese K.M.B. *Short-fibre reinforced reactive powder concrete*. Concrete Communication Conference, BCA, 1999, pp. 67-77.

Karihaloo B.L. and Jefferson A.D. *Looking into concrete*. Magazine of Concrete Research, 53, No.2, April, 2001, pp. 135-147.

Karihaloo B.L. and Lange-Kornbak D. *Optimisation techniques for the design of high performance fibre-reinforced concrete*. Structural and Multidisciplinary Optimisation, 21, 2001, pp. 32-39.

Karihaloo B.L. and Wang J. *Mechanics of fibre-reinforced cementitious composites*. Computers and Structures, 76, 2000, pp. 19-34.

Karihaloo B.L. and Xiao Q.Z. *Higher order terms of the crack tip asymptotic field for a notched three-point bend beam*. International Journal of Fracture 112, 2001, pp. 111-128.

Karihaloo B.L. *Fracture mechanics and structural concrete*. Addison Wesley Longman, London, 1995.

Karihaloo B.L., Abdalla H.M and Imjai T. *A simple method for determining the true specific fracture energy of concrete*. Magazine of Concrete Research, 55, No.5, October, 2003, pp. 471-481.

Karihaloo B.L., Alaee F.J. and Benson S.D.P. *A new technique for retrofitting damaged concrete structures*. Concrete Communication Conference, 2001, pp. 293-304.

Karihaloo B.L., Alaee F.J. and Benson S.D.P. *A new technique for retrofitting damaged concrete structures*. Proceeding of the Institution of Civil Engineers, Building and Structures, 152(4), 2002, pp. 309-318.

Karihaloo B.L., Benson S.D.P, Didiuk P.M., Fraser S.A., Hamill N. and Jenkins T.A. *Retrofitting damaged RC beams with high-performance fibre-reinforced concrete.* Proc Concrete Communication Conf, British Cement Association, 2000, pp. 153-164.

Karihaloo B.L., Wang J. and Grzybowski M. *Doubly periodic arrays of bridged cracks and short fibre-reinforced cementitious composites.* Journal of the mechanics and physics of solids, 44(10), 1996, pp. 1565-1586.

Kessler C. and Muller H.S. *Experimental investigations on fracture and damage of concrete due to fatigue.* Proceedings of FRAMCOS-3, AEDIFICATIO Publishers, D-79104 Freiburg, Germany, 1997.

Kim J.K. and Kim Y.Y. *Experimental study of the fatigue behaviour of high strength concrete.* Cement and Concrete Research, 26(10), 1996, pp. 1513-1523.

Kim J.K. and Kim Y.Y. *Fatigue crack growth of high strength concrete in wedge splitting test.* Cement and Concrete Research, 29, 1999, pp. 705-712.

Klepaczko J.R. and Brara A. *An experimental method for dynamic tensile testing of concrete by spalling.* International Journal of Impact Engineering, 25, 2001, pp. 387-409.

Kolsky H. *An investigation of the mechanical properties of materials at very high rates of loading.* Proceedings of Physics Society, London, B 62:676, 1949.

Lambert D. and Ross C. *Dynamic fracture, crack velocity and strength response of cementitious materials.* Proceedings of FRAMCOS-3, AEDIFICATIO Publishers, D-79104 Freiburg, Germany, 1997.

Lambert D.E. and Ross C.A. *Strain rate effects on dynamic fracture and strength.* International Journal of Impact Engineering, 24(10), 2000, pp. 985-998.

Lange-Kornbak D. and Karihaloo B.L. *Tension softening of fibre-reinforced cementitious composites.* Cement and Concrete Composites, 19, 1997, pp. 315-328.

Lankard D.R. and Newell, J.K. *Preparation of highly reinforced steel fibre reinforced concrete composites*. ACI Special Publication, SP-81, American Concrete Institute, Detroit, 1984, pp. 286-306.

Lee M.K. and Barr B.I.G. *An overview on the fatigue behaviour of plain and fibre reinforced concrete*. Cement and Concrete Composites, 26, 2004, pp. 299-305.

Lewis J.A and Kriven W.M. *Microstructure property relationships in Macro-Defect-Free Cement*. MRS Bulletin, 1993, pp. 72-77.

Li V.C. and Matsumoto T. *Fatigue crack growth analysis of fiber reinforced concrete with effect of interfacial bond degradation.* Cement and Concrete Composites, 20, 1998, pp. 339-351.

Li V.C. *A simplified micromechanical model of compressive strength of fibre reinforced cementitious composites*. Cement and Concrete Composites, 14, 1992b, pp. 131-141.

Li V.C. *Engineered cementitious composites-tailored composites through micromechanical modelling.* Fiber reinforced concrete: Present and Future, Canadian Society for Civil Engineering, Montreal, 1998, pp. 64-97.

Li V.C. *From micromechanics to structural engineering- the design of cementitious composites for civil engineering applications. JSCE* Journal of Structural Mechanics and Earthquake Engineering, 10(2), 1993, pp. 37-48.

Li V.C., Stang H. and Krenchell H. *Micromechanics of crack bridging in fibre-reinforced concrete*. Materials and Structures, 26, 1993, pp. 486-494.

Li V.C., Wang Y. and Backer S. *A micromechanical model of tension softening and bridging toughening of short random fibre reinforced brittle matrix composites.* Journal of the Mechanics and physics of Solids, 39(5), 1991, pp. 607-625.

Lyons P. *The influence of superplasticiser on the mechanical properties of CARDIFRC®*. BEng Thesis, Cardiff University, 2002.

Matsumoto T. and Li V.C. *Fatigue life analysis of fiber reinforced concrete with a fracture mechanics based model*. Cement and Concrete Composites, 21, 1999, pp. 249-261.

Mihashi H. and Wittmann F.H. *Stochastic approach to study the influence of rate of loading on strength of concrete*. Heron, 25(3), 1980.

Mobasher B., Stang H. and Shah S.P. *Microcracking in fibre reinforced concrete*. Cement and Concrete Research, 20, 1990, pp. 665-676.

Morin V., Cohen Tenoudji F., Feylessoufi A. and Richard P. *Superplasticizer effects on setting and structuration mechanisms of ultrahigh-performance concrete*. Cement and concrete Research, 31, 2001, pp. 63-71.

Morton R.R.A. *The expected number and angle of intersections between random curves in a plane*. J. Appl. Probability, 3, 1966, pp. 559-562.

Naaman A.E. and Hammoud H. *Fatigue characteristics of high performance fiber-reinforced concrete*. Cement and Concrete Composites, 20, 1998, pp. 353-363.

Naaman A.E. and Harajli M.H. *Mechanical properties of high performance fiber concretes: a state-of-the-art report (SHRP-C/WP-90-004)*. SHRP National Research Council, Washington DC, 1990.

Naaman A.E. *SIFCON: tailored properties for structural performance, in high performance fibre reinforced cement composites*. Proceedings of the International RILEM/ACI Workshop, Reinhardt H.W. and Naaman A.E. (eds), Mains, Germany, 1991, pp. 18-38.

Naaman A.E., Reinhardt H.W. and Fritz C. *Reinforced concrete beams using SIFCON as a matrix*. Darmstadter Massivbau Report, Germany, 1990, 85 pages.

Naaman, A.E. and Shah S.P. *Pull-out mechanism in steel fibre reinforced concrete.* ASCE Journal of the Structural Division, 102(ST8), 1976, pp. 1537-1548.

Nanakorn P. and Horii H. *Back analysis of tension softening relationship of concrete.* Journal of Materials, Concrete Structures and Pavements, JSCE, 544/32, 1997, pp. 265-275.

Neville A.M. *Properties of concrete*, 4th Edn. Longman Group, UK and New York: John Wiley & Sons, 1995.

Nielsen L.F. *Stiffness of fibre composite.* Report TR-264, Technical University of Denmark, 1992.

Okada T. and Horii H. *Effect of specimen size and loading rate on the tension softening curve obtained by back analysis method.* Proceedings of FRAMCOS-3, AEDIFICATIO Publishers, D-79104 Freiburg, Germany, 1997.

Olesen J.F. *Fictitious crack propagation in fiber-reinforced concrete beams.* Journal of Engineering Mechanics, 127(3), 2001, pp. 272-280.

Ortiz M. *Microcrack coalescence and macroscopic crack growth initiation in brittle solids.* International Journal of Solids and Structures, 24, 1988, pp. 231-250.

Parthasarathy T.A and Kerans R.J. *Failure of ceramic composites.* Air Force Research Laboratory, Materials and Manufacturing Directorate, AFRL/MLLM, 2002.

Peng X. and Meyer C. *A continuum damage mechanics model for concrete reinforced with randomly distributed short fibers.* Computers and Structures, 78, 2000, pp. 505-515.

Petersson P.E. *Fracture energy of concrete: method of determination.* Cement and Concrete Research, 10, 1980, pp. 78-89.

Petersson P.E. *Fracture energy of concrete: practical performance and experimental results*. Cement and Concrete Research, 10, 1980, pp. 91-101.

Ramakrishnan V. and Lokvik B.J., *Flexural fatigue strength of fiber reinforced concretes*. High performance fiber reinforced cement composites (eds. Reinhardt H.W. and Naaman A.E.), RILEM Proceedings 15, Chapman and Hall, London, 1992.

Ramakrishnan V., Meyer C., Naaman A.E., Zhao G., Fang L. *Cyclic behaviour, fatigue strength, endurance limit and models for fatigue behaviour of FRC*. High performance fiber reinforced cement composites (eds. Naaman A.E. and Reinhardt H.W.), E & FN Spon, London, ISBN 0 419 21180 2, UK, 1996.

Reinhardt H.W. *Fibres and cement, a useful co-operation.* Introductory note, High Performance Fibre Reinforced Cement Composites, Proceedings of the International RILEM/ACI Workshop, Reinhardt H.W. and Naaman A.E. (eds), Mains, Germany, 1991.

Reinhardt H.W. *Loading rate, temperature and humidity effects*. University of Stuttgart, Stuttgart, Germany, 1990.

Richard P. and Cheyrezy M.H. *Composition of reactive powder concretes*. Cement and Concrete Research, 25(7), 1995, pp.1501-1511.

Richard P. and Cheyrezy M.H. *Reactive powder concretes with high ductility and 200-800 MPa compressive strength.* ACI Spring Convention, San Francisco, USA, 1994.

RILEM Committee FMC 50, *Determination of the fracture energy of mortar and concrete by means of the three-point bend tests on notched beams*. Materials and Structures, 18, 1985, pp. 285-290.

Rokugo K., Iwase H., Kunieda M., Kamada T., Suzuki M., Taki K. and Fujimoto Y. *Evaluation and improvement of performance of concrete beams against impact loading*. Proceedings of FRAMCOS-2001 (ed. de Borst et al.), Swets & Zeitlinger, Lisse, ISBN 90 2651 825 0, France, 2001.

Russ. J.C. *The image processing handbook*. CRC Press, USA, 1995.

Sarkar B.K. and Roy R. *Behaviour of carbon fibre reinforced vinylester resin composite under impact fatigue*. Proceedings of ACUN-3 Technology Convergence in Composites Applications, UNSW, Sydney, 2001, pp. 368-376.

Server W.L, Wullaert R.A and Sheckhard J.W. *Evaluation of current procedures for dynamic fracture toughness testing*. ASTM STP 631, 1977, pp. 446-461.

Shah S.P, Peled A., Aldea C.M. and Akkaya Y. *Scope of high performance fibre reinforced cement composites*. In Third International Workshop on High Performance Fibre Reinforced Cement Composites (HPFRCC3), Reinhardt H.W. and Naaman A.E. (eds), Mains, Germany, 1999, pp. 113-129.

Shah S.P. and Young J.F. *Current research at the NSF Science and Technology Centre for Advanced Cement-Based Materials*. American Ceramic Society Bulletin, 1990, pp. 1319-1331.

Shah S.P., Swartz S.E. and Ouyang C. *Fracture mechanics of concrete: applications of fracture mechanics to concrete, rock and other quasi-brittle materials*. John Wiley and Sons, USA, 1995.

Shannag M.J. and Hansen W. *Tensile properties of fibre-reinforced very high strength DSP mortar*. Magazine of Concrete Research, 52(2), 2000, pp. 101-108.

Singh S.P. and Kaushik S.K. *Fatigue strength of steel fibre reinforced concrete in flexure*. Cement and Concrete Composites, 25, 2003, pp. 779-786.

Singh S.P. and Kaushik S.K. *Flexural fatigue life distributions and failure probability of steel fibrous concrete.* ACI Materials Journal, November-December, 2000.

Solomon H. *Geometric probability.* Society for Industrial and Applied Mathematics, USA, 1978.

Suaris W. and Shah S.P. *Inertial effects in the instrumented impact testing of cementitious composites.* ASTM Journal of Cement, Concrete and Aggregates, 3(2), 1981, pp. 77-83.

Suaris W. and Shah S.P. *Properties of concrete subjected to impact.* ASCE Journal of Structural Division, 109(7), 1983, pp. 1727-1741.

Suaris W. and Shah S.P. *Strain rate effects in fibre-reinforced concrete subjected to impact and impulsive loading.* Composites, April, 1982.

Sullivan A.P. *The effect of hydrothermal curing at 90℃ and the use of 12 mm steel fibres on reactive powder concrete.* MSc Thesis, Cardiff University, 1999.

Tada H., Paris P. and Irwin G. *The stress analysis of cracks handbook.* 1st Edition, St. Louis, Missouri: Paris Productions, 1985.

Tada H., Paris P. and Irwin G. *The stress analysis of cracks handbook.* 2nd Edition, St. Louis, Missouri: Paris Productions, 1985b.

Tjiptobroto P. and Hansen W. *Tensile strain hardening and multiple cracking in high-performance cement-based composites containing discontinuous fibres.* ACI Materials Journal, 90(1), 1993, pp. 16-25.

Toumi A., Bascoul A. and Turatsinze A. *Microscopical observation of mode I crack propagation in concrete subjected to fatigue.* Proceedings of FRAMCOS-3, AEDIFICATIO Publishers, D-79104 Freiburg, Germany, 1997.

Uchida Y., Kurihara N., Rokugo K. and Koyanagi W. *Determination of tension softening diagrams of various kinds of concrete by numerical analysis*. Proceedings of FRAMCOS-2 (ed. Wittmann F.H.), AEDIFICATIO Publishers, Zurich, Germany, 1995.

Ueda T., Sato Y., Kakuta Y. and Tadokoro T. *A study on crack propagation in concrete under cyclic loading*. Proceedings of FRAMCOS-3, AEDIFICATIO Publishers, D-79104 Freiburg, Germany, 1997.

Ulfkjær J., Krenk S. and Brincker R. *Analytical model for fictitious crack propagation in concrete beams*. Journal of Engineering Mechanics, 121(1), 1995, pp. 7-15.

Ulfkjaer J., Labibes K., Solomos G. and Albertini C. *Tensile failure of normal concrete and steel fibre reinforced concrete at high strain rates*. Proceedings of FRAMCOS-2001 (ed. de Borst et al.), Swets & Zeitlinger, Lisse, ISBN 90 2651 825 0, France, 2001.

Wang J. and Karihaloo B.L. *Material instability in the tensile response of short-fibre-reinforced quasi-brittle composites*, Archives of Mechanics, 52, 2000, pp. 839-855.

Weerheijm J. and Reinhardt H.W. *Modelling of concrete fracture under dynamic tensile loading*. Fracture of concrete and rock-recent developments (eds. Shah S.P., Swartz S.E. and Barr B.), Elsevier, London, 1989, pp. 721-728.

Wei S., Jianming G. and Yun Y. *Study of the fatigue performance and damage mechanism of steel fiber reinforced concrete*. ACI Materials Journal, May-June, 1996.

Yan H., Sun W. and Chen H. *The effect of silica fume and steel fiber on the dynamic mechanical performance of high strength concrete*. Cement and Concrete Research, 29, 1999, pp. 423-426.

Zanni H., Cheyrezy M., Maret V., Philipot S. and Nieto P. *Investigation of hydration and pozzolanic reaction in reactive powder concrete (RPC) using ^{29}Si NMR*. Cement and Concrete Research, 26(1), 1996, pp. 93-100.

Zhang B., Bicanic N., Pearce C.J. and Balabanic G. *Residual fracture properties of normal- and high-strength concrete subject to elevated temperatures*. Magazine of Concrete Research, 52, No.2, April, 2000, pp. 123-136.

Zhao H. and Gary G. *Analysis of specific experimental problems in dynamic testing of concrete*. Proceedings of FRAMCOS-3, AEDIFICATIO Publishers, D-79104 Freiburg, Germany, 1997.

Zhao H. and Gary G. *On the use of SHPB techniques to determine the dynamic behaviour of materials in the range of small strains*. International Journal of Solids and Structures, 33, 1996, pp. 3363-3375.

Appendix A

Fatigue Test Results

Fatigue Response (10-80% P_u) of CARDIFRC® - Mix I Beams (360x90x35 mm)

Test 1 (1000000 Cycles)

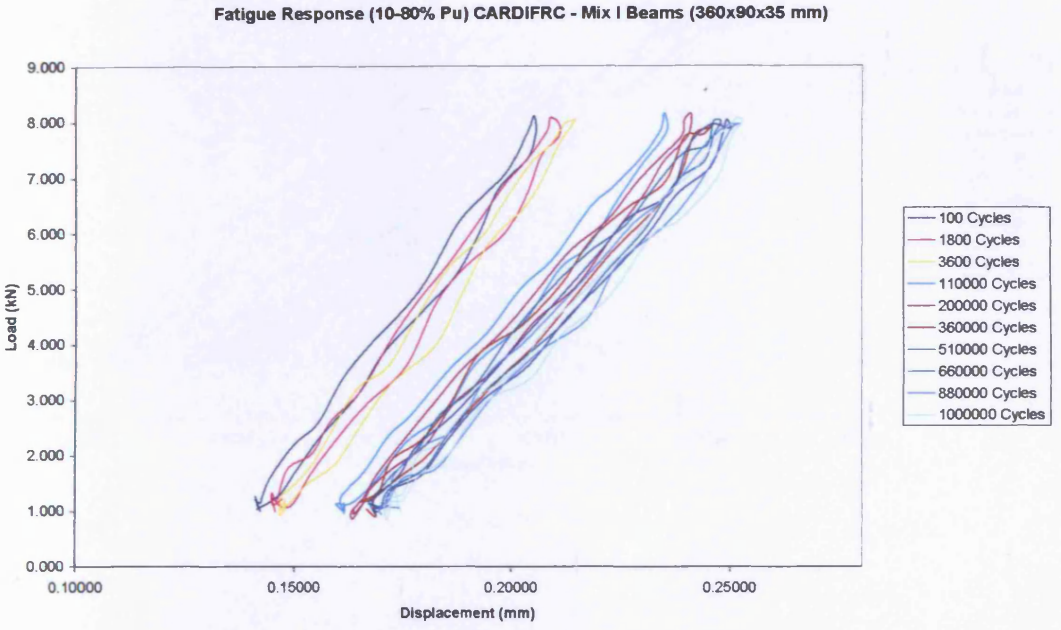

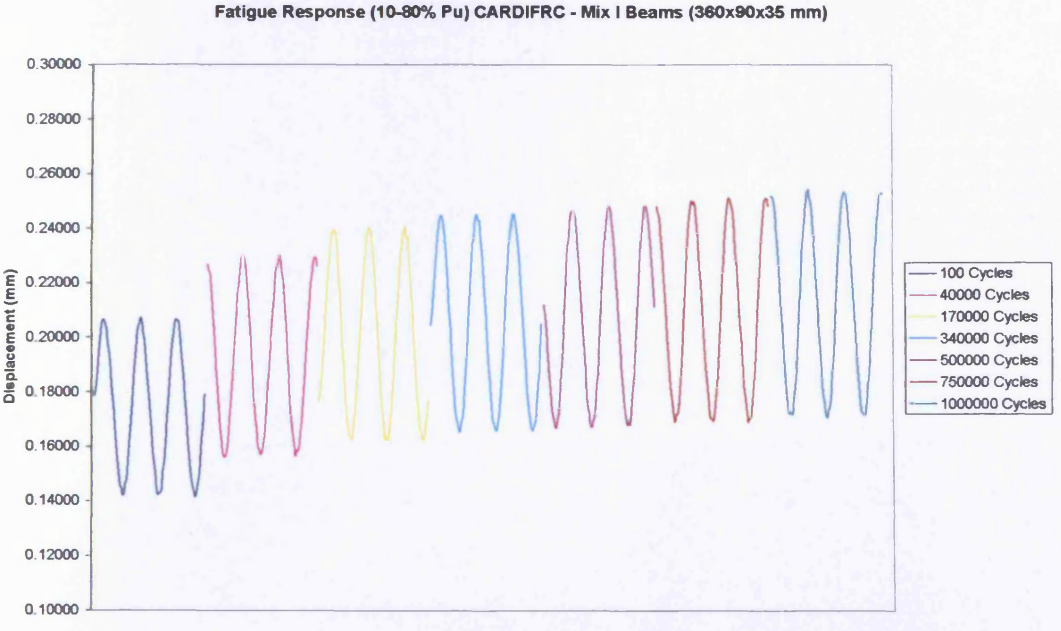

Test 2 (1000000 Cycles)

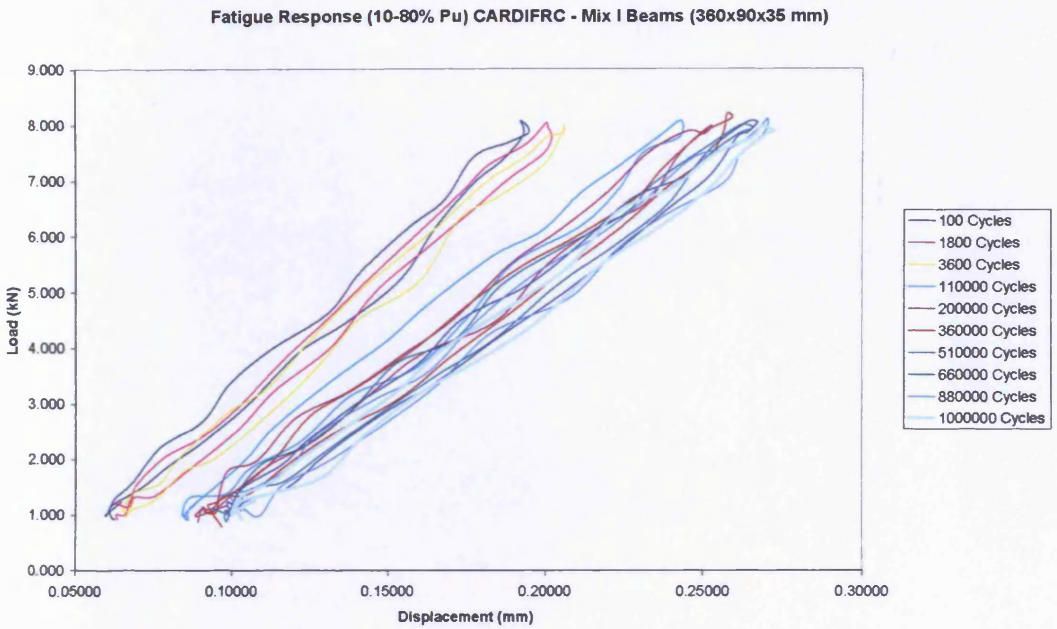

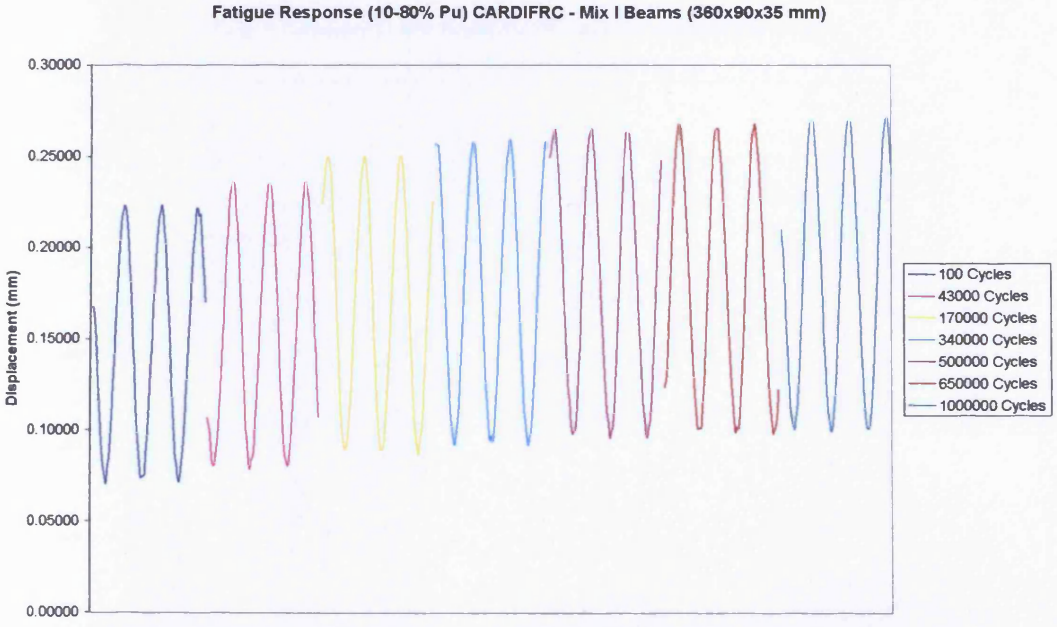

Test 3 (1000000 Cycles)

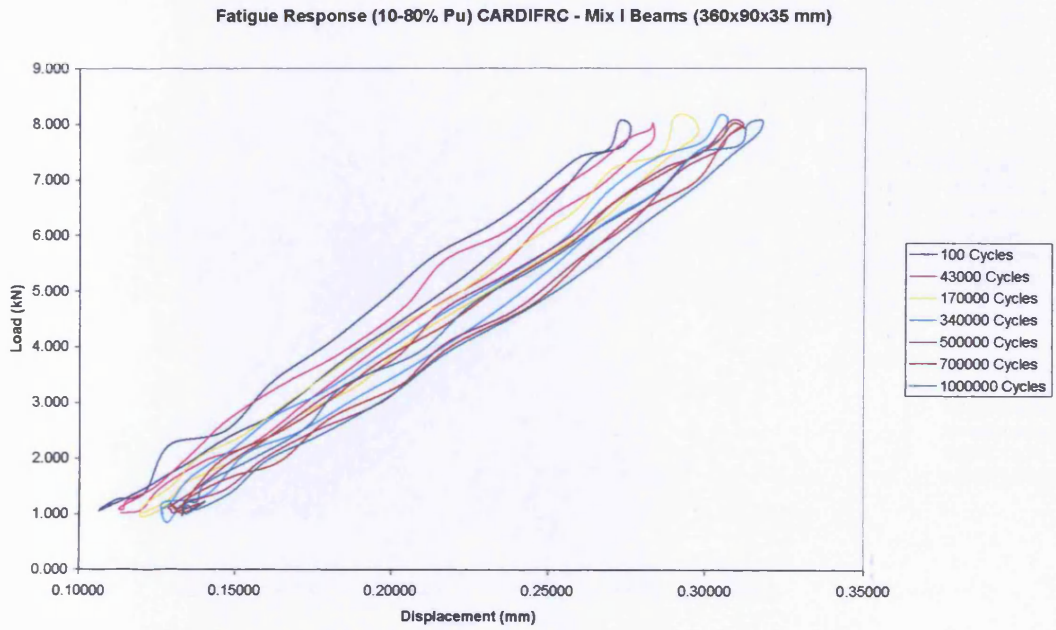

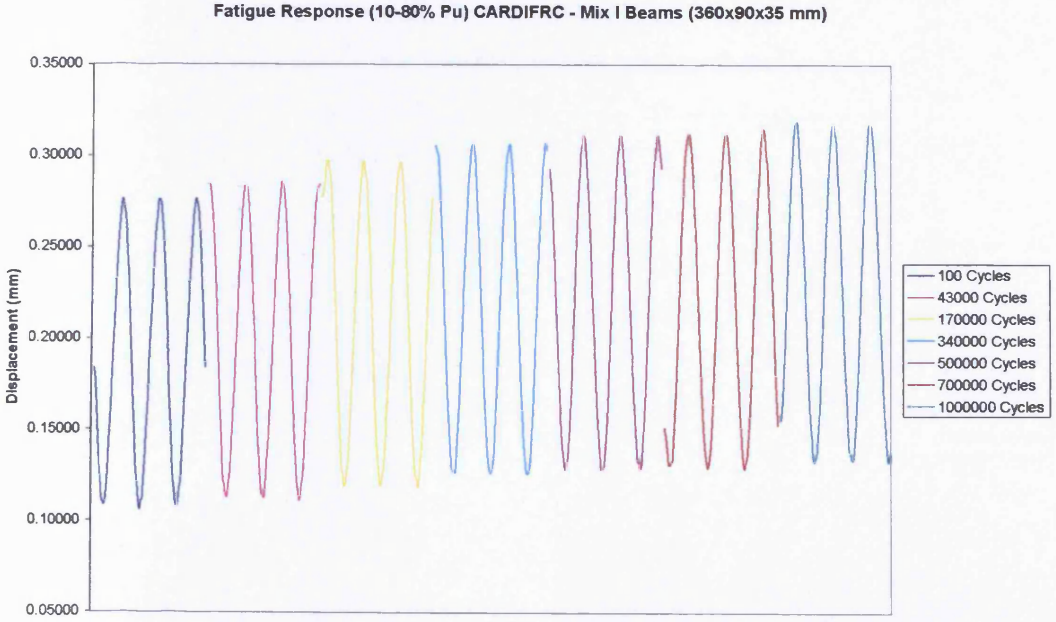

Test 4 (2000000 Cycles)

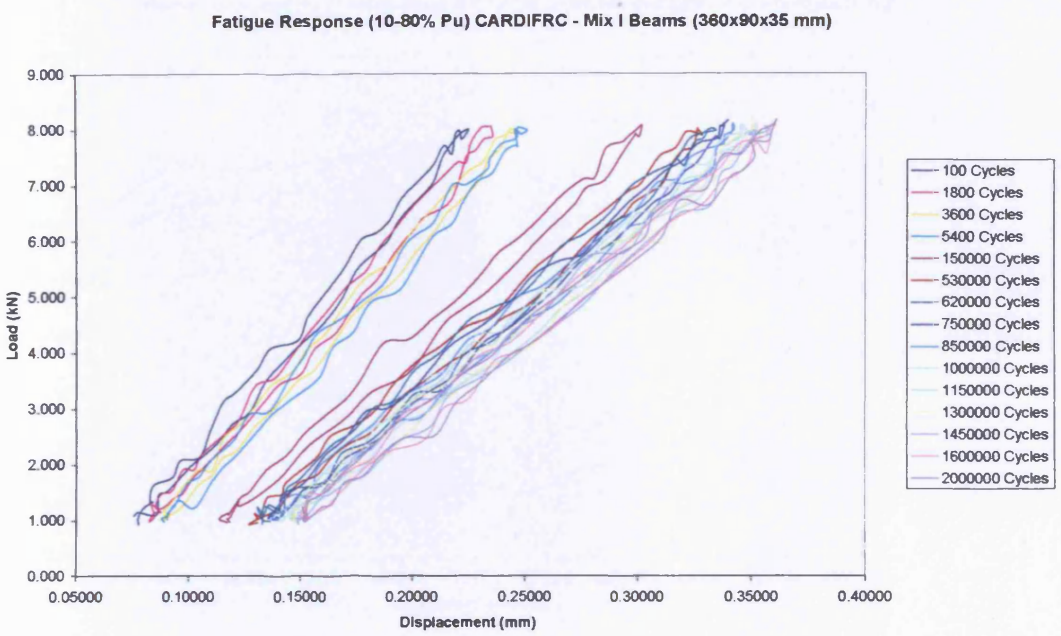

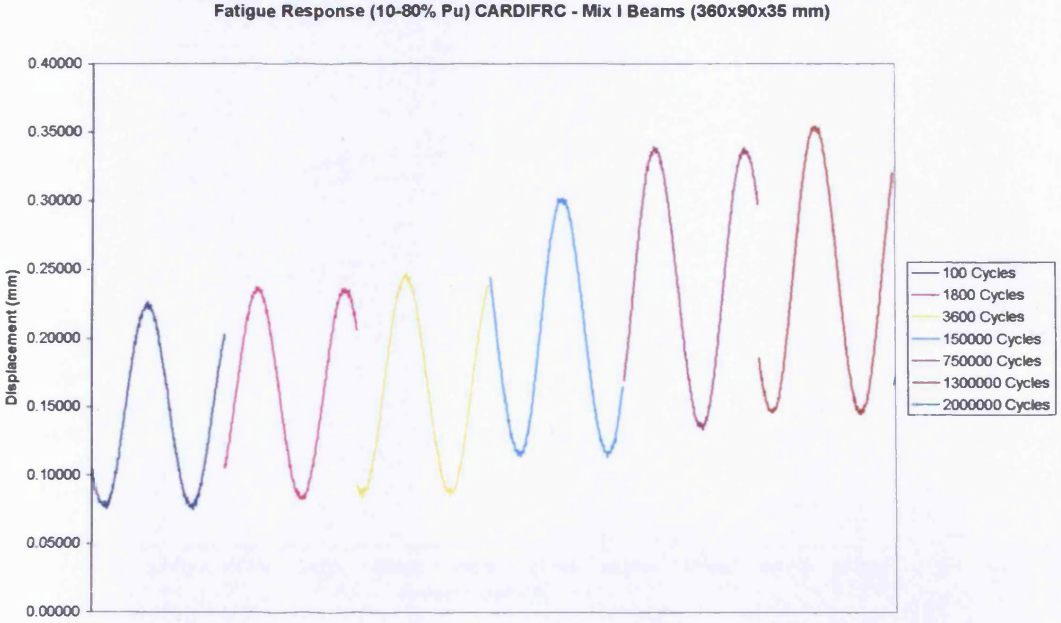

Fatigue Compliances (Tests 1-4)

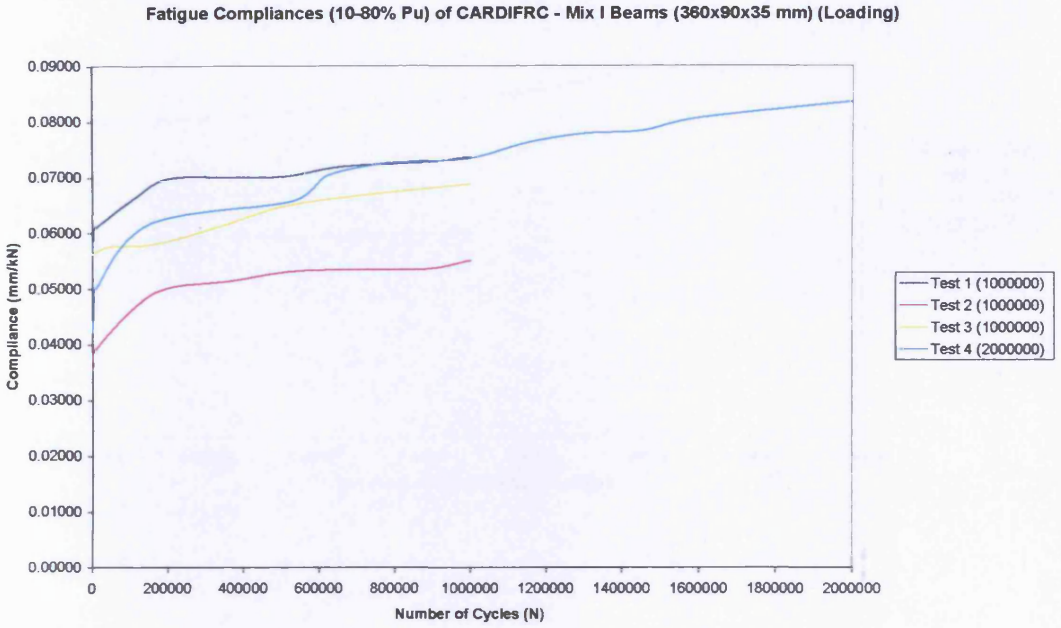

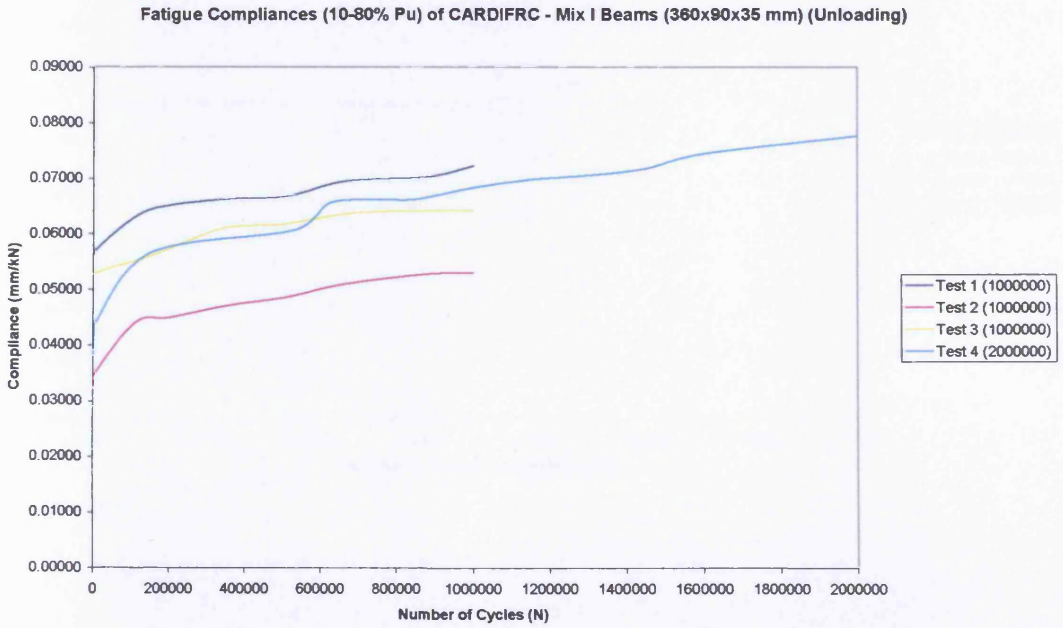

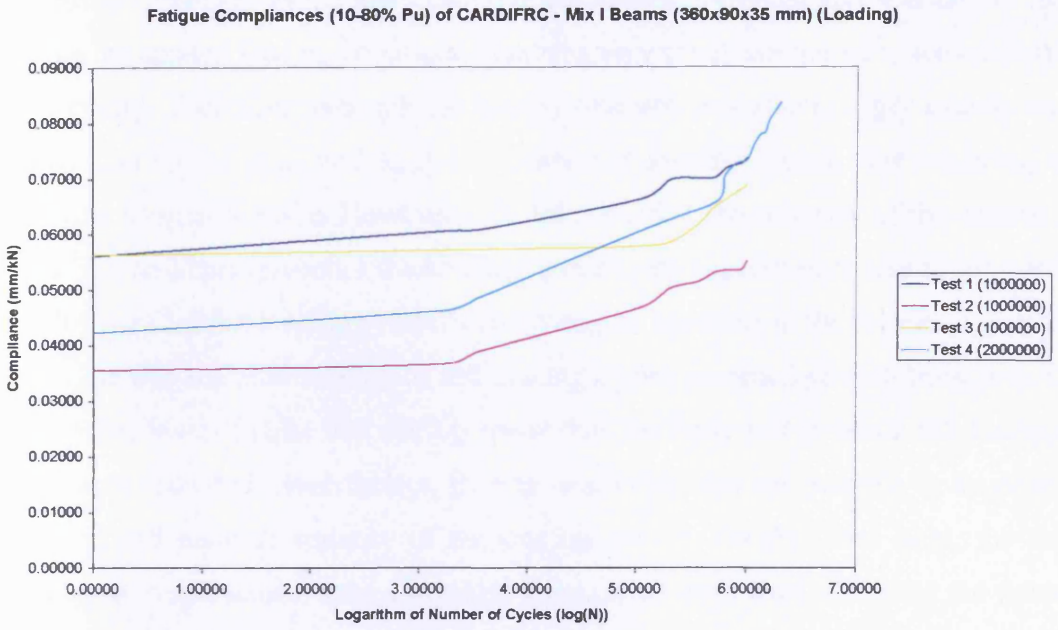
Fatigue Compliances (10-80% Pu) of CARDIFRC - Mix I Beams (360x90x35 mm) (Loading)
Compliance (mm/kN)
0.09000
0.08000
0.07000
0.06000
0.05000
0.04000
0.03000
0.02000
0.01000
0.00000
0.00000
1.00000
2.00000
3.00000
4.00000
5.00000
6.00000
7.00000
Logarithm of Number of Cycles (log(N))
Test 1 (1000000)
Test 2 (1000000)
Test 3 (1000000)
Test 4 (2000000)

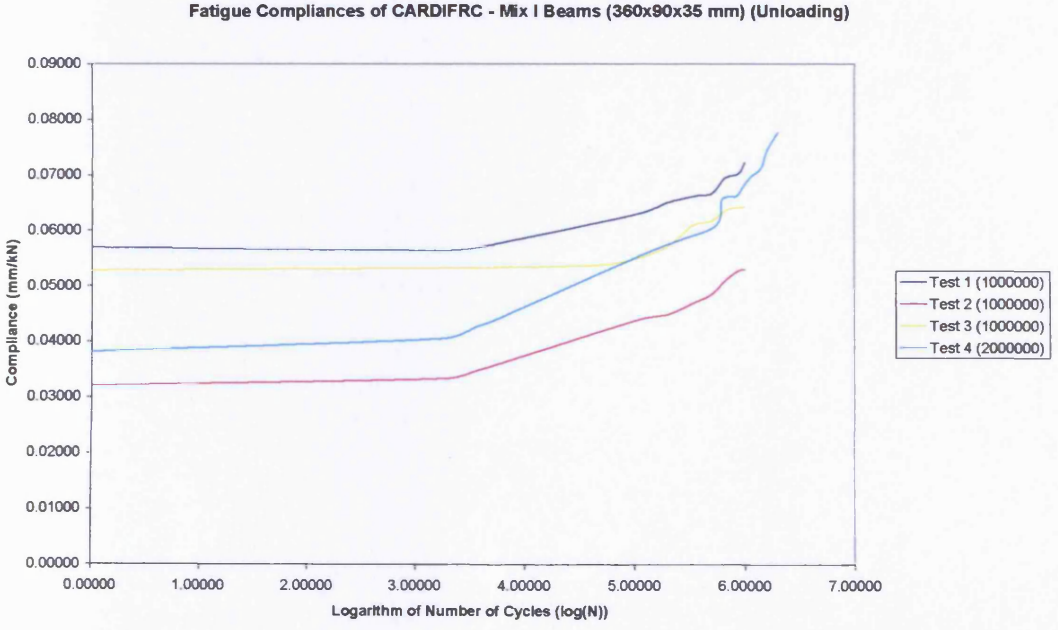
Fatigue Compliances of CARDIFRC - Mix I Beams (360x90x35 mm) (Unloading)
Compliance (mm/kN)
0.09000
0.08000
0.07000
0.06000
0.05000
0.04000
0.03000
0.02000
0.01000
0.00000
0.00000
1.00000
2.00000
3.00000
4.00000
5.00000
6.00000
7.00000
Logarithm of Number of Cycles (log(N))
Test 1 (1000000)
Test 2 (1000000)
Test 3 (1000000)
Test 4 (2000000)

The "noise" observed in the load-displacement curves presented above is due to the fact that the applied load in the fatigue tests was very small, compared to the machine load capacity. Therefore, although the loading machine was able to apply exactly the defined load values (S_{max} and S_{min}), the connected logging system was recording a significant amount of noise. However, this did not affect the accuracy of the obtained results. For an improvement of the obtained picture, the experimental results recorded at each burst (2-3 full loading cycles) were averaged, resulting in the presented graphs. In the case that the total number of full loading cycles recorded at each burst was 3, the recorded level of noise was slightly lower than the noise level when 2 full loading cycles were recorded. Nevertheless, in most cases this was not possible to be done, due to limited memory capacity of the logging system. On the other hand, for the recording of displacement values sensitive transducers were used, therefore the noise level was negligible.

Fatigue Response (10-85% P_u) of CARDIFRC® - Mix I Beams (360x90x35 mm)

Test 1 (1000000 Cycles)

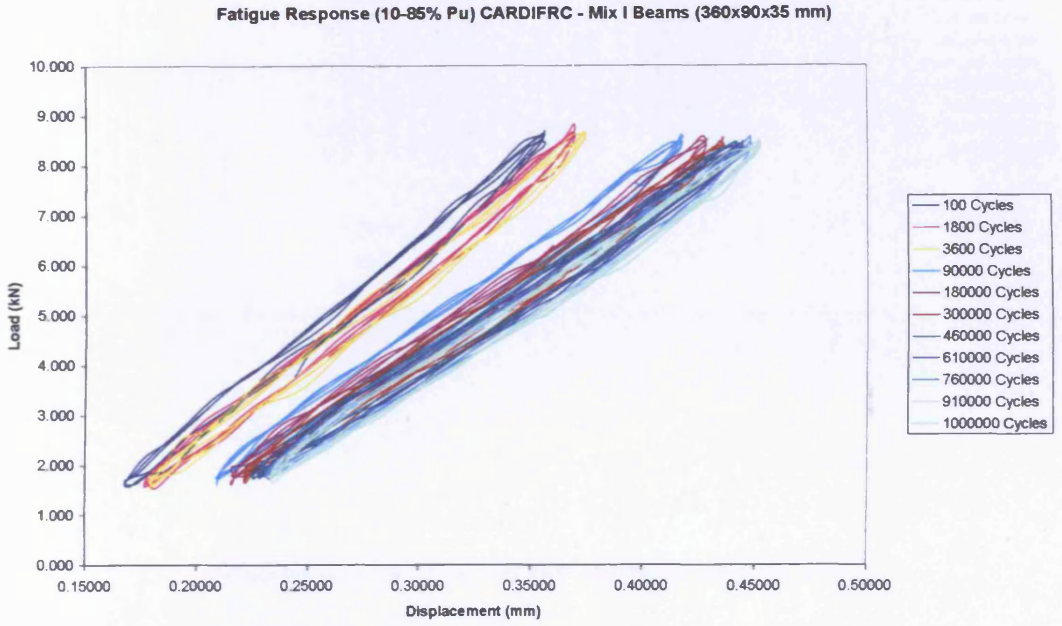

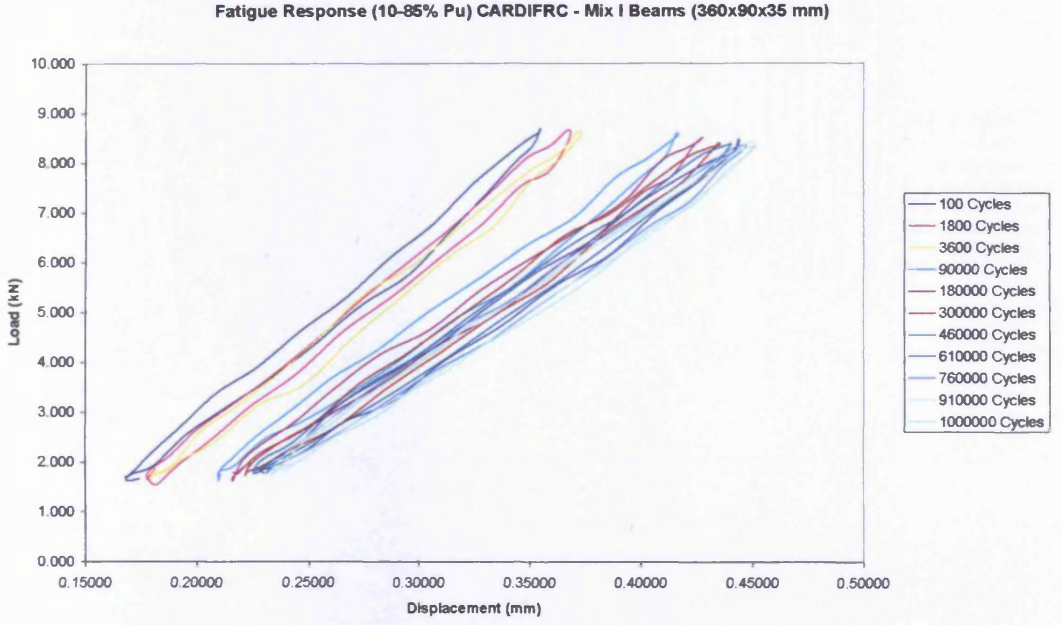

In the two graphs above is shown the same experimental data before and after being averaged, which have been logged during the several recording bursts of the logger.

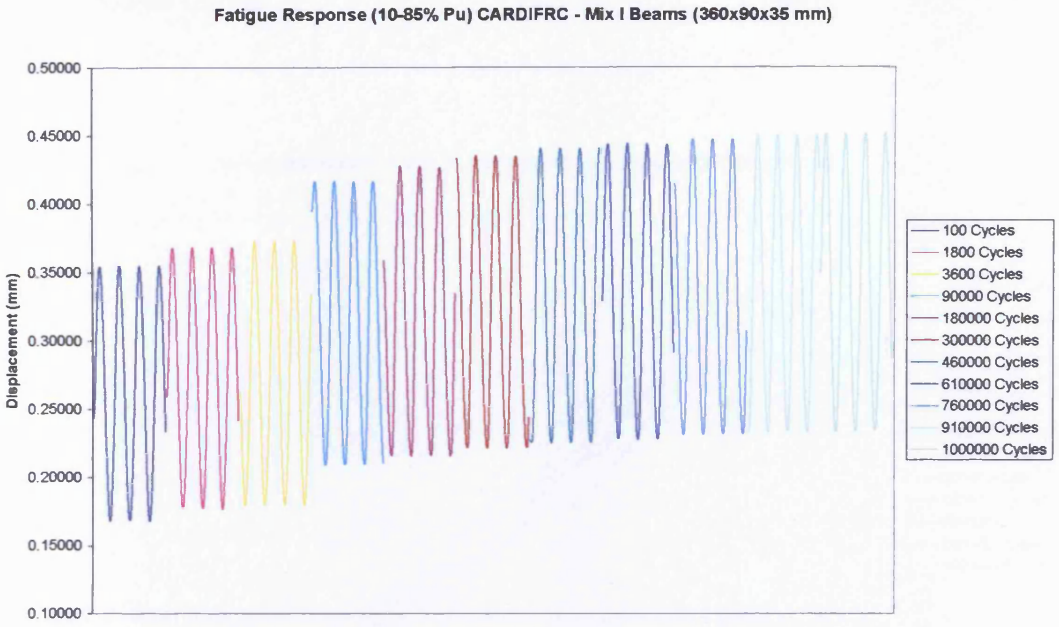
Fatigue Response (10-85% Pu) CARDIFRC - Mix I Beams (360x90x35 mm)
Displacement (mm)
0.50000
0.45000
0.40000
0.35000
0.30000
0.25000
0.20000
0.15000
0.10000
100 Cycles
1800 Cycles
3600 Cycles
90000 Cycles
180000 Cycles
300000 Cycles
460000 Cycles
610000 Cycles
760000 Cycles
910000 Cycles
1000000 Cycles

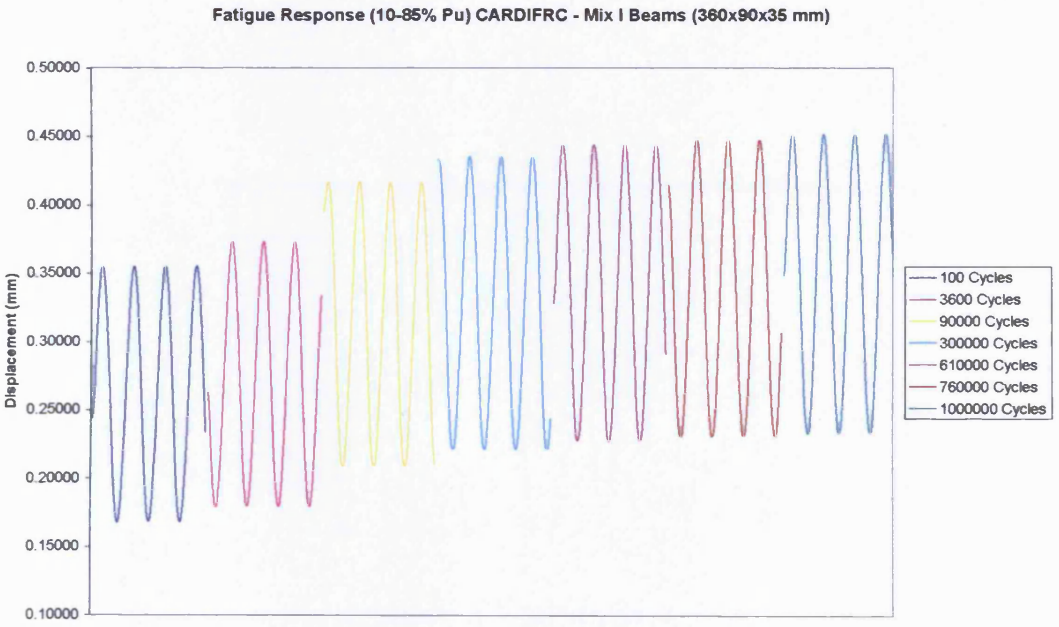
Fatigue Response (10-85% Pu) CARDIFRC - Mix I Beams (360x90x35 mm)
Displacement (mm)
0.50000
0.45000
0.40000
0.35000
0.30000
0.25000
0.20000
0.15000
0.10000
100 Cycles
3600 Cycles
90000 Cycles
300000 Cycles
610000 Cycles
760000 Cycles
1000000 Cycles

Test 2 (1000000 Cycles)

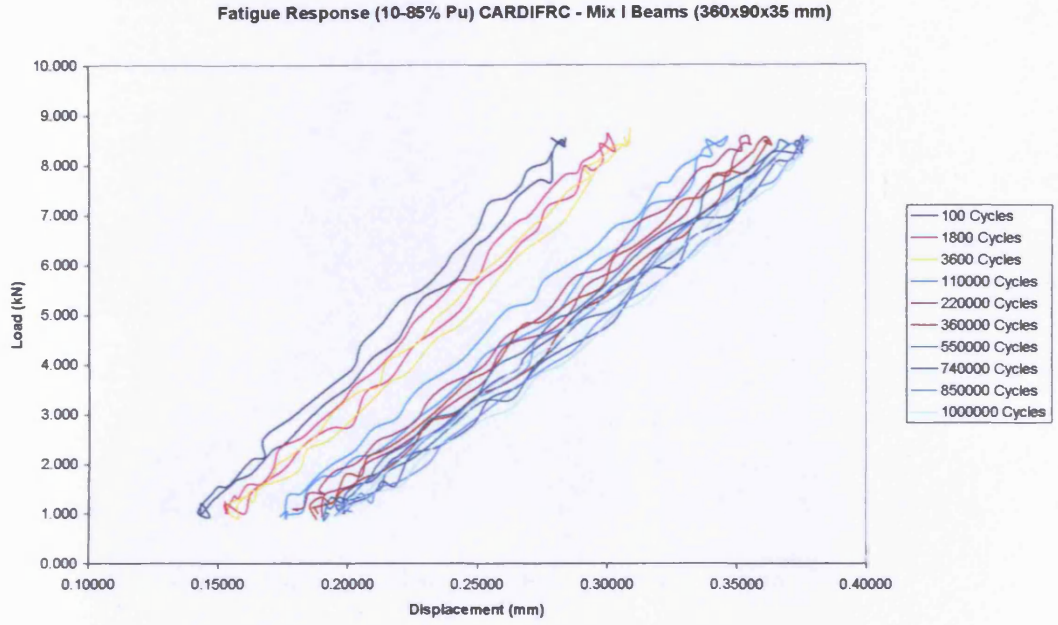

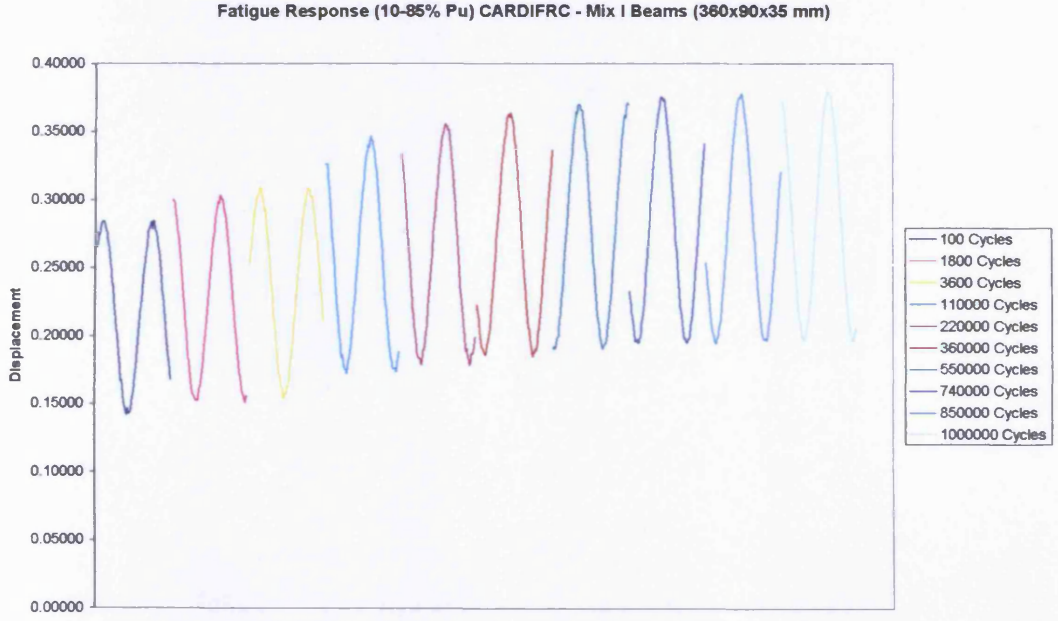

Test 3 (1000000 Cycles)

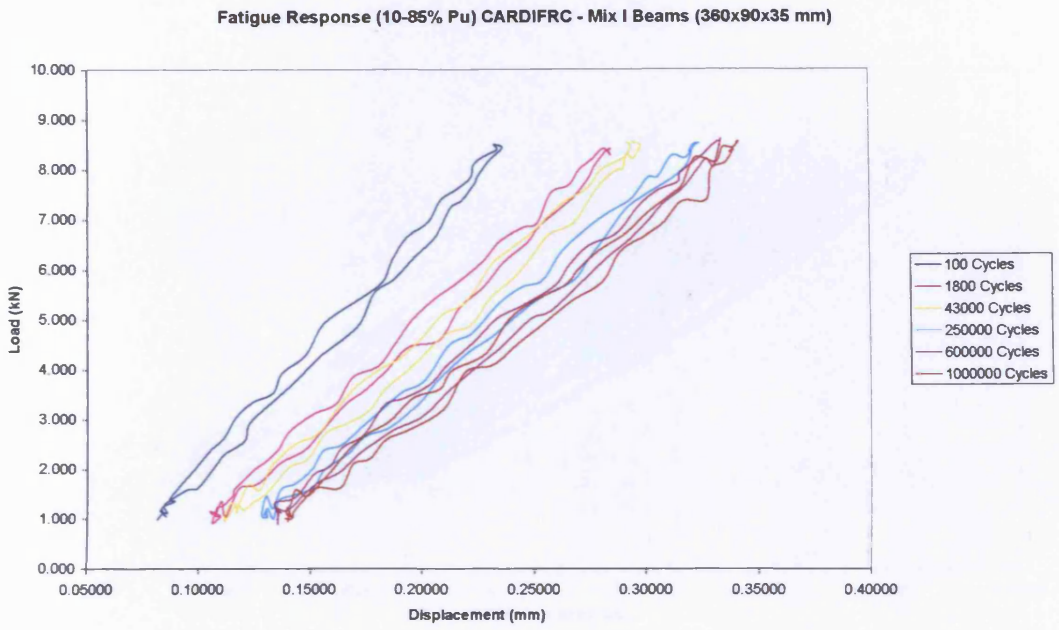

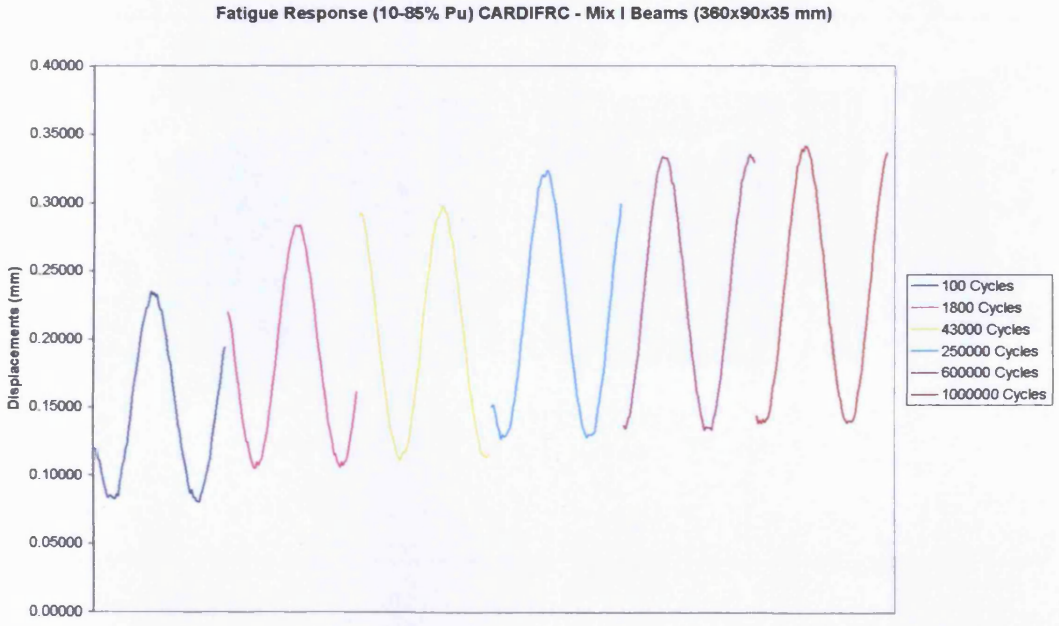

Test 4 (20500000 Cycles)

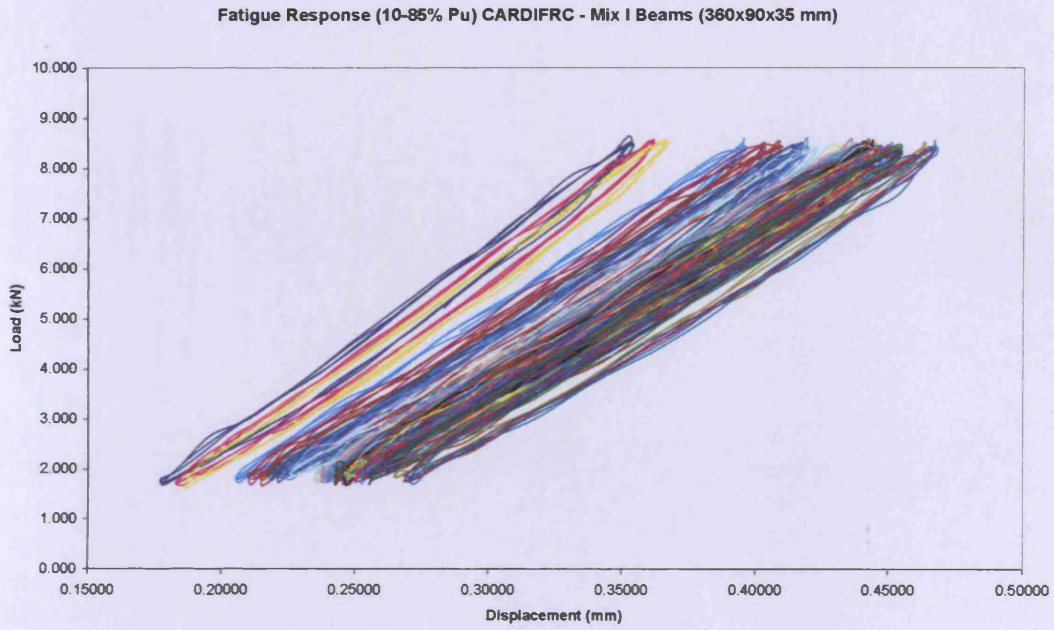

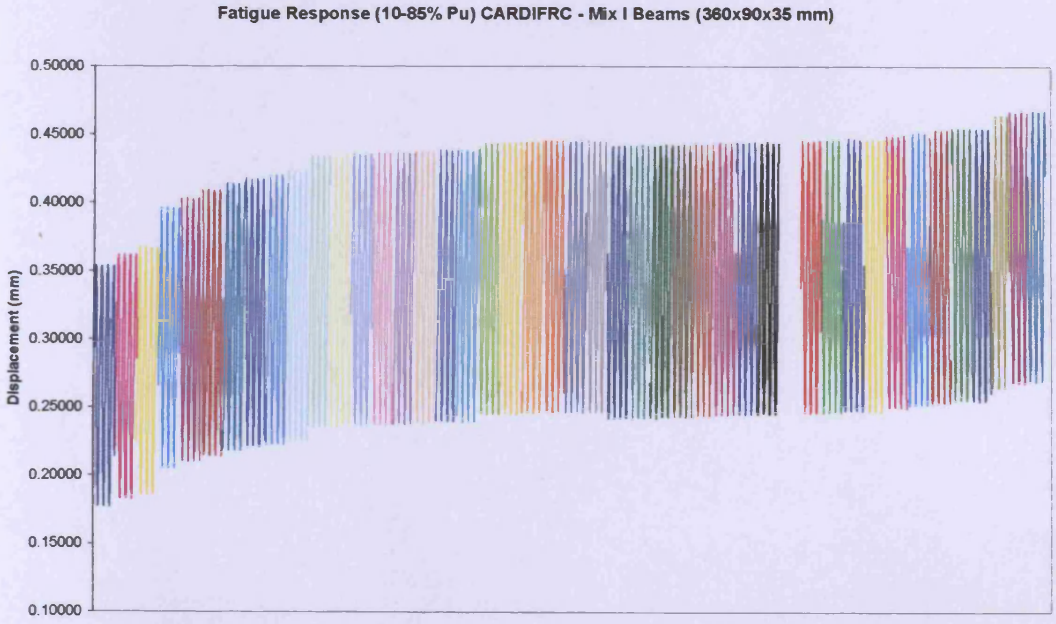

The number of cycles corresponding to each colour is not presented in this graph, due to the very big number of loading cycles represented and also the limited space.

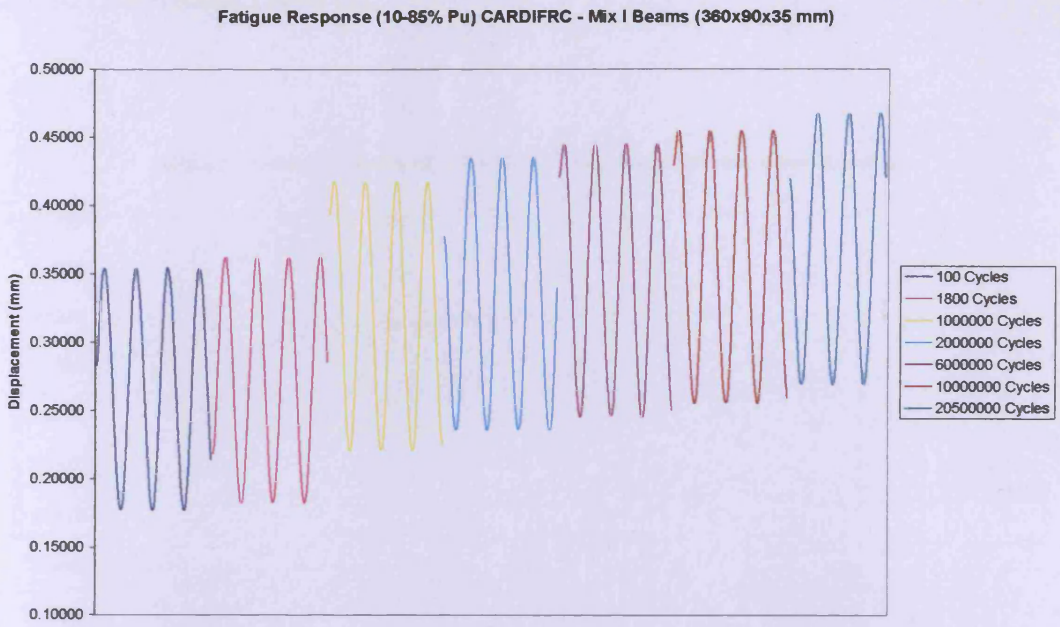
Fatigue Response (10-85% Pu) CARDIFRC - Mix I Beams (360x90x35 mm)
Displacement (mm)
0.50000
0.45000
0.40000
0.35000
0.30000
0.25000
0.20000
0.15000
0.10000
100 Cycles
1800 Cycles
1000000 Cycles
2000000 Cycles
6000000 Cycles
10000000 Cycles
20500000 Cycles

Fatigue Compliances (Tests 1-4)

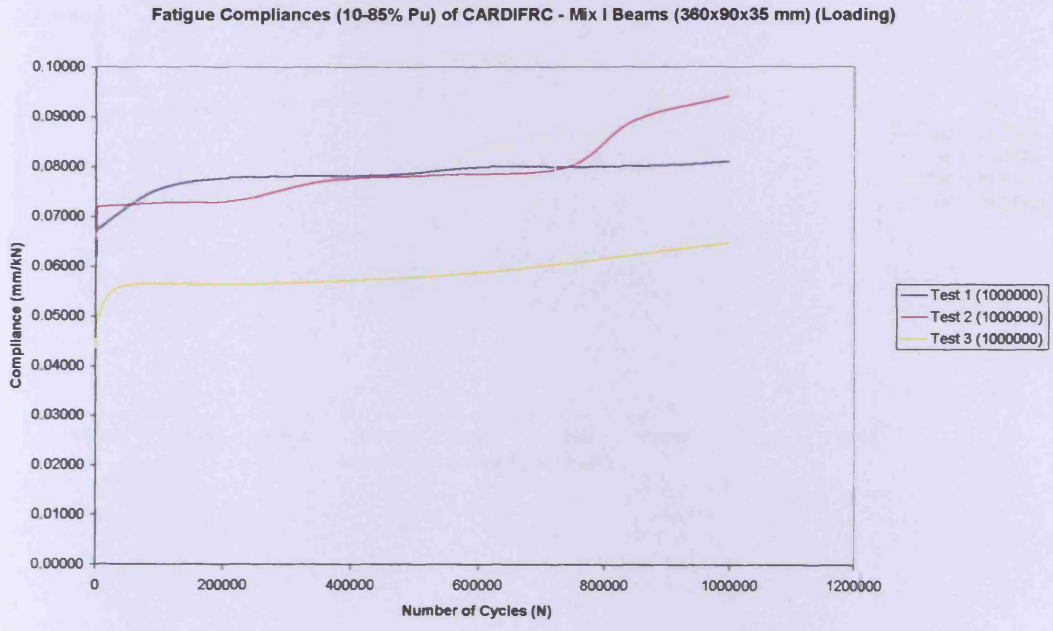

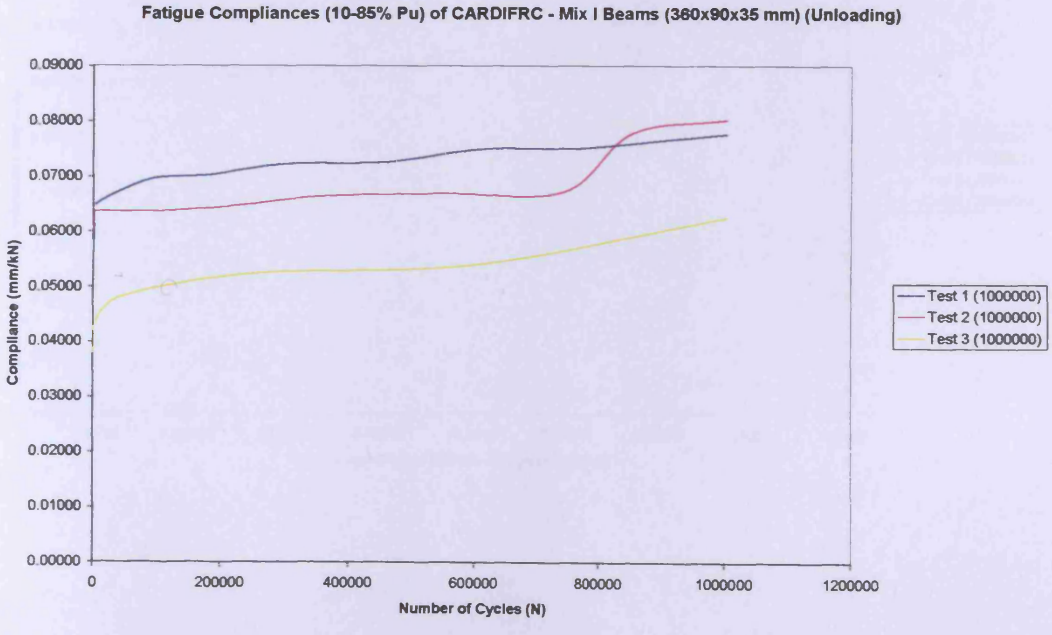

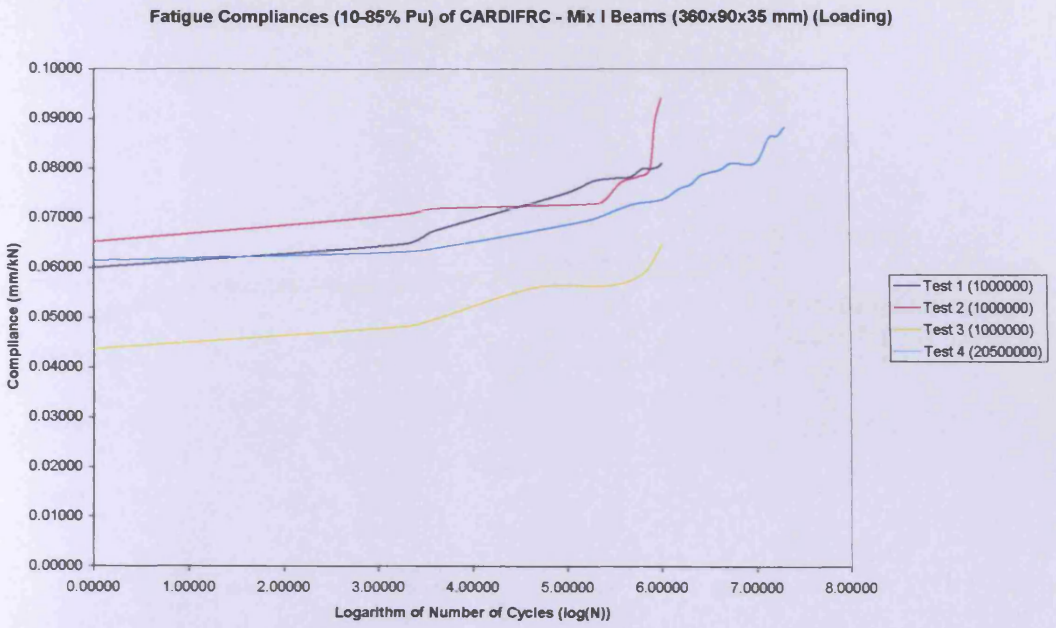
Fatigue Compliances (10-85% Pu) of CARDIFRC - Mix I Beams (360x90x35 mm) (Loading)
Compliance (mm/kN)
0.10000
0.09000
0.08000
0.07000
0.06000
0.05000
0.04000
0.03000
0.02000
0.01000
0.00000
0.00000
1.00000
2.00000
3.00000
4.00000
5.00000
6.00000
7.00000
8.00000
Logarithm of Number of Cycles (log(N))
Test 1 (1000000)
Test 2 (1000000)
Test 3 (1000000)
Test 4 (20500000)

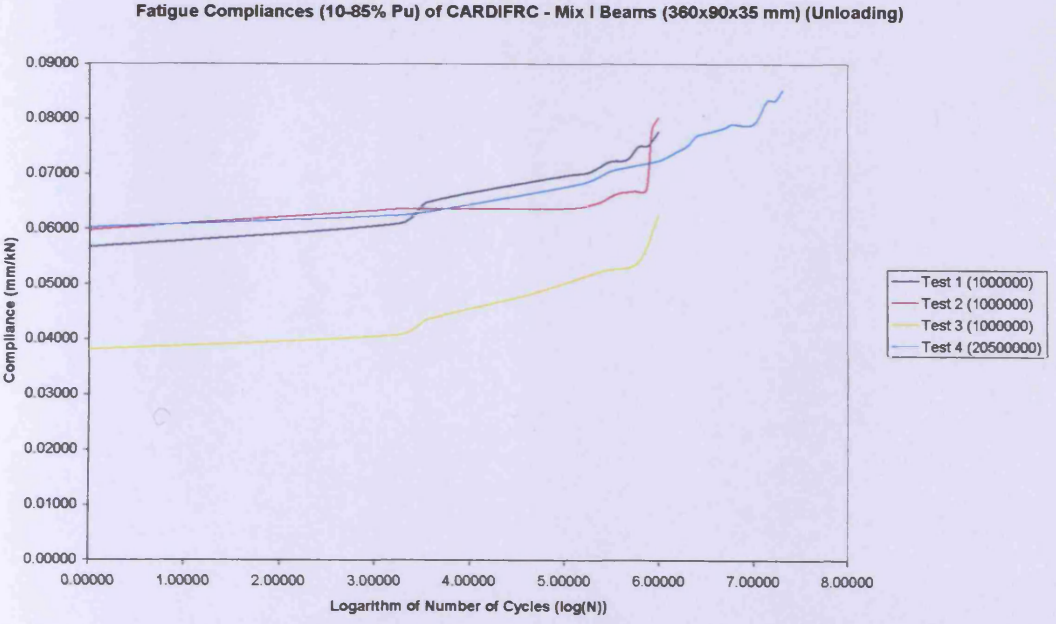
Fatigue Compliances (10-85% Pu) of CARDIFRC - Mix I Beams (360x90x35 mm) (Unloading)
Compliance (mm/kN)
0.09000
0.08000
0.07000
0.06000
0.05000
0.04000
0.03000
0.02000
0.01000
0.00000
0.00000
1.00000
2.00000
3.00000
4.00000
5.00000
6.00000
7.00000
8.00000
Logarithm of Number of Cycles (log(N))
Test 1 (1000000)
Test 2 (1000000)
Test 3 (1000000)
Test 4 (20500000)

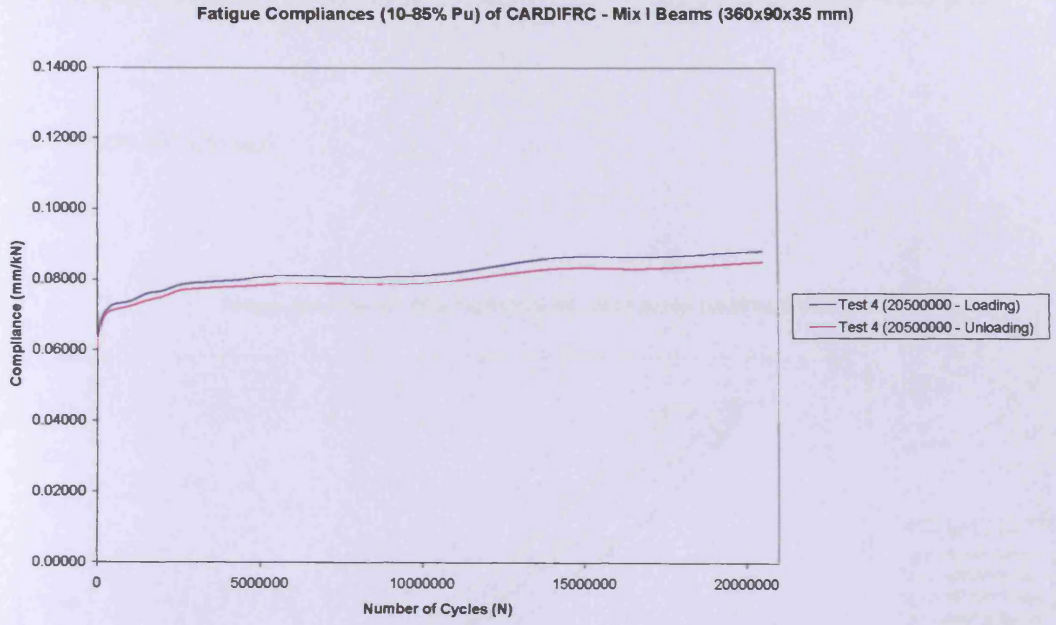
Fatigue Compliances (10-85% Pu) of CARDIFRC - Mix I Beams (360x90x35 mm)
Compliance (mm/kN)
0.14000
0.12000
0.10000
0.08000
0.06000
0.04000
0.02000
0.00000
0
5000000
10000000
15000000
20000000
Number of Cycles (N)
Test 4 (20500000 - Loading)
Test 4 (20500000 - Unloading)

Fatigue Response (10-90% P_u) of CARDIFRC® - Mix I Beams (360x90x35 mm)

Test 1 (1000000 Cycles)

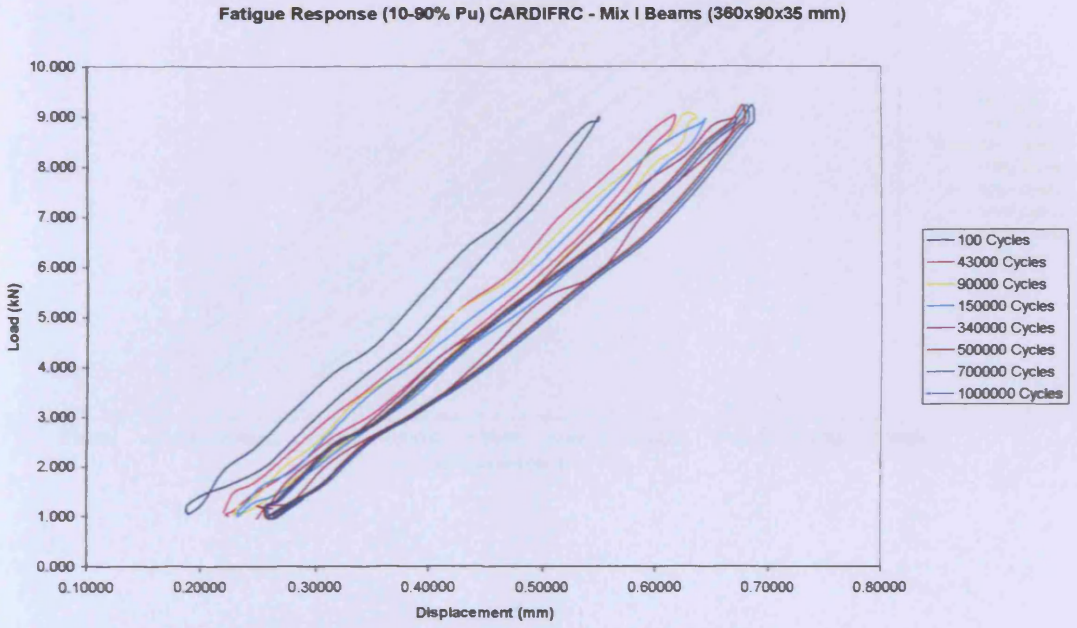

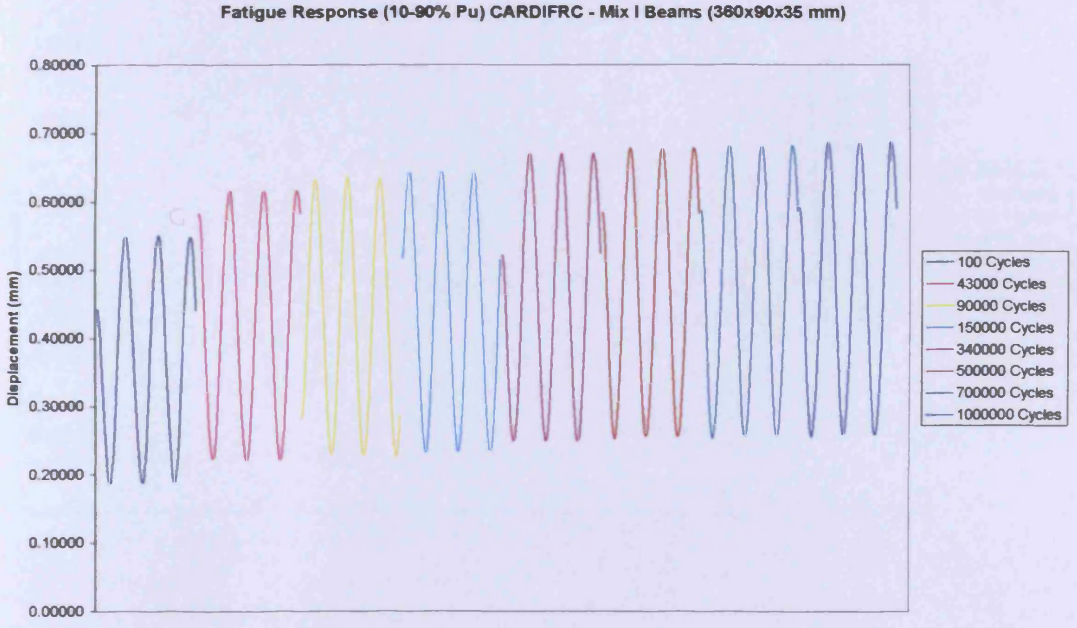

Test 2 (21564 Cycles)

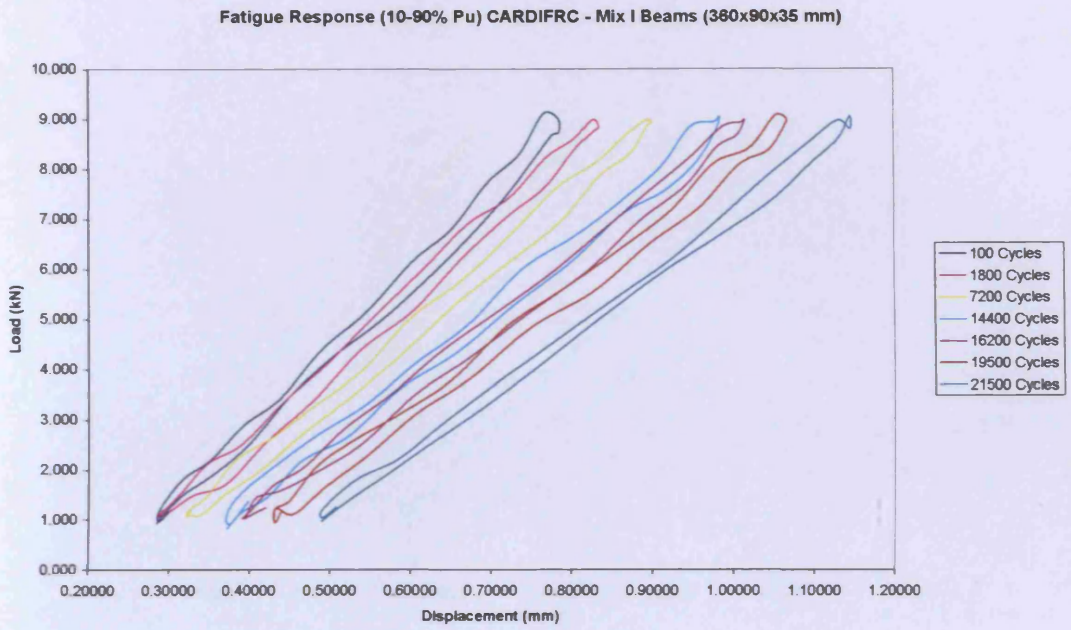

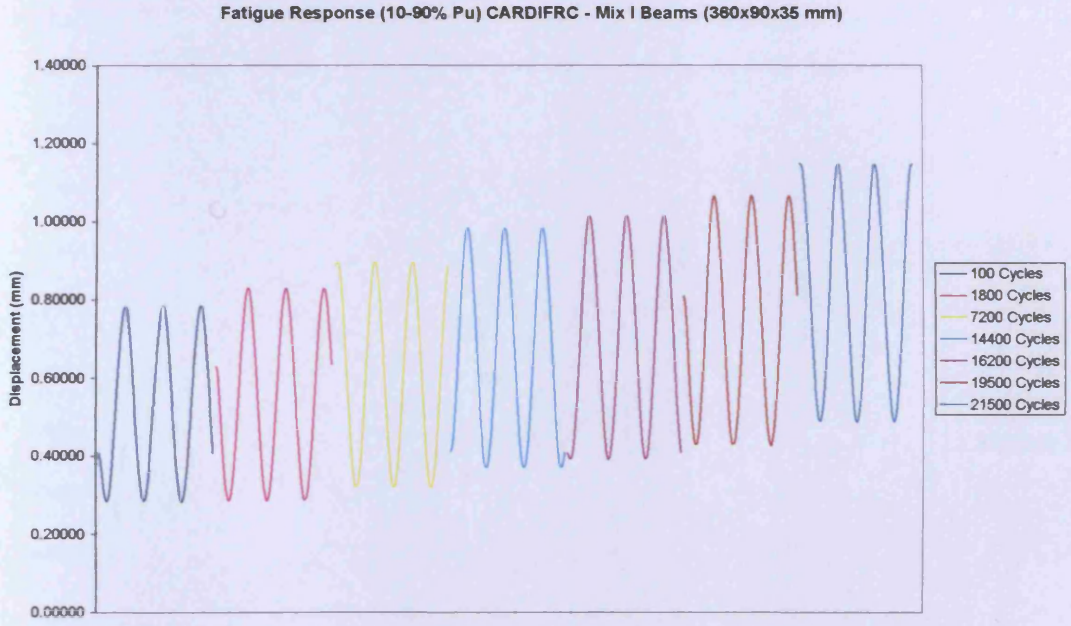

Test 3 (9315 Cycles)

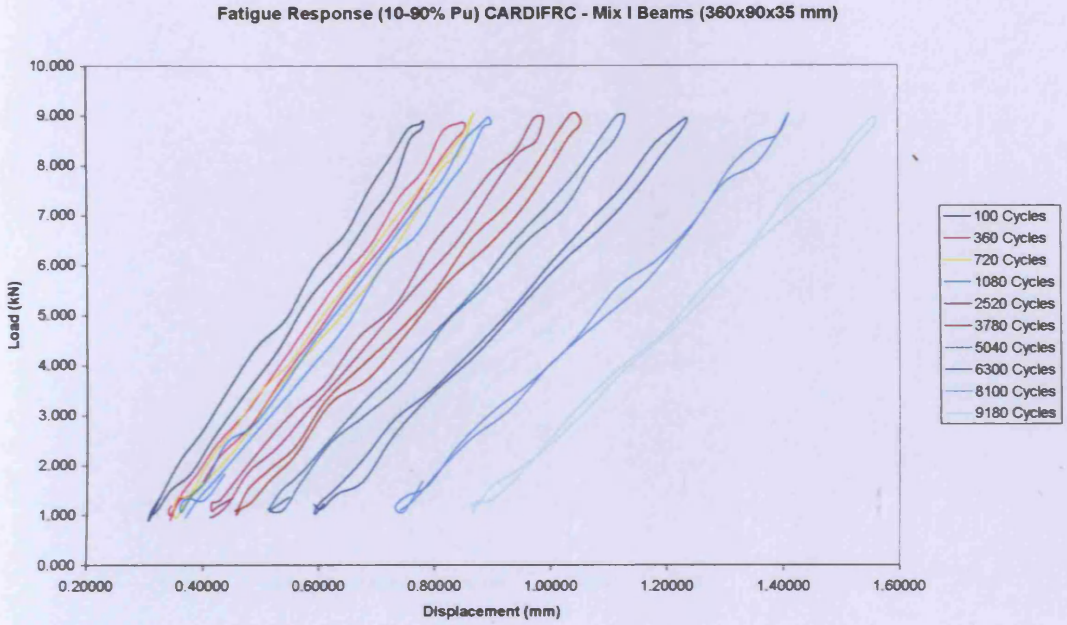

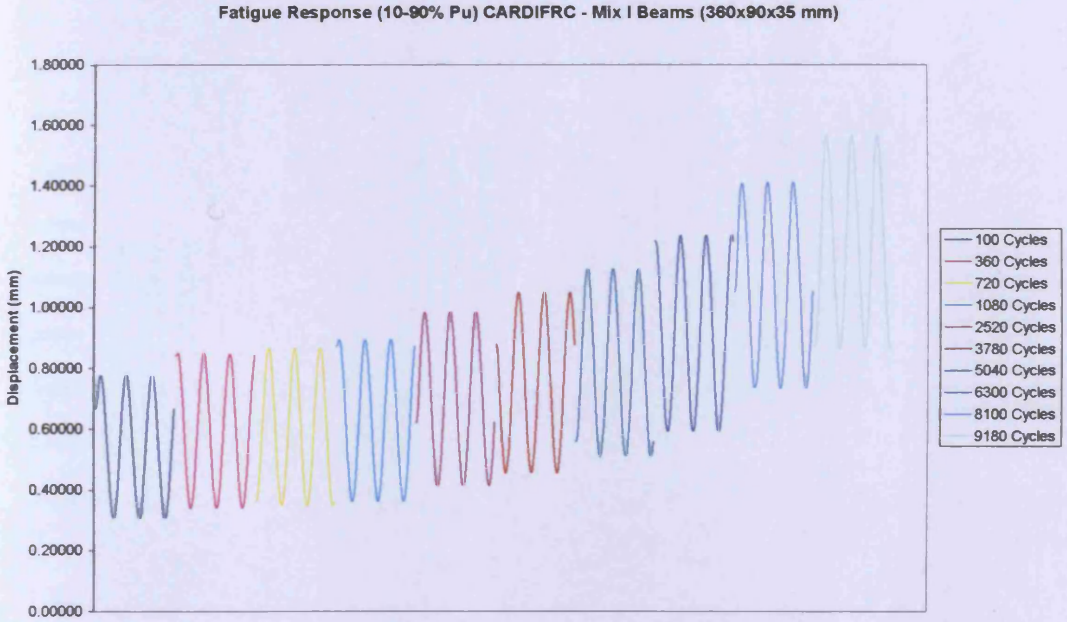

Test 4 (1000000 Cycles)

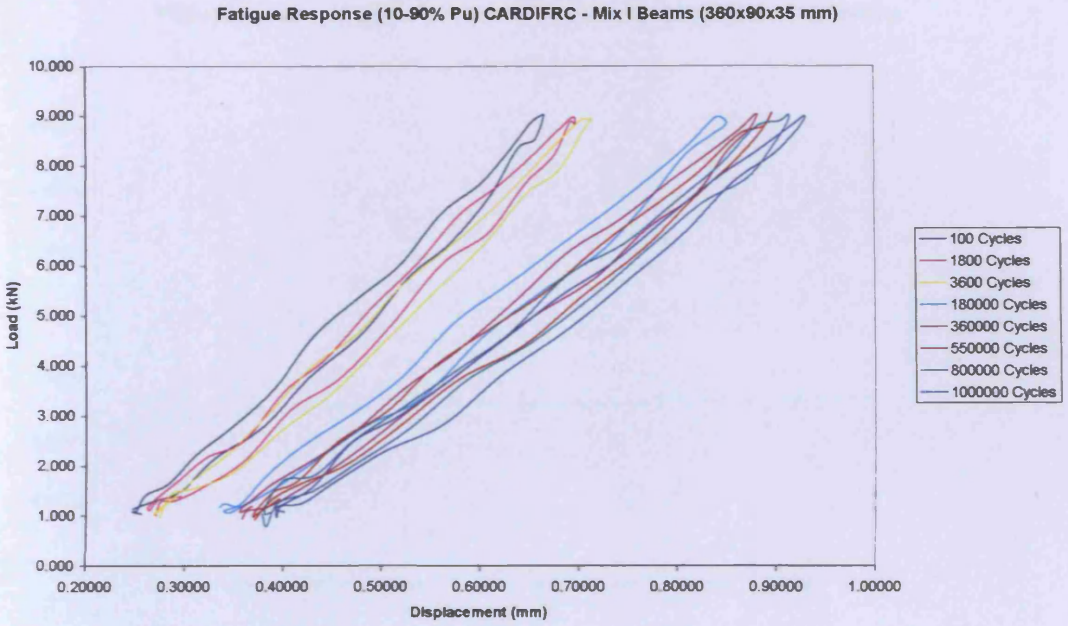

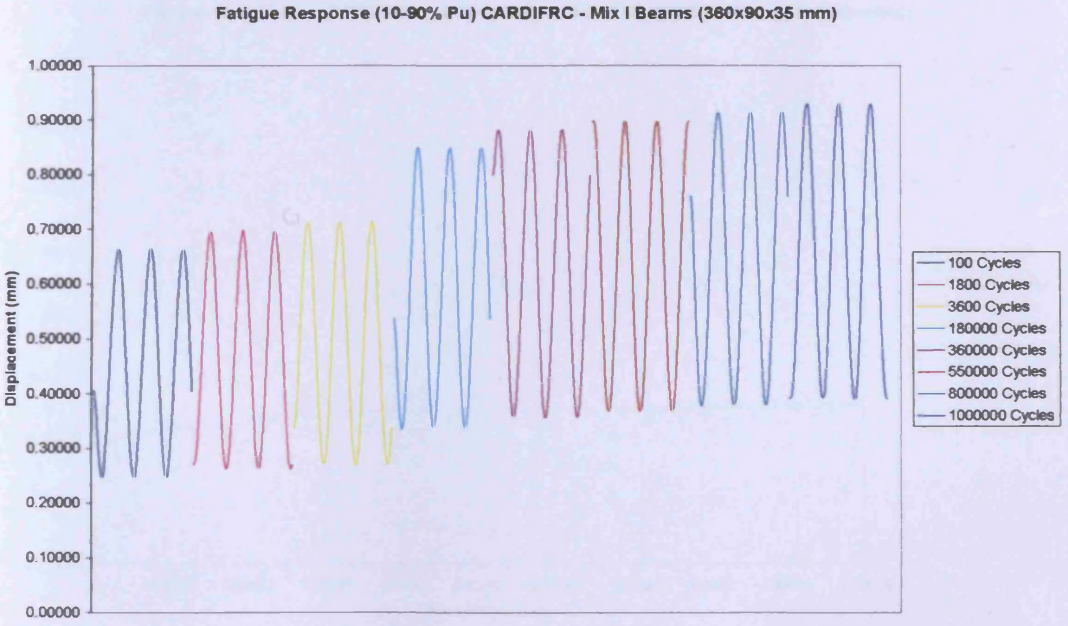

Fatigue Compliances (Tests 1-4)

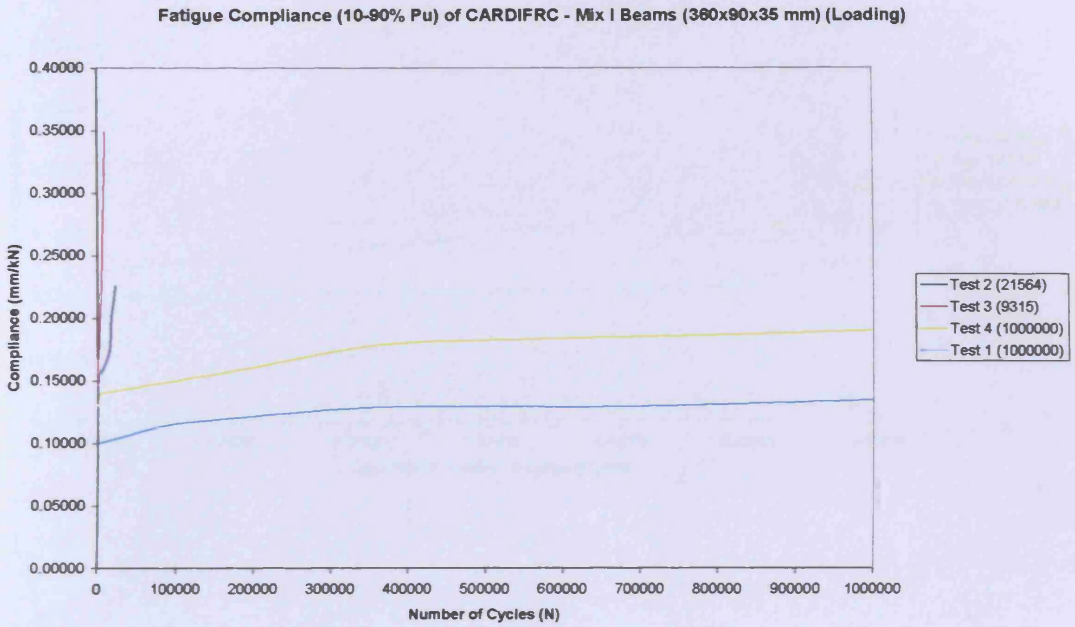

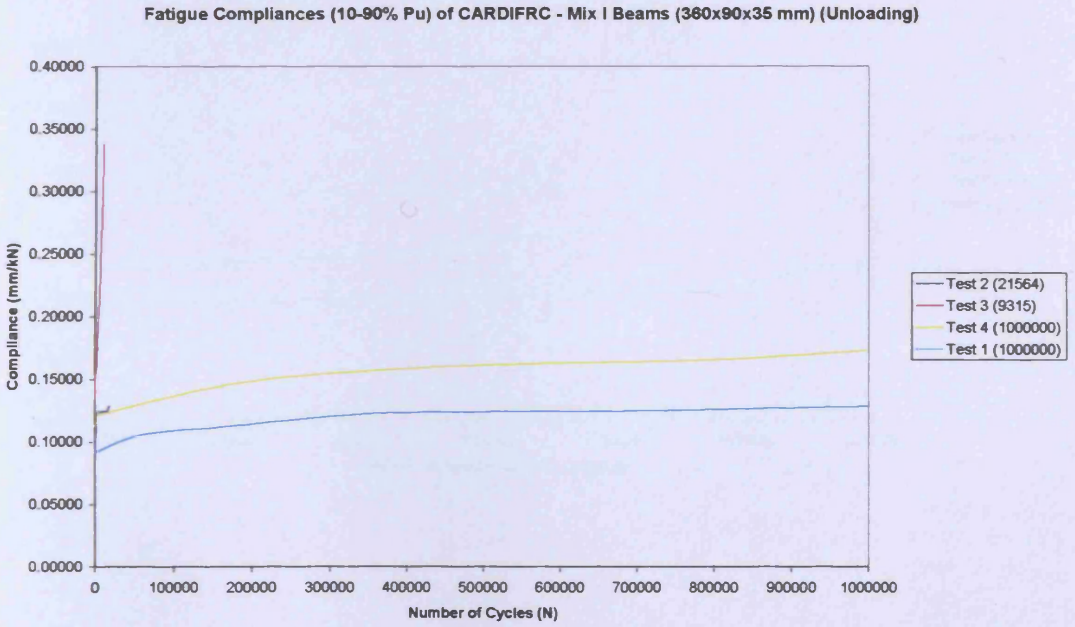

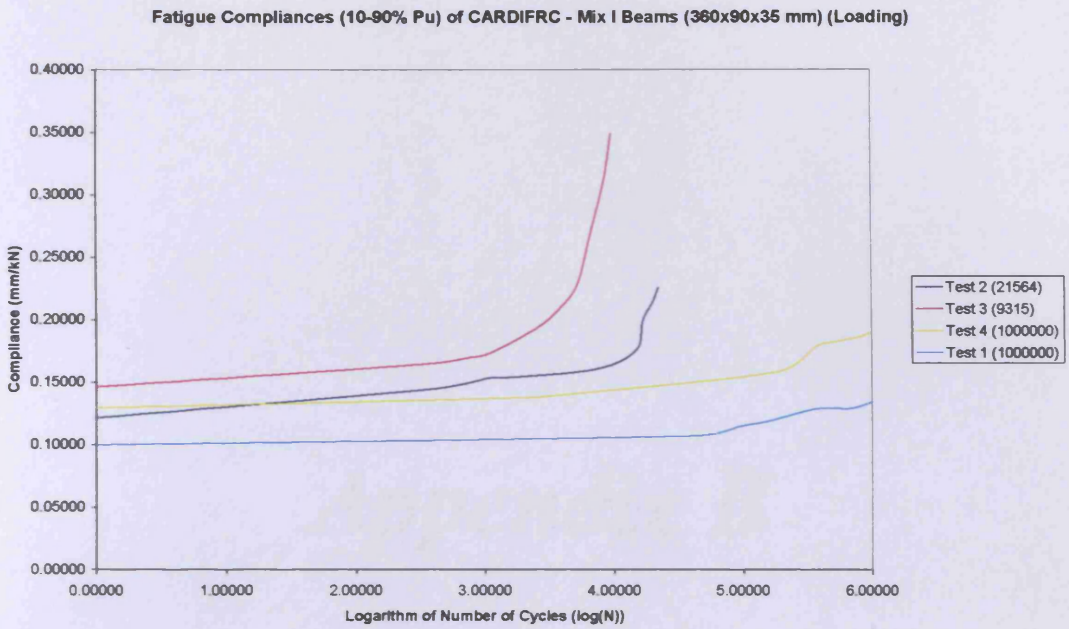
Fatigue Compliances (10-90% Pu) of CARDIFRC - Mix I Beams (360x90x35 mm) (Loading)
Compliance (mm/kN)
0.40000
0.35000
0.30000
0.25000
0.20000
0.15000
0.10000
0.05000
0.00000
0.00000
1.00000
2.00000
3.00000
4.00000
5.00000
6.00000
Logarithm of Number of Cycles (log(N))
Test 2 (21564)
Test 3 (9315)
Test 4 (1000000)
Test 1 (1000000)

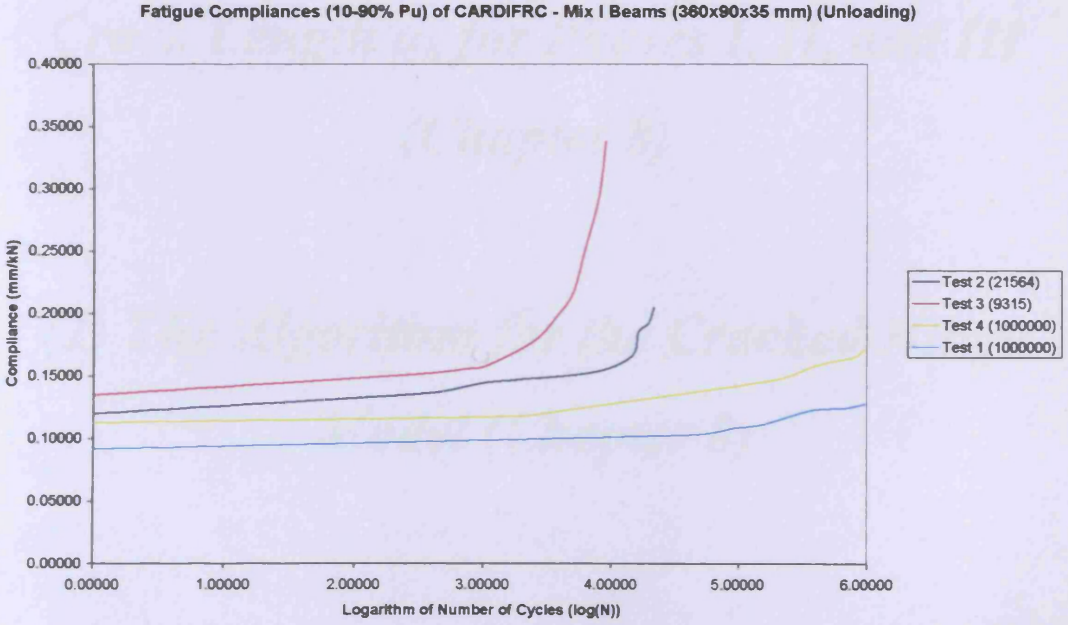
Fatigue Compliances (10-90% Pu) of CARDIFRC - Mix I Beams (360x90x35 mm) (Unloading)
Compliance (mm/kN)
0.40000
0.35000
0.30000
0.25000
0.20000
0.15000
0.10000
0.05000
0.00000
0.00000
1.00000
2.00000
3.00000
4.00000
5.00000
6.00000
Logarithm of Number of Cycles (log(N))
Test 2 (21564)
Test 3 (9315)
Test 4 (1000000)
Test 1 (1000000)

Appendix B

(1) Derivation of the Moment μ and the Crack Length a_h for Phases I, II, and III (Chapter 8)

(2) The Algorithm for the Cracked Hinge Model (Chapter 8)

Appendix B1: Derivation of the Moment,μ, and Crack Length, α_h, for Phases I, II, III

Phase 0 $\alpha = 0$

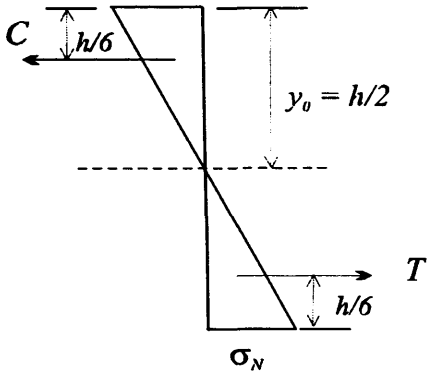

$$\frac{M}{I} = \frac{E}{R} \quad \Rightarrow \quad \frac{\mu f_t h^2 t}{6\frac{th^3}{12}} = \frac{2E\varphi}{s} = \frac{2Esf_t}{hEs}\theta$$

$$\Rightarrow \frac{2\mu f_t}{h} = \frac{2f_t}{h}\theta \qquad \Rightarrow \mu = \theta$$

Note that $h=h_g$ and $\alpha=\alpha_h$ appears in Chapter 8.

The balance of longitudinal forces requires that $\sigma_N < f_t$

$$\frac{N}{ht} < f_t \qquad \Rightarrow \qquad \frac{N}{f_t ht} < 1 \quad \Rightarrow \quad \rho < 1$$

Note: $N = \sigma_N \cdot \frac{1}{2} \cdot \frac{th}{2}$, $M = \frac{2}{3}hN = \frac{\sigma_N th^2}{6}$

$$\theta = \frac{hE}{2f_t}k^* \ , \qquad k^* = \frac{1}{R} = \frac{M}{EI} = \frac{\sigma_N th^2}{6E.\frac{th^3}{12}} = \frac{2\sigma_N}{Eh}$$

$$\theta = \frac{\sigma_N}{f_t} < 1$$

Transition from phase 0 to phase I at $\theta = 1$

Phase I $\alpha \neq 0 \quad < 1$

In phase I, the stress is decreasing along the first branch of the bilinear $\sigma(w)$ diagram.

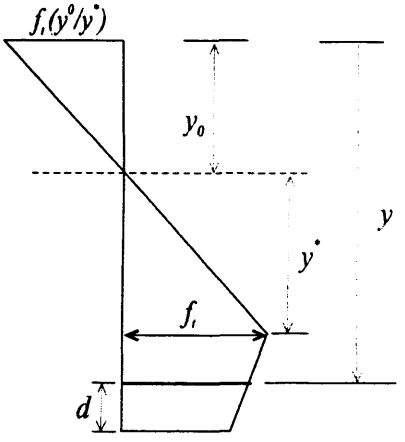

$$s\frac{\sigma_w(w(y))}{E} + w(y) = 2s(y - y_0)\frac{\varphi}{s} = 2(y - y_0)\varphi$$

$$\sigma_w(w(y)) = \frac{1}{s}\{2E(y - y_0)\varphi - Ew(y)\} = \frac{E}{s}\{2(y - y_0)\varphi - w(y)\} \qquad (8.6)$$

Also, $\sigma_w(w(y) = f_t\{b_i - a_i w(y)\}$ (8.7)

By subtracting (8.7) from (8.6), we get:

$$-f_t\{b_i - a_i w(y)\} + \frac{E}{s}\{2(y-y_0)\varphi - w(y)\} = 0$$

$$\Rightarrow \quad \frac{f_t s}{E}\{(b_i - a_i w(y)\} - \{2(y-y_0)\varphi - w(y)\} = 0$$

$$\Rightarrow \quad -\frac{f_t s}{E} b_i + 2(y-y_0)\varphi = w(y) - \frac{f_t s}{E} a_i w(y) = w(y)\{1 - \frac{f_t s a_i}{E}\}$$

$$\Rightarrow \quad w(y) = \frac{2(y-y_0)\varphi - \zeta_i}{1-\beta_i} \tag{8.8a}$$

$$\sigma_w(w(y) = f_t b_i - f_t a_i \left\{\frac{2(y-y_0)\varphi - \zeta_i}{1-\beta_i}\right\}$$

$$= \zeta_i \frac{E}{s} - \beta_i \frac{E}{s}\left\{\frac{2(y-y_0)\varphi - \zeta_i}{1-\beta_i}\right\}$$

$$\zeta_i \frac{E}{s}\left\{\frac{1-\beta_i+\beta_i}{1-\beta_i}\right\} - \frac{2(y-y_0)\varphi\beta_i}{1-\beta_i}\frac{E}{s}$$

$$= \frac{\zeta_i - 2(y-y_0)\varphi\beta_i}{1-\beta_i}\frac{E}{s} \tag{8.8b}$$

$$\beta_i = \frac{f_t s a_i}{E} \quad , \quad \zeta_i = \frac{f_t s b_i}{E} \tag{8.9 a, b}$$

Tensile force = ½ $f_t y^* t$ + contribution from tension softening zone of length d.

The latter contribution is obtained from the stress at distance y from top, given by equation (8.8b)

$$\sigma_w(w(y) = \frac{\zeta_1 - 2(y-y_0)\varphi\beta_i}{1-\beta_i}\frac{E}{s}$$

$$\sigma_w(w(h) = \frac{\zeta_1 - 2(h-y_0)\varphi\beta_1}{1-\beta_1}\frac{E}{s}$$

$$\sigma_w(w(h-d) = \frac{\zeta_1 - 2(h-d-y_0)\varphi\beta_1}{1-\beta_1}\frac{E}{s}$$

Area of trapezium $= \frac{dt}{2}\{\sigma(w(h)) + \sigma(w(h-d))\}$

$$= \frac{dtE}{2s}\left\{\frac{2\zeta_1 - 2(2h-d-2y_0)\varphi\beta_1}{1-\beta_1}\right\} \quad , \zeta_1 = \frac{f_t b_1 s}{E} = \frac{f_t s}{E}$$

$$= \frac{dt}{(1-\beta_1)}\left\{f_t - (2-\alpha-2\frac{y_0}{h})\frac{h\varphi E}{E}\beta_1\right\}$$

$$= \frac{dtf_t}{(1-\beta_1)}\left\{1-(2-\alpha-2\frac{y_0}{h})\theta\beta_1\right\}$$

$$= \frac{\alpha dtf_t}{(1-\beta_1)}\left\{1-2\theta\beta_1+\alpha\theta\beta_1+2\frac{y_0}{h})\theta\beta_1\right\}$$

Total tensile force $= \frac{\alpha(thf_t)}{(1-\beta_1)}\left\{1-(2-\alpha-2\frac{y_0}{h})\theta\beta_1\right\}+\frac{1}{2}f_t y^* t$

$$y^* = \frac{sf_t}{2\varphi E} = \frac{sf_t.hE}{2.sf_t\theta E} = \frac{h}{2\theta}, \quad \text{Note also: } h - y_0 = d + y^*,$$

so that $$1-\frac{y_0}{h} = \alpha + \frac{y^*}{h}\alpha + \frac{1}{2\theta} = \frac{(1+2\alpha\theta)}{2\theta}$$

Total tensile force =

$$T = \frac{\alpha(thf_t)}{(1-\beta_1)}\left\{1-(2\alpha-\frac{1}{\theta}-\alpha)\theta\beta_1\right\}+\frac{f_t th}{4\theta}$$

$$= \frac{f_t th}{(1-\beta_1)}\left\{\alpha-(2\alpha^2+\frac{\alpha}{\theta})\theta\beta_1\right\}+\frac{f_t th}{4\theta}$$

$$= \frac{f_t th}{(1-\beta_1)}\left\{(1-\beta_1)\alpha-\alpha^2\theta\beta_1\right\}+\frac{f_t th}{4\theta}$$

$$= (f_t th)\left\{\alpha-\frac{\alpha^2\theta\beta_1}{(1-\beta_1)}+\frac{1}{4\theta}\right\}$$

Total compressive force $= \frac{1}{2}f_t\frac{y_0}{y^*}.y_0 t = \frac{1}{2}(f_t ht)\frac{y_0}{y^*}.\frac{y_0}{h}$

Now $$\frac{y_0}{h} = 1-\alpha-\frac{1}{2\theta}$$

Also $$\frac{y^*}{h} = 1-\alpha-\frac{y_0}{h} = 1-\alpha-1+\alpha+\frac{1}{2\theta} = \frac{1}{2\theta}$$

$$\frac{y^*}{h}\left(\frac{y_0}{y^*}+1\right) = 1-\alpha \qquad (\text{from } y_0 + y^* = h-d)$$

$$\Rightarrow \quad \frac{1}{2\theta}\left(\frac{y_0}{y^*}+1\right) = 1-\alpha \quad \Rightarrow \quad \frac{y_0}{y^*}+1 = (1-\alpha)2\theta$$

$$\Rightarrow \frac{y_0}{y^*} = (1-\alpha)2\theta - 1$$

C = Total compressive force $= \frac{1}{2}(f_t ht)\{(1-\alpha)2\theta - 1\}\left\{1-\alpha-\frac{1}{2\theta}\right\}$

$$= \frac{f_t ht}{\theta}\left\{(1-\alpha)\theta - \frac{1}{2}\right\}\left\{(1-\alpha)\theta - \frac{1}{2}\right\}$$

$$= \frac{f_t ht}{\theta}\left\{(1-\alpha)\theta - \frac{1}{2}\right\}^2$$

$C = T \quad \Rightarrow$

$$\alpha - \frac{\alpha^2\theta\beta_1}{(1-\beta_1)} + \frac{1}{4\theta} = (1-\alpha)^2\theta - (1-\alpha) + \frac{1}{4\theta}$$

$$(1-2\alpha-\alpha^2)\theta - 1 = -\frac{\alpha^2\theta\beta_1}{(1-\beta_1)}$$

$$\Rightarrow \quad \alpha^2\theta\left\{1+\frac{\beta_1}{1-\beta_1}\right\} - 2\alpha\theta - (1-\theta) = 0$$

$$\Rightarrow \quad \frac{\alpha^2\theta}{(1-\beta_1)} - 2\alpha\theta - -(1-\theta) = 0$$

$$\Rightarrow \quad \alpha^2 - 2(1-\beta_1)\alpha - (1-\beta_1)\left(\frac{1-\theta}{\theta}\right) = 0$$

$$\alpha = \frac{2(1-\beta_1) \pm \sqrt{(1-\beta_1)^2 + 4(1-\beta_1)\left(\frac{1}{\theta}-1\right)}}{2}$$

$$\alpha = (1-\beta_1) \pm \sqrt{(1-\beta_1)^2 + (1-\beta_1)\left(\frac{1}{\theta}-1\right)}$$

$$\alpha = (1-\beta_1) - \sqrt{(1-\beta_1) + \left(1-\beta_1+\frac{1}{\theta}-1\right)} \qquad \alpha << 1$$

$$\boxed{\alpha = (1-\beta_1) - \sqrt{(1-\beta_1) + \left(\frac{1}{\theta}-\beta_1\right)}}$$

Phase I (moment)

Now take moments about neutral axis:

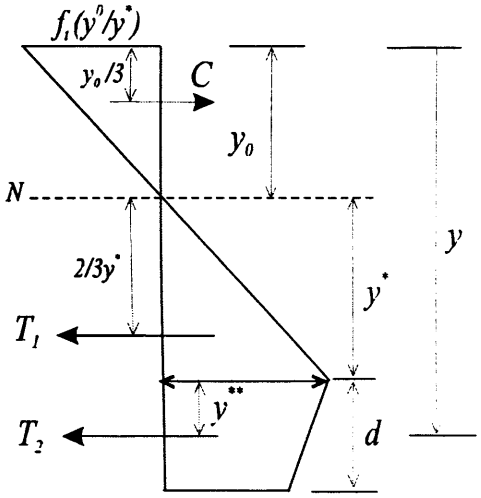

$$M = C\left(\frac{2y_0}{3}\right) + T_1\left(\frac{2y^*}{3}\right) + T_2\left(y^* + y^{**}\right)$$

The distance y^{**} can be calculated by dividing the trapezium into a rectangle and a triangle.

$$\sigma(w(h)) = \frac{\frac{f_t s}{E} - 2(h - y_0)\varphi\beta_1}{(1-\beta_1)}\frac{E}{s}$$

$$= \frac{f_t - 2(h - y_0)\frac{\theta f_t}{h}\beta_1}{(1-\beta_1)}$$

$$= \frac{f_t}{(1-\beta_1)}\left\{1 - 2(d + y^*)\frac{\theta}{h}\beta_1\right\}$$

$$= \frac{f_t}{(1-\beta_1)}\left\{1 - 2\left(\alpha + \frac{1}{2\theta}\right)\theta\beta_1\right\}$$

$$= \frac{f_t}{(1-\beta_1)}\{1 - 2\alpha\theta\beta_1 - \beta_1\}$$

$$= \frac{f_t}{(1-\beta_1)}\{(1-\beta_1) - 2\alpha\theta\beta_{11}\}$$

$$= f_t\left\{1 - \frac{2\alpha\theta\beta_1}{(1-\beta_1)}\right\}$$

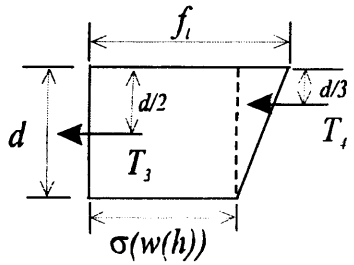

$$T_2 = f_t th\left\{\alpha - \frac{2\alpha^2\theta\beta_1}{1-\beta}\right\}$$

$$T_3 = f_t dt\left\{1 - \frac{2\alpha\theta\beta_1}{1-\beta}\right\}$$

$$T_4 = \frac{1}{2} f_t dt \frac{2\alpha\theta\beta_1}{(1-\beta_1)}$$

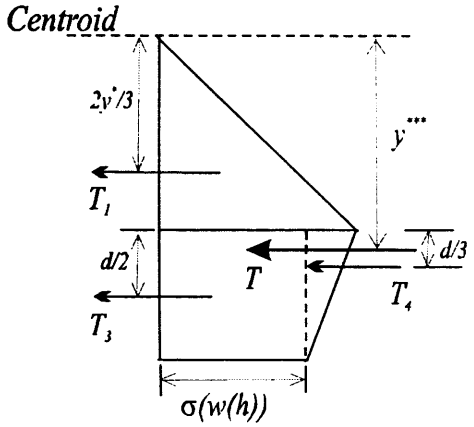

$$T_2 y^{**} = T_3\frac{d}{2} + T_4\frac{d}{3} \quad \Rightarrow y^{**} = \frac{T_3\frac{d}{2} + T_4\frac{d}{3}}{T_2}$$

We need $T_2 y^{**}$, so no need to calculate y^{**}.

$$y^{***} = \frac{T_1\left(\frac{2y^*}{3}\right) + T_3\left(y^* + \frac{d}{2}\right) + T_4\left(y^* + \frac{d}{3}\right)}{T_1 + T_3 + T_4}$$

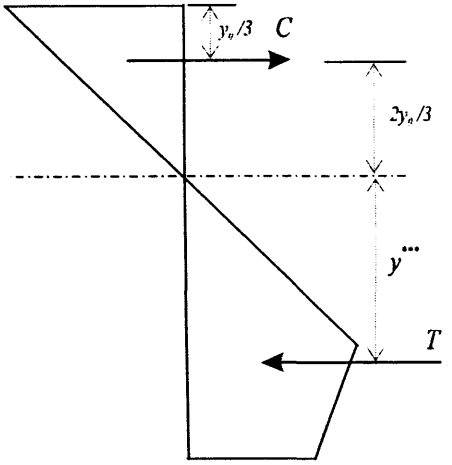

Note: $T_1+T_3+T_4 = C = T$

$$M = C\left(\frac{2y^*}{3} + y^{***}\right)$$

$$= C\left(\frac{2y^*}{3}\right) + Cy^{***}$$

$$= C\left(\frac{2y_0}{3}\right) + T_1\left(\frac{2y^*}{3}\right) + T_3\left(y^*\right) + T_3\left(\frac{d}{2}\right) + T_4\left(y^*\right) + T_4\left(\frac{d}{3}\right)$$

$$= C\left(\frac{2y_0}{3}\right) + \left(T_1 + T_3 + T_4\right)y^* - T_1\left(\frac{y^*}{3}\right) + T_3\left(\frac{d}{2}\right) + T_4\left(\frac{d}{3}\right)$$

$$= C\left(y^* + \frac{2y_0}{3}\right) - T_1\left(\frac{y^*}{3}\right) + T_3\left(\frac{d}{2}\right) + T_4\left(\frac{d}{3}\right)$$

$$= C\left(h - y_0 - d + \frac{2y_0}{3}\right) - T_1\left(\frac{y^*}{3}\right) + T_3\left(\frac{d}{2}\right) + T_4\left(\frac{d}{3}\right)$$

$$= C\left(h - d + \frac{y_0}{3}\right) - T_1\left(\frac{y^*}{3}\right) + T_3\left(\frac{d}{2}\right) + T_4\left(\frac{d}{3}\right)$$

$$= \frac{f_t h^2 t}{\theta}\left\{(1-\alpha)\theta - \frac{1}{2}\right\}^2\left(1 - \alpha - \frac{y_0}{3h}\right) - \frac{1}{2}f_t y^* t.\frac{y^*}{3}$$

$$+ \frac{f_t d^2 t}{2}\left(1 - \frac{2\alpha\theta\beta_1}{1-\beta_1}\right) + \frac{f_t d^2 t}{3}.\frac{\alpha\theta\beta_1}{1-\beta_1}$$

$$\frac{6M}{f_t h^2 t} = \frac{6}{\theta}\left(1 - \alpha - \frac{1}{3} + \frac{\alpha}{3} + \frac{y^*}{3h}\right)\left\{(1-\alpha)\theta - \frac{1}{2}\right\}^2 - \frac{y^{*2}}{h^2} + \frac{3d^2}{h^2}\left(1 - \frac{2\alpha\theta\beta_1}{1-\beta_1}\right)$$

$$+ \frac{2d^2}{h^2}.\frac{\alpha\theta\beta_1}{1-\beta_1}$$

$$\mu = \frac{6}{\theta}\left(\frac{2}{3} - \frac{2\alpha}{3} - \frac{1}{3} + \frac{\alpha}{3} + \frac{1}{6\theta}\right)\left\{(1-\alpha)\theta - \frac{1}{2}\right\}^2 - \frac{1}{4\theta^2} + 3\alpha^2\left(1 - \frac{2\alpha\theta\beta_1}{1-\beta_1}\right)$$

$$+ \frac{2\alpha^3\theta\beta_1}{1-\beta_1}$$

$$\mu = \frac{4}{\theta}\left(1 - \alpha + \frac{1}{4\theta}\right)\left\{(1-\alpha)\theta - \frac{1}{2}\right\}^2 - \frac{1}{4\theta^2} + \alpha^2\left(3 - \frac{6\alpha\theta\beta_1}{1-\beta_1} + \frac{2\alpha\theta\beta_1}{1-\beta_1}\right)$$

$$\mu = \frac{4}{\theta}\left(1 - \alpha + \frac{1}{4\theta}\right)\left\{(1-\alpha)\theta - \frac{1}{2}\right\}^2 - \frac{1}{4\theta^2} + \alpha^2\left(3 - \frac{4\alpha\theta\beta_1}{1-\beta_1}\right)$$

$$
\begin{aligned}
\mu &= \frac{4\theta^2}{\theta}\left((1-\alpha)+\frac{1}{4\theta}\right)\left\{(1-\alpha)-\frac{1}{2\theta}\right\}^2 - \frac{1}{4\theta^2} + \alpha^2\left(3-\frac{4\alpha\theta\beta_1}{1-\beta_1}\right) \\
&= 4\theta\left(1-\alpha+\frac{1}{4\theta}\right)\left(1-2\alpha-\alpha^2-\frac{1-\alpha}{\theta}+\frac{1}{4\theta^2}\right)-\frac{1}{4\theta^2}+\alpha^2\left(3-\frac{4\alpha\theta\beta_1}{1-\beta_1}\right) \\
&= \{4(1-\varepsilon)\theta+1\}\left\{(1-\alpha)^2-\frac{(1-\alpha)}{\theta}+\frac{1}{4\theta^2}\right\}-\frac{1}{4\theta^2}+3\alpha^2-\frac{4\alpha^3\theta\beta_1}{1-\beta_1} \\
&= (1-\alpha)^2-\frac{1-\alpha}{\theta}+\frac{1}{4\theta^2}+4(1-\alpha)^3\theta-4(1-\alpha)^2+\frac{1-\alpha}{\theta}-\frac{1}{4\theta^2}+3\alpha^3 \\
&\quad -\frac{4\alpha^3\theta\beta_1}{1-\beta_1} \\
&= 4(1-\alpha)^3\theta-3(1-2\alpha+\alpha^2)+3\alpha^3-\frac{4\alpha^3\theta\beta_1}{1-\beta_1} \\
&= 4\theta\left\{1-3\alpha+3\alpha^2-\alpha^3-\frac{\alpha^3\beta_1}{1-\beta_1}\right\}-3+6\alpha
\end{aligned}
$$

$$
\boxed{= 4\theta\left(1-3\alpha+3\alpha^2-\frac{\alpha^3}{1-\beta_1}\right)-3+6\alpha}
$$

Phase II (crack length, α)

$$\frac{y^*}{h}=\frac{1}{2\theta}\ ;\ \frac{y_0}{h}=1-\alpha-\frac{1}{2\theta}$$

$$h-d=y^*+d,\qquad y^*=\frac{sf_t}{2\varphi E}$$

$$y_1=y_0+\frac{1}{2\varphi}\left[\zeta_1-w_1(\beta_1-1)\right]\varphi=\frac{\theta s f_t}{hE}\quad,\quad \zeta_1=\frac{f_t s b_1}{E}=\frac{f_t s}{E}\qquad (b_1=1)$$

$$y_1=y_0+\frac{hE}{2\varphi s f_t}\left[\frac{f_t s}{E}-w_1(\beta_1-1)\right]$$

$$\sigma_w(w(h)=\frac{\zeta_2-2(y-y_0)\varphi\beta_2}{1-\beta_2}\frac{E}{s}\quad ;\ \zeta_2=\frac{f_t b_2 s}{E},$$

$$\sigma_w(w(y_1)=\frac{\zeta_1-2(y_1-y_0)\varphi\beta_1}{1-\beta_i}\frac{E}{s}$$

$$(h-y_0)=y^*+d=\frac{h}{2\theta}+d$$

$$(y_1-y_0)=\frac{hE}{2\varphi s f_t}\left[\frac{f_t s}{E}-w_1(\beta_1-1)\right]$$

Total compressive force, C

$$C=\frac{1}{2}f_t\frac{y_0}{y^*}.y_0 t=\frac{f_t h t}{\theta}\left\{(1-\alpha)\theta-\frac{1}{2}\right\}^2,\quad \text{as before}$$

Note:

$$y_1-y_0=\frac{h}{2\theta}\left[1+\frac{f_t s}{E}w_1(1-\beta_1)\right]$$

$$y_1-y_0-y^*=\frac{f_t s}{E}\frac{h}{2\theta}w_1(1-\beta_1)=\frac{a_1}{\beta_1}\frac{h}{2\theta}w_1(1-\beta_1)$$

Appendix B1: Derivation of the Moment μ and Crack Length α_h for Phases I, II, and III

Total tensile force, T

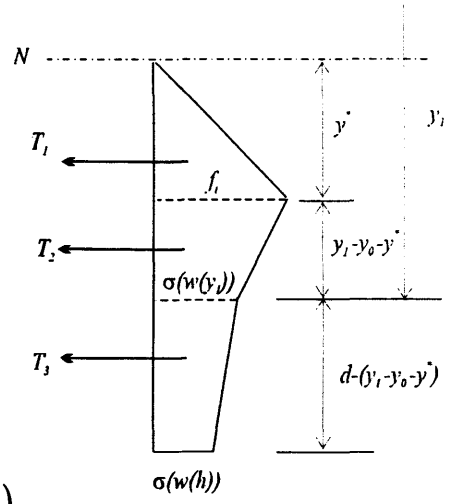

$$T_1 = \frac{1}{2} f_t y^* t = \frac{f_t t h}{4\theta}$$

$$T_2 = \frac{t}{2}\{f_t + \sigma(w(y_1))\}(y_1 - y_0 - y^*)$$

$$T_3 = \frac{t}{2}\{\sigma(w(y_1)) + \sigma(w(h))\}\{d - (y_1 - y_0 - y^*)\}$$

$$T_2 + T_3 = \frac{t}{2}\{f_t(y_1 - y_0 - y^*)\} + \frac{t}{2}\sigma(w(y_1))(y_1 - y_0 - y^*)$$
$$+ \frac{t}{2}\sigma(w(y_1))d + \frac{t}{2}\sigma(w(h))d - \frac{t}{2}\sigma(w(y_1))(y_1 - y_0 - y^*)$$
$$- \frac{t}{2}\sigma(w(h))(y_1 - y_0 - y^*)$$
$$= \frac{t}{2}\{f_t - \sigma(w(h))\}(y_1 - y_0 - y^*) + \frac{t}{2} d\{\sigma(w(y_1)) + \sigma(w(h))\}$$

$$w_1 = \frac{1 - b_2}{a_1 - a_2}, \qquad w_2 = \frac{b_2}{a_2} \tag{8.3}$$

Note: $1 - a_1 w_1 = 1 - \dfrac{(1-b_2)a_1}{a_1 - a_2} = \dfrac{b_2\beta_1 - \beta_2}{(\beta_1 - \beta_2)}$

$$y_1 - y_0 - y^* = \frac{w_1}{2\varphi}(1 - \beta_1) = \frac{h}{2\theta} \cdot \frac{(1-b_2)(1-\beta)}{(\beta_1 - \beta_2)}$$

$$T_2 + T_3 = \frac{f_t t h}{4\theta}\left\{1 - \frac{[b_2 - (1 + 2\alpha\theta)]\beta_2}{1 - \beta_2}\right\}\frac{(1-b_2)(1-\beta_1)}{(\beta_1 - \beta_2)}$$
$$+ \frac{f_t t d}{2}\left\{\frac{b_2\beta_1 - \beta_2}{\beta_1 - \beta_2} + \frac{b_2 - (1 + 2\alpha\theta)\beta_2}{(1 - \beta_2)}\right\}$$
$$= \frac{f_t t h}{4\theta}\left\{\frac{(1-b_2) + 2\alpha\theta\beta_2}{(1-\beta_2)}\right\}\frac{(1-b_2)(1-\beta_1)}{(\beta_1 - \beta_2)}$$
$$+ \frac{f_t t d}{2}\left\{\frac{b_2\beta_1 - \beta_2}{\beta_1 - \beta_2} + \frac{b_2 - (1 + 2\alpha\theta)\beta_2}{(1 - \beta_2)}\right\}$$

$$T_1 + T_2 = \frac{f_t t h}{4\theta}\left\{1 + \frac{(1-b_2) + 2\alpha\theta\beta_2}{(1-\beta_2)}\right\}\frac{(1-b_2)(1-\beta_1)}{(\beta_1 - \beta_2)}$$

$$T_1 + T_2 + T_3 = \frac{f_t t h}{4\theta}\left\{1 + \left[\frac{(1-b_2) + 2\alpha\theta\beta_2}{(1-\beta_2)}\right]\frac{(1-b_2)(1-\beta_1)}{(\beta_1 - \beta_2)}\right\}$$
$$+ \frac{f_t t h}{4\theta}\left\{2\alpha\theta\left[\frac{b_2\beta_1 - \beta_2}{\beta_1 - \beta_2} + \frac{b_2 - (1 + 2\alpha\theta)\beta_2}{1 - \beta_2}\right]\right\} = C$$

$$4\left\{(1-\alpha)\theta - \frac{1}{2}\right\}^2 = RHS$$

Appendix B1: Derivation of the Moment μ and Crack Length α_h for Phases I, II, and III

$$4\theta^2\left\{\alpha^2-2\left(1-\frac{1}{2\theta}\right)\alpha+\left(1+\frac{1}{2\theta}\right)^2\right\}=RHS$$

$$RHS=1+\frac{(1-b_2)^2(1-\beta_1)}{(1-\beta_2)(\beta_1-\beta_2)}+\frac{2\alpha\theta\beta_2(1-b_2)(1-\beta_1)}{(1-\beta_2)(\beta_1-\beta_2)}+\frac{2\alpha\theta(b_2\beta_1-\beta_2)}{(\beta_1-\beta_2)}$$
$$+\frac{2\alpha\theta b_2}{1-\beta_2}-\frac{2\alpha\theta\beta_2}{1-\beta_2}-\frac{(2\alpha\theta)^2\beta_2}{1-\beta_2}$$
$$=1+\frac{(1-b_2)^2(1-\beta_1)}{(1-\beta_2)(\beta_1-\beta_2)}-\frac{(2\alpha\theta)^2\beta_2}{1-\beta_2}+\frac{2\alpha\theta}{(1-\beta_2)(\beta_1-\beta_2)}$$
$$+\{\beta_2(1-b_2)(1-\beta_1)+(1-\beta_2)(b_2\beta_1-\beta_2)+(b_2-\beta_2)(\beta_1-\beta_2)\}$$
$$=1+\frac{(1-b_2)^2(1-\beta_1)}{(1-\beta_2)(\beta_1-\beta_2)}-\frac{4\alpha^2\theta^2\beta_2}{1-\beta_2}+\frac{4\alpha\theta(b_2-\beta_2)}{1-\beta_2}$$

$C=T\Rightarrow$

$$4\alpha^2\theta^2+\frac{4\alpha^2\theta^2\beta_2}{1-\beta_2}-8\alpha\theta^2+4\alpha\theta-\frac{4\alpha\theta(b_2-\beta_2)}{1-\beta_2}+4\theta^2\left(1-\frac{1}{2\theta}\right)^2$$
$$-\frac{(1-b_2)^2(1-\beta_1)}{(1-\beta_2)(\beta_1-\beta_2)}-1=0$$

$$\Rightarrow\frac{4\alpha^2\theta^2}{1-\beta_2}-8\alpha\theta^2+\frac{4\alpha\theta-4\alpha\theta(b_2-\beta_2)}{1-\beta_2}+4\theta^2\left(1-\frac{1}{2\theta}\right)^2-\frac{(1-b_2)^2(1-\beta_1)}{(1-\beta_2)(\beta_1-\beta_2)}-1=0$$

$$\Rightarrow\alpha^2-2(1-\beta_2)\alpha+\frac{1}{\theta}(1-b_2)\alpha+(1-\beta_2)\left(1-\frac{1}{2\theta}\right)^2-\frac{(1-b_2)^2(1-\beta_1)}{(1-\beta_2)(\beta_1-\beta_2)}-\frac{(1-\beta_2)}{4\theta^2}=0$$

$$\Rightarrow\alpha^2-2\alpha\left\{(1-\beta_2)-\frac{(1-b_2)}{2\theta}\right\}+(1-\beta_2)\left(1-\frac{1}{\theta}\right)-\frac{(1-b_2)^2(1-\beta_1)}{(1-\beta_2)(\beta_1-\beta_2)4\theta^2}=0$$

$$\alpha=(1-\beta_2)-\frac{(1-b_2)}{2\theta}--\frac{1}{2}\sqrt{\begin{matrix}4\left\{(1-\beta_2)-\frac{(1-b_2)}{2\theta}\right\}^2-4(1-\beta_2)\left(1-\frac{1}{\theta}\right)\\+\frac{4(1-b_2)^2(1-\beta_1)}{(\beta_1-\beta_2)4\theta^2}\end{matrix}}$$

$$=\left(1-\beta_2-\frac{1-b_2}{2\theta}\right)-\sqrt{\begin{matrix}(1-\beta_2)^2-\frac{(1-b_2)(1-\beta_2)}{\theta}+\frac{(1-b_2)^2}{4\theta^2}-(1-\beta_2)\left(1-\frac{1}{\theta}\right)\\+\frac{(1-b_2)^2(1-\beta_1)}{(\beta_1-\beta_2)4\theta^2}\end{matrix}}$$

$$=\left(1-\beta_2-\frac{1-b_2}{2\theta}\right)-\sqrt{(1-\beta_2)^2-(1-\beta_2)\left(1-\frac{b_2}{\theta}\right)+\frac{(1-b_2)^2(1-\beta_2)}{4\theta^2(\beta_1-\beta_2)}}$$

$$=\left(1-\beta_2-\frac{1-b_2}{2\theta}\right)-\sqrt{(1-\beta_2)\left\{1-\beta_2-1+\frac{b_2}{\theta}+\frac{(1-b_2)^2}{4\theta^2(\beta_1-\beta_2)}\right\}}$$

$$\boxed{\alpha=1-\beta_2-\frac{1-b_2}{2\theta}-\sqrt{(1-\beta_2)\left\{\frac{(1-b_2)^2}{4\theta^2(\beta_1-\beta_2)}-\beta_2+\frac{b_2}{\theta}\right\}}}$$

Phase II (moment, μ)

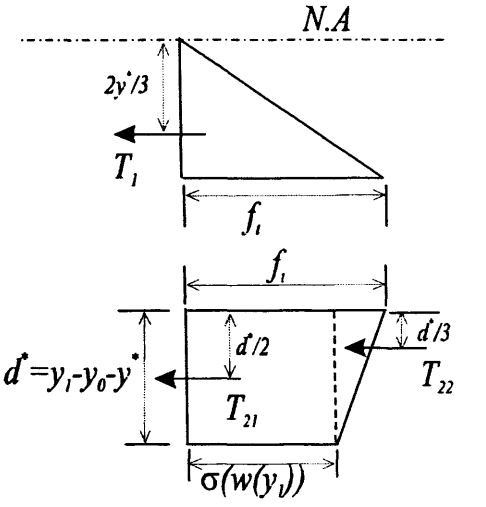

$$T_1 = \frac{1}{2} f_t y^* t = \frac{f_t t h}{4\theta}$$

$$T_2 = T_{21} + T_{22}$$

$$T_{21} = \sigma(w(y_1)) t d^*$$

$$T_{22} = \frac{1}{2}\{f_t - \sigma(w(y_1))\} t d^*$$

$$T_3 = T_{31} + T_{32}$$

$$T_{31} = \{\sigma(w(h))\} t (d - d^*)$$

$$T_{32} = \frac{1}{2}\{\sigma(w(y_1)) - \sigma(w(h))\} t (d - d^*)$$

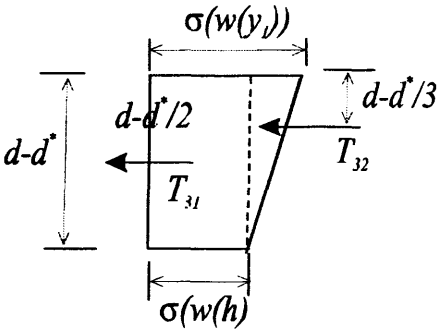

$$d^* = y_1 - y_0 - y^*$$

$$d - d^* = h - y_1$$

$$\sigma(w(y_1)) = \frac{f_t(b_2\beta_1 - \beta_2)}{(\beta_1 - \beta_2)}$$

$$\sigma(w(h)) = \frac{f_t(b_2 - (1+2\alpha\theta)\beta_2)}{(1_1 - \beta_2)}$$

$$T_{21} = \frac{f_t t d^* (b_2\beta_1 - \beta_2)}{(\beta_1 - \beta_2)}$$

$$T_{22} = \frac{t d^* f_t}{2}\left\{1 - \frac{(b_2\beta_1 - \beta_2)}{(\beta_1 - \beta_2)}\right\}$$

$$T_{31} = \left\{\frac{f_t t (d - d^*)(b_2 - (1+2\alpha\theta)\beta_2)}{(1_1 - \beta_2)}\right\}$$

$$T_{32} = \frac{f_t t (d - d^*)}{2}\left\{\frac{(b_2\beta_1 - \beta_2)}{(\beta_1 - \beta_2)} - \frac{(b_2 - (1+2\alpha\theta)\beta_2)}{(1_1 - \beta_2)}\right\}$$

Note: $T_1+T_2+T_3 = C = T$

$$y^{***} = \frac{T_1\left(\frac{2y^*}{3}\right)+T_{21}\left(y^*+\frac{d^*}{2}\right)+T_{22}\left(y^*+\frac{d^*}{3}\right)+T_{31}\left(y^*+d^*+\frac{d-d^*}{2}\right)+T_{32}\left(y^*+d^*+\frac{d-d^*}{3}\right)}{T_1+T_{21}+T_{22}+T_{31}+T_{32}}$$

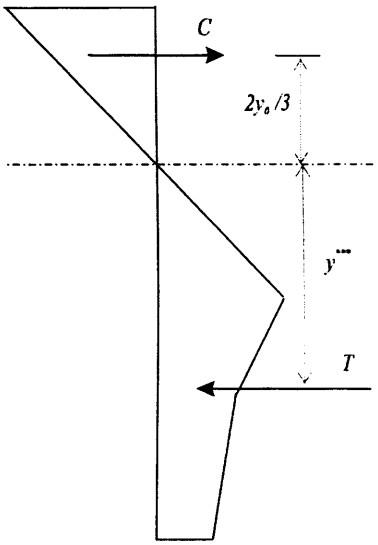

$$M = C\left(\frac{2y_0}{3}+y^{***}\right)$$
$$= C\left(\frac{2y_0}{3}\right)+Cy^{***}$$

$$M = C\left(\frac{2y_0}{3}\right)+T_1\left(\frac{2y^*}{3}\right)+T_{21}\left(y^*+\frac{d^*}{2}\right)+T_{22}\left(y^*+\frac{d^*}{3}\right)$$
$$+T_{31}\left(y^*+d^*+\frac{d-d^*}{2}\right)+T_{32}\left(y^*+d^*+\frac{d-d^*}{3}\right)$$

$$M = C\left(\frac{2y_0}{3}\right)+T_1\left(\frac{2y^*}{3}\right)+T_{21}(y^*)+T_{21}\left(\frac{d^*}{2}\right)+T_{22}(y^*)+T_{22}\left(\frac{d^*}{3}\right)+T_{31}(y^*)+T_{31}(d^*)$$
$$+T_{31}\left(\frac{d-d^*}{2}\right)+T_{32}(y^*)+T_{32}(d^*)+T_{32}\left(\frac{d-d^*}{3}\right)$$

$$M = C\left(\frac{2y_0}{3}\right)+(T_1+T_{21}+T_{22}+T_{31}+T_{32})y^*-T_1\left(\frac{y^*}{3}\right)+(T_1+T_{21}+T_{22}+T_{31}+T_{32})d^*-T_1d^*$$
$$-\frac{1}{2}T_{21}d^*-\frac{2}{3}T_{22}d^*-\frac{1}{2}T_{31}d^*-\frac{1}{2}T_{32}d^*+\frac{1}{2}T_{31}d+\frac{1}{2}T_{32}d$$

$$M = C\left(\frac{2y_0}{3}\right)+Cy^*-T_1\left(\frac{y^*}{3}\right)+Cd^*-d^*(T_1+T_{21}+T_{22}+T_{31}+T_{32})+\frac{1}{2}T_{21}d^*+\frac{1}{3}T_{22}d^*$$
$$+\frac{1}{2}T_{31}d^*+\frac{1}{2}T_{32}d^*+\frac{1}{2}T_{31}d+\frac{1}{2}T_{32}d$$

$$M = C\left(\frac{2y_0}{3}\right)+Cy^*-T_1\left(\frac{y^*}{3}\right)+Cd^*-Cd^*+\frac{1}{2}T_{21}d^*+\frac{1}{3}T_{22}d^*+\frac{1}{2}T_{31}d^*+\frac{1}{2}T_{32}d^*$$
$$+\frac{1}{2}T_{31}d+\frac{1}{2}T_{32}d$$

$$M = \frac{f_t ht}{\theta}\left\{(1-\alpha)\theta - \frac{1}{2}\right\}^2\left(\frac{2y_0}{3}\right) + \frac{f_t ht}{\theta}\left\{(1-\alpha)\theta - \frac{1}{2}\right\}^2 y^* - T_1\left(\frac{y^*}{3}\right) + \frac{1}{2}T_{21}d^* + \frac{1}{3}T_{22}d^* + \frac{1}{2}T_{31}d^* + \frac{1}{2}T_{32}d^* + \frac{1}{2}T_{31}d + \frac{1}{2}T_{32}d$$

$$M = \frac{f_t ht}{\theta}\left\{(1-\alpha)\theta - \frac{1}{2}\right\}^2\left(y^* + \frac{2y_0}{3}\right) - \frac{f_t th}{4\theta}\left(\frac{y^*}{3}\right) + \frac{d^*}{2}\frac{f_t t\, d^*(b_2\beta_1 - \beta_2)}{(\beta_1 - \beta_2)} + \frac{1}{3}\frac{t\,d^{*2} f_t}{2}\left\{1 - \frac{(b_2\beta_1 - \beta_2)}{(\beta_1 - \beta_2)}\right\} + \frac{d^*}{2}\left\{\frac{f_t t(d-d^*)(b_2 - (1+2\alpha\theta)\beta_2)}{(1_1 - \beta_2)}\right\} + \frac{d^*}{2}\frac{f_t t(d-d^*)}{2}\left\{\frac{(b_2\beta_1 - \beta_2)}{(\beta_1 - \beta_2)} - \frac{(b_2 - (1+2\alpha\theta)\beta_2)}{(1_1 - \beta_2)}\right\} + \frac{d}{2}\left\{\frac{f_t t(d-d^*)(b_2 - (1+2\alpha\theta)\beta_2)}{(1_1 - \beta_2)}\right\} + \frac{d}{2}\frac{f_t t(d-d^*)}{2}\left\{\frac{(b_2\beta_1 - \beta_2)}{(\beta_1 - \beta_2)} - \frac{(b_2 - (1+2\alpha\theta)\beta_2)}{(1_1 - \beta_2)}\right\}$$

$$d^* = y_1 - y_0 - y^* == \frac{h}{2\theta}\cdot\frac{(1-b_2)(1-\beta)}{(\beta_1 - \beta_2)} \quad , \qquad d - d^* = h - y_1$$

$$M = \frac{f_t ht}{\theta}\left\{(1-\alpha)\theta - \frac{1}{2}\right\}^2\left(h - d - \frac{y_0}{3}\right) - \frac{f_t th}{4\theta}\left(\frac{y^*}{3}\right) + \left\{\frac{h}{4\theta}\cdot\frac{(1-b_2)(1-\beta)}{(\beta_1 - \beta_2)}\right\}^2\frac{f_t t(b_2\beta_1 - \beta_2)}{2(\beta_1 - \beta_2)} + \frac{t f_t}{6}\left\{\frac{h}{4\theta}\cdot\frac{(1-b_2)(1-\beta)}{(\beta_1 - \beta_2)}\right\}^2\left\{1 - \frac{(b_2\beta_1 - \beta_2)}{(\beta_1 - \beta_2)}\right\} + \frac{1}{2}\frac{h}{4\theta}\cdot\frac{(1-b_2)(1-\beta)}{(\beta_1 - \beta_2)}\left\{\frac{f_t t(h-y_1)(b_2 - (1+2\alpha\theta)\beta}{(1_1 - \beta_2)}\right\} + \frac{1}{2}\frac{h}{4\theta}\cdot\frac{(1-b_2)(1-\beta)}{(\beta_1 - \beta_2)}\frac{f_t t(h-y_1)}{2}\left\{\frac{(b_2\beta_1 - \beta_2)}{(\beta_1 - \beta_2)} - \frac{(b_2 - (1+2\alpha\theta)\beta_2)}{(1_1 - \beta_2)}\right\} + \frac{d}{2}\left\{\frac{f_t t(h-y_1)(b_2 - (1+2\alpha\theta)\beta_2)}{(1_1 - \beta_2)}\right\} + \frac{d}{2}\frac{f_t t(h-y_1)}{2}\left\{\frac{(b_2\beta_1 - \beta_2)}{(\beta_1 - \beta_2)} - \frac{(b_2 - (1+2\alpha\theta)\beta_2)}{(1_1 - \beta_2)}\right\}$$

$$\boxed{\mu = 4\theta\left(1 - 3\alpha + 3\alpha^2 - \frac{\alpha^3}{1-\beta_2}\right) - 3 + 6\alpha - \frac{(1-b_2)(3\alpha^2 - (c/2\theta)^2)}{1-\beta_2}}$$

Phase III (crack length, α_h)

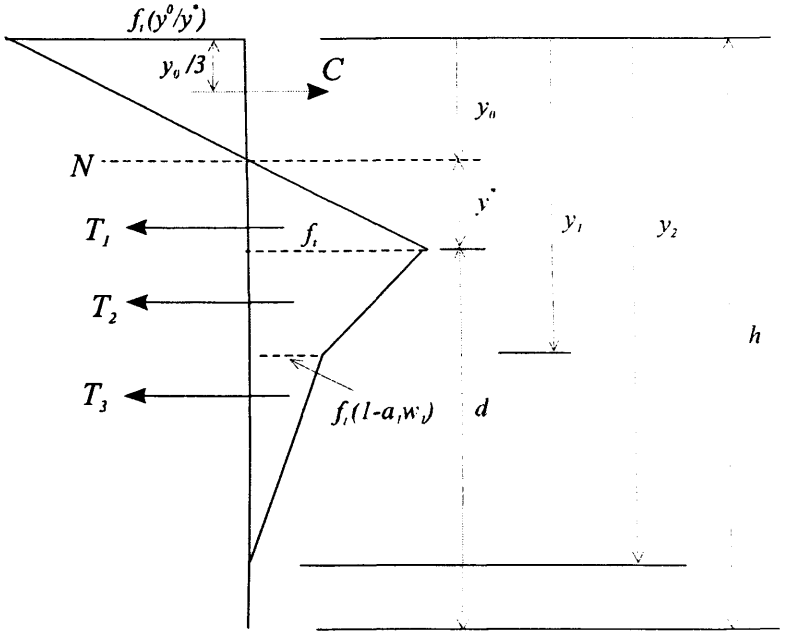

$$C = \frac{1}{2} f_t \frac{y_0}{y^*} . y_0 t = \frac{f_t h t}{\theta} \left\{ (1-\alpha)\theta - \frac{1}{2} \right\}^2, \quad \text{as before}$$

$$T_1 = \frac{1}{2} f_t y^* t = \frac{f_t t h}{4\theta} \quad , \quad \text{as before}$$

$$T_2 = \frac{t}{2} \{ f_t + f_t(1 - a_1 w_1) \} (y_1 - y_0 - y^*)$$

$$T_3 = \frac{t}{2} \{ f_t(1 - a_1 w_1) \} (y_2 - y_1)$$

$$y_1 = y_0 + \frac{1}{2\varphi} [\zeta_1 + w_1(1 - \beta_1)] \qquad \zeta_1 = \frac{f_t s b_1}{E} = \frac{f_t s}{E}$$

$$y_2 = y_0 + \frac{1}{2\varphi} [\zeta_2 + w_2(1 - \beta_2)] \qquad \zeta_2 = \frac{f_t b_2 s}{E}$$

$$y_1 - y_0 - y^* = \frac{1}{2\varphi} \left[\frac{f_t s}{E} + w_1(1 - \beta_1) \right] - \frac{h}{2\theta}$$

$$= y^* + \frac{w_1}{2\varphi}(1 - \beta_1) - y^* = \frac{w_1}{2\varphi}(1 - \beta_1); \qquad y^* = \frac{s f_t}{2\varphi E}$$

$$y_2 - y_1 = \frac{1}{2\varphi} [\zeta_2 - \zeta_1 + w_2(1 - \beta_2) - w_1(1 - \beta_1)]$$

$$= y^*(b_2 - 1) + \frac{1}{2\varphi} [w_2(1 - \beta_2) - w_1(1 - \beta_1)]$$

$$= -\frac{h}{2\theta}(b_2 - 1) + \frac{1}{2\varphi} [w_2(1 - \beta_2) - w_1(1 - \beta_1)]$$

Note: $w_1 = \dfrac{1-b_2}{a_1-a_2}$, $\qquad w_2 = \dfrac{b_2}{a_2}$

$$y_1 - y_0 - y^* = \frac{w_1}{2\varphi}(1-\beta_1) = \frac{(1-b_2)(1-\beta_1)}{2\varphi(a_1-a_2)} = \frac{(1-b_2)(1-\beta_1)}{\frac{2\varphi E}{f_t s}(\beta_1-\beta_2)} = \frac{y^*(1-b_2)(1-\beta_1)}{(\beta_1-\beta_2)}$$

$$= \frac{h}{2\theta}\frac{(1-b_2)(1-\beta_1)}{(\beta_1-\beta_2)}$$

$$y_2 - y_1 = \frac{h}{2\theta}(1-b_2) + \frac{1}{2\varphi}\left[\frac{b_2}{a_2}(1-\beta_2) - \frac{(1-b_2)}{a_2-a_1}(1-\beta_1)\right]$$

$$= \frac{h}{2\theta}(1-b_2) + \frac{1}{2\varphi}\left[\frac{b_2(1-\beta_2)}{\beta_2} - \frac{(1-b_2)(1-\beta_1)}{\beta_1-\beta_2}\right]$$

$$= \frac{h}{2\theta}\left[\frac{-(1-b_2)\beta_2(\beta_1-\beta_2) + b_2(1-\beta_2)(\beta_1-\beta_2) - (1-b_2)(1-\beta_2)\beta_2}{\beta_2(\beta_1-\beta_2)}\right]$$

$$= \frac{h}{2\theta}\left[\frac{(1-\beta_2)(\beta_1 b_2 - \beta_2)}{\beta_2(\beta_1-\beta_2)}\right]$$

$$T_2 + T_3 = \frac{f_t th}{4\theta}(2-a_1w_1)\frac{(1-b_2)(1-\beta_1)}{(\beta_1-\beta_2)} + \frac{f_t th}{4\theta}(1-a_1w_1)\frac{(1-\beta_2)(\beta_1 b_2-\beta_2)}{\beta_2(\beta_1-\beta_2)}$$

Note: $\qquad a_1w_1 = \dfrac{(1-b_2)a_1}{(a_1-a_2)} = \dfrac{(1-b_2)\beta_1}{\beta_1-\beta_2}$

$$1 - a_1w_1 = 1 - \frac{(1-b_2)\beta_1}{\beta_1-\beta_2} = \frac{b_2\beta_1-\beta_2}{(\beta_1-\beta_2)}$$

$$2 - a_1w_1 = 2 - \frac{(1-b_2)\beta_1}{\beta_1-\beta_2} = \frac{\beta_1-2\beta_2+b_2\beta_1}{(\beta_1-\beta_2)} = 1 + \frac{b_2\beta_1-\beta_2}{\beta_1-\beta_2}$$

$$T_2 + T_3 = \frac{f_t th}{4\theta}\left\{\left[1+\frac{b_2\beta_1-\beta_2}{\beta_1-\beta_2}\right]\frac{(1-b_2)(1-\beta_1)}{(\beta_1-\beta_2)} + \frac{(b_2\beta_1-\beta_2)^2(1-\beta_2)}{(\beta_1-\beta_2)^2\beta_2}\right\}$$

$$= \frac{f_t th}{4\theta}\left\{\frac{(1-b_2)(1-\beta_1)}{(\beta_1-\beta_2)} + \frac{(b_2\beta_1-\beta_2)(1-b_2)(1-\beta_1)}{(\beta_1-\beta_2)^2} + \frac{(b_2\beta_1-\beta_2)^2(1-\beta_2)}{(\beta_1-\beta_2)^2\beta_2}\right\}$$

$$= \frac{f_t th}{4\theta}\left\{\frac{(1-b_2)(1-\beta_1)}{(\beta_1-\beta_2)} + \frac{(b_2\beta_1-\beta_2)}{(\beta_1-\beta_2)^2\beta_2}[(1-b_2)(1-\beta_1)\beta_2 + (b_2\beta_1-\beta_2)\beta_2]\right\}$$

$$= \frac{f_t th}{4\theta}\left\{\frac{(1-b_2)(1-\beta_1)}{(\beta_1-\beta_2)} + \frac{(b_2\beta_1-\beta_2)(b_2-\beta_2)}{(\beta_1-\beta_2)\beta_2}\right\}$$

$$= \frac{f_t th}{4\theta}\left\{\frac{\beta_2 - b_2\beta_2 - \beta_1\beta_2 + b_2\beta_1\beta_2 + b_2^2\beta_1 - \beta_2 b_2 - b_2\beta_1\beta_2 + \beta_2^2}{\beta_2(\beta_1-\beta_2)}\right\}$$

$$T_1 + T_2 + T_3 = \frac{f_t th}{4\theta}\left\{1 + \frac{\beta_2 - b_2\beta_2 - \beta_1\beta_2 + b_2^2\beta_1 - \beta_2 b_2 + \beta_2^2}{\beta_2(\beta_1 - \beta_2)}\right\}$$

$$= \frac{f_t th}{4\theta}\left\{\frac{\beta_1\beta_2 - \beta_2^2 + \beta_2 - b_2\beta_2 - \beta_1\beta_2 + b_2^2\beta_1 - \beta_2 b_2 + \beta_2^2}{\beta_2(\beta_1 - \beta_2)}\right\}$$

$$= \frac{f_t th}{4\theta}\left\{\frac{\beta_2(1-b_2) + b_2(b_2\beta_1 - \beta_2)}{\beta_2(\beta_1 - \beta_2)}\right\}$$

$C = T \quad \Rightarrow$

$$4\left\{(1-\alpha)\theta - \frac{1}{2}\right\}^2 = \frac{\beta_2(1-b_2) + b_2(b_2\beta_1 - \beta_2)}{\beta_2(\beta_1 - \beta_2)}$$

$$\alpha^2 - 2\left(1 - \frac{1}{2\theta}\right)\varepsilon + \left(1 - \frac{1}{2\theta}\right)^2 - \frac{\beta_2(1-b_2) + b_2(b_2\beta_1 - \beta_2)}{4\theta^2\beta_2(\beta_1 - \beta_2)} = 0$$

$$\alpha = \left(1 - \frac{1}{2\theta}\right) - \frac{1}{2}\sqrt{4\left(1 - \frac{1}{\theta}\right)^2 - 4\left(1 - \frac{1}{\theta}\right)^2 + \frac{4\beta_2(1-b_2) + 4b_2(b_2\beta_1 - \beta_2)}{4\theta^2\beta_2(\beta_1 - \beta_2)}}$$

$$\alpha = 1 - \frac{1}{2\theta} - \frac{1}{2\theta}\sqrt{\frac{\beta_2(1-b_2) + 4b_2(b_2\beta_1 - \beta_2)}{\beta_2(\beta_1 - \beta_2)}}$$

$$\boxed{\alpha = 1 - \frac{1}{2\theta}\left\{1 + \sqrt{\frac{(1-b_2)^2}{\beta_1 - \beta_2} + \frac{b_2^2}{\beta_2}}\right\}}$$

Phase III (moment, μ)

$$C = \frac{f_t ht}{\theta}\left\{(1-\alpha)\theta - \frac{1}{2}\right\}^2, \quad \text{as before}$$

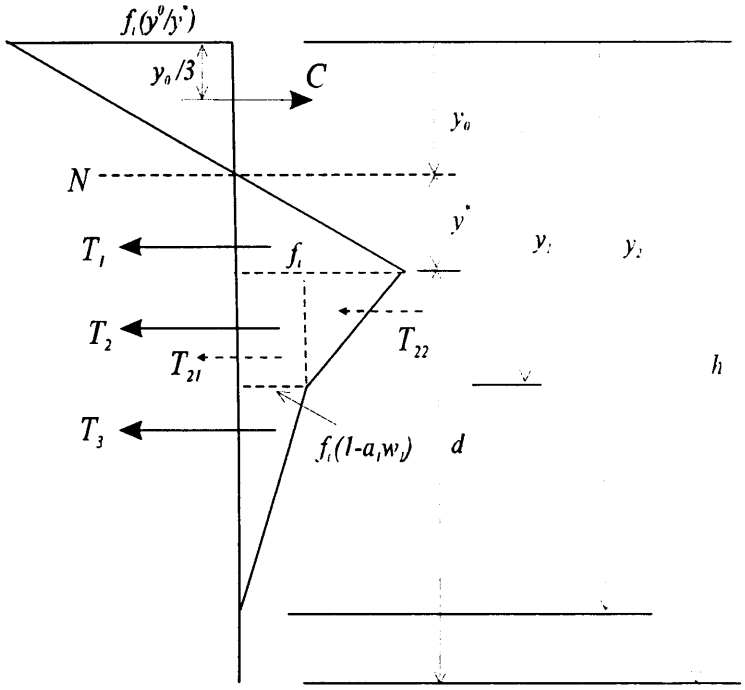

$$T_1 = \frac{1}{2} f_t y^* t = \frac{f_t th}{4\theta}, \quad \text{as before}$$

$$T_2 = T_{21} + T_{22}$$

$$T_{21} = tf_t(1-a_1w_1)(y_1 - y_0 - y^*)$$

$$T_{22} = \frac{t}{2}\{f_t - f_t(1-a_1w_1)\}(y_1 - y_0 - y^*)$$

$$T_3 = \frac{t}{2}\{f_t(1-a_1w_1)\}(y_2 - y_1)$$

$$y_1 - y_0 - y^* = = \frac{h}{2\theta}\cdot\frac{(1-b_2)(1-\beta)}{(\beta_1 - \beta_2)}, \quad \text{as before}$$

$$y_2 - y_1 = \frac{h}{2\theta}\left[\frac{(1-\beta_2)(\beta_1 b_2 - \beta_2)}{\beta_2(\beta_1 - \beta_2)}\right], \quad \text{as before}$$

$$y^{***} = \frac{T_1\left(\frac{2y^*}{3}\right) + T_{21}\left(\frac{y_1 - y_0 - y^*}{2} + y^*\right) + T_{22}\left(\frac{y_1 - y_0 - y^*}{3} + y^*\right) + T_3\left(\frac{y_2 - y_1}{3} + (y_1 - y_0)\right)}{T_1 + T_{21} + T_{22} + T_3}$$

Note: $T_1+T_2+T_3 = C = T$

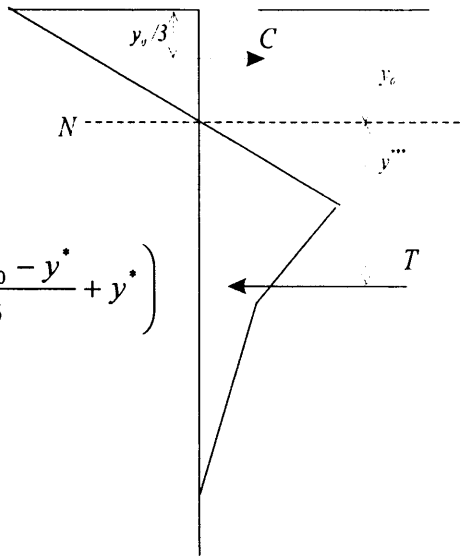

$$M = C\left(\frac{2y_0}{3} + y^{***}\right)$$

$$= C\left(\frac{2y_0}{3}\right) + Cy^{***}$$

$$M = C\left(\frac{2y_0}{3}\right) + T_1\left(\frac{2y^*}{3}\right) + T_{21}\left(\frac{y_1 - y_0 - y^*}{2} + y^*\right) + T_{22}\left(\frac{y_1 - y_0 - y^*}{3} + y^*\right)$$

$$+ T_3\left(\frac{y_2 - y_1}{3} + (y_1 - y_0 - y^*) + y^*\right)$$

let $c = \frac{(1-b_2)(1-\beta)}{(\beta_1 - \beta_2)}$ *then,* $y_1 - y_0 - y^* = \frac{hc}{2\theta}$

$$M = C\left(\frac{2y_0}{3}\right) + T_1\left(\frac{2y^*}{3}\right) + T_{21}\left(\frac{hc}{4\theta} + y^*\right) + T_{22}\left(\frac{hc}{6\theta} + y^*\right) + T_3\left(\frac{h}{6\theta}\left[\frac{(1-\beta_2)(\beta_1 b_2 - \beta_2)}{\beta_2(\beta_1 - \beta_2)}\right] + \frac{hc}{2\theta} + y^*\right)$$

$$M = C\left(\frac{2y_0}{3}\right) + (T_1 + T_{21} + T_{22} + T_3)y^* - T_1\left(\frac{y^*}{3}\right) + T_{21}\left(\frac{hc}{4\theta}\right) + T_{22}\left(\frac{hc}{6\theta}\right) + T_3\left(\frac{h}{6\theta}\left[\frac{(1-\beta_2)(\beta_1 b_2 - \beta_2)}{\beta_2(\beta_1 - \beta_2)}\right] + \frac{hc}{2\theta}\right)$$

$$\frac{2y_0}{3} + y^* = 1 - \alpha - \frac{y_0}{3h}, \quad y^* = \frac{h}{2\theta} \qquad \text{, as before}$$

$$M = C\left(\frac{2y_0}{3} + y^*\right) - T_1\left(\frac{y^*}{3}\right) + T_{21}\left(\frac{hc}{4\theta}\right) + T_{22}\left(\frac{hc}{6\theta}\right) + T_3\left(\frac{h}{6\theta}\left[\frac{(1-\beta_2)(\beta_1 b_2 - \beta_2)}{\beta_2(\beta_1 - \beta_2)}\right] + \frac{hc}{2\theta}\right)$$

$$M = \frac{f_t ht}{\theta}\left\{(1-\alpha)\theta - \frac{1}{2}\right\}^2\left(1 - \alpha - \frac{y_0}{3h}\right) - \frac{f_t th}{4\theta}\left(\frac{h}{6\theta}\right) + f_t(1 - a_1 w_1)\frac{hc}{2\theta}\left(\frac{hc}{4\theta}\right) + \frac{t}{2}\{f_t - f_t(1 - a_1 w_1)\}\frac{hc}{2\theta}\left(\frac{hc}{6\theta}\right) + \left\{\frac{t}{2}\{f_t(1 - a_1 w_1)\}\frac{h}{2\theta}\left[\frac{(1-\beta_2)(\beta_1 b_2 - \beta_2)}{\beta_2(\beta_1 - \beta_2)}\right]\right\}\left(\frac{h}{6\theta}\left[\frac{(1-\beta_2)(\beta_1 b_2 - \beta_2)}{\beta_2(\beta_1 - \beta_2)}\right] + \frac{hc}{2\theta}\right)$$

$$1 - a_1 w_1 = \frac{b_2\beta_1 - \beta_2}{(\beta_1 - \beta_2)} \qquad \text{, as before}$$

$$M = \frac{f_t ht}{\theta}\left\{(1-\alpha)\theta - \frac{1}{2}\right\}^2\left(1 - \alpha - \frac{y_0}{3h}\right) - \frac{f_t th}{4\theta}\left(\frac{h}{6\theta}\right) + tf_t\frac{b_2\beta_1 - \beta_2}{(\beta_1 - \beta_2)}\frac{hc}{2\theta}\left(\frac{hc}{4\theta}\right) + \frac{f_t t}{2}\left\{1 - \frac{b_2\beta_1 - \beta_2}{(\beta_1 - \beta_2)}\right\}\frac{hc}{2\theta}\left(\frac{hc}{6\theta}\right) + \left\{\frac{ft}{2}\left\{\frac{b_2\beta_1 - \beta_2}{(\beta_1 - \beta_2)}\right\}\frac{h}{2\theta}\left[\frac{(1-\beta_2)(\beta_1 b_2 - \beta_2)}{\beta_2(\beta_1 - \beta_2)}\right]\right\}\left(\frac{h}{6\theta}\left[\frac{(1-\beta_2)(\beta_1 b_2 - \beta_2)}{\beta_2(\beta_1 - \beta_2)}\right] + \frac{hc}{2\theta}\right)$$

$$M = \frac{f_t ht}{\theta}\left\{(1-\alpha)\theta - \frac{1}{2}\right\}^2\left(1-\alpha-\frac{1}{3}\left(1-\alpha-\frac{1}{2\theta}\right)\right) - \frac{f_t th^2}{24\theta^2}$$
$$+ \frac{f_t h^2 c^2}{8\theta^2}\frac{b_2\beta_1-\beta_2}{(\beta_1-\beta_2)} + \frac{f_t th^2 c^2}{24\theta^2}\left\{1-\frac{b_2\beta_1-\beta_2}{(\beta_1-\beta_2)}\right\}$$
$$+ \frac{fth^2}{24\theta^2}\left\{\frac{b_2\beta_1-\beta_2}{(\beta_1-\beta_2)}\right\}\left[\frac{(1-\beta_2)(\beta_1 b_2-\beta_2)}{\beta_2(\beta_1-\beta_2)}\right]^2 + \frac{fth^2 c}{8\theta^2}\left\{\frac{b_2\beta_1-\beta_2}{(\beta_1-\beta_2)}\right\}\frac{(1-\beta_2)(\beta_1 b_2-\beta_2)}{\beta_2(\beta_1-\beta_2)}$$

$$\frac{6M}{f_t h^2 t} = \frac{6}{h\theta}\left\{(1-\alpha)\theta - \frac{1}{2}\right\}^2\left(\frac{2}{3}+\frac{1}{2\theta}\right) - \frac{1}{4\theta^2} + \frac{3c^2}{4\theta^2}\frac{b_2\beta_1-\beta_2}{(\beta_1-\beta_2)} + \frac{c^2}{4\theta^2}\left\{1-\frac{b_2\beta_1-\beta_2}{(\beta_1-\beta_2)}\right\}$$
$$+ \frac{1}{4\theta^2}\left\{\frac{b_2\beta_1-\beta_2}{(\beta_1-\beta_2)}\right\}\left[\frac{(1-\beta_2)(\beta_1 b_2-\beta_2)}{\beta_2(\beta_1-\beta_2)}\right]^2 + \frac{3c}{4\theta^2}\left\{\frac{b_2\beta_1-\beta_2}{(\beta_1-\beta_2)}\right\}\frac{(1-\beta_2)(\beta_1 b_2-\beta_2)}{\beta_2(\beta_1-\beta_2)}$$

$$\boxed{\mu = 4\left(1-3\alpha+3\alpha^2-\alpha^3\right)\theta + (6\alpha-3) - 3\beta^2 + \frac{1}{4\theta}\left(1-\frac{b_2}{\beta_1}\right)\left(1+\frac{b_2}{\beta_2}+c\right)\left(1+\frac{\beta_1 c}{1-\beta_1}\right) + \left(\frac{c}{2\theta}\right)^2}$$

Appendix B2: The Algorithm for the Cracked Hinge Model

```
Program P_cod
!-------------------------------------------------------------------------
! Determination of the static response of FRC beams under three-point bending,
! using a bilinear tension-softening (stress - crack opening) relationship,
! based on the fictitious crack model.
!
! References:
! Hillerborg A. (1980). Analysis of fracture by means of the fictitious crack
!   model, particularly for fibre-reinforced concrete, Int J Cement Composites,
!   2, 177-184.
!
! Hillerborg A., Modeer M. and Petersson P. (1976). Analysis of crack formation
!   and crack growth in concrete by means of fracture mechanics and finite
!   elements, Cement Concrete Research, 6, 773-782.
!
! Olesen J.F. (2001). Fictitious crack propagation in fibre-reinforced concrete
!   beams, J Engineering Mechanics, 127, 272-280.
!
! The formulas referred in the program below are from Olesen (2001)
! Last modified: March 20 2003
!-------------------------------------------------------------------------
implicit none
character:: title(10)*8
integer(kind(1)), parameter:: ikd = kind(1), rkd = kind(0.d0)
real(rkd):: a1, a2, b2, alp0, db, E, ft, h, L, s, t
real(rkd):: alp, bet1, bet2, c, mu, rho, the01, the12, the23
real(rkd):: cod, P, the, v

call openfile

read (10,'( 10a8)')title
write (11,'(/10a8)')title

read (10,'( 10a8)')title
write (11,'(/10a8)')title
```

```
!~~~~~~~~~~~~~~~~~~~~~~~~~~~~~~~~~~~~~~~~~~~~~~~~~~~~~~~~~~~~~~~~~~~~~~~~~~~~~~~~
! alp0    initial notch depth to beam depth ratio
! db      beam depth                                    (mm)
! h       Height of the hinge                           (mm)
! L       Span length of the TPB                        (mm)
! t       Out-of-plane thickness of the hinge           (mm)
! s       Width of the hinge                            (mm)
!~~~~~~~~~~~~~~~~~~~~~~~~~~~~~~~~~~~~~~~~~~~~~~~~~~~~~~~~~~~~~~~~~~~~~~~~~~~~~~~~
read (10,*) alp0, db, L, t
h = (1.-alp0)*db
s = 0.5*h
write (11,'(/,4(a,f12.4))') ' alp=', alp0, ' h =', h, ' L =', L, ' t =', t

read (10,'(10a8)')title
!~~~~~~~~~~~~~~~~~~~~~~~~~~~~~~~~~~~~~~~~~~~~~~~~~~~~~~~~~~~~~~~~~~~~~~~~~~~~~~~~
! a1, b1(=1), a2 and b2 are parameters for the bilinear relation (2)
! a1 & a2                                       (/mm)
! E       Young modulus                         (GPa)
! ft      Tensile strength                      (GPa)
!~~~~~~~~~~~~~~~~~~~~~~~~~~~~~~~~~~~~~~~~~~~~~~~~~~~~~~~~~~~~~~~~~~~~~~~~~~~~~~~~
read (10,*)a1, a2, b2, E, ft
write (11,'(/,5(a,f12.4))') ' a1 =', a1, ' a2 =', a2, ' b2 = ', b2, ' E =', E, ' ft =', ft

rho=0.

call paramet(a1, a2, b2, bet1, bet2, c, E, ft, rho, s, the01, the12, the23)

write(11,'(//,1x,a,4x,a,7x,a)') 'Deflection (mm)', 'cmod (mm)', 'P (KN)'

the=-1.
do
 the=the+1.
 call moment(alp, b2, bet1, bet2, c, mu, rho, the, the01, the12, the23)

 v = deflect(E, ft, h, L, mu, s, the)

 if(v>10.)exit
```

```
 P = load(ft, h, L, mu, t)
 cod = cmod(alp, b2, bet1, bet2, db, E, ft, h, L, p, s, t, the, the01, the12, the23)

 write(11,'(3x,3(1x,f12.5))') v, cod, p
end do
stop

contains

subroutine openfile
!----------------------
! Open files
!----------------------
character :: fn*46 , res*50
integer(ikd):: it, ierr

input: do it=1,10
        write(*,'(/,a,/)')' Please enter your input file name:'
        read(*,*)fn              ;        fn = adjustl(fn)
        open(10, file= fn, status= 'old', action = 'read',iostat=ierr)
        if(ierr==0) exit
        write(*,'(/,a,/)')' Failing in opening your input file, please enter filename again:'
end do input

write(*,'(/,a,a,/)')' Your input file is: ', fn

fn = adjustr(fn)
res = fn//".out"    ;        res =   adjustl(res)

open(11, file= res, status= 'replace', action= 'write', iostat= ierr)
if(ierr/=0) stop ' Failing in opening file 11 '

write(*,'(a,a,/)')' Ouput your result in: ', res

return
end subroutine openfile
```

```
subroutine paramet(a1, a2, b2, bet1, bet2, c, E, ft, rho, s, the01, the12, the23)
!-----------------------------------------------------------------
!
! Define some parameters used later
!
!-----------------------------------------------------------------
real(rkd), intent(in ):: a1, a2, b2, E, ft, rho, s
real(rkd), intent(out):: bet1, bet2, c, the01, the12, the23

bet1=ft*a1*s/E                                          ! formula (9a)
bet2=ft*a2*s/E                                          ! formula (9a)
c = (1.-b2)*(1.-bet1)/(bet2-bet1)

the01=1.-rho                                            ! formula (16a)

the12=1./2.*(1.-rho-c+sqrt((1.-rho-c)**2+c*c/(bet1-1.)))        ! formula (16b)

the23=1./2.*(rho*(bet2-1.)+b2/bet2+sqrt(rho*rho*(bet2-1.)**2+2.*rho*(bet2-
1.)*b2/bet2+(1.-b2)**2/(bet1-bet2)+b2*b2/bet2))                 ! formula (16c)

return
end subroutine paramet


function load(ft, h, L, mu, t)              result(P)
!---------------------------------------
!
! Calculate load P via formula (27) for TPB
!
!---------------------------------------
real(rkd), intent(in):: ft, h, L, mu, t
real(rkd) :: P

P = 2./3.*ft*h*h*t/L*mu

end function load
```

```
function cmod(alp, b2, bet1, bet2, db, E, ft, h, L, p, s, t, the, the01, the12, the23)    result(cod)
!-------------------------------------------------------------------------
!
! Calculate cmod via formulae (17) and (18)
!
!-------------------------------------------------------------------------
real(rkd), intent(in):: alp, b2, bet1, bet2, db, E, ft, h, L, p, s, t, the, the01, the12, the23
real(rkd) :: a0, alp0, bi, beti, cod, cod0, m, sigm

! CMOD due to elastic deformation of the initial notch

a0 = db-h
alp0 = a0/db
m = p*L/4.
sigm = 6.*m/db/db/t
cod0 = 4.*sigm*a0/E*(0.76-2.28*alp0+3.87*alp0*alp0-2.04*alp0**3+0.66/(1.-alp0)/(1.-
alp0) )

! For phase I

if(the01<=the .and. the<the12)then
  bi = 1.
  beti = bet1

! For phase II

else if(the12<=the .and. the<the23)then
  bi = b2
  beti = bet2

! For phase III

else if(the23<=the) then
  bi =0.
  beti = 0.
end if
```

```
! For phase 0

if(0.<= the .and. the<= the01) then
  cod = 0.

! For phases I ~ III

else
  cod = s*ft/E*(1.-bi+2.*alp*the)/(1.-beti) !+s*ft/E*2.*the/h/(1.-beti)*(db-h)
end if

cod = cod + cod0

end function cmod


function deflect(E, ft, h, L, mu, s, the)      result(v)
!-----------------------------------------------------------------------
!
! Calculate the midspan deflection v via formulae (23) and (26) for TPB
!
!-----------------------------------------------------------------------
real(rkd), intent(in):: E, ft, h, L, mu, s, the
real(rkd) :: del, v

del = the+(L/3./s-1.)*mu
v = del*L/2.*s*ft/h/E

end function deflect
```

```
subroutine moment(alp, b2, bet1, bet2, c, mu, rho, the, the01, the12, the23)
!-------------------------------------------------------------------------
! Give the normalized moment mu in terms of the(ta) for the four phases
! 0 ~ III via formulae (13) ~ (15)
!-------------------------------------------------------------------------
real(rkd),intent(in ):: b2, bet1, bet2, c, rho, the, the01, the12, the23
real(rkd),intent(out):: alp, mu

! For phase 0

if(0.<=the .and. the<the01) then
  alp = 0.
  mu = the

! For phase I

else if(the01<=the .and. the<the12) then
  alp = 1.-bet1-sqrt((1.-bet1)*((1.-rho)/the-bet1))
  mu = 4.*(1.-3.*alp+3.*alp*alp-alp**3/(1.-bet1))*the+(6.*alp-3.)*(1.-rho)

! For phase II

else if(the12<=the .and. the<the23) then
  alp = 1.-bet2-(1.-b2)/2./the-sqrt((1.-bet2)*((1.-b2)**2/4./the/the/(bet1-bet2)-bet2+(b2-
rho)/the))
  mu = 4.*(1.-3.*alp+3.*alp**2-alp**3/(1.-bet2))*the+(6.*alp-3.)*(1.-rho)-(1.-
b2)*(3.*alp**2-(c/2/the)**2)/(1.-bet2)

! For phase III

else if(the23<=the) then
  alp = 1.-1./2./the*(1.+sqrt((1.-b2)**2/(bet1-bet2)+b2*b2/bet2-4.*rho*the))
  mu = 4.*(1.-3.*alp+3.*alp*alp-alp**3)*the+(6.*alp-3.)*(1.-rho)-
3.*alp*alp+1./4./the/the*(1.-b2/bet2)*(1.-b2/bet2+c)*(1.+bet1*c/(1.-bet1))+(c/2./the)**2
```

```
end if
return
end subroutine moment

end program P_cod
```

Appendix C

A Comparison of Hinge Model Prediction with Test Results

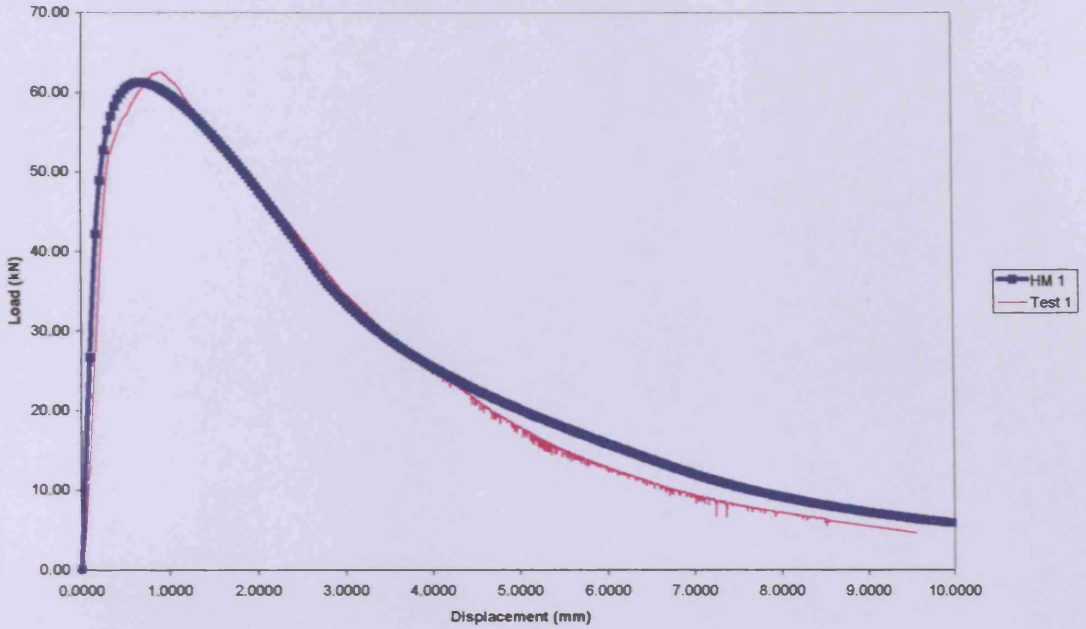

Figure C1: The experimental load-deformation curve for CARDIFRC® - Mix I specimen (100x100x500 mm) and the load-deformation curve generated by the hinge model (HM1).

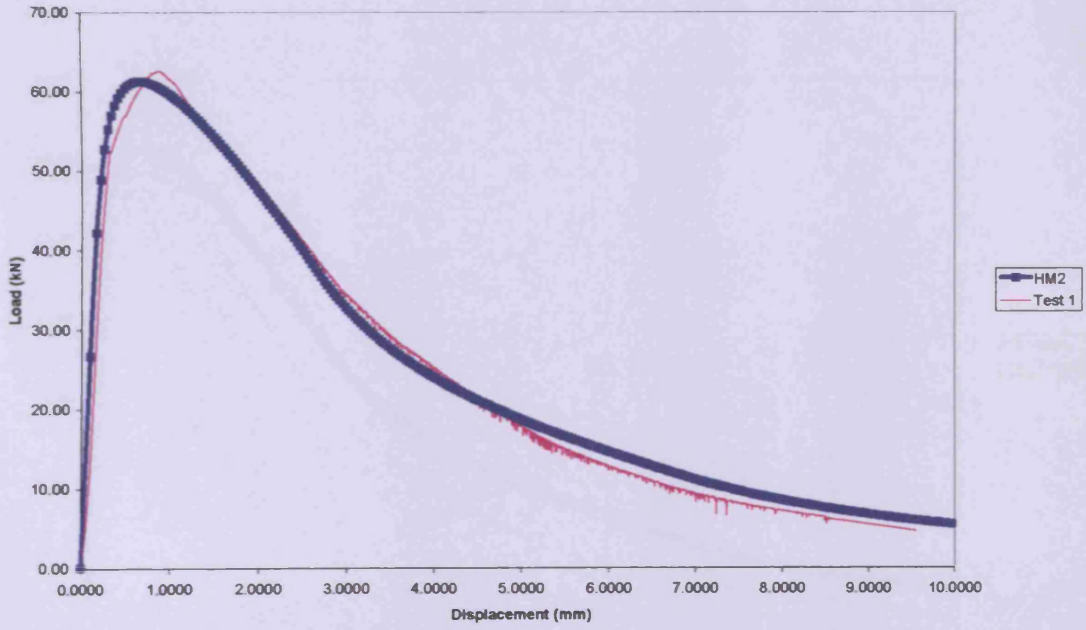

Figure C2: The experimental load-deformation curve for CARDIFRC® - Mix I specimen (100x100x500 mm) and the load-deformation curve generated by the hinge model (HM2).

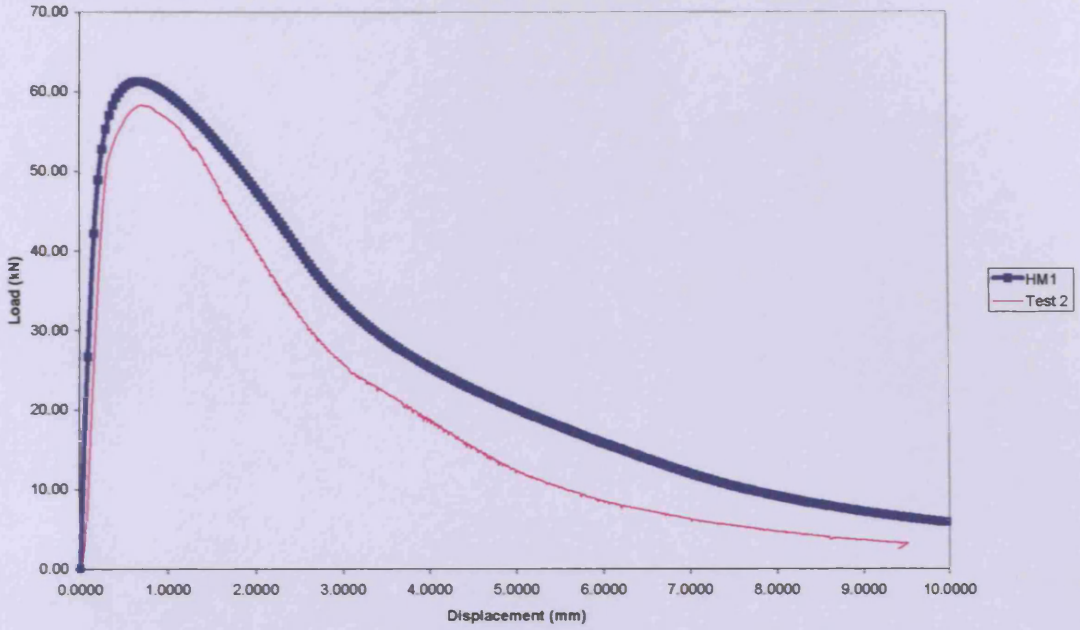

Figure C3: The experimental load-deformation curve for CARDIFRC® - Mix I specimen (100x100x500 mm) and the load-deformation curve generated by the hinge model (HM1).

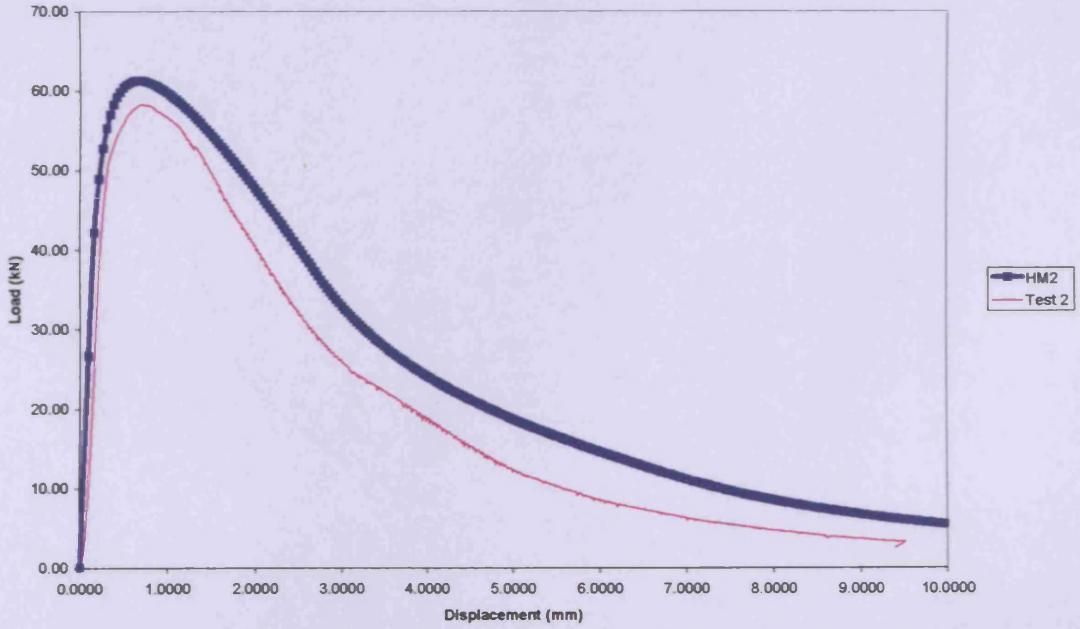

Figure C4: The experimental load-deformation curve for CARDIFRC® - Mix I specimen (100x100x500 mm) and the load-deformation curve generated by the hinge model (HM2).

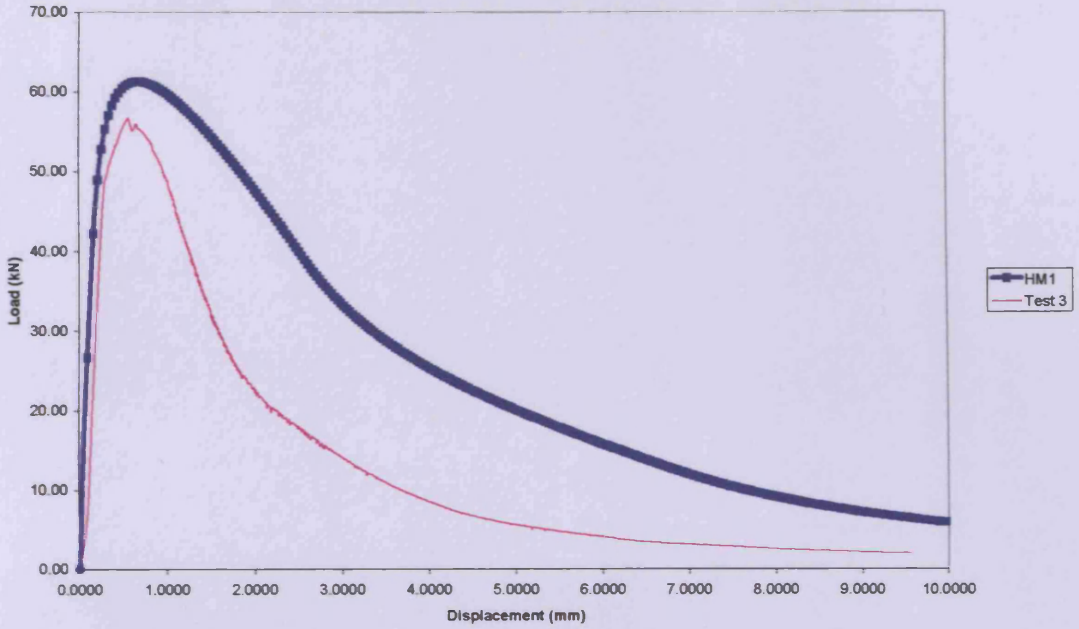

Figure C5: The experimental load-deformation curve for CARDIFRC® - Mix I specimen (100x100x500 mm) and the load-deformation curve generated by the hinge model (HM1).

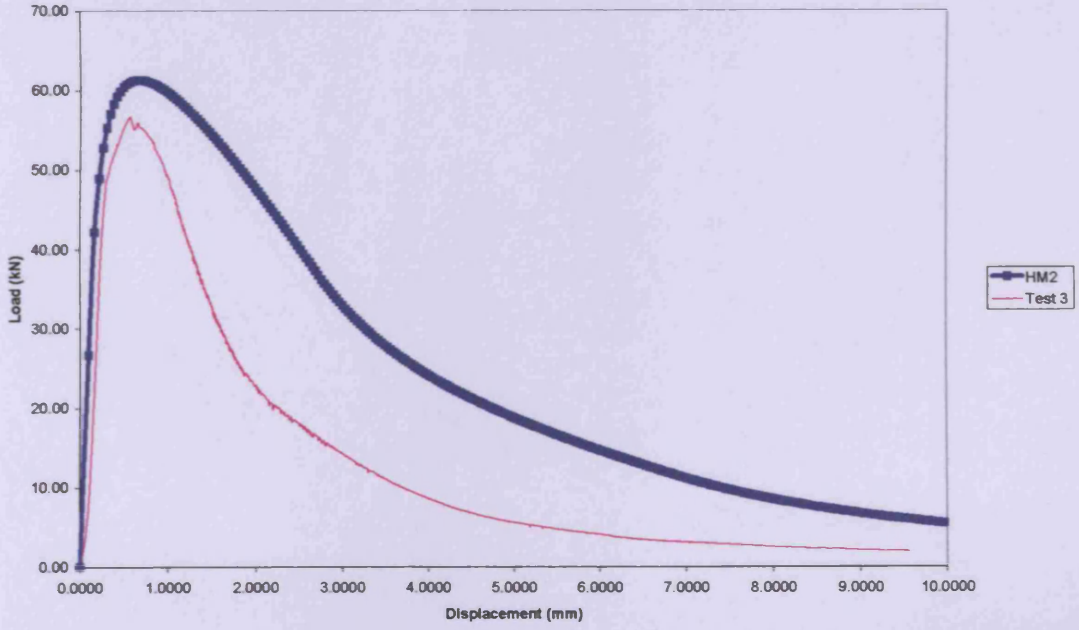

Figure C6: The experimental load-deformation curve for CARDIFRC® - Mix I specimen (100x100x500 mm) and the load-deformation curve generated by the hinge model (HM2).

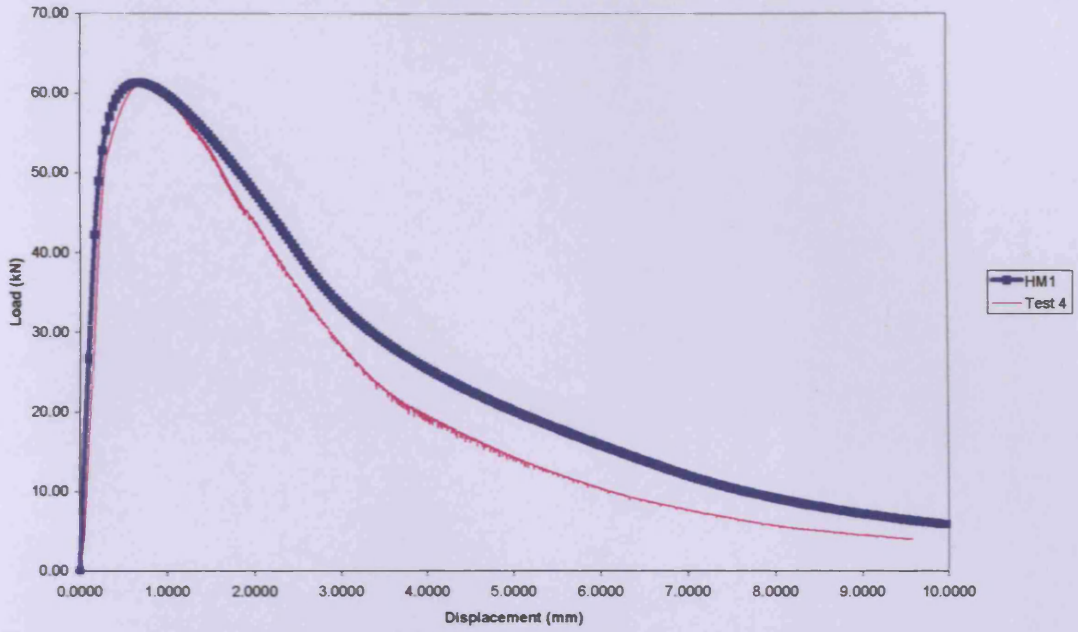

Figure C7: The experimental load-deformation curve for CARDIFRC® - Mix I specimen (100x100x500 mm) and the load-deformation curve generated by the hinge model (HM1).

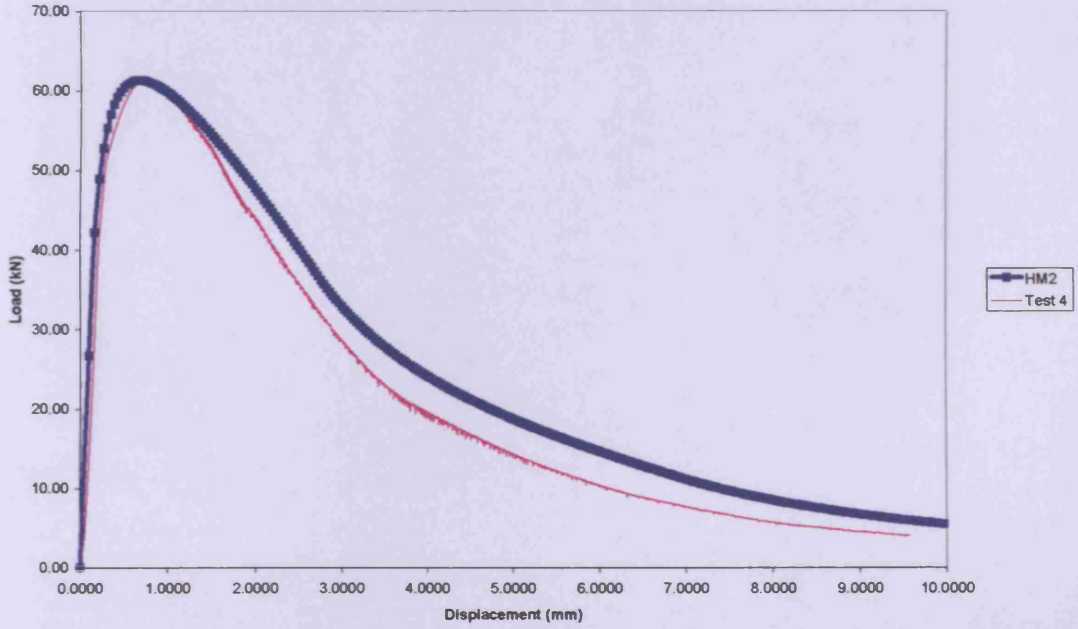

Figure C8: The experimental load-deformation curve for CARDIFRC® - Mix I specimen (100x100x500 mm) and the load-deformation curve generated by the hinge model (HM2).

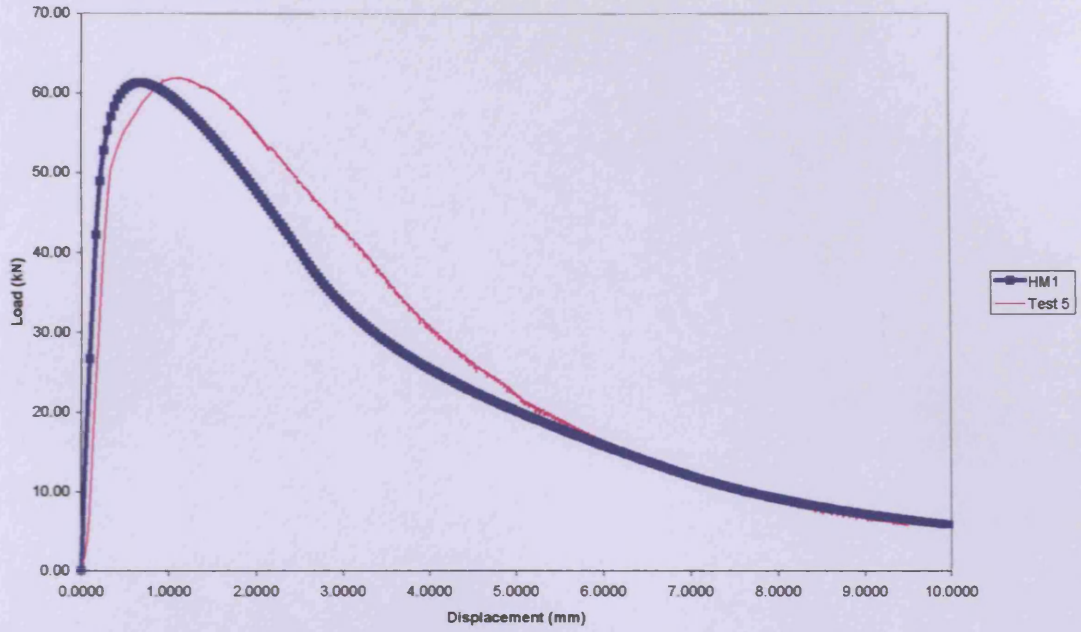

Figure C9: The experimental load-deformation curve for CARDIFRC® - Mix I specimen (100x100x500 mm) and the load-deformation curve generated by the hinge model (HM1).

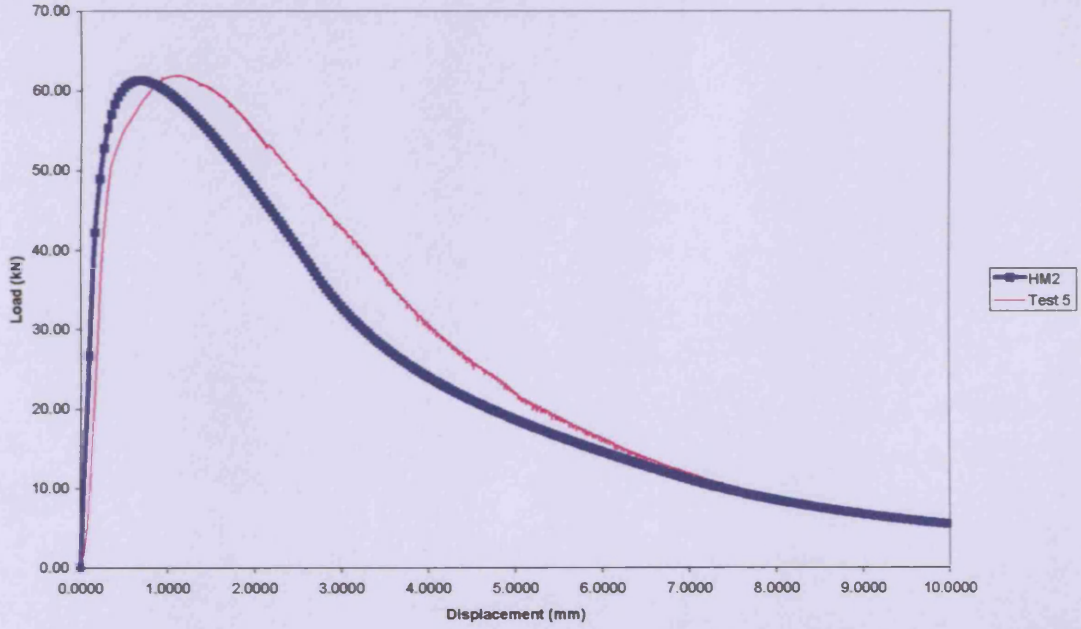

Figure C10: The experimental load-deformation curve for CARDIFRC® - Mix I specimen (100x100x500 mm) and the load-deformation curve generated by the hinge model (HM2).